

UNIVERSITY OF SOUTHERN QUEENSLAND



**Implementation of Conditional Moment
Closure in a Zero-Dimensional Model for HCCI
Engines and Comparison with Experiment**

A Dissertation Submitted by

Abdul Aziz Hairuddin
B. Eng (Mechanical)

for the award of

Doctor of Philosophy

2014

© 2014

Abdul Aziz Hairuddin, B.Eng (Mechanical)

All Rights Reserved

DEDICATION

To my beloved parents,

Hairuddin Ma'aruf & Darwilis Abdul Malik

My wife: Nor Azlin Kamarudin

& my daughter: Nur Aina Abdul Aziz

ABSTRACT

Homogeneous charge compression ignition (HCCI) engines have been an active research area recently due to their advantages in reducing emissions levels. Regulatory bodies, such as those in Europe, the United States and Japan, are imposing stringent vehicle emissions quality standards. Most automotive manufacturers are moving towards fuel efficient vehicles by developing hybrid (combination of two or more power sources) vehicles or improving on any conventional engine technology that can reduce emissions levels. Hybrid vehicles are receiving increasing attention from most manufacturers because they offer advantages including reduced emissions and providing good mileage per fuel tank. The HCCI engine has the potential to replace the current conventional engine used in hybrid vehicles, which can reduce the emissions levels further.

To improve the development work, simulations are undertaken to reduce research costs while maintaining good productivity because of their cost efficiency compared to experiments. For engine research, a zero-dimensional model is known for its advantage in reducing computational time compared with a multi-dimensional Computational Fluid Dynamics (CFD) approach. CFD yields more accurate results but requires greater computational resources and time, while a zero-dimensional model offers versatility in a reduced simulation time. However, the zero-dimensional model has the limitation of a shorter combustion duration and rapid pressure rise compared to the experiment. Also, the zero-dimensional model is incapable of using the actual intake air temperature and needs to be set higher than the actual.

Conditional Moment Closure (CMC) is a model for the mixing in the combustion chamber at modest computational cost, which considers the turbulent-chemistry interactions. An implementation of CMC into a zero-dimensional model for an HCCI engine application is new in the literature; most of the CMC studies use the CFD approach. The combined model is expected to improve the zero-dimensional model limitation while still keeping the advantages of the latter of not using relatively modest computational resources and time.

The goals of the thesis are to write a new computer program that implements the combined model and develop a new experimental test rig for HCCI. The main focus of the thesis is to obtain an improved result for the combined model against the zero-dimensional model, while the experimental results will be used for the purpose of validation. The thesis consists of nine chapters. The first two chapters after the introduction cover the HCCI engine background and performance irrespective of the fuel being used and a background to turbulence, which introduces some turbulent theories and conservation equations. Chapter 4 discusses the details of the numerical part, which consists of all the formulations being used in the combined model. Then Chapter 5 will validate the combined models against two experimental works from others, which use diesel and gasoline fuelled HCCI engines. Chapters 6 and 7 introduce the experimental work setup and engine performance comparison between SI and HCCI modes. Chapter 8 continues the validation of the combined model based on the HCCI engine developed in the experimental work, followed by the Conclusion.

The results show that the combined model has improved the zero-dimensional model limitation by using the actual intake air temperature instead of artificially increasing it. To some extent, the combined model has shown the ability to reduce the short burn duration in the zero-dimensional model, where the maximum in-cylinder pressure trace is slightly lower than with the zero-dimensional model, with a smooth profile in the vicinity of the peak. However, the combined model has a limitation in predicting the ignition point accurately when the air-to-fuel ratio varies. Besides these observed limitations, the combined model shows good agreement with the experiments. The experimental results that were obtained are consistent with the literature, including the limitation that the HCCI engine only operates with a low load operating condition. The emissions levels also agree with the literature, where the HCCI engine produces high unburned hydrocarbon and carbon monoxide in the exhaust. Therefore, future work is recommended to improve the combined model and also further develop the HCCI engine.

CERTIFICATION OF DISSERTATION

I certify that the ideas, designs and experimental work, simulation and software, results, analyses and conclusion set out in this dissertation are entirely my own effort, except where otherwise indicated and acknowledged.

I further certify that the work is original and has not been previously submitted for assessment in any other course or institution, except where specifically stated.

ABDUL AZIZ HAIRUDDIN

W0108673

Signature of Candidate

Date

ENDORSEMENT

Signature of Principal Supervisor,
Dr. Andrew Wandel

Date

Signature of Associate Supervisor,
Assoc. Prof. Dr. Talal Yusaf

Date

ACKNOWLEDGEMENTS

First and foremost, a special thank you to my principal supervisor, Dr. Andrew Wandel, for his strategic advice, guidance, constructive criticism and technical assistance with the numerical part of the study. To my associate supervisor, Assoc. Prof. Dr. Talal Yusaf, for his generosity, grounding advice and help with the experimental part of the study. I am truly appreciative of their help and support throughout the duration of my studies, which has helped me broaden my knowledge and develop new skills.

I would also like to thank P7 technical staff Joshua Hopf and Dr. Paul Baker for their help in developing my experimental setup. Mechanical workshop technicians Brian Aston and Chris Galligan for their help in fabricating the experimental apparatus. I have not forgotten Dean Beliveau and Richard Landers who helped develop the data acquisition system. Also to Adrian Blokland and Terry Byrne for providing technical support and help with providing the required resources.

A big thank to my parents and siblings for their endless support throughout my studies. My wife and daughter who helped brighten life in Australia. Also to my extended family members for their direct or indirect support. Their support in this manner is much appreciated.

Last but not least, I would like to express my greatest appreciation to the Ministry of Education Malaysia and Universiti Putra Malaysia which sponsored my studies. Without them, I would not have been able to achieve my goal.

ABDUL AZIZ HAIRUDDIN

University of Southern Queensland

November 2013

LIST OF PUBLICATIONS AND PRESENTATIONS

2013

Hairuddin, AA, Wandel, AP & Yusaf, T 2013, 'Implementation of CMC in a 0-D single-zone model of a diesel HCCI engine', in the Proceedings of the Australian Combustion Symposium (ACS2013), 6-8 Nov 2013, Perth, Australia.

Hairuddin, AA, Wandel, AP & Yusaf, T 2013, 'A homogeneous charge compression ignition engine: an introduction', in the 3rd Malaysian Postgraduate Conference (MPC 2013), 4-5 Jul 2013, Sydney, Australia.

Hairuddin, AA, Wandel, AP & Yusaf, T 2013, 'The effect of different heat transfer models on a diesel homogeneous charge compression ignition (HCCI) engine', *International Journal of Automotive and Mechanical Engineering*, vol. 8, pp. 1305-17, ISSN 2229-8649.

Hairuddin, AA, Yusaf, T & Wandel, AP 2014, 'A review of hydrogen and natural gas addition in diesel HCCI engines', *Renewable and Sustainable Energy Reviews*, vol. 32(April 2014), pp. 739-61.

2012

Hairuddin, AA, Yusaf, TF & Wandel, AP 2012, 'HCCI engine: numerical and experimental approach', in the USQ Combustion Meeting, 26 Sep 2012, Toowoomba, Australia. (Unpublished)

Noor, MM, Hairuddin, AA, Wandel, AP & Yusaf, TF 2012, 'Modelling of non-premixed turbulent combustion of hydrogen using conditional moment closure method', *IOP Conference Series: Materials Science and Engineering*, 36 (012036). pp. 1-17. ISSN 1757-899X

2011

Noor, MM, Hairuddin, AA, Wandel, AP & Yusaf, TF 2011, 'Implementation of conditional moment closure using the Taylor expansion and finite differences', in the 1st International Conference of Mechanical Engineering Research (ICMER 2011), 5-8 Dec 2011, Kuantan, Malaysia.

Hairuddin, AA, Yusaf, TF & Wandel, AP 2011, 'Predicting the combustion behaviour of a diesel HCCI engine using a zero-dimensional single-zone model', in the Australian Combustion Symposium 2011 (ACS 2011), 29 Nov-1 Dec 2011, Newcastle, Australia.

2010

Hairuddin, AA, Wandel, AP & Yusaf, T 2010, 'Hydrogen and natural gas comparison in diesel HCCI engines -a review', in the 2010 Southern Region Engineering Conference (SREC2010), 11-12 Nov 2010, Toowoomba, Australia.

TABLE OF CONTENTS

Dedication	iii
Abstract	iv
Certification of Dissertation	vi
Acknowledgements	vii
List of Publications and Presentations	viii
Table of Contents	x
List of Figures	xvii
List of Tables.....	xxvii
Chapter 1	1
Introduction	1
1.1 Background.....	1
1.2 Introduction	3
1.3 Research Focus	5
1.4 Objectives	8
1.5 Thesis Outline.....	9
Chapter 2	11
Literature Review	11
2.1 Introduction	11
2.2 Performance Comparison	11
2.2.1 State of the Art Current Internal Combustion Engines	11
2.2.2 Fuels Used in HCCI Engines	13
2.2.3 Natural Gas and Hydrogen with Diesel Operating Conditions	16
2.2.4 Gasoline Operated HCCI Engines.....	18
2.2.5 Peak Pressure and Temperature	19
2.2.6 Brake Thermal Efficiency	20
2.2.7 Brake Mean Effective Pressure	21
2.2.8 Exhaust Gas Emissions	23
2.2.9 Knocking	25
2.3 Injection Methods for Homogeneous Mixtures.....	26
2.3.1 Port Injection.....	27
2.3.2 Early Injection	27

Table of Contents

2.3.3	Late Injection	29
2.4	Ignition Control in HCCI Engines.....	30
2.4.1	Pre-Heat Intake Air	31
2.4.2	Pressurized Intake Air	32
2.4.3	Hydrogen Addition	32
2.4.4	Exhaust Gas Recirculation (EGR)	35
2.4.5	Addition of Dimethyl Ether (DME).....	36
2.4.6	Charge Stratification	36
2.5	Numerical Study of HCCI Engines	37
2.5.1	Chemical Kinetics	37
2.5.2	Numerical and CFD Environments.....	45
2.5.3	Single-Zone and Multi-Zone Models.....	46
2.5.4	Multi-Dimensional Models: CFD	48
2.5.5	Effect of Operating Parameters on Ignition Delay Time	49
2.5.6	Heat Transfer Model	53
2.5.7	Turbulence Models: RANS vs. LES	54
2.5.8	Mixing Models for Non-premixed Combustion	57
2.6	Conditional Moment Closure (CMC) Model in HCCI Engines.....	62
2.6.1	CMC Modelling in Zero-Dimensional Simulations.....	63
2.6.2	CMC Modelling in Multi-Dimensional Simulations	64
2.7	Conclusion.....	65
Chapter 3	67
Turbulence Modelling background	67
3.1	Introduction	67
3.2	Conservation Equations.....	68
3.2.1	Mass	68
3.2.2	Momentum	68
3.2.3	Species	69
3.2.4	Energy	69
3.3	Chemical Reactions	70
3.4	PDF and Statistical Descriptions	72
3.5	Turbulence Modelling	73
3.5.1	Averaging Techniques	75

Table of Contents

3.5.1.1	Reynolds Averaging.....	75
3.5.1.2	Favre Averaging.....	75
3.5.2	Turbulence Models.....	77
3.5.2.1	Zero-equation models	77
3.5.2.2	One-equation models	78
3.5.2.3	Two-equation models.....	79
3.5.3	Turbulent Reacting Flows	79
3.5.3.1	Dissipation and Scalar Transport	79
3.5.3.2	Mixture Fraction	80
3.5.4	Turbulent Combustion Models.....	81
3.5.4.1	Eddy Break-Up	81
3.5.4.2	Flamelet Models.....	82
3.5.4.3	Presumed PDF Methods	84
3.6	Conclusion.....	85
Chapter 4	87
Numerical Models	87
4.1	Introduction	87
4.2	Single-Zone Model.....	88
4.2.1	Zero-Dimensional Modelling.....	88
4.2.1.1	Engine Parameters	88
4.2.1.2	Valve Geometry	92
4.2.1.3	Conservation of Mass	96
4.2.1.4	Conservation of Species.....	96
4.2.1.5	Conservation of Energy	96
4.2.1.6	Heat Loss Model in Zero-Dimensional Model	98
4.2.2	Quasi-Dimensional Modelling	98
4.2.2.1	Turbulence Models	99
4.2.2.2	Heat Loss Model in Quasi-Dimensional Model	100
4.3	Mixing Model: Conditional Moment Closure.....	101
4.3.1	Conditional Transport Equations	101
4.3.1.1	Conditional Mass Fraction.....	102
4.3.1.2	Conditional Enthalpy Equation.....	107
4.3.2	Sub-models for the Unclosed Terms.....	108

Table of Contents

4.3.2.1	Conditional Scalar Dissipation	108
4.3.2.2	Presumed PDF	109
4.3.2.3	Chemical Source Term	112
4.3.2.4	Other sub-models	112
4.4	Implementation of CMC in Zero-Dimensional Model.....	114
4.4.1	Interfacing the Zero-Dimensional and CMC Codes	114
4.4.2	Numerical Solutions.....	116
4.4.2.1	Zero-Dimensional Solution	116
4.4.2.2	CMC Solution.....	119
4.4.2.3	Chemical Kinetics Mechanism: Cantera	122
4.4.3	Boundary Conditions	123
4.5	Conclusion.....	124
Chapter 5	127
Validation of CMC Models.....		127
5.1	Introduction	127
5.1.1	Chemical Reactions Mechanism for n-Heptane.....	128
5.1.2	Chemical Reactions Mechanism for Gasoline	128
Part 1: Diesel HCCI	130
5.2	Experimental Data	130
5.3	Zero-Dimensional Single-Zone Model.....	130
5.3.1	Validation.....	131
5.3.2	Heat Transfer Coefficient Models.....	132
5.3.2.1	Heat Fluxes	135
5.3.2.2	Heat Transfer Behaviour of Different AFR.....	137
5.4	CMC with Zero-Dimensional Model	139
5.4.1	Boundary and Initial Conditions	139
5.4.2	Comparison with Experiment	140
5.4.3	Turbulence Interactions.....	142
5.4.4	CMC Characteristics	144
5.4.4.1	Independence Test: Effects of Different CD	144
5.4.4.2	Grid Independence Test: Number of Bins of the CMC Model ..	147
5.4.4.3	Scalar Dissipation Rate	149
5.4.4.4	Chemical Reactions	151

Table of Contents

5.4.4.5	Conditional Temperature	164
5.5	Behaviour of CMC and Zero-D.....	167
5.5.1	Effect of Intake Temperature	167
5.5.2	Effect of Air-to-Fuel Ratio (AFR)	171
Part 2:	Gasoline HCCI.....	173
5.6	Experimental Data	173
5.7	CMC with Zero-Dimensional Model Validation.....	173
5.7.1	Independence Test.....	175
5.7.2	Chemical Reactions.....	178
5.7.3	Conditional Temperature.....	182
5.8	Conclusion.....	183
Chapter 6	185
Experimental Methodology	185
6.1	Introduction	185
6.2	Experimental Apparatus	187
6.2.1	Engine Test Bed	187
6.2.2	Dynamometer	190
6.2.3	Instrumentations	191
6.2.3.1	Thermocouples and Pressure Sensors	191
6.2.3.2	Rotary Encoder	193
6.2.3.3	Lambda Sensor.....	193
6.2.3.4	Airflow Meter	193
6.2.3.5	Exhaust Gas Analyser	194
6.2.4	Fuel Measurement.....	194
6.3	Modification to an HCCI Engine.....	195
6.3.1	Air Intake Heater.....	196
6.4	Electronic Control Unit (ECU).....	201
6.4.1	ECU Program	202
6.5	Experimental Techniques	207
6.6	Conclusion.....	209
Chapter 7	211
Experimental Performance Study of a Gasoline HCCI Engine	211
7.1	Introduction	211

Table of Contents

7.2	Power Curve Comparison of SI Engine with Manufacturer Data.....	211
7.3	Experimental Conditions.....	213
7.4	Engine Performance Comparison.....	214
7.4.1	In-Cylinder Pressure	214
7.4.2	Engine Power	218
7.4.3	Fuel Consumption	220
7.4.4	Engine Efficiency.....	223
7.4.5	Emissions Levels.....	224
7.4.5.1	NO _x	225
7.4.5.2	Unburned HC.....	228
7.4.5.3	CO and CO ₂	229
7.5	Conclusion.....	231
Chapter 8	233
CMC in a Zero-Dimensional Single-Zone Model of a Gasoline HCCI Engine	233
8.1	Introduction	233
8.2	Comparison with Experiment.....	233
8.2.1	Boundary and Initial Conditions	233
8.2.2	Validation.....	234
8.3	CMC Characteristics	236
8.3.1	Independence Test: Constant CD	236
8.3.2	Independence Test: Number of Bins of the CMC Model	240
8.3.3	Conditional Mass Fractions	242
8.3.4	Conditional Temperature	246
8.4	Parametric Study	247
8.4.1	Intake Temperature	247
8.4.2	Compression Ratio (CR).....	250
8.5	Conclusion.....	252
Chapter 9	253
Conclusion	253
9.1	Summary and Future Work	253
References	255
Appendix A	A.1
Derivation of Temperature Equation	A.1

Table of Contents

Appendix B	B.1
Experimental Setup Details	B.1
B.1 In-Cylinder Pressure Calibration	B.1
B.2 Electronic Control Unit (ECU)	B.3
B.3 Fuel Delivery System	B.6
B.4 Ignition System: TCI vs. CDI	B.9
Appendix C	C.1
Engineering Drawings	C.1
Appendix D	D.1
Engineering Drawings	D.1
Appendix E	E.1
Experiment: SWP	E.1

LIST OF FIGURES

Figure 1.1 Simulated earth surface air temperature increase by the year 2060 (Rob 2005).	2
Figure 1.2 The differences between SI, CI and HCCI engines, reproduced from William and Charles (2011).	4
Figure 1.3 Concentration of radicals H, OH, H ₂ O ₂ and HO ₂ for a pressure of 0.2 MPa (Aceves <i>et al.</i> 2000).	6
Figure 2.1 Movable flap is used inside the intake manifold (left) to generate tumble effects (right) in the combustion chamber with specially designed piston crown (Wurms, Grigo & Hatz 2003)	12
Figure 2.2 Intake temperature required for fuels to operate under HCCI mode with varying compression ratios, reproduced from (Aceves & Flowers 2004).	13
Figure 2.3 BMEP for different intake temperatures with varying energy ratio between natural gas and diesel. The shaded region shows the best energy ratio for natural gas-diesel HCCI engines, reproduced from (Nathan, Mallikarjuna & Ramesh 2010).	23
Figure 2.4 Knocking phenomena in a hydrogen HCCI engine for a single combustion event, reproduced from (Szwaja & Grab-Rogalinski 2009)	26
Figure 2.5 Spray structure simulation result for various initial conditions, reproduced from (Ryu, Kim & Lee 2005). The dark curved areas at the centre represent the piston crown surface, the black circle line is the piston crown edges, the outer circle is the cylinder wall which in turn resembles piston edge and the five radial lines represent fuel being injected from the centre. Spray structure behaviour does not change much with initial conditions, while it does with injection timing.....	28
Figure 2.6 Schematic diagram of the narrow spray angle injector, reproduced from (Kim & Lee 2007).	29
Figure 2.7 Piston bowl with toroidal geometry, reproduced from (Liu 2006).....	30
Figure 2.8 Hydrogen effect on the in-cylinder peak temperature and the ignition delay (Rattanapaibule & Aung 2005).	35
Figure 2.9 Ignition delay time for <i>n</i> -heptane validated against experiment for different pressures (Ra & Reitz 2008).	38

List of Figures

Figure 2.10 Summary of ignition burn rate and delay time for different type of fuels (Tanaka <i>et al.</i> 2003).	39
Figure 2.11 General layout of the quasi-dimensional simulation showing the interacting adiabatic core, thermal boundary layer and crevice regions, reproduced from (Fiveland & Assanis 2002).	46
Figure 2.12 Multi-zone model geometric configuration difference (a) HCCI engine, reproduced from (Komninos, Hountalas & Kouremenos 2004) (b) SI engines, reproduced from (Liu & Chen 2009).	47
Figure 2.13 Effects of various turbulence models in in-cylinder pressure trace compared with experiment in the single-zone zero-dimensional model (Agarwal <i>et al.</i> 1998).	48
Figure 2.14 The effect of initial temperature on ignition delay time for different fuels (Tanaka, Ayala & Keck 2003).	50
Figure 2.15 The effect of equivalence ratio on the ignition delay and burn rate for <i>n</i> -heptane, <i>iso</i> -octane and primary reference fuel (PRF) (Tanaka, Ayala & Keck 2003).	51
Figure 2.16 The effect of different pressure on the auto-ignition delay time for a stoichiometric mixture of <i>n</i> -heptane/air (Puduppakkam <i>et al.</i> 2010).	51
Figure 2.17 Effect of EGR on ignition delay for <i>n</i> -heptane fuel (Taylor 2006).	52
Figure 2.18 Ignition timing stability captured over time-lapse (Olsson <i>et al.</i> 2002).	53
Figure 2.19 Heat transfer model comparison with experiment, (a) heat transfer coefficient, (b) in-cylinder temperature difference, reproduced from (Soyhan <i>et al.</i> 2009).	54
Figure 2.20 The in-cylinder pressure comparison for experiment, modelling with chemical kinetics only and modelling with both chemical kinetics and turbulent mixing, reproduced from (Kong & Reitz 2002).	55
Figure 2.21 Illustration of an overall model for transient simulations (<i>Combustion</i> 2009; Janicka & Sadiki 2005; Peters 2000).	56
Figure 2.22 Scatter plots of temperature versus mixture fraction from experiment and simulations using LES, a) experimental data, b) IEM, c) MC and d) EMST. All figures reproduced from (Bisetti & Chen 2005).	59
Figure 2.23 Temperature at stoichiometric mixture fraction for various mixing models (Mitarai, Riley & Kosaly 2005; Wandel & Klimenko 2005).	62

List of Figures

Figure 2.24 Result for in-cylinder pressure at 1000 rpm between simulation and experiment, as reported by Kwon <i>et al.</i> (2011).....	63
Figure 2.25 In-cylinder pressure comparison between CMC model using CFD and experiment, reproduced from (De Paola <i>et al.</i> 2008).....	64
Figure 3.1 Turbulent kinetic energy spectrum as a function of the wavenumber, reproduced from (Peters 2000).	74
Figure 4.1 Engine geometry of the piston and crank mechanisms.....	89
Figure 4.2 Instantaneous piston speed: zero at TDC and BDC, maximum at the middle of the stroke.....	91
Figure 4.3 Valve geometry for most engines with parameters defining the valve....	92
Figure 4.4 Valve lift profile for typical poppet valves with mechanical lifters.	94
Figure 4.5 Discharge coefficient for one valve event	95
Figure 4.6 Coupling between CMC and zero-dimensional single-zone model.	115
Figure 4.7 A flow chart for zero-dimensional single-zone model simulation	118
Figure 4.8 The fundamental difference between EFDM and IFDM (Chapra & Canale 2006).	121
Figure 4.9 Bin configuration of the CMC model.....	123
Figure 5.1 A validation for reduced gasoline mechanism used in this study (Golovitchev 2003). LLNL prf is a detailed gasoline mechanism from Lawrence Livermore National Laboratory. CTH is a reduced gasoline mechanism from Chalmers University of Technology.	129
Figure 5.2 Comparison between zero-dimensional model (with modified Woschni heat transfer coefficient model) with experimental data and another single-zone model (Guo <i>et al.</i> 2010). CR=10.0, N=900 rpm, $T_{in}=40^{\circ}\text{C}$, $P_{in}=95\text{ kPa}$, AFR=50.	132
Figure 5.3 Combustion phasing for different heat transfer coefficient models showing high temperature region (HTR) and low temperature region (LTR). In-cylinder pressure on the left and temperature on the right for different heat transfer coefficient models.	134
Figure 5.4 Heat release rate (left) and heat transfer coefficient (right) comparison among Woschni, modified Woschni and Hohenberg models.....	135
Figure 5.5 Comparison of heat transfer coefficient with same scaling factor.....	136
Figure 5.6 Comparison of characteristic velocity between the Woschni, modified Woschni, and Hohenberg models.	137

List of Figures

Figure 5.7 In-cylinder pressure comparison with different AFRs and different heat transfer coefficient models, CR=10.0, N=900 rpm, $T_{in}=40^{\circ}C$, $P_{in}=95$ kPa.	138
Figure 5.8 Heat release rate comparison with varying AFRs and different heat transfer coefficient models, CR=10.0, N=900 rpm, $T_{in}=40^{\circ}C$, $P_{in}=95$ kPa.	138
Figure 5.9 Initial condition of the air-fuel mixture in the intake manifold.	140
Figure 5.10 Comparison of the in-cylinder pressure between experiment (Guo <i>et al.</i> 2010), zero-dimensional model from Guo <i>et al.</i> (2010), zero-dimensional model without CMC and CMC with zero-dimensional model.	141
Figure 5.11 Zero-dimensional CMC and a multi-dimensional simulation (STAR EBU) compared with experiment (Wright 2005).....	141
Figure 5.12 Combustion behaviours when the intake temperature was changed for both models.	142
Figure 5.13 Intake mass flow rate and piston speed pattern for the simulated engine. CR=10.0, N=900 rpm, $T_{in}=40^{\circ}C$, $P_{in}=95$ kPa, AFR=50	143
Figure 5.14 The difference in mean kinetic energy, turbulent kinetic energy and turbulent dissipation rate across the crank angle cycle.	144
Figure 5.15 In-cylinder pressure comparison between experiment and CMC model with varying CD	145
Figure 5.16 Effects of varying CD on the mean SDR (left) and mixture fraction variance (right).	146
Figure 5.17 Oxidiser and fuel behaviour for the entire simulation with varying CD	147
Figure 5.18 Comparison between CMC model and experiment with varying number of bins.....	148
Figure 5.19 Peak pressure comparison between experiment and varying number of bins of the CMC model.	149
Figure 5.20 Mean SDR for direct-injected diesel in a multi-dimensional CMC model (Seo <i>et al.</i> 2010).	150
Figure 5.21 Mean scalar dissipation rate for port injected diesel of CMC with zero-dimensional model.	150
Figure 5.22 Mean mass fraction for the entire simulation, which shows the mean mass fraction of O_2 , H_2O_2 , CO_2 , C_7H_{16} and CO	151

List of Figures

Figure 5.23 Mean mass fractions behaviour during combustion event compared with in-cylinder temperature trace, A: C_7H_{16} and O_2 , B: OH and H_2O_2 C: H and HO_2 , D: CO and CO_2	155
Figure 5.24 PDF of mixture fraction during the combustion event.	158
Figure 5.25 Conditional mass fraction of <i>n</i> -heptane (C_7H_{16}) during combustion with varying CA. The x-axis range is slowly increased from image A-D because the ignition started at the lean side before propagating to the rich side of the mixture fraction space. The dotted red line shows the location of the stoichiometric mixture fraction.....	159
Figure 5.26 Conditional mass fraction of oxygen (O_2) during combustion with varying CA. The x-axis range is slowly increased from image A-D because the ignition started at the lean side before propagating to the rich side of the mixture fraction space. The dotted red line shows the location of the stoichiometric mixture fraction.....	160
Figure 5.27 Conditional mass fraction of hydroxyl (OH) radical during combustion with varying CA. The dotted red line shows the location of the stoichiometric mixture fraction.	161
Figure 5.28 Conditional mass fraction of hydrogen peroxide (H_2O_2) during combustion with varying CA. The x-axis range is slowly increased from image A-D because the ignition started at the lean side before propagating to the rich side of the mixture fraction space. The dotted red line shows the location of the stoichiometric mixture fraction.....	162
Figure 5.29 Conditional mass fraction of carbon monoxide (CO) during combustion with varying CA. The x-axis range is slowly increased from image A-D because the ignition started at the lean side before propagating to the rich side of the mixture fraction space. The dotted red line shows the location of the stoichiometric mixture fraction.	163
Figure 5.30 Conditional mass fraction of carbon dioxide (CO_2) during combustion with varying CA. The x-axis range is slowly increased from image A-D because the ignition started at the lean side before propagating to the rich side of the mixture fraction space. The dotted red line shows the location of the stoichiometric mixture fraction.	164
Figure 5.31 Conditional temperature during combustion with varying CA. The x-axis range is slowly increased from image A-D because the ignition started at the lean side before propagating to the rich side of the mixture fraction space. The dotted red line shows the location of the stoichiometric mixture fraction.	166

List of Figures

Figure 5.32 A comparison between experiment, zero-dimensional model and CMC model with various intake air temperatures.	168
Figure 5.33 The effect of different intake air temperatures on in-cylinder pressure trace between zero-dimensional and CMC models.....	168
Figure 5.34 Effect of varying intake air temperature on ignition timing and start of combustion (SOC) temperature for CMC and zero-dimensional models.	170
Figure 5.35 In-cylinder peak pressure comparison between CMC and zero-dimensional models with varying intake air temperature.	170
Figure 5.36 A comparison between experiment, zero-dimensional and CMC models with various AFR.	171
Figure 5.37 The effect of different AFR on in-cylinder pressure trace between zero-dimensional and CMC models, where the stoichiometric AFR for <i>n</i> -heptane is 15.1.	172
Figure 5.38 In-cylinder peak pressure comparison between CMC and zero-dimensional models with varying AFR.....	172
Figure 5.39 In-cylinder pressure comparison between the experiment (Puduppakkam <i>et al.</i> 2009), the CMC and zero-dimensional models, where the zero-dimensional model was tested with different intake temperatures.	174
Figure 5.40 A comparison between the CMC model and the experiment, where the CMC model varies with 100 and 150 bins.....	176
Figure 5.41 A comparison of constant of <i>CD</i> used in the gasoline study and compared with the experiment.....	177
Figure 5.42 Global mean SDR (left) and variance (right) comparison over the entire simulation with varying <i>CD</i>	177
Figure 5.43 Oxidisers and fuels behaviour for the entire simulation with varying <i>CD</i>	178
Figure 5.44 Mean mass fraction for the entire simulation for fuels (C_7H_{16} , C_8H_{18} , C_7H_8) and oxidisers (N_2 , O_2).....	179
Figure 5.45 Mean mass fractions behaviour during the combustion event compared with in-cylinder temperature trace, A: C_7H_{16} , C_8H_{18} , C_7H_8 and O_2 , B: OH and H_2O_2 C: H and HO_2 , D: CO and CO_2	181
Figure 5.46 Conditional temperature for gasoline combustion with varying CA. The dotted red line shows the location of the stoichiometric mixture fraction.	182
Figure 6.1 Cross-sectional view of the standard engine (Honda 2012).	187

List of Figures

Figure 6.2 Experimental setup diagram for an HCCI engine.....	189
Figure 6.3 Engine setup in the engine laboratory.	189
Figure 6.4 The dynamometer connected to the engine (left) with its controller (right).	190
Figure 6.5 Intake temperature sensor location next to the intake port, as circled in red.	191
Figure 6.6 Exhaust temperature sensor was installed after the exhaust port, as circled in red.	192
Figure 6.7 Intake pressure sensors from Land and Sea (left) and for ECU (right). 192	
Figure 6.8 Air flow meter connected to the inlet manifold before the throttle body.	194
Figure 6.9 The burette and fuel tank were installed side-by-side (left) and an enlarged picture of the area circled in red contains the ball valve, three-way valve and fuel flow direction (right)	195
Figure 6.10 Failure occurred on the plastic part of the fly valve of the carburettor due to the hot air, where the plastic part melted. The carburettor was then removed and replaced with an EFI.	197
Figure 6.11 HCCI conversion by using a heater installed in the intake system.....	198
Figure 6.12 Engineering drawing shows the modification of the inlet manifold to install the heater	199
Figure 6.13 Top: The bare heater was installed in between the throttle body and the EFI in the inlet manifold. Bottom: The heater in the final setup with heat shield and also a water jacket installed around the EFI to prevent the plastic part from melting.	200
Figure 6.14 Exploded view of the water cooling system for the EFI and pressure sensors.....	201
Figure 6.15 ProCAL version 7.2.4 user interface, which can show the readings from all the sensors connected to the ECU.....	202
Figure 6.16 Engine displacement setting	203
Figure 6.17 The setting for the maximum engine speed.....	203
Figure 6.18 Start fuel factor used for this engine.....	204
Figure 6.19 Engine map used for engine operating conditions.....	206
Figure 6.20 Engine map plotted in 3D to ensure there is no spike at any point.....	206

List of Figures

Figure 7.1 The comparison of SI engine power and torque between manufacturer data and experiment. Manufacturer uses carburettor with short intake manifold while experiment uses long intake manifold with EFI.....	212
Figure 7.2 Airflow module used in the air intake manifold of modern engines to implement the effect of short or long air intake (Proton 2013).....	213
Figure 7.3 In-cylinder pressure comparison for SI mode in this study between no load (left) and full load (right).	215
Figure 7.4 In-cylinder pressure for HCCI engine when knocking occurred. Straight blue line is the TDC location at 360°CA with encoder having a 0.5°CA resolution.	216
Figure 7.5 In-cylinder pressure comparison between SI and HCCI engines.	217
Figure 7.6 In-cylinder pressure rate of change comparison between SI and HCCI engines.....	218
Figure 7.7 Engine power comparison between SI and HCCI modes	219
Figure 7.8 FC comparison between SI and HCCI engines, where the FC for the HCCI engine was recorded over a range of intake air temperatures and uses the minimum and maximum.....	221
Figure 7.9 BSFC for the HCCI engine over a range of intake air temperatures	222
Figure 7.10 BSFC comparison between SI and HCCI engines with the HCCI engine using the minimum and maximum values over a range of intake air temperatures.	222
Figure 7.11 HCCI engine efficiency for a range of intake air temperatures.	224
Figure 7.12 Engine efficiency comparison between SI and HCCI engines, where the HCCI engine has a minimum and maximum range for a set of air intake temperatures.	224
Figure 7.13 Emissions levels of HC and NO _x (above) and CO ₂ and CO (below) for HCCI engines for a range of intake air temperatures.....	225
Figure 7.14 NO _x comparison between SI and HCCI modes, where HCCI mode has a minimum and maximum range for different intake air temperatures.	227
Figure 7.15 Unburned HC comparison between SI and HCCI modes, where HCCI mode has a minimum and maximum range for different intake air temperatures. ..	229
Figure 7.16 CO ₂ and CO comparison between SI and HCCI modes, where HCCI mode has a minimum and maximum range for different intake air temperatures	230
Figure 8.1 Initial condition of the air-fuel mixture in the intake manifold.	234

List of Figures

Figure 8.2 In-cylinder pressure comparison between CMC and zero-dimensional models. $T_{in} = 250^{\circ}\text{C}$, $\text{CR} = 9$, $\text{AFR} = 16$, $N = 1500\text{rpm}$	235
Figure 8.3 In-cylinder pressure comparison between experiment and CMC model with varying CD . $T_{in} = 250^{\circ}\text{C}$, $\text{CR} = 9$, $\text{AFR} = 16$, $N = 1500\text{rpm}$	236
Figure 8.4 Oxidisers (O_2 and N_2) and fuels (C_7H_{16} , C_8H_{18} and C_7H_8) behaviour for the entire simulation for $CD = 1.5$ and $CD = 1.0$. $T_{in} = 250^{\circ}\text{C}$, $\text{CR} = 9$, $\text{AFR} = 16$, $N = 1500\text{rpm}$	237
Figure 8.5 Oxidisers (O_2 and N_2) and fuels (C_7H_{16} , C_8H_{18} and C_7H_8) behaviour for the entire simulation for $CD = 2.5$ and $CD = 2.0$. $T_{in} = 250^{\circ}\text{C}$, $\text{CR} = 9$, $\text{AFR} = 16$, $N = 1500\text{rpm}$	238
Figure 8.6 The effect of different CD values on mean scalar dissipation rate (A) and variance (B) for the entire simulation.	239
Figure 8.7 Turbulent quantities (k and ε) behaviour when CD varies. Images B and D are enlarged at the peak of images A and C.	240
Figure 8.8 In-cylinder pressure comparison between experiment and CMC model with varying number of bins. $T_{in} = 250^{\circ}\text{C}$, $\text{CR} = 9$, $\text{AFR} = 16$, $N = 1500\text{rpm}$	241
Figure 8.9 In-cylinder peak pressure comparison for different number of bins of the CMC model.	241
Figure 8.10 Mean mass fractions behaviour during combustion event compared with in-cylinder temperature trace for Honda engine, A: C_7H_{16} , C_8H_{18} , C_7H_8 and O_2 , B: OH and H_2O_2 C: H and HO_2 , D: CO and CO_2	243
Figure 8.11 Conditional mass fraction comparison for different CA location during combustion for species O_2 , C_7H_{16} , C_8H_{18} and C_7H_8 . The dotted red line shows the location of the stoichiometric mixture fraction.	244
Figure 8.12 Conditional mass fraction comparison for different CA location during combustion for species H_2O_2 , OH , CO and CO_2 . The dotted red line shows the location of the stoichiometric mixture fraction.	245
Figure 8.13 Conditional temperature profile during combustion with varying CA. The dotted red line shows the location of the stoichiometric mixture fraction.	247
Figure 8.14 Comparison between CMC and zero-dimensional models against experiment with varying intake air temperature. $\text{CR} = 9$, $\text{AFR} = 16$, $N = 1500\text{rpm}$	249
Figure 8.15 Comparison of in-cylinder peak pressure between CMC and zero-dimensional models against experiment. $\text{CR} = 9$, $\text{AFR} = 16$, $N = 1500\text{rpm}$	249

List of Figures

Figure 8.16 In-cylinder pressure comparison between CMC and zero-dimensional models with varying CR and intake air temperature.....	251
Figure 8.17 A comparison for in-cylinder peak pressure (A) and ignition location (B) with varying CR and intake temperature.....	252
Figure B.1 A dead weight tester was used for calibrating the pressure transducer, where the load was placed on top of the piston to measure the equivalent static pressure.....	B.2
Figure B.2 Linear relationships obtained between voltage reading from the pressure transducer and load tester.....	B.2
Figure B.3 ECU configurations with different sensors.....	B.4
Figure B.4 a) In-cylinder peak pressure difference with advanced and retarded ignition timing. b) Relative torque decreases when the ignition timing is not at MBT (Gupta, 2006).....	B.6
Figure B.5 The difference between the carburettor and the EFI system is in the fuel delivery system a) The carburettor system uses pressure difference to suck the fuel from the float chamber b) In the EFI system, the fuel is injected straightaway from the fuel line at a pressure of about 3 bar.....	B.8
Figure B.6 Fuel delivery to EFI.....	B.9
Figure B.7 Old ignition module using TCI system.....	B.11
Figure B.8 A hall effect sensor was installed next to the flywheel and connected to the ECU.....	B.11

LIST OF TABLES

Table 1.1 Comparison of newly developed engine technology (Chan 2002)	3
Table 1.2 Comparison of simulation types ranging from zero-dimensional to multi-dimensional (Wang, G. <i>et al.</i> 2006)	8
Table 2.1 The Difference in Natural Gas Composition between Some Countries (<i>Chemical safety data sheet</i> 2011; Jonathan 2006; Kong & Reitz 2002; Olsson <i>et al.</i> 2002; Papagiannakis & Hountalas 2004; Ramli 2009).....	14
Table 2.2 Diesel Properties Compared to Hydrogen and Natural Gas (Liu & Karim 2008; Saravanan & Nagarajan 2010; Saravanan <i>et al.</i> 2008; Verhelst & Wallner 2009)	17
Table 2.3 Characteristics of gasoline and diesel fuels (Kim & Lee 2006).....	19
Table 2.4 In-Cylinder Peak Pressure and Temperature Comparison for Natural Gas and Hydrogen in Various Configurations (Amneus <i>et al.</i> 1998; Antunes, Mikalsen & Roskilly 2008, 2009; Garcia, Aguilar & Lencero 2009; Nathan, Mallikarjuna & Ramesh 2010; Zheng, Zhang & Zhang 2005).....	20
Table 2.5 Maximum BTE for Hydrogen-Diesel Fuel Compared with Hydrogen HCCI, Direct Injection (DI) Diesel and Dual Fuel (Antunes, Mikalsen & Roskilly 2009; Tsolakis & Megaritis 2005)	21
Table 2.6 BMEP Range for Various Engines Types (Heywood 1988).....	23
Table 2.7 Chemical kinetic mechanisms available for different fuels.	43
Table 5.1 Engine parameters used in the simulation of a diesel fuelled HCCI engine (Guo <i>et al.</i> 2010)	130
Table 5.2 Engine parameters used in the simulation of a gasoline fuelled HCCI engine (Bunting <i>et al.</i> 2008)	173
Table 6.1 Engine parameters used in this study	188
Table 7.1 Engine operating conditions.....	214

List of Tables

Chapter 1

INTRODUCTION

1.1 Background

The greenhouse effect is a worldwide issue as more and more greenhouse gases are released into the atmosphere, leading to global climate change. The effects include an increase in temperature, unstable weather and an increase in ocean levels, resulting in ice melting in the North and South Poles (Bates *et al.* 2008; Graham, Turner & Dale 1990; Houghton *et al.* 2001). This has become a global issue with the members of the Copenhagen Climate Conference in December 2009 (Bodansky 2010) unable to reach an agreement on climate change.

The increase of the earth's surface air temperature due to global warming has been simulated by Rob (2005) from NASA (see Figure 1.1), showing an increase in surface air temperature from 1960 to 2060. According to the report of the World Resources Institute (Jonathan 2006), transportation accounted for about 14% of the global greenhouse gases in 2000, making it a major contributor to global climate change and equivalent to 18% of global CO₂ emissions. Thus, it is imperative to minimise the emissions level from the transportation sector.

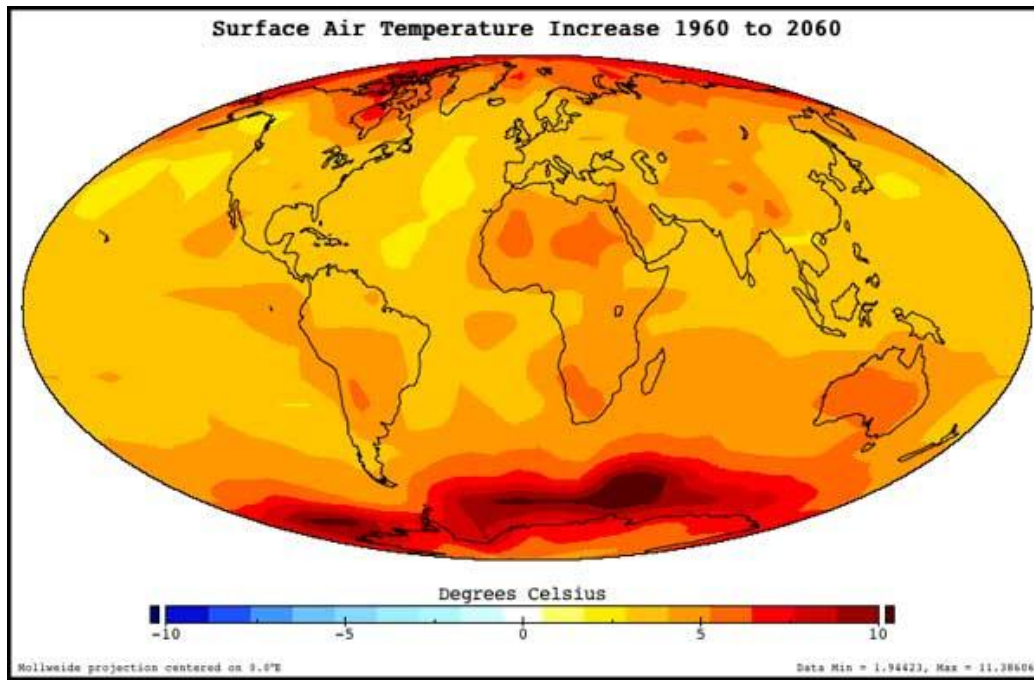


Figure 1.1 Simulated earth surface air temperature increase by the year 2060 (Rob 2005).

To counter this issue, many automotive manufacturers are developing electric, fuel-cell or hybrid engines. An electric vehicle is driven by an electric motor, with the energy supplied by a high capacity battery stored in the car boot or under the car body. The operation of the fuel-cell engine is similar to the electric vehicle in that it uses an electric motor to drive the wheels. However, the difference is the electricity generation method. Most fuel-cell driven vehicles use hydrogen and oxygen to generate electricity (Ogden, Steinbugler & Kreutz 1999; Trimm & Onsan 2001). This electric energy is stored in a high capacity battery and is used to drive the electric motor. A hybrid vehicle uses a combination of the conventional internal combustion (IC) engine and an electric motor. The IC engine could be a Spark Ignition (SI) or Compression Ignition (CI) engine, which is connected to the electric motor either in parallel or in series to drive the wheels. A high capacity battery is again used to power the electric motor. Therefore, it can be summarised that the vehicle is driven by two or more power sources in hybrid configurations.

Table 1.1 summarises the advantages and disadvantages of those technologies. The high implementation cost for each of them leads to a slow commercialisation rate. Thus, an interim solution is required to improve the current IC engines with relatively low development costs.

Chapter 1

Table 1.1 Comparison of newly developed engine technology (Chan 2002)

Engine Type	Advantages	Disadvantages
Hydrogen Fuel Cell	<ul style="list-style-type: none">• compact design• relatively long operating life• high efficiency• low temperature operation	<ul style="list-style-type: none">• higher loads reduce efficiency considerably• high energy cost• high manufacturing cost• heavy auxiliary equipment• complex heat and water management• safety issues
Electric	<ul style="list-style-type: none">• no fuel• 100% emissions free at the vehicle (substantially reduced emissions overall)• fewer moving parts to wear out	<ul style="list-style-type: none">• limited battery operating ranges• long recharge time• battery size and weight issues• high battery replacement costs• limited charging facilities
Hybrid	<ul style="list-style-type: none">• lower emissions level• better fuel economy over conventional engines	<ul style="list-style-type: none">• unachievable break-even point before replacing the battery• high and costly maintenance• battery size adds extra weight to the vehicle

1.2 Introduction

IC engines are widely used in numerous applications throughout the world: vehicle engines, power generation and ships. The emissions generated from these applications have a high impact on the environment, thus alternative solutions have been investigated to achieve low emissions levels (Chan 2002; Cho & He 2007; Jonathan 2006; Taylor 2008). A new mode of combustion is being sought in order to reduce the emissions levels from these engines: a potential candidate is the Homogeneous Charge Compression Ignition (HCCI) engine. Figure 1.2 shows the differences between SI, CI and HCCI engines. SI engines have a spark plug to initiate the combustion with a flame front propagating across the combustion chamber. CI engines have a fuel injector to inject the diesel and the combustion takes place in a compressed hot air region. HCCI

engines have no spark plug or fuel injector and the combustion starts spontaneously in multiple locations. High engine efficiency can be achieved with low NO_x and soot emissions.

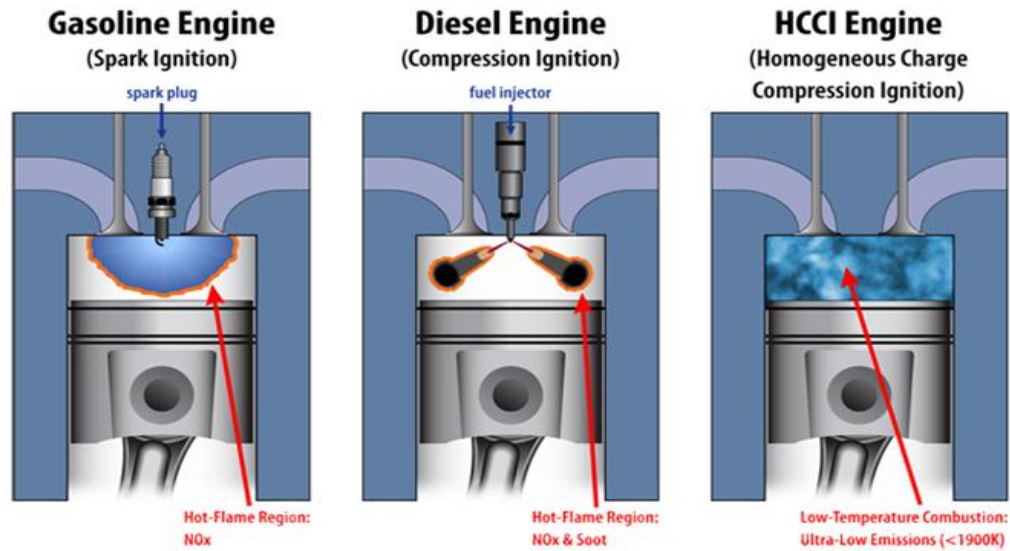


Figure 1.2 The differences between SI, CI and HCCI engines, reproduced from William and Charles (2011).

In HCCI combustion, a homogeneous mixture of air and fuel is compressed until auto-ignition occurs near the end of the compression stroke, followed by a combustion process that is significantly faster than either CI or SI combustion (Rattanapaibule & Aung 2005). Epping *et al.* (2002) and Christensen and Johansson (1998) reported that an HCCI engine using *iso*-octane as a fuel with a high compression ratio (18:1) has improved the engine efficiency to as much as 37% (typical SI engine efficiency is approximately 25%) and maintains low emissions levels. The efficiency and compression ratio obtained by Epping *et al.* (2002) and Christensen and Johansson (1998) are in the range of CI engines. The technology can be implemented by modifying either SI or CI engines using any fuel or combination of fuels. The air/fuel mixture quality in HCCI engines is normally lean, it auto-ignites in multiple locations and is then burned volumetrically without discernible flame propagation (Kong & Reitz 2002; Yao, Zheng & Liu 2009). Combustion takes place when the homogeneous fuel mixture has reached the chemical activation energy and is fully controlled by chemical kinetics (Najt & Foster 1983) rather than spark or injection timing.

Since the mixture is lean and is fully controlled by chemical kinetics, there are new challenges in developing HCCI engines as it is difficult to control the auto-ignition of the mixture and the heat release rate at high load operation, achieve cold start, meet emission standards and control knock (Kong & Reitz 2003; Soylu 2005). The advantages of using HCCI technology in IC engines are:

1. High efficiency relative to SI engines - approaching the efficiency of CI engines due to the ability of these engines to use high compression ratio (CR) and fast combustion (Killingsworth *et al.* 2006; Mack, Aceves & Dibble 2009). The HCCI engine has also no throttling losses, which improves the engine efficiency as well (Aceves *et al.* 2001; Haraldsson *et al.* 2004);
2. The ability to operate on a wide range of fuels (Aceves & Flowers 2004; Christensen, Johansson & Einewall 1997; Mack, Aceves & Dibble 2009); and
3. Low emissions levels of NO_x relative to SI and CI engines and low particulate matter relative to CI engines (Nathan, Mallikarjuna & Ramesh 2010).

HCCI engines have promising advantages and once the disadvantages have been resolved, the engine can then be commercialised. Thus, it is important to study the engine performance before implementing methods that resolve the current issues. Simulation techniques can be implemented to reduce the time in investigating the HCCI engine performance. Therefore, a combination of simulation and experiment will be useful in investigating HCCI engines.

1.3 Research Focus

The fuel mixture in an HCCI engine's combustion chamber is not completely homogeneous and both turbulence and inhomogeneity will have effects on the mixing process. A study from Aceves *et al.* (2000) reported that turbulence has a minor direct effect on HCCI combustion, but may also have an indirect effect of changing the temperature distribution. Kong and Reitz (2002) showed that the use of detailed chemical kinetics with Computational Fluid Dynamics (CFD) models is able to predict the combustion phasing in three different HCCI engines. However, the use of detailed chemical kinetics alone was not sufficient to obtain accurate results. They also argued

that the mixture was completely homogeneous and turbulent mixing has no effect on the combustion. High degrees of mixture inhomogeneity result in significant changes in ignition timing and emissions levels (Bhave *et al.* 2006; Bisetti *et al.* 2008). Thus, the effect of turbulence on HCCI combustion still requires investigation.

Bhave *et al.* (2006) found that a lower in-cylinder wall temperature results in higher CO and UHC emissions while a higher wall temperature leads to lower emissions of CO and UHC. They concluded that the incomplete oxidation is influenced by fluid-wall interactions and mostly located within piston ring crevices (Aceves *et al.* 2000; Kong & Reitz 2003).

Flowers *et al.* (2001) described the HCCI (fuelled with propane) ignition by H_2O_2 decomposition, which accumulates due to low-temperature reactions in the compression stroke. Once the in-cylinder temperature reaches 1050-1100 K, H_2O_2 decomposes rapidly into two OH radicals, forming a large pool of OH radicals, and these radicals will rapidly consume the fuel. Reduction in OH concentration in low temperature regions leads to incomplete combustion, which delays the high-temperature oxidation (Shudo & Yamada 2007). This process is shown in Figure 1.3, where the concentration of H_2O_2 decreases while the concentration of OH increases rapidly during the combustion process.

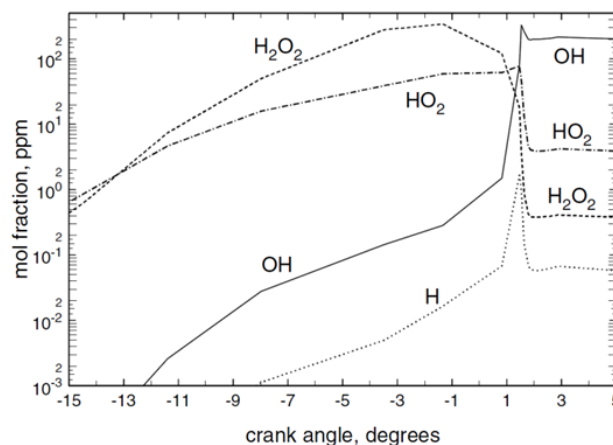


Figure 1.3 Concentration of radicals H, OH, H_2O_2 and HO_2 for a pressure of 0.2 MPa (Aceves *et al.* 2000).

Turbulence is capable of transporting heat, chemical species and particles in a rapid fashion (Tennekes & Lumley 1972). If a fully homogeneous mixture exists in HCCI engines, turbulence has a relatively minor direct effect on HCCI combustion, but this

may have an indirect effect of changing the temperature distribution (Aceves *et al.* 2004; Aceves *et al.* 2001). The small temperature differences could significantly affect the combustion behaviour (Cabra *et al.* 2002).

A zero-dimensional model assumes that the combustion chamber is homogeneous and the chemical kinetics mechanism can be used to study the combustion behaviour. However, the turbulence effect is not considered. To some extent, the zero-dimensional model can be modified to include the turbulence effect by using different heat loss models (Agarwal *et al.* 1998; Fiveland & Assanis 2002), but no interactions between turbulence and chemistry. Due to its homogeneity assumptions, the zero-dimensional single-zone model has limitations in short burn duration, high in-cylinder peak pressure and cannot use the actual intake air temperature (Guo *et al.* 2010; Morsy 2007). The assumption ignores the spatial variations in the chamber, which treats the heat loss proportional to the temperature difference between average charge temperature and a time-averaged wall temperature (Aceves *et al.* 1998). In practice, the boundary layer is at a lower temperature than the bulk gas near TDC, which causes the boundary layer to always burn last and extend the heat release rate duration. Due to this assumption, the burn duration of a single-zone model is shorter than the experiment.

To investigate the HCCI combustion behaviour with turbulence-chemistry effect, a Conditional Moment Closure (CMC) method will be used with a zero-dimensional model. Instead of using CMC with CFD, which is common in the literature (De Paola *et al.* 2008; Seo *et al.* 2010; Wright *et al.* 2009; Wright *et al.* 2005), a CMC with zero-dimensional approach was chosen. This is because the CMC model has the ability to model the in-cylinder inhomogeneity in terms of the fuel concentration. Even though the HCCI engine is assumed to be homogenous, there is an argument stating that mixture inhomogeneities were present in HCCI engines even for effectively premixed charges (Richter *et al.* 2000). Kong and Reitz (2002) also reported that there could be mixture inhomogeneity and the appearance of turbulent mixing, as discussed above. This has led to the use of CMC model in HCCI engines, which can model the mixture fluctuations in the combustion chamber. A zero-dimensional model was selected as the main ‘body’ of simulation because of its faster computation time.

Chapter 1

Thus, a combination of CMC and zero-dimensional models would help in performing a detailed preliminary study. Currently the use of multi-dimensional models leads to high computation time and resources, as shown in Table 1.2, where CFD with detailed chemistry has the longest computation time. A zero-dimensional simulation would be an interim solution until the cost and time of running a multi-dimensional model is comparable with the current cost of the zero-dimensional model. Also, the implementation of CMC with a zero-dimensional model is relatively new in the literature. CMC accounts for the turbulence-chemistry mixing effects, while the zero-dimensional model simulates the engine by assuming that the mixture in the cylinder is homogeneous. By combining with the CMC approach, it is expected to overcome the zero-dimensional model disadvantages. The use of chemical kinetics mechanisms also helps in investigating the combustion behaviour of an HCCI engine.

Table 1.2 Comparison of simulation types ranging from zero-dimensional to multi-dimensional (Wang, G. *et al.* 2006)

HCCI MODEL	Advantages	Disadvantages	Application Cases	Executing time (min)
0D single-zone with detailed chemistry	Lowest computational cost	HC and CO can't be predicted	Ignition timing prediction Fast parameter studies	<10
Quasi-dimensional multi-zone with detailed chemistry	Temperature and concentration inhomogeneity considered	Initial conditions of each zone are necessary	HC, CO prediction Heat release rate	<10 ²
1D engine cycle with detailed chemistry in-cylinder	No initial conditions of cylinder specification, parameter studies for engine performance	Fuel spray, flow and turbulence, mixture formation can't be considered	Engine performance prediction Optimize of gas exchange system and VVT strategies	<10 ²
Multi-CFD with multi-zone detailed chemistry	Temperature and concentration inhomogeneity considered	Turbulence can't be considered	HC, CO prediction Heat release rate	<10 ³
Multi-CFD with simplified chemistry	Fuel spray, flow and turbulence, mixture formation considered	Simplified combustion	Optimization of combustion system	<10 ³
Multi-CFD with detailed chemistry	Detailed chemistry and fluid-dynamics, turbulence influence mixture formation and combustion rate considered	Highest computational cost	HC,CO,NO _x prediction HCCI physicochemical processes studies Combustion optimization	10 ³ ~ 10 ⁵

1.4 Objectives

The objectives of this research are to:

1. Investigate the combustion behaviour in an HCCI engine by using a combined CMC and zero-dimensional model, where the CMC model takes into consideration the turbulence-chemistry mixing effect.
2. Evaluate the performance of a gasoline HCCI engine experimentally and compared with an SI engine. The experiment is also used to validate the combined model.

1.5 Thesis Outline

The thesis consists of nine chapters. Chapter 2 contains the literature review, which discusses HCCI engines in general, and also covers the experimental and numerical parts of the study. The first three sections of the chapter discuss the experimental part of the study, which consists of the performance comparison, injection methods to achieve HCCI mode and the ignition control for HCCI engines. The last two sections before the Conclusion give a general overview of the numerical study.

Chapter 3 discusses the background of the turbulence modelling and all the equations involved in multi-dimensional modelling. The conservation equations are introduced first: mass, momentum, species and energy. Then the chemical reactions are discussed, followed by the discussion of the Probability Density Function (PDF) in addition to statistical descriptions. The turbulence modelling section before the Conclusion covers the averaging techniques, turbulence models, turbulent reacting flows and turbulent combustion models.

Chapter 4 introduces the methodology of combining the zero-dimensional and CMC models. The equations used in the zero-dimensional model are discussed in Section 2 of the chapter, followed by the CMC equations in the following sections. The technique to combine both models is discussed before the Conclusion.

Chapter 5 will validate the combined model discussed in Chapter 4 against the experimental data from others. The chapter consists of two parts. Part 1 discusses the validation using a diesel fuelled HCCI engine, while Part 2 discusses the validation for a gasoline fuelled HCCI engine. The chemical reaction mechanisms used for both tests

Chapter 1

are discussed in Section 1. The details of the experimental engine are discussed in Section 2. These are followed by the validation of the zero-dimensional model using diesel fuel and performance of the heat transfer models for HCCI engines. The validation and performance of the combined model for a diesel fuelled HCCI engine is discussed in Sections 4 and 5. Part 2 commences with the engine data used in the gasoline HCCI engine experiment. The validation and model behaviour is discussed in Section 7 before the chapter ends with the Conclusion.

Chapter 6 discusses the experimental methodology in this study, which describes how to convert a commercially available single-cylinder SI engine to an HCCI engine. The experimental apparatus is discussed in Section 2 of the chapter and followed by the modification technique using the intake air heater. The electronic control unit (ECU) used as part of the modification work is also discussed. The last sections before the Conclusion discuss the experimental techniques needed in order to run the engine in HCCI mode.

Chapter 7 will then discuss the experimental performance of the HCCI engine. The HCCI engine is directly compared with an SI engine using the same engine operating conditions at the same engine power. The engine performance comparison covers the in-cylinder pressure, engine power, fuel consumption, engine efficiency and emissions levels. The chapter then closes with the Conclusion.

Chapter 8 will validate the combined model discussed in Chapter 4 against the experimental work in this thesis. The boundary condition and validation of the combined model is discussed in Section 2 of the chapter. Section 3 discusses the characteristic results from CMC. The parametric study (the effect of intake air temperature, air-to-fuel ratio and compression ratio) is discussed in Section 4.

The thesis ends with the Conclusion and Recommendations.

Chapter 2

LITERATURE REVIEW

2.1 Introduction

The performance of an HCCI engine is strongly dependent on the fuel type, and this affects the emission levels as well. Since emission levels have become one of the factors driving engine technology today, HCCI development has moved to the next level. Due to the importance of HCCI technology, which potentially can replace conventional SI and CI engines, there is a need to report the recent developments in HCCI engines. This chapter discusses the current issues for this technology, where Section 2.2 contains the performance comparison of HCCI engines. Section 2.3 presents the methods to create homogeneous mixtures, with ignition control of HCCI engines in Section 2.4. Sections 2.5 and 2.6 will discuss relevant numerical studies of zero-dimensional modelling and the Conditional Moment Closure (CMC) model, concluding with section 2.7.

2.2 Performance Comparison

2.2.1 State of the Art Current Internal Combustion Engines

Producing homogeneous mixtures to achieve near-complete combustion is a common goal that will lead to the development of low polluting engines. Some technologies, including Fuel-Stratified Injection (FSI), Turbo-Stratified Injection (TSI) and HCCI, are used to improve the combustion efficiency.

FSI and TSI are commercially used by the Volkswagen Aktiengesellschaft (AG), which consists of other child companies Audi, Skoda, Seat, Bugatti, Lamborghini,

Chapter 2

Bentley and Scania (Volkswagen 2009). FSI uses directly injected fuel with a high injection pressure, where the evaporating fuel has a significant cooling effect on the cylinder charge (Audi 2012). This effect helps in reducing knocking and therefore a higher compression ratio can be used. The air enters the combustion chamber at a certain angle by using a moveable flap inside the intake manifold (Wurms, Grigo & Hatz 2003), while fuel is directly injected to the chamber, as shown in Figure 2.1. The fuel injector is located close to the intake valve in the cylinder head. With the help of the piston crown design, a tumbling effect is generated inside the chamber. This in turn will help the fuel mix with air homogeneously.

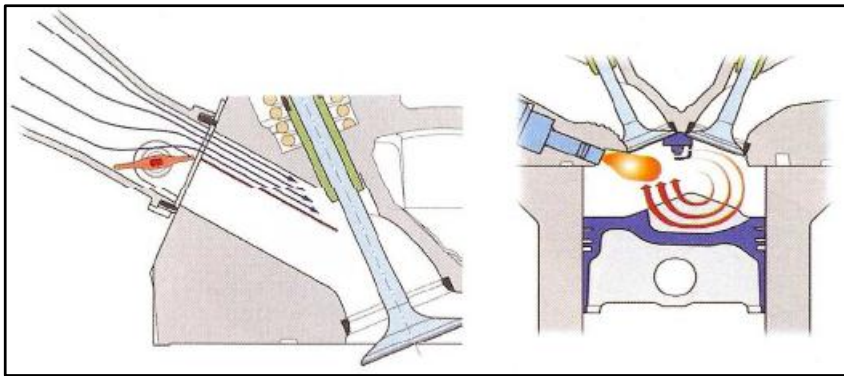


Figure 2.1 Movable flap is used inside the intake manifold (left) to generate tumble effects (right) in the combustion chamber with specially designed piston crown (Wurms, Grigo & Hatz 2003)

TSI engines, on the other hand, use a high intake pressure (using multipoint injectors) on an FSI engine (Böhme *et al.* 2006). The pressurised intake air will assist the combustion and therefore produce better efficiency, allowing smaller engines to be built with power and torque similar to that of bigger engines. The first engine to use direct injection technology to stratified charge engine was the Texaco combustion process (Barber, Reynolds & Tierney 1955), as reported by Takagi (1998).

HCCI engines can be considered new technology (Yao, Zheng & Liu 2009) even though the research was initially undertaken by Onishi *et al.* (1979). Researchers worldwide are investigating HCCI engines as this technology has not yet been sufficiently developed and is not commercially available. General Motors (GM) Corporation has unveiled a prototype car with a gasoline HCCI engine, which could

cut fuel consumption by 15% (Premier 2007). The engine is able to reduce the emissions levels and lower throttling losses, which improves fuel economy.

2.2.2 Fuels Used in HCCI Engines

HCCI engines can operate using any fuel as long as the fuel can be vaporized and mixed with the air before ignition (Aceves & Flowers 2004). Since HCCI engines are fully controlled by chemical kinetics, it is important to evaluate the fuel's auto-ignition point to produce smooth engine operation: no knocking or misfiring. Different fuels will have different auto-ignition points. Figure 2.2 shows the intake temperature required for different fuels to auto-ignite at different compression ratios when operating in HCCI mode (Aceves & Flowers 2004). It can be seen that methane requires the highest intake temperature and highest compression ratio to auto-ignite compared to other fuels. Thus, a fuel requiring a high intake temperature to auto-ignite is less reactive. This is also reported by Sjorberg and Dec (2008) that a low-reactivity fuel requires a high intake temperature and compression ratio to auto-ignite.

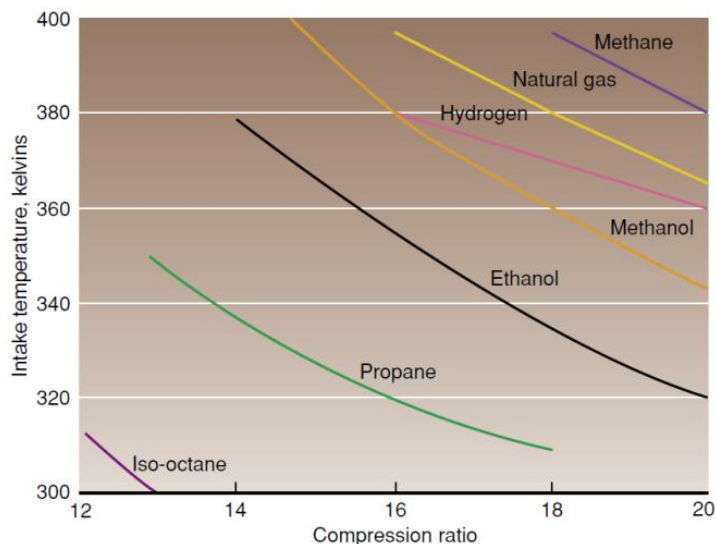


Figure 2.2 Intake temperature required for fuels to operate under HCCI mode with varying compression ratios, reproduced from (Aceves & Flowers 2004).

The composition of natural gas varies for different countries as shown in Table 2.1. It is easily adapted for use as a fuel due to its wide availability, it is economical and has environmental benefits (Papagiannakis & Hountalas 2004; Tobin *et al.* 1999). Natural gas is also more readily available than crude oil, with a cost that has been competitive

Chapter 2

for a long time (Cho & He 2007). Natural gas is able to operate as a single fuel in an SI engine with low HC and CO emissions. However, it produces less power output in HCCI engines (Flowers *et al.* 2001; Rousseau, Lemoult & Tazerout 1999; Zeng *et al.* 2006). Its high auto-ignition point (about 810K) gives it a significant advantage over diesel-natural gas operation by maintaining the high CR of a diesel engine and lowering emissions at the same time (Duc & Wattanavichien 2007; Papagiannakis & Hountalas 2004; Saravanan & Nagarajan 2010). Duc and Wattanavichien (2007) claimed that the high octane number of methane (about 120) allows engines to operate at a high CR. Results from a four-stroke HCCI engine simulation have shown that methane did not ignite if the intake temperature was less than 400K with a CR of 15:1, as reported by Fiveland and Assanis (2000). This is supported by Figure 2.2, where methane will only auto-ignite with an intake temperature less than 400K when the CR is greater than 18:1.

Table 2.1 The Difference in Natural Gas Composition between Some Countries (*Chemical safety data sheet* 2011; Jonathan 2006; Kong & Reitz 2002; Olsson *et al.* 2002; Papagiannakis & Hountalas 2004; Ramli 2009).

Components	% Volume				
	<i>Australia</i>	<i>Greece</i>	<i>Sweden</i>	<i>US</i>	<i>Malaysia</i>
Methane (CH ₄)	90.0	98.0	87.58	91.1	92.74
Ethane (C ₂ H ₆)	4.0	0.6	6.54	4.7	4.07
Propane (C ₃ H ₈)	1.7	0.2	3.12	1.7	0.77
Butane (C ₄ H ₁₀)	0.4	0.2	1.04	1.4	0.14
Pentane (C ₅ H ₁₂)	0.11	0.1	0.17	-	-
Hexane (C ₆ H ₁₄)	0.08	-	0.02	-	-
Heptane (C ₇ H ₁₆)	0.01	-	-	-	-
Carbon Dioxide (CO ₂)	2.7	0.1	0.31	0.5	1.83
Nitrogen (N ₂)	1.0	0.8	1.22	0.6	0.45

Automotive manufacturers are producing vehicles powered by fuel-cells, as well as vehicles fuelled by compressed natural gas (CNG) (Jahirul *et al.* 2010; Mercuri, Bauen & Hart 2002). The vehicles are purpose-built to reduce emissions and are more economical than vehicles using gasoline and diesel. There are commercialization difficulties for fuel-cells because of their complexity to produce, high material cost

and safety issues. CNG, on the other hand, has been successfully commercialized with 48% of global market share for on-road vehicles, but it has difficulties with high capital cost, existing refuelling infrastructure and competition from other alternative fuels (Johannes *et al.* June 2009).

The Indicated Mean Effective Pressure (IMEP) is a measure of the engine's capacity to do work in each stroke, before considering all the losses. If IMEP is increased, it can reduce the intake temperature needed in an HCCI engine; increasing the CR has the same effect (Olsson *et al.* 2002). Antunes, Mikalsen and Roskilly (2008) have investigated the performance of an HCCI engine fuelled with hydrogen, and they found that the IMEP increases when the air intake temperature is decreased. Hydrogen requires a lower air intake temperature than natural gas for the same CR, as shown in Figure 2.2, due to hydrogen having a lower auto-ignition temperature. Therefore, it is important to control the intake temperature and the operating conditions of an HCCI engine to achieve an optimized combustion point. The methods to achieve this will be discussed in section 2.4.

Hydrogen can operate as a single fuel in an HCCI engine but it is often unstable and is prone to generating knocking (Szwaja & Grab-Rogalinski 2009). It has the highest diffusivity of any gas in air, about 3-8 times faster than that of natural gas, which leads to fast mixing (Saravanan & Nagarajan 2010) and the intake charge can be considered homogeneous when premixed with air (Szwaja & Grab-Rogalinski 2009). The net heating value for hydrogen is almost three times higher than diesel (119.93MJ/kg compared to 42.5MJ/kg) with a high self-ignition temperature to initiate combustion (858K) (Saravanan *et al.* 2008). Hydrogen cannot be used as a single fuel, because the HCCI engine operates in an unstable condition. Thus, most researchers use hydrogen as an additive: either to control the ignition timing or to increase the engine performance (Flowers *et al.* 2001; Park *et al.* 2010; Peucheret *et al.* 2005; Rattanapaibule & Aung 2005; Saravanan & Nagarajan 2010).

Iso-octane is used as a surrogate fuel for gasoline in HCCI engine experiments while *n*-heptane is used for diesel (Komninos, Hountalas & Kouremenos 2004; Naik *et al.* 2005; Pitz *et al.* 2007). Alcohol-derived fuels, as shown in Figure 2.2, are not widely used due to their complexity to produce, leading to high manufacturing costs. Most of

the alcohol-derived fuels like biofuels are still subject to worldwide investigations as they create engine durability problems such as injector cocking, piston ring sticking, severe engine deposits and fuel filter clogging (Bari, Lim & Yu 2002; Fazal, Haseeb & Masjuki 2011; Jayed *et al.* 2011). Even though biofuels have their own challenges, they have received increasing attention from researchers as a renewable energy source, as reported by Komninos and Rakopoulos (2012).

2.2.3 Natural Gas and Hydrogen with Diesel Operating Conditions

The combination of natural gas or hydrogen with diesel was reported to yield low emissions and, to some extent, increase the engine efficiency, either in HCCI or CI combustion mode (de Risi *et al.* 2008; Saravanan, Nagarajan & Narayanasamy 2008; Saravanan *et al.* 2008; Verhelst & Wallner 2009). Diesel alone is not suitable for HCCI engines due to its low volatility and high propensity to auto-ignite, while natural gas has a high resistance to auto-ignition as reported by Kong (2007).

Combinations of high octane number fuels (such as natural gas and hydrogen) with high cetane number fuels (such as diesel) are able to increase the engine durability and, under certain operating conditions, reduce emissions such as soot, HC, CO and NO_x (Szwaja & Grab-Rogalinski 2009; Tomita 2004; Tomita *et al.* 2001; Tomita *et al.* 2002). It was also reported that these combinations (diesel and methane) have a high thermal efficiency under early injection timing (Tomita 2004; Tomita *et al.* 2002). Fuels with a higher octane number have better resistance to knocking while fuels with a higher cetane number have a shorter ignition delay time, thus providing more time for the fuel to complete the combustion. Therefore, a combination of both (high cetane number fuels and high octane number fuels) with proper blend ratio provides soft (without knocking) engine run (Szwaja & Grab-Rogalinski 2009), whereby the mixture can be operated at a high CR and has a longer combustion duration.

Hydrogen has a high octane number (approximately 130) and a high Lower Heating Value (LHV) (119.93MJ/kg). Its combination with diesel helps to increase engine efficiency (Saravanan, Nagarajan & Narayanasamy 2008) and control the auto-

Chapter 2

ignition point in HCCI engines (Szwaja & Grab-Rogalinski 2009). Natural gas, on the other hand, has a higher auto-ignition temperature and it can be used in high CR engines (Akansu *et al.* 2004). Table 2.2 compares the physical and chemical properties of diesel with natural gas and hydrogen.

Table 2.2 Diesel Properties Compared to Hydrogen and Natural Gas (Liu & Karim 2008; Saravanan & Nagarajan 2010; Saravanan *et al.* 2008; Verhelst & Wallner 2009)

Properties	Diesel	Hydrogen	Natural Gas
Main component	C ₁₂ H ₂₃	H ₂	Methane (CH ₄)
Auto-ignition temperature (K)	553	858	923
Lower heating value (MJ/kg)	42.5	119.93	50
Density (kg/m ³)	833-881	0.08	0.862
Molecular weight (g/mol)	170	2.016	16.043
Flammability limits in air (vol%) (LFL–UFL)	0.7-5	4-75	5-15
Flame velocity (m/s)	0.3	2.65-3.25	0.45
Specific gravity	0.83	0.091	0.55
Boiling point (K)	453-653	20.2	111.5
Cetane number	40-60	-	-
Octane number	30	130	120
CO ₂ emissions (%)	13.4	0	9.5
Diffusivity in air (cm ² /s)	-	0.61	0.16
Min ignition energy (mJ)	-	0.02	0.28

Hydrogen has the highest LHV or Lower Calorific Value (LCV) compared to both diesel and natural gas, which means it releases a high amount of energy during combustion and thus produces the highest flame speed. A wide range of flammability limits in air allows a wider range of engine power outputs through changes in the mixture equivalence ratio. Flammable mixtures of hydrogen can go from as lean as $\lambda = 10$ to as rich as $\lambda = 0.14$ (Verhelst & Wallner 2009), where λ is the air-to-fuel ratio actual divided by the air-to-fuel ratio stoichiometric.

2.2.4 Gasoline Operated HCCI Engines

Gasoline could be operated in HCCI mode on its own. However, it would also be unstable in a high load operating range. High load difficulties are a common problem for HCCI engines regardless of the fuel being used. The solution for this issue for gasoline fuel is to operate the engine in HCCI mode in the medium load range, and switch to SI mode in the high load range (Yingnan *et al.* 2010). Wang *et al.* (2006) studied the gasoline HCCI engine with secondary injections and reported that the operating load range could be extended by using two-zone HCCI mode, which utilises secondary injections. However, the two-zone mode yields higher NO_x emissions due to the fuel-rich zone developed in the chamber.

Iso-octane is generally used as a gasoline surrogate fuel in numerical studies due to its high octane rating. Higher octane numbers cause difficulties in achieving the HCCI mode for low CR engines (Hosseini & Checkel 2009) due to higher ignition temperature. The intake temperature must be very high, if pre-heating is the only option to achieve HCCI. This would be difficult as this method requires a high power heater with a precise temperature controller. Thus the ignition has to be controlled using other means, which will be discussed in Section 2.4. The use of high octane number fuels such as gasoline in a low CR engine allows the engine to be switchable to SI mode in a high load range (Fuerhapter, Unger & Piock 2004). It has been found that a high CR engine (as high as 18:1) has the advantages of producing ultra-low NO_x emissions (1ppm) and higher thermal efficiency (43%) at a fixed operating condition (John & Magnus 2002).

Gasoline can also be mixed with diesel to operate in HCCI mode. A study by Kim and Lee (2006) on the effect of blended fuels on emissions showed that the combination of diesel and gasoline (diesel is direct injected while gasoline is port injected) is an effective way to reduce NO_x levels, with the increase of the premixed ratio. The premixed ratio is defined as the ratio of the energy of the premixed (port injected) fuel to the energy of the total fuel (direct and port injected). Zhong *et al.* (2005) also studied the effect of fuels which are a blend of gasoline and diesel, and reported that UHC and NO_x were significantly reduced throughout the HCCI engine load ranges compared to

a gasoline only HCCI engine. The purpose of blending gasoline and diesel is that gasoline has a high volatility and is easy to vaporise, thus can be used to form a homogeneous mixture. Gasoline also has a high octane number, where higher numbers show higher resistance to knocking. Diesel, on the other hand, has good ignitability and fast combustion due to its high cetane number. Table 2.3 compares the characteristics of the gasoline and diesel fuels, where for the selected gasoline (octane number 98) the heating values are almost identical between those fuels.

Table 2.3 Characteristics of gasoline and diesel fuels (Kim & Lee 2006)

	Gasoline	Diesel
Octane number	98	-
Cetane number	-	54
Higher heating value (kJ/kg)	47,300	44,800
Lower heating value (kJ/kg)	44,000	42,500
Boiling point (K)	468	553
Density (kg/m ³)	750	814
Stoichiometric air-fuel ratio	14.6	14.5

2.2.5 Peak Pressure and Temperature

The variations of heat release rate during combustion affect the in-cylinder peak pressure and temperature. All these quantities (heat release rate, temperature and pressure) depend on the speed of the engine, equivalence ratio, load, intake pressure, temperature and energy content of the fuel configurations. Higher loads and richer mixtures typically produce higher peak pressures. Table 2.4 shows how the in-cylinder peak pressure and temperature vary for HCCI and conventional CI modes. These are general data to illustrate which mode produces a higher in-cylinder peak pressure irrespective of the load produced by the engines. The data for maximum temperature is not fully reported but, in general, temperature increases with pressure. HCCI configurations generally produce a lower peak pressure than conventional CI modes for every fuel configuration, leading to significant impacts on emission levels: the impacts refer to whether the emission of a particular gas decreases or increases. As for HCCI engines with lower peak pressure, the emissions for NO_x are generally improved, as are particulate matter. However, the emissions for some gases such as CO and unburned HC are not improved due to the limitations of the HCCI engines,

which are currently being investigated. The addition of hydrogen to diesel influences the peak pressure generation. The greater the amount of hydrogen added, the higher the peak pressure, and the addition of hydrogen is able to reduce ignition delay as well (Szwaja & Grab-Rogalinski 2009). It is shown that the hydrogen fuel configuration yields the highest peak pressure.

Table 2.4 In-Cylinder Peak Pressure and Temperature Comparison for Natural Gas and Hydrogen in Various Configurations (Amneus *et al.* 1998; Antunes, Mikalsen & Roskilly 2008, 2009; Garcia, Aguilar & Lencero 2009; Nathan, Mallikarjuna & Ramesh 2010; Zheng, Zhang & Zhang 2005)

Mode	Max Pressure (MPa)		Max Temperature (K)	
	<i>HCCI</i>	<i>CI</i>	<i>HCCI</i>	<i>CI</i>
H ₂	~ 8	~ 12	-	-
NG	~ 7	~ 7.5	~ 1300	~ 1850
Diesel	~ 6.1	~ 6.6	-	~ 2300
NG + Diesel	~ 3	~ 5.5	~ 1450	-
H ₂ + Diesel	~ 7	~ 7.8	-	-

2.2.6 Brake Thermal Efficiency

The brake thermal efficiency (BTE) of an engine is the ratio of brake output power to input power and describes the brake power produced by an engine with respect to the energy supplied by the fuel. A study has been performed (Nathan, Mallikarjuna & Ramesh 2010) to determine the best BTE for biogas fuels with an energy ratio range from 40% to 57% of biogas and an intake temperature of 80°C, 100°C and 135°C. The biogas' main component was methane (>60%), which was produced by anaerobic fermentation of cellulose biomass materials (Duc & Wattanavichien 2007). It was reported that the best energy ratio with diesel in HCCI mode was 51% biogas and the optimum efficiency occurred when the intake temperature was 135°C. High energy ratios lower the heat release rate and the efficiency (Nathan, Mallikarjuna & Ramesh 2010). However, even when operated at the optimum biogas energy ratio, the BTE was no better than diesel running in CI mode. Duc and Wattanavichien (2007) reported that biogas-diesel running in dual-fuel non-HCCI engines has a lower efficiency than diesel single fuel in either HCCI or non-HCCI mode.

Hydrogen, on the other hand, had a higher BTE than pure diesel in non-HCCI mode, increasing the BTE by 13-16% (Saravanan & Nagarajan 2010). Szwaja and Grab-Rogalinski (2009) reported that the BTE was increased from 30.3% to 32% with an addition of 5% hydrogen. The increase of BTE in hydrogen-diesel mode might be due to the uniformity of mixing of hydrogen with air (Saravanan *et al.* 2008). Hydrogen as a single fuel running in HCCI mode gives a BTE of up to 45% (Antunes, Mikalsen & Roskilly 2008), showing that hydrogen is able to operate with extremely lean mixtures and still maintain a relatively high efficiency compared to diesel engines. Table 2.5 shows that hydrogen in HCCI mode yields better results compared to the conventional mode (45% compared to 42.8%) and hydrogen with diesel in non-HCCI mode produces a higher efficiency than diesel alone (Antunes, Mikalsen & Roskilly 2009). It is expected that the combination of hydrogen and diesel in HCCI mode will produce a higher BTE than diesel in CI mode. This conclusion was reached with partially premixed charge compression ignition (PPCCI) configurations when reformed exhaust gas recirculation (REGR) was used with hydrogen-rich gas (no more than 24%) added to the intake manifold (Tsolakis & Megaritis 2005). PPCCI has the potential to reduce NO_x and PM emissions like the HCCI engine does, and maintaining or improving the engine efficiency.

Table 2.5 Maximum BTE for Hydrogen-Diesel Fuel Compared with Hydrogen HCCI, Direct Injection (DI) Diesel and Dual Fuel (Antunes, Mikalsen & Roskilly 2009; Tsolakis & Megaritis 2005)

	Diesel DI	Dual fuel (H ₂ +diesel)	H ₂ +Diesel PPCCI	H ₂ HCCI	H ₂ DI
BTE (%)	27.9	33.9	36.5	45.0	42.8

2.2.7 Brake Mean Effective Pressure

The brake mean effective pressure (BMEP) is an effective comparison tool to measure engine performance and indicates an engine's capacity to produce power output over the full engine speed range. It is also used to compare one engine's performance with another. A high BMEP shows the ability of the engine to perform high load operations. One of the HCCI engine's challenges is its limited load range because high load operations tend to produce knock (Kong 2007). Table 2.6 shows the BMEP ranges of standard engines. In comparison, the BMEP range for passenger cars (Saab 5-cylinder

engine) operating in HCCI mode is only between 0-0.36MPa (Hyvonen, Haraldsson & Johansson 2003), which is lower than conventional SI engines.

Natural gas-diesel in HCCI mode operates in the BMEP range of 0.25-0.4MPa (Nathan, Mallikarjuna & Ramesh 2010), which is low compared with the engines in Table 2.6. To increase the BMEP, the concentration of natural gas has been increased but if its concentration compared to diesel is too high, this will lead to knocking (Nathan, Mallikarjuna & Ramesh 2010). Figure 2.3 shows that the best energy ratio for natural gas-diesel HCCI mode is about 51% and within the shaded region. For this optimized energy ratio, the maximum BMEP is only 0.4MPa, which is a very limited load range and is not suitable for high load engine operations.

Hydrogen with diesel in HCCI mode is stable up to 0.6MPa BMEP (Tsolakis & Megaritis 2005; Tsolakis, Megaritis & Yap 2008). If a supercharger is used in hydrogen-diesel dual-fuel mode on a non-HCCI engine, a maximum BMEP of 0.91MPa was reported (Roy *et al.* 2010). Thus, hydrogen and diesel in HCCI mode might be able to be used for high load engine operations.

When gasoline is used in an HCCI engine, the achievable BMEP is 0.35MPa on a two-stroke engine and approximately 0.5MPa on a four-stroke high CR engine, where CR varies from 15.0 to 18.0 (Duret 2002). This BMEP is considered low when compared with other engines in Table 2.6, where small SI engines can achieve BMEP of 1MPa. This is also reported by Kaneko *et al.* (2003), where the HCCI engine has the disadvantage of low BMEP. The BMEP of a gasoline HCCI engine can be improved by using high CR engines (Duffy *et al.* 2005).

Table 2.6 BMEP Range for Various Engines Types (Heywood 1988)

Engine Type	Compression Ratio	BMEP Range (MPa)
SI Engines		
Small (Motorcycles)	6-11	0.4-1
Passenger cars	8-10	0.7-1
Trucks	7-9	0.65-0.7
Large gas engines	8-12	0.68-1.2
Diesel Engines		
Passenger cars	17-23	0.5-0.75
Trucks	16-22	0.6-0.9
Large trucks	14-20	1.2-1.8
Locomotive	12-18	0.7-2.3
Marine engines	10-12	0.9-1.7

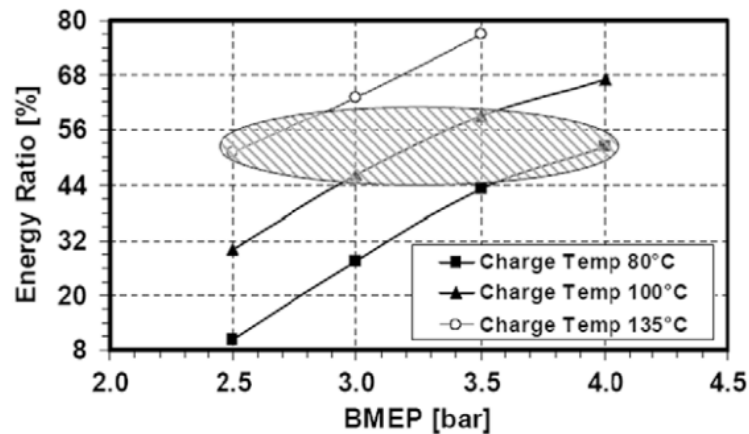


Figure 2.3 BMEP for different intake temperatures with varying energy ratio between natural gas and diesel. The shaded region shows the best energy ratio for natural gas-diesel HCCI engines, reproduced from (Nathan, Mallikarjuna & Ramesh 2010).

2.2.8 Exhaust Gas Emissions

Emissions in HCCI engines consist of UHC, CO, NO_x, soot and particulates. UHC and CO emissions in HCCI engines are generally higher than conventional CI engines as reported by (Ganesh & Nagarajan 2010; Kong & Reitz 2003; Park & Reitz 2007). There are no exact numbers reported in this study because the value was inconsistent for all engines and across all engine loads. High emissions level of CO and UHC might be due to incomplete combustion caused by low combustion temperatures (Bression *et al.* 2008; Ganesh, Nagarajan & Ibrahim 2008; Yap *et al.* 2006), which cause deposition of fuel in boundary layers and crevices (Garcia, Aguilar & Lencero 2009).

The low combustion temperature will reduce the combustion efficiency as a result of the lower oxidation activity of the hydrocarbons and the lower conversion rate of CO to CO₂ (Alkidas 2007). Results of simulations confirm that the piston-ring crevice needs to be resolved in order to accurately predict UHC and CO emissions (Kong & Reitz 2003). UHC and CO emissions originate in the crevices and boundary layer, which are too cold for complete combustion (Aceves *et al.* 2001). Higher concentrations of hydrogen and natural gas in diesel engines have the ability to reduce UHC and CO emission levels, because the gaseous state of hydrogen and natural gas will reduce the wall wetting effect on the cylinder liner (He & Cho 2007).

However, the difference in NO_x concentration between natural gas and hydrogen in diesel HCCI mode could be due to different combustion temperatures, because hydrogen has a higher temperature and flame speed compared to natural gas and diesel (Soberanis & Fernandez 2010). A survey of research papers by Akansu *et al.* (2004) shows that the NO_x level is increased when the hydrogen content in natural gas-hydrogen mixtures is increased. It shows that the combustion temperature and the flame speed of hydrogen contribute to a higher level of NO_x emissions.

In biogas-diesel HCCI engines, the NO_x level was low when the biogas energy was increased (Nathan, Mallikarjuna & Ramesh 2010). This might be due to a higher homogeneity level achieved between air and fuels. Van Blarigan (2002) in his study reported that the mixture must be homogeneous, lean or highly diluted in order to eliminate the production of NO_x. Olsson *et al.* (2002) stated that the NO_x level is low in natural gas HCCI engines and when combined with Exhaust Gas Recirculation (EGR), it drops further (Yap *et al.* 2006). Even in natural gas-diesel non-HCCI mode, the NO_x level is lower than in diesel conventional CI engines (Yusaf *et al.* 2010). Hydrogen, on the other hand, produces zero UHC, CO and CO₂, due to the absence of carbon in the fuel, but still produces NO_x (Verhelst & Wallner 2009). Hydrogen operated as a single fuel in CI mode yielded lower NO_x levels than diesel (Antunes, Mikalsen & Roskilly 2009). Saravanan and Nagarajan (2010) in their study of hydrogen addition to diesel in non-HCCI mode showed that lower NO_x emissions were obtained for all load ranges compared to diesel in conventional mode. They reported that the formation of NO_x depends on temperature more than the availability of

oxygen. Therefore, hydrogen-diesel in HCCI mode results in extremely low NO_x emissions levels with no significant amount of soot (Tsolakis, Megaritis & Yap 2008).

When the HCCI engine is operated with a gasoline fuel, the engine is reported to be unstable if the EGR is less than 40% or greater than 60% (Yingnan *et al.* 2010). This is also reported by Hosseini and Checkel (2009), where EGR is not suitable to be used for ignition control in a gasoline fuelled HCCI engine because EGR effects are different at different operating conditions.

2.2.9 Knocking

Knocking in SI engines is a phenomenon where the unburned mixture in the compressed gas ignites before it is reached by the propagating flame front (Stiesch 2003). Knock is physically detected when the engine vibrates excessively and a pinging sound can be heard outside as a result of the combustion activity. It causes loss of power and, if not controlled, knocking could lead to severe engine damage and shorten its life. Knocking can occur in any reciprocating engine. HCCI engines are prone to knock since they are controlled by chemical kinetics and there is no fixed mechanism to control knock in them. Knocking phenomena limit the load range of an HCCI engine: high load operations can easily initiate knock, so upper load limits have to be applied (Yap *et al.* 2006). In all engines, generally knocking occurs when the combustion starts before the piston reaches TDC, while misfire is when combustion commences after TDC. Knocking and misfire are two different behaviours which must be avoided in engine operation as both of them can contribute to deterioration of engine performance (Andreae *et al.* 2007; Jun, Ishii & Iida 2003; Kong & Reitz 2003; Nathan, Mallikarjuna & Ramesh 2010; Yelvington & Green 2003).

Knocking occurs when a rapid release of energy in the remaining unburned mixture causes a rapid increase in local pressure. Knocking phenomena can be detected in the in-cylinder pressure variations, observing a rapid instantaneous local pressure rise. The graph formed depends on the knocking frequency: the higher the frequency, the more severe the knock (Szwaja & Grab-Rogalinski 2009). Figure 2.4 shows knocking behaviour in a hydrogen-fuelled HCCI engine for a single combustion event with a

compression ratio of 17 by monitoring its in-cylinder pressure. It can be seen that the in-cylinder pressure suddenly increases to the peak before following the normal pressure trend: the peak pressure is higher than the normal in-cylinder peak pressure without knocking. The maximum increase in pressure for knocking is unpredictable and this abnormality usually occurs when there is an incorrect operating condition.

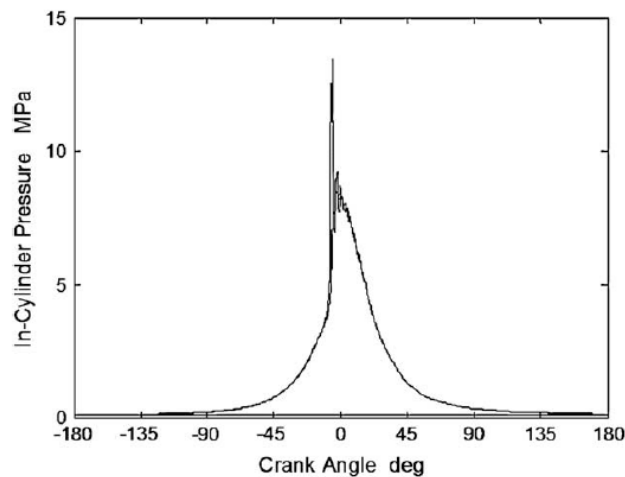


Figure 2.4 Knocking phenomena in a hydrogen HCCI engine for a single combustion event, reproduced from (Szwaja & Grab-Rogalinski 2009)

2.3 Injection Methods for Homogeneous Mixtures

Vaporized fuels are needed to initiate combustion in conventional CI engines. Therefore, a high fuel injection pressure is required. A higher injection pressure leads to better fuel vaporization and forms many small droplets of fuel leading to efficient fuel-air diffusion processes. Compression of air generates high in-cylinder temperatures, which is important to achieve the auto-ignition point of the fuel. CI engines using common rail injection systems employ injection pressures of at least 35MPa to ensure the injected fuel is vaporized before the combustion takes place. However, in HCCI combustion it is quite challenging to form a homogeneous fuel-air mixture before the initiation of combustion. Therefore, there are three methods to achieve homogeneous mixtures in HCCI engines (Yao, Zheng & Liu), and these could be applied to any fuel:

1. Port injection
2. Early injection

3. Late injection

2.3.1 Port Injection

Port injection is the method of locating the fuel injector in the intake manifold, where the injection pressure is not as high as in a direct injection system. Ganesh and Nagarajan (2010) have studied the HCCI combustion with port injection, which they called “external mixture formation”. It is used to form a homogeneous fuel-air mixture with injection pressures of no more than 0.6MPa.

Because the port injection pressure is not high, the fuel will not vaporize when entering the inlet manifold, creating an undesirable inhomogeneity problem. To overcome this, the fuel vaporizer must be mounted in the air intake manifold system so that the fuel is supplied in vapour form (Ganesh & Nagarajan 2010; Ganesh, Nagarajan & Ibrahim 2008). However, there are drawbacks when using port injection systems to form a homogeneous mixture: the soot is quite significant and NO_x emission is not as low as in SI engines (Yao, Zheng & Liu 2009). This might be due to the poor vaporization of the fuel, creating inhomogeneous mixtures.

2.3.2 Early Injection

Early injection uses the direct injection method, but with injection timing earlier in the compression stroke; there is no modification of the injection pressure from CI engines. Garcia, Aguilar and Lencero (2009) have studied the performance of an HCCI engine with early injection by varying the injection timing between 17° and 144° crank angle (CA) before top dead centre (BTDC). It was found that CO and HC were higher in HCCI mode compared to the conventional CI mode due to fuel impingement on the cylinder walls (Garcia, Aguilar & Lencero 2009). Another study of the spray structure of common rail type high-pressure injectors in HCCI engines obtained similar results (Ryu, Kim & Lee 2005). The spray structure was simulated for early injection timing between 240° and 340°CA BTDC with an increment of 20°CA with injection pressures of 80MPa and 100MPa. It was found that if the fuel was injected earlier than 280° BTDC, the fuel would impinge on the cylinder wall and create a rich mixture, leading

Chapter 2

to incomplete combustion due to wall and crevice effects. However, if the fuel was injected at 300°CA BTDC, the fuel would impinge on the outer surface of the piston area. Any injection earlier than 320°CA BTDC results in impingement on the piston bowl. This process is shown in Figure 2.5.

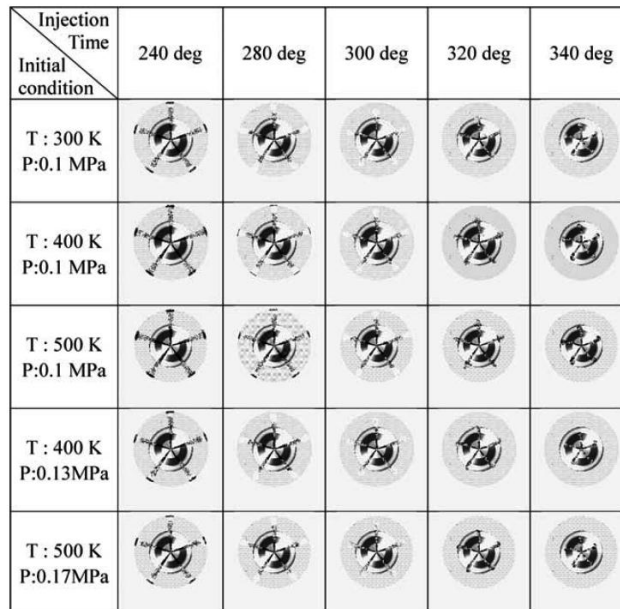


Figure 2.5 Spray structure simulation result for various initial conditions, reproduced from (Ryu, Kim & Lee 2005).

The dark curved areas at the centre represent the piston crown surface, the black circle line is the piston crown edges, the outer circle is the cylinder wall which in turn resembles piston edge and the five radial lines represent fuel being injected from the centre. Spray structure behaviour does not change much with initial conditions, while it does with injection timing.

It is obvious that early injection systems lead to fuel impingement problems on the cylinder wall and crevice areas. There are few methods to address this issue: using multiple injectors, multi-pulse fuel injection and narrow spray angle injectors. Multiple injectors will increase costs while multi-pulse fuel injection requires very precise control over injection timing by managing the injection pulse and its period (Yao, Zheng & Liu 2009). Therefore, it is hard to control the injection for different engine loads. Narrow spray angles might be an easier and cheaper way, which can be achieved by replacing the conventional injector (spray angle of about 156°) with a narrow spray angle injector (of about 60°). Kim and Lee (2007) have studied the effect of narrow spray angle injectors in an HCCI engine with an injection pressure of 100MPa. They found that a narrow spray angle injector in HCCI engines using early injection timing is effective in maintaining a high IMEP (Kim & Lee 2007). The schematic diagram for narrow spray angle injectors is shown in Figure 2.6. By using

narrow spray angle injectors, the fuel will hit the piston bowl instead of the cylinder wall. However, the obvious drawback of using early injection is the difficulty in controlling the start of combustion. Therefore, one has to pay extra attention to the ignition delay effects.

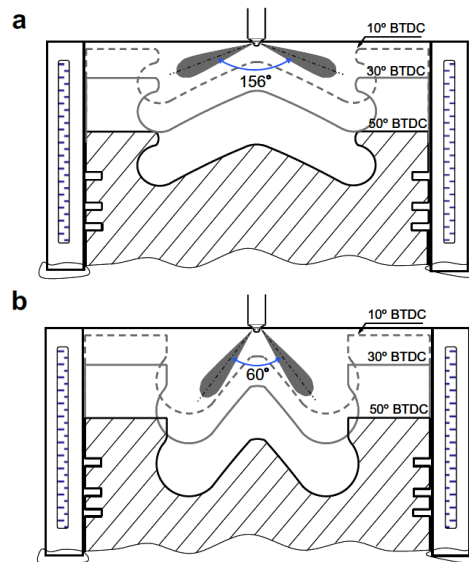


Figure 2.6 Schematic diagram of the narrow spray angle injector, reproduced from (Kim & Lee 2007).

2.3.3 Late Injection

Late injection still uses a direct injection approach in order to minimize modification to the injection system. However, a high-injection pressure system is used with retarded injection timing at the end of the compression stroke or at the early power stroke. Conventional ignition timing for CI engines varies from 23° BTDC to 5° after top dead centre (ATDC) depending on the equivalence ratio (Roy *et al.* 2009). For late injection systems, typically the ignition timing is retarded up to 7° ATDC (Yao, Zheng & Liu 2009). Late injection systems require a long ignition delay and rapid mixing rate (Ganesh & Nagarajan 2010; Yao, Zheng & Liu 2009). The former can be achieved by implementing EGR (as discussed in Section 2.4.4), while the latter is dependent on the geometry of the combustion chamber. The Nissan Motor Company has developed a successful late injection system for HCCI engines by using Modulated Kinetics (MK) combustion systems (Yao, Zheng & Liu 2009). They implemented high swirl effects in a toroidal combustion bowl to achieve rapid mixing with a bigger piston bowl

diameter. A higher piston bowl diameter is better as it can minimize the potential of fuel impingement on the piston bowl and the cylinder walls; Figure 2.7 shows an overview of a piston bowl with toroidal geometry. This late injection system is able to control the start of combustion better than the first two methods.

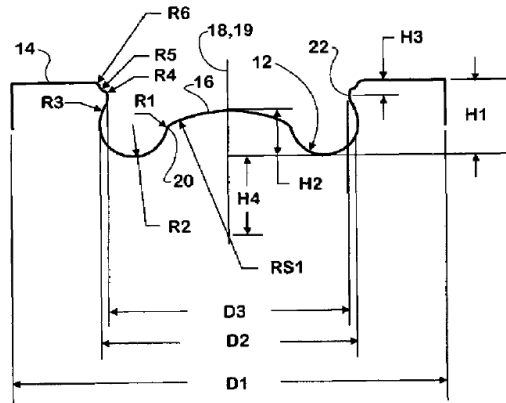


Figure 2.7 Piston bowl with toroidal geometry, reproduced from (Liu 2006).

2.4 Ignition Control in HCCI Engines

Ignition control is one of the challenges in developing HCCI engines. The challenges include (Kong & Reitz 2003; Park & Reitz 2007): 1) auto-ignition control; 2) limiting the heat release rate at high load operations; 3) meeting emissions standards; 4) providing smooth engine operation by achieving cold starts ('startability' of the engine); and 5) limited load range. Various studies have suggested that ignition can be controlled by using promoters or additives, blending of low cetane number fuels with high cetane number fuels (Morsy 2007), pre-heating of the intake air (Yap *et al.* 2006), pressurizing the intake air (Fiveland & Assanis 2002), hydrogen addition and varying the amount of exhaust gas recirculation (EGR) (Flowers *et al.* 2001) through early closure of the exhaust valve.

Managing the ignition delay is one of the effective ways to control the start of combustion. Ignition delay is the time lag between the start of injection and the start of combustion. This is difficult to control because the combustion in HCCI engines is

fully controlled by chemical kinetics. The ignition delay is affected by the rate of the heat loss through the cylinder wall, in-cylinder temperature and pressure, injection pressure and also the type of fuel used. Too short an ignition delay leads to knocking while too long an ignition delay leads to misfiring. The ignition delay is strongly dependent on the gas temperature: an increase in temperature accelerates the chemical reactions, thereby helping to reduce the ignition delay (Antunes, Mikalsen & Roskilly 2009; Reitz 2007). Tanaka *et al.* (2003) studied two-stage ignition in HCCI combustion, suggesting that the ignition delay can be controlled by the fuel-air ratio, initial temperature and additive dosages. The ignition delay can also be controlled by varying the compression ratio (Kim *et al.* 2006).

2.4.1 Pre-Heat Intake Air

As discussed in Section 2.2, using natural gas and hydrogen in HCCI require a high intake temperature. By pre-heating the intake air, ignition delay is reduced and thus the ignition timing can be controlled. As shown in Figure 2.2, methane and natural gas require high temperatures to auto-ignite and methane did not ignite for an intake temperature of 400K at low CR (Morsy 2007). Gasoline, on the other hand, requires an intake temperature of at least 303K for a relatively high CR engine (CR=14.5) (Bunting *et al.* 2008). Therefore, it is imperative to pre-heat the intake air to make the fuels combust smoothly.

Antunes, Mikalsen and Roskilly (2008) stated that heating the intake air is the most useful method to control the ignition timing. Questions may arise regarding the practicality of including electric heaters (Jun, Ishii & Iida 2003) in an engine bay just for this purpose: the heater causes the operation and maintenance costs to increase and contributes to extra engine weight. In addition, a heater with fast response time is required, which increases the cost further. Implementation of a heater also reduces the charge density, which affects the amount of fuel to be burnt (Ganesh, Nagarajan & Ibrahim 2008). However, installing a heater is an option used by most researchers as it is the easiest way to get intake air heated to a specific temperature. Exhaust gas recirculation (EGR) could be another option to reduce the need for a high intake

temperature (Ganesh, Nagarajan & Ibrahim 2008; Peucheret *et al.* 2005; Yap *et al.* 2006).

2.4.2 Pressurized Intake Air

Turbochargers and superchargers are commonly used in real engine applications because they can be applied to any internal combustion engine. The operational concepts of these two devices are the same: to provide a high intake pressure into the combustion chamber, increase the charge density and thereby increase the engine performance. Some studies (Agarwal & Assanis 1998; Fiveland & Assanis 2002; Liu *et al.* 2009) show that the start of combustion (SOC) is advanced if the intake pressure is increased by 0.1 MPa. This indicates that pressurised intake air is able to improve the auto-ignition of the fuel. However, these situations also depend on the type of fuel used, and in this case they used primary reference fuels and gasoline. By increasing the intake pressure, it was possible to get the auto-ignition to start at 15° before top dead centre (BTDC). On the other hand, supercharging (pressurising intake air) is able to increase engine efficiency (Soylu 2005). A supercharged hydrogen-diesel engine, but in non-HCCI mode, was able to maintain high thermal efficiencies and it was possible to use more than 90% hydrogen energy substitution for the diesel (Tsolakis & Megaritis 2005). Another study by Guo *et al.* (2011) shows that hydrogen-diesel in HCCI mode with pressurized intake air (150kPa) is able to improve the atomization process, and therefore improve the combustion efficiency. CO, HC and NO_x emissions were also decreased in this case.

2.4.3 Hydrogen Addition

Hydrogen is one of the promising renewable fuels because it is naturally available on the earth and can be produced from various resources such as fossil energy and biomass (Najjar 2013; Sun *et al.* 2012). Hydrogen can be used as a sole fuel in an SI engine but cannot be used in a CI engine due to its higher ignition point compared to diesel (de Morais *et al.* 2013; Saravanan & Nagarajan 2008). The used of hydrogen in internal combustion engines requires extra care due to safety reasons. According to

Najjar (2013), there are three hazards associated with the use of hydrogen: physiological (frostbite and suffocation), physical effect (embrittlement and component failures) and chemical (burning or explosion). Proper hydrogen installation such as high pressure vessel is required to avoid physiological effects. The ability of hydrogen to permeate through steel may cause an embrittlement effect and lead to component failures. Fayaz *et al.* (2012) reported that to avoid the embrittlement effect on some metals, the following alloys can be used in a hydrogen engine application: brass and copper alloys, aluminium and its alloys and copper beryllium. The crank case design of the engine should also be taken into consideration so that it has good ventilation. The blow-by effect causes unburned hydrogen to enter the crankcase and at certain concentrations may lead to combustion. The hydrogen injection method also plays an important role in avoiding undesired explosions. Direct injection is a preferred method over port injection to avoid the backfire effect (Fayaz *et al.* 2012). Backfire is combustion occurring during the intake stroke due to hot spots and could also occur in the intake manifold (Verhelst & Wallner 2009). It is of the utmost importance to avoid any undesired combustion behaviour for safety reasons.

Hydrogen can be produced in many ways including natural gas conversion, coal gasification, electrolysis, biomass gasification and photolytic processes (Fayaz *et al.* 2012). However, the conversion cost of hydrogen using current technology is still very expensive (Najjar 2013) and it is not practical to have a separate hydrogen vessel for a vehicle with dual fuel technology because the combined fuel cost becomes higher. Thus, an on-board hydrogen generator is a possible solution to overcome this high hydrogen conversion cost and also the problems associated with storage and handling (Christodoulou & Megaritis 2013). Tsolakis and Megaritis (2008) used a fuel reforming reactor in the diesel exhaust system to extract hydrogen. Bromberg (2001) used a plasmatron fuel converter to convert a gas containing hydrogen, while Bari and Esmail (2010) used water electrolysis to generate hydrogen.

Hydrogen addition in a CI engine is able to reduce UHC, CO and smoke emissions, however, NO_x emissions are typically increased due to the high combustion temperature (Christodoulou & Megaritis 2013; de Morais *et al.* 2013; Fayaz *et al.* 2012; Frolov *et al.* 2013; Nguyen & Mikami 2013; Saravanan & Nagarajan 2008; Sun *et al.* 2012). To reduce the NO_x, intake charge dilution with nitrogen can be used

(Christodoulou & Megaritis 2013), or EGR (Fayaz *et al.* 2012). With nitrogen dilution, the NO_x level is reduced substantially, however, smoke, CO and fuel consumption are increased. EGR, on the other hand, causes increase in PM, UHC, CO and also engine wear. Thus, Miyamoto *et al.* (2011) recommended using large amounts of EGR and late diesel-fuel injection timing for diesel engines with hydrogen addition. They reported that the NO_x emissions were low without the increase in UHC due to the low combustion temperature.

Hydrogen addition to the HCCI engine is one of the effective ways to reduce the ignition delay due to its high diffusivity in air, which causes rapid mixing between fuels and oxidizers. Hydrogen addition in a natural gas mixture is able to increase the in-cylinder peak pressure, reduce ignition delay time and ignition temperature, and increase indicated power (Rattanapaibule & Aung 2005). It also allows the extension of the lean limit of the natural gas mixture without entering the lean misfire region, while achieving extremely low emissions (Verhelst & Wallner 2009).

Hydrogen addition in ultra-low sulphur diesel (ULSD) promotes partially-premixed compression ignition and results in improved performance and reduction in emissions (Tsolakis & Megaritis 2005). In HCCI engines, hydrogen is able to form a homogeneous mixture due to its rapid mixing behaviour, and thus increase the efficiency of the engine (Saravanan *et al.* 2008). Furthermore, hydrogen can be produced from the exhaust gases of the engine itself using a reformer, which is called an “on-board hydrogen producer” (Tsolakis, Megaritis & Yap 2008; Yap *et al.* 2006). As the amount of hydrogen is increased, the auto-ignition delay time reduces accordingly while as the in-cylinder peak pressure is increased, the ignition temperature reduces and indicated power increases (Rattanapaibule & Aung 2005). The addition of hydrogen is not costly because it uses a lower-pressure fuel-injection system (Aceves *et al.* 2001).

Furthermore, the addition of hydrogen increases the engine efficiency by a significant margin, about 13-20% (Saravanan & Nagarajan 2010; Saravanan *et al.* 2008). By using a catalytic reforming aid in HCCI, the addition of hydrogen in natural gas HCCI engines helps in decreasing the need for high intake temperatures and also is a means of extending the lower limit of HCCI operations (Peucheret *et al.* 2005). It can be seen

from Figure 2.8 that the in-cylinder peak temperature increases and the ignition delay time reduces as the amount of hydrogen increases.

Szwaja and Grab-Logarinski (2009) studied hydrogen addition (in HCCI mode) with diesel in a CI engine and found that the addition of hydrogen in small amounts (e.g. about 5% in energy ratio) was able to reduce the ignition delay and improve engine performance. They also concluded that the addition of hydrogen to diesel should not be more than 15% in energy ratio to avoid severe knock.

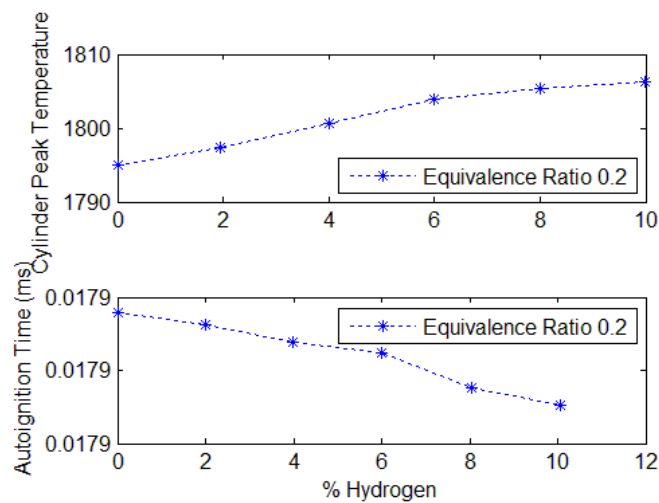


Figure 2.8 Hydrogen effect on the in-cylinder peak temperature and the ignition delay (Rattanapaibule & Aung 2005).

2.4.4 Exhaust Gas Recirculation (EGR)

EGR is a system where some portions of the exhaust gas are returned to the combustion chamber, controlled by using a valve. Exhaust gas contains less oxygen (O_2) and more CO_2 : combustion with reduced O_2 will lower the combustion temperature, and thus reduce the NO_x emissions. It is also used to reduce the large temperature difference between peak pressure and intake pressure: as a consequence, the rate of heat release is reduced. This means that the intake temperature using EGR is high and certainly helps in auto-ignition of the mixture. Saravanan and Nagarajan (2010) reported that EGR is able to increase the BTE of the engine, while reducing the NO_x formation. Furthermore, EGR improved auto-ignition of the engine and reduced the in-cylinder peak pressure. EGR used in an HCCI engine showed an improvement of 1.1% engine

efficiency, advanced the auto-ignition by 10° and reduced the heat release rate by $11 \text{ J}^\circ\text{CA}$ compared to a CI engine (Ganesh, Nagarajan & Ibrahim 2008). Ganesh and Nagarajan (2010) found that by using EGR on HCCI engines they were able to reduce the heat release rate with a lower combustion temperature. They could control ignition delay and reduce the in-cylinder peak pressure. The ignition delay is increased (combustion phasing is retarded) when the EGR rate increases (Lu, Chen & Huang 2005). However, this resulted in about 20% power loss (Garcia, Aguilar & Lencero 2009). Cooled EGR is preferred because it can suppress advanced auto-ignition of the premixed fuel with reduced emissions levels compared to hot EGR (Kim & Lee 2006).

2.4.5 Addition of Dimethyl Ether (DME)

Additives do not seem to lead to any major practical improvements, due to the addition of extra chemical compounds, which leads to an increase in operational cost. However, with the help of additives such as DME, the start of combustion of DME in a natural gas/DME mixture is improved by reducing the ignition delay time. It was found that methane-fuelled HCCI engines with an intake temperature of 400K ignited only if small amounts of additives were added (Morsy 2007). This shows the advantage of using additives, which can control the auto-ignition timing, but with extra drawbacks.

2.4.6 Charge Stratification

Stratification methods result in different mixture compositions while still retaining the chemical-kinetics dominated auto-ignition to control HCCI combustion. This has led to various control strategies, which has moved away from truly homogeneous mixtures. The term that is sometimes used is stratification charge compression ignition (SCCI) engines (Yao, Zheng & Liu 2009; Zheng & Yao 2007). SCCI is achieved with a combination of port fuel injection and direct-injection methods (Dec & Sjoberg 2004; Sjoberg & Dec 2006). A study from Dec and Sjoberg (2004) on the potential of fuel stratification for ignition control reported that they used port fuel injection to achieve a homogeneous mixture, with direct-injection at the early stages of the compression stroke to achieve a stratified charge. Direct-injection at the early stages of the compression stroke is to prevent the fuel from entering the crevice areas. They

concluded that charge stratification can be used to control the ignition timing and also improve the low-load combustion efficiency.

Thermal stratification can also be applied for ignition control. Sjoberg and Dec (2005) investigated the potential of thermal stratification and combustion retardation for reducing pressure-rise rates in HCCI engines. They used numerical methods of a highly tuned (adjusting wall zone temperature, in-cylinder pressure at BDC and CR) multi-zone model from Sandia National Laboratories (Lutz 2002) to match the experimental results. The multi-zone model can be used to assign a different wall temperature to a different zone. They reported that the combustion rate in HCCI engines can be reduced by adjusting the wall zone temperature. They also suggested that the combination of slow combustion and thermal stratification allow the HCCI engine to achieve higher loads. However, it is unclear how to use thermal stratification in practical engines by controlling different combustion zone temperatures (Zheng & Yao 2007).

2.5 Numerical Study of HCCI Engines

Simulations are undertaken to reduce research costs while maintaining good productivity because of their cost efficiency compared to experimentation alone. By using numerical methods, one can optimize engine parameters before conducting experiments and obtain optimized parameters within a short time and at low cost. Many researchers use KIVA-3V CFD software in combination with detailed chemical kinetics solutions using CHEMKIN from Sandia National Laboratories (Agarwal & Assanis 1998, 2000; Babajimopoulos, Lavoie & Assanis 2003; Chen, Konno & Goto 2001; McTaggart-Cowan *et al.* 2009). Good agreement between simulations and experiments has been achieved.

2.5.1 Chemical Kinetics

In a CI engine, the fuel is direct-injected in the chamber with a high injection pressure when the piston is nearly at TDC. Then, the fuel ignites rapidly in the hot air

environment. In SI engines, the spark plug is triggered when the piston is approximately at TDC to initiate the combustion. HCCI engines, on the other hand, have no mechanism to control the ignition timing and rely solely on chemical kinetics for combustion, as discussed in Section 2.3. The combustion in an HCCI engine is triggered when the heat in the chamber has reached the fuel activation energy. To numerically investigate the combustion behaviour, chemical kinetic mechanisms which represent the actual fuels have been developed (Curran *et al.* 1998, 2002; Golovitchev 2003; Lee, Kim & Min 2011; Mehl, Pitz, *et al.* 2011; William & Charles 2011). A detailed mechanism such as those developed for diesel fuel consists of a blend of components such as *n*-alkanes, *iso*-alkanes, *cyclo*-alkanes, aromatics and others (Westbrook *et al.* 2009). Those components were then combined to represent the real fuels (Farrell *et al.* 2007). Most studies on developing the chemical kinetic mechanism (Curran *et al.* 1998, 2002; Mehl, Curran, *et al.* 2009; Mehl, Pitz, *et al.* 2011; Naik *et al.* 2005; Westbrook *et al.* 2009) for HCCI engines use the Arrhenius-like plot (such as shown in Figure 2.9) to relate the fuel activation energy with ignition delay time, where the activation energy is proportional to the slope of the graph (Taylor 2006).

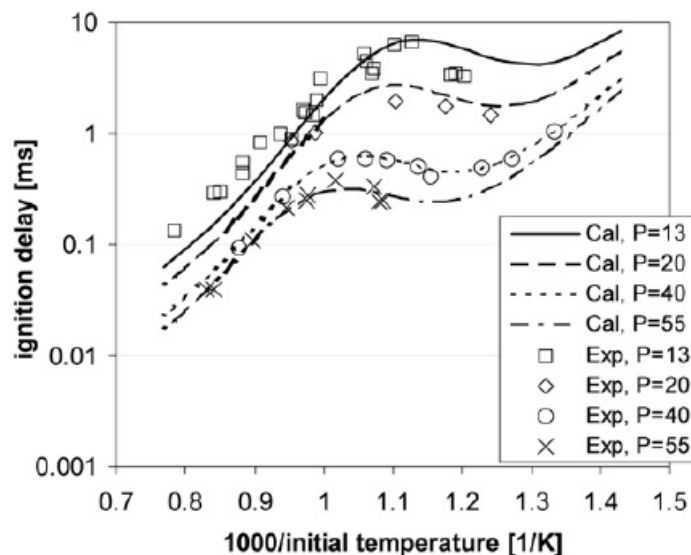


Figure 2.9 Ignition delay time for *n*-heptane validated against experiment for different pressures (Ra & Reitz 2008).

Small variations in fuel properties affect the HCCI combustion by having a different ignition delay time. Figure 2.10 shows the ignition delay time and burn rate of different fuels (Tanaka *et al.* 2003). The *n*-heptane has the lowest ignition delay time, while *iso*-octane is the highest with a slower burn rate. This shows that the ignition delay time

(for multiple ignition stages as in Figure 2.10) and burn rates are dependent on the fuel structure. Tanaka et al. (2003) reported that the failure of toluene auto-ignition is due to the high activation energy required to abstract the hydrogen (H) radical from the carbon chain.

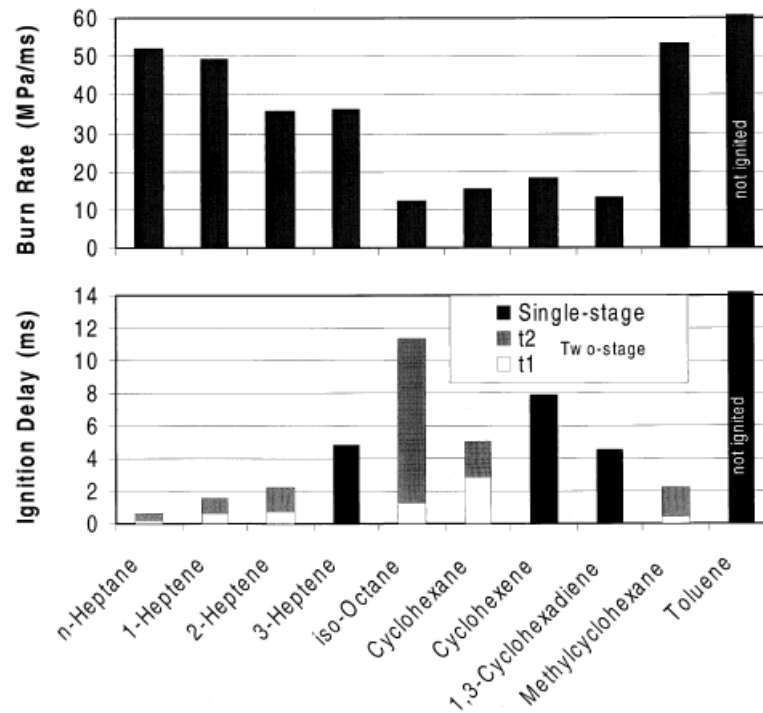


Figure 2.10 Summary of ignition burn rate and delay time for different type of fuels (Tanaka et al. 2003).

Westbrook et al. (2009) studied detailed chemical kinetic models for large *n*-alkanes, which can be used to represent the diesel fuel. The aim was to investigate the model that can use fewer computing resources by having an almost identical ignition behaviour compared to the experiment. They found that the ignition delay time is not affected significantly for different carbon lengths. Thus, they concluded that a small *n*-alkane such as *n*-octane can be used as a surrogate fuel for diesel which has the same ignition behaviour of a much larger *n*-alkane like *n*-hexadecane. Many studies have been conducted to develop a chemical kinetic mechanism that can represent the actual fuels. This is summarised in Table 2.7, which shows different chemical kinetic mechanisms to represent different fuels.

It is common to use *n*-heptane as a surrogate fuel for diesel (Guo et al. 2010; Hernandez et al. 2008; Pitz & Mueller 2011; Westbrook, Pitz & Curran 2006) because

the chemical properties between those two are very similar, particularly in terms of cetane number. The intake temperature when *n*-heptane is used as a fuel in an HCCI engine is not as high as methane or natural gas. A study by Guo *et al.* (2010) showed that *n*-heptane can easily be ignited when the inlet temperature is 313K on a low CR engine (CR=10). Methane, on the other hand, is reported to have no ignition when the inlet temperature is less than 400K on a high CR engine (CR=15) (Fiveland & Assanis 2000). Thus, it is important to have the right fuel and its chemical kinetic mechanism in order to study the combustion behaviour of an HCCI engine.

Curran *et al.* (1998) developed a detailed mechanism for *n*-heptane and validated the result over a wide range of operating conditions. They found that the ignition delay is in very good agreement with experiments using flow reactors, shock tubes and rapid compression machines. Because a detailed mechanism uses more computational resources, Seiser *et al.* (2000) and Golovitchev (2003) developed a reduced mechanism for *n*-heptane. Patel (2004) reduced the mechanism by more to obtain 26 species and 52 reactions. He reported that the CPU time is reduced by 50-70% and the validation was completed under both constant-volume reactor and HCCI engine conditions. The ignition delay result is similar to those of detailed mechanisms. The use of *n*-heptane as the only main component in the mechanism is not sufficient to predict the soot emission from CI and HCCI engines. Thus, Wang *et al.* (2013) improved the mechanism by blending the *n*-heptane and toluene mechanisms. They reported that the mechanism gives reliable soot predictions and combustion phasing under various engine conditions.

An *iso*-octane mechanism was used as a surrogate fuel for gasoline and it can also be blended with *n*-heptane to represent a real fuel (Curran *et al.* 2002; Tanaka, Ayala & Keck 2003). A real gasoline fuel consists of thousands of hydrocarbon compounds (Ogink & Golovitchev 2001; Zheng *et al.* 2002) and the fuel should be modelled using a combination of a few components. Mehl *et al.* (2011) developed a mechanism that represents a commercial grade gasoline, which consists of *n*-heptane, *iso*-octane, toluene and olefins. They reported that the result is in good agreement over a wide range of pressures and temperatures relevant to internal combustion engine applications. A reduced mechanism was also developed by Mehl and Chen *et al.* (2011) and further reduced by Lee *et al.* (2011). A reduced mechanism shows an

advantage when used in a complex CFD model, which requires more computational resources (Lee, Kim & Min 2011).

The main component of natural gas mainly is methane, as shown in Table 2.1 and Table 2.2. A mechanism for methane called Gri-Mech (Smith *et al.* 1999) has received wide attention (Fiveland & Assanis 2000; Morsy 2007; Sato *et al.* 2005). A further development of the methane mechanism has ended with the final version being Gri-Mech 3.0. Then, reduced mechanisms have been developed based on the Gri-Mech mechanisms such as those from Msaad *et al.* (2012). A recent development of the methane mechanism is by Slavinskaya *et al.* (2013). The mechanism was validated for high- and low-pressure conditions for rocket applications. They take into consideration the depletion of ozone layer. The result shows that a methane-air propelled liquid rocket engine influences the formation of nitrogen compounds and thereby depleted the ozone.

Hydrogen mechanisms, on the other hand, show a matured development, where the species and reactions are not substantially varied. A well-developed hydrogen mechanism in 1995 by Marinov *et al.* (1995) has been validated over a wide range of operating conditions, including high-pressure combustion. A recent development by Burke *et al.* (2012) focused on the discrepancies (in reaction rate parameters) between experiment and simulation. They reported the characterisation of the non-linear mixture for $H+O_2(M)=HO_2(+M)$ might be necessary to predict high pressure flame speed within an accuracy of 5%.

Biofuel is considered as an alternative fuel and is produced from long-chain fatty acids derived from either vegetable or animal oil. The trans-esterification method is used to transform these large molecules into esters, where methanol is commonly used during the trans-esterification process (Herbinet, Pitz & Westbrook 2010). The focus of using biofuels has received increasing attention (Komninos & Rakopoulos 2012) because of their advantages as alternative fuels. Biofuel can be extracted from fats or vegetable oils (An, Wilhelm & Searcy 2011) and also algae (Amin 2009). The chemical kinetics development for biofuels has advanced to the next level by blending the *n*-heptane and methyl esters to represent rapeseed and soybean derived biodiesels, such as those developed by Herbinet *et al.* (2010). They reported that the ignition delay is in good

Chapter 2

agreement with experiments using rapeseed oil. The mechanism can also be used for modelling the biofuel from various origins by adjusting the mole or mass fractions of the components (methyl decenoate, methyl-5-decenoate, methyl-9-decenoate and *n*-heptane) according to the actual biofuel blends. For more detail on chemical kinetic reaction mechanisms available for biofuels, one can refer to a review paper by Komninos and Rakopoulos (2012).

Chapter 2

Table 2.7 Chemical kinetic mechanisms available for different fuels.

Fuel	Main Components	References	Number of Species / Number of Reactions	Temperature Range (K)	Pressure Range (bar)	Equivalence Ratio Range
Diesel	<i>n</i> -heptane	1998 (Curran <i>et al.</i>)	565/2540	550 - 1700	1 - 42	0.3 – 1.5
	<i>n</i> -heptane	2000 (Seiser <i>et al.</i>)	159/770	625-1667	1-13.5	-
	<i>n</i> -heptane	2003 (Golovitchev)	57/290	600-1300	6-42	0.5-3.0
	<i>n</i> -heptane	2004 (Patel, Kong & Reitz)	26/52	700-1100	40-50	0.2-1.0
	<i>n</i> -heptane/toluene	2013 (Wang <i>et al.</i>)	71/360	-	-	-
Gasoline	<i>iso</i> -octane	2001 (Ogink & Golovitchev)	101/479	600-1400	10-40	0.22-2
	<i>iso</i> -octane	2002 (Curran <i>et al.</i>)	857/3606	550 - 1700	1 - 45	0.3 - 1.5
	<i>iso</i> -octane	2002 (Zheng <i>et al.</i>)	45/69	-	-	0.2-0.7
	<i>iso</i> -octane	2003 (Tanaka, Ayala & Keck)	32/55	750-900	30-50	0.2-0.6
	<i>n</i> -heptane/ <i>iso</i> -octane/toluene	2003 (Golovitchev)	119/621	600-1300	20-50	1
	<i>n</i> -heptane/ <i>iso</i> -octane/toluene/olefins	2011 (Mehl, Pitz, <i>et al.</i>)	1389/5935	650-1200	3-50	0.5-1.3
	<i>n</i> -heptane/ <i>iso</i> -octane/toluene/olefins	2011 (Mehl, Chen, <i>et al.</i>)	312/2469	650-1200	3-50	0.5-1.3
	<i>n</i> -heptane/ <i>iso</i> -octane/toluene	2011 (Lee, Kim & Min)	48/67	700-1200	40	0.5-2.0
Natural gas	Methane	1999 (Smith <i>et al.</i>)	53/325	1000-2500	0.01-10	0.1-5
	Methane	2001 (Hughes <i>et al.</i>)	37/351	-	-	-
	Methane	2006 (Huang & Bushe)	55/278	900-1400	16-40	1
	Methane	2007 (Lu & Law)	19/15	1000-2000	1-30	0.5-1.5
	Methane	2012 (Msaad <i>et al.</i>)	14/9	300-1800	40-60	0.7-1

Chapter 2

	Methane	2013 (Slavinskaya <i>et al.</i>)	37/354	300-1800	0.02-100	0.5-3.0
Hydrogen	Hydrogen	1995 (Marinov, Westbrook & Pitz)	9/20	250-2500	0.05-87	0.2-6
	Hydrogen	2004 (O Conaire <i>et al.</i>)	10/18	298-2700	0.05-87	0.2-6
	Hydrogen	2012 (Zhukov)	9/14	900-1400	1	0.5-5
	Hydrogen	2012 (Burke <i>et al.</i>)	11/19	1000	1-30	0.5-4.5
Biofuels	Ethanol	1999 (Marinov)	57/383	300-2500	1	0.5-2.0
	Methanol	2002 (Lindstedt & Meyer)	52/326	-	-	-
	Ethanol	2006 (Mosbach <i>et al.</i>)	112/484	-	-	-
	Methyl butanoate	2007 (Gail <i>et al.</i>)	295/1498	800-1350	1-13	0.35-1.5
	Methyl butanoate/ <i>n</i> -heptane	2008 (Brakora <i>et al.</i>)	53/156	650-1350	40-60	0.4-1.5
	Methyl decanoate/methyl-5-decenoate/methyl-9-decenoate/ <i>n</i> -heptane	2010 (Herbinet, Pitz & Westbrook)	3036/8555	800-1400	10	0.5
	Methyl decanoate/methyl 9-decenoate/ <i>n</i> -heptane	2012 (Luo <i>et al.</i>)	115/460	700-1800	1-100	0.5-2
	Butanol	2012 (Sarathy <i>et al.</i>)	426/2335	720-1700	0.04-80	0.6-1.7
	Methyl decanoate/methyl 9-decenoate/ <i>n</i> -heptane	2013 (Brakora)	69/192			

2.5.2 Numerical and CFD Environments

Numerical modelling can be categorized by the number of dimensions considered: zero-dimensional, quasi-dimensional and multi-dimensional. CFD is a multi-dimensional method whereby it resolves very small-scale zones (discretisation of domain into many small control volumes). Once the domain is discretised, the CFD method solves all the governing equations in all directions. The smaller the discretisation zone (at the domain of interest), typically produces a more accurate result as it can solve boundary layer or turbulent effects more efficiently. A zero-dimensional model is the simplest model where there is only one independent variable, typically either time or crank angle, and a heat transfer model is normally applied. The advantage of a zero-dimensional model is that the run time is fast (computationally effective) and therefore it can be utilized for immediate use of engine design and analysis. However, the disadvantage of this method is that the simulated combustion duration is shorter than the actual duration due to inhomogeneities in reality (Yao, Zheng & Liu 2009). The calculated results of zero-dimensional models produce rapid pressure increases and very high heat release rates compared to actual HCCI engine combustion due to the assumption that the model is perfectly homogeneous (Sato *et al.* 2005). A quasi-dimensional model uses a turbulent sub-model for turbulent combustion and to derive a heat release model. Figure 2.11 shows three different interacting regions for a quasi-dimensional model which is typically used to improve upon the zero-dimensional model. However, UHC emissions are over-predicted by 5-15% and CO emissions exhibit a 50% error. This is due to the inability of the model to capture small temperature differences in the crevices (Fiveland & Assanis 2001, 2002).

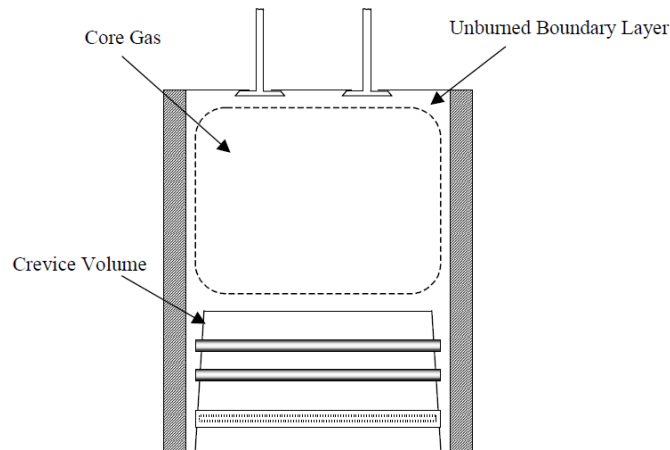


Figure 2.11 General layout of the quasi-dimensional simulation showing the interacting adiabatic core, thermal boundary layer and crevice regions, reproduced from (Fiveland & Assanis 2002).

2.5.3 Single-Zone and Multi-Zone Models

A single-zone model is where the combustion chamber area is treated as one homogeneous block. A multi-zone model separates the combustion chamber into several zones and the zone distribution depends on the type of the engine, either based upon flame propagation or homogeneous mixtures, thereby representing the inhomogeneity in the cylinder prior to combustion (Yao, Zheng & Liu 2009). The zone distribution for HCCI engines is shown in Figure 2.12(a) while Figure 2.12(b) is a multi-zone model for SI engines. Multi-zone modelling of HCCI engines is organized in such a way because the heat generated in an HCCI engine comes from the core of the combustion chamber. This is different to SI engines where the zone is started from the spark plug (the location of the heat source), and propagated according to the flame front motion.

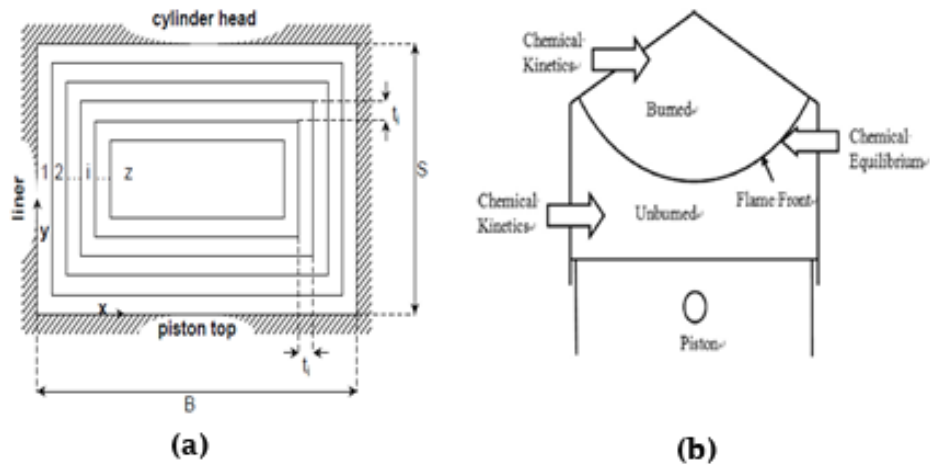


Figure 2.12 Multi-zone model geometric configuration difference (a) HCCI engine, reproduced from (Kominos, Hountalas & Kouremenos 2004) (b) SI engines, reproduced from (Liu & Chen 2009).

The single-zone model has some limitations due to the assumption that the whole combustion chamber is treated as homogeneous. Peak cylinder pressure and rate of pressure rise can be over-predicted. It also predicts a short burn duration and cannot accurately predict CO and HC emissions, which primarily depend on crevices (Morsy 2007). Crevices and the boundary layer are the cold areas for HC and CO to react during combustion. On the other hand, the multi-zone model predicts the pressure trace and the peak cylinder pressure very well, but it also cannot consider boundary layer effect and crevices and thus cannot predict CO and HC emissions (Aceves *et al.* 2000). Better agreement in combustion phasing is achieved when the single-zone model is coupled with turbulent effects, as shown in Figure 2.13. In a zero-dimensional model, the turbulence affects the heat loss model by changing the characteristic velocity in the Nusselt-Reynolds heat transfer model. The characteristic velocity is obtained by taking into consideration the contribution from mean velocity, turbulent intensity and piston motion.

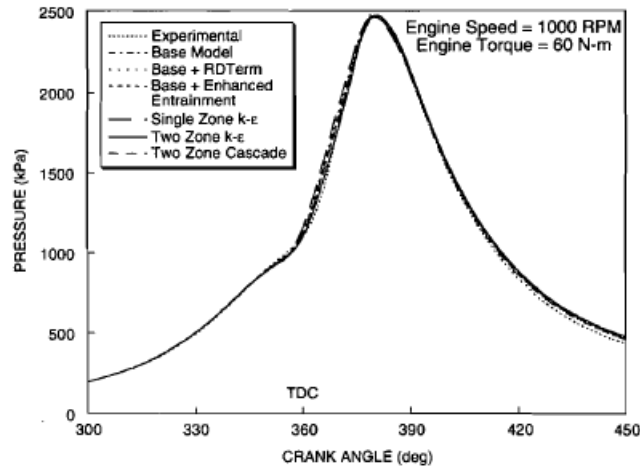


Figure 2.13 Effects of various turbulence models in in-cylinder pressure trace compared with experiment in the single-zone zero-dimensional model (Agarwal *et al.* 1998).

If there is any inhomogeneity in the mixture, turbulence has an effect on combustion, while for a completely homogeneous mixture, turbulent mixing has little effect on the combustion heat release rate. However, it is suspected that there will be inhomogeneities in the mixture as there is often insufficient time to mix down to the smallest relevant scales, which would cause turbulent mixing to directly affect reaction rates (Kong & Reitz 2002, 2003). In actual combustion chambers, transportation of chemical species, heat transfer and heterogeneity of temperature and species concentration exist (Peucheret *et al.* 2005). A multi-zone model of HCCI combustion predicted maximum pressure, burn duration, indicated efficiency and combustion efficiency with the worst error of 10% (Aceves *et al.* 2000). However, UHC and CO emissions were under-predicted; Aceves *et al.* (2000) suggested that this might be due to some crevices not being considered in the analysis. They used a multi-zone model including zones in crevice regions, producing more accurate results.

2.5.4 Multi-Dimensional Models: CFD

A multi-dimensional model solves the equations for mass, momentum, energy and species conservation to obtain more accurate results at the expense of computational time and resources. When solving detailed chemical kinetics, a sequential operation is used to reduce computational time by solving the flow field then the chemistry rather than attempting to satisfy both simultaneously. Two common approaches to multi-dimensional modelling are multi-zone models and CFD. A multi-zone model requires

substantially less computational time and resources than CFD, at the expense of accuracy. However, Aceves *et al.* (2002) showed that a 40-zone model can successfully predict the effect of crevice geometry on HCCI combustion with combustion efficiency predicted to within 5% error compared to experiment.

A study has been performed using two-step processes in CFD to analyse combustion (Aceves & Flowers 2004). First, KIVA CFD was used for the effect of turbulence to solve the transport of all variables. Then the result from KIVA was used in the hydrodynamics, chemistry and transport (HCT) code to calculate the combustion parameters. This two-step method made it possible to obtain accurate predictions for turbulent combustion within a reasonable computational time (Aceves & Flowers 2004). The proposed approach using the CFD method can provide an accurate prediction of the combustion process and accounts for mixture inhomogeneities in both temperature and composition (Babajimopoulos, Assanis & Fiveland 2002).

2.5.5 Effect of Operating Parameters on Ignition Delay Time

As discussed in Section 2.4, the ignition in HCCI engines can be controlled using a number of parameters. This can also be discussed using a numerical approach, where the chemical kinetics was used to investigate the ignition delay time for different fuels. Tanaka *et al.* (2003) developed a reduced chemical kinetic model for a Primary Reference Fuel (PRF), which is a blend of *n*-heptane and *iso*-octane. They validated the model in a Rapid Compression Machine (RCM) to represent HCCI combustion. The comparison was made between *iso*-octane, PRFs and *n*-heptane. The results in Figure 2.14 and Figure 2.15 show the ignition delay time for the selected fuel mechanisms with varying initial temperature and equivalence ratio. The results indicate that *n*-heptane has the fastest ignition delay time compared to PRFs and *iso*-octane. When the inlet temperature increases, the ignition delay time reduces further, where all fuels follow the same trend, as expected. The ignition delay time is also decreased when the equivalence ratio is increased towards the rich mixture, where the *n*-heptane has the fastest ignition delay time irrespective of the equivalence ratio compared to other fuels, as shown in Figure 2.15. The *n*-heptane also has the highest burn rate, which shows its characteristic of susceptibility to auto-ignite.

The results for the ignition delay time between *n*-heptane and *iso*-octane by Tanaka *et al.* (2003) is consistent with experiment. As discussed in Section 2.5.1, the *n*-heptane can easily be ignited using an inlet temperature of 313K on a low CR engine. Gasoline, on the other hand, requires an inlet temperature of 453K to auto-ignite for a high CR engine (CR=14.5) (Puduppakkam *et al.* 2009). This shows that gasoline has a higher chemical activation energy compared with *n*-heptane. Different fuels require different inlet temperatures to auto-ignite, as shown in Figure 2.2, which result in different ignition delay times. The inlet temperature requirement reduces as the compression ratio of the engine increases. This is also consistent with Olsson *et al.* (2002), where they studied the effect of compression ratio on a natural gas fuelled HCCI engine. They found that as the compression ratio increased, the required inlet temperature decreased, which reduced the ignition delay time.

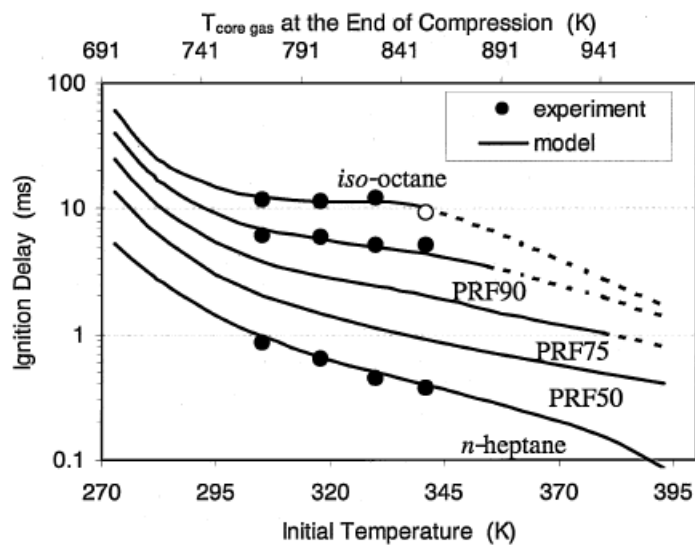


Figure 2.14 The effect of initial temperature on ignition delay time for different fuels (Tanaka, Ayala & Keck 2003).

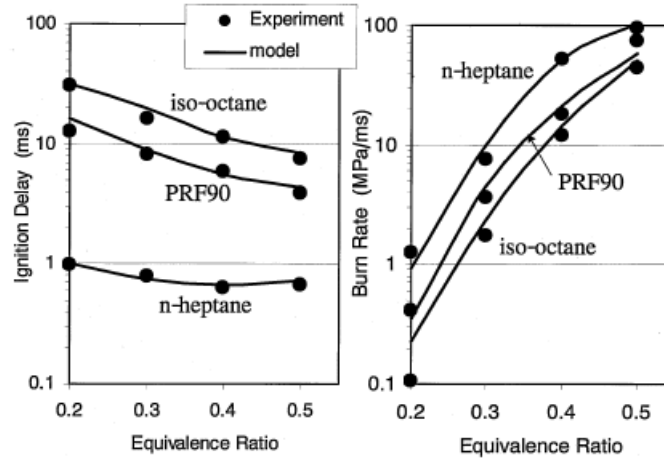


Figure 2.15 The effect of equivalence ratio on the ignition delay and burn rate for *n*-heptane, *iso*-octane and primary reference fuel (PRF) (Tanaka, Ayala & Keck 2003).

The effect of different inlet pressures using chemical kinetics was investigated by Puduppakkam *et al.* (2010). They studied the ignition delay time between diesel and gasoline using detailed chemical reaction mechanisms. The *n*-heptane mechanism used as a surrogate fuel for diesel consists of 3809 species and 15678 reactions. The surrogate fuel for gasoline consists of 1833 species and 8764 reactions. Both surrogate fuels use a blend of several chemical classes, such as normal-, cyclo- and *iso*-alkanes, alkenes and aromatics. The result is shown in Figure 2.16 for *n*-heptane, where the ignition delay time reduced as the inlet pressure increased. The pressurised intake air is able to increase the charge density and engine performance, and also can be used as an effective tool to control the ignition in HCCI engines, as discussed in Section 2.4.2.

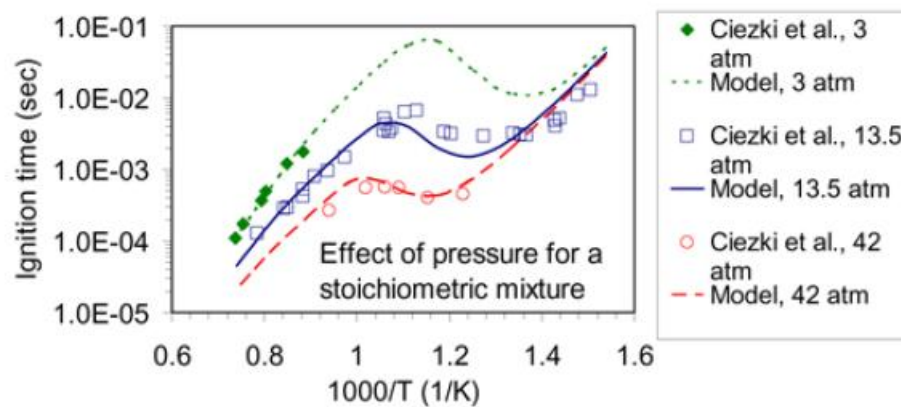


Figure 2.16 The effect of different pressure on the auto-ignition delay time for a stoichiometric mixture of *n*-heptane/air (Puduppakkam *et al.* 2010).

Chapter 2

Figure 2.17 shows the effect on ignition delay time when EGR is employed. It shows that the ignition delay time is slightly increased when EGR increases (reduction in O₂ mole fraction). The result in Figure 2.17 also shows that the ignition delay time reduces when the inlet pressure increases. The effect of EGR is also discussed by Christensen and Johansson (1998), where they studied the mixture quality using *iso*-octane, ethanol and commercial-grade natural gas in a high CR HCCI engine. They reported that the ignition delay time also increased when EGR was used. This in return gives retarded combustion and slows the combustion rate, which is useful to reduce the combustion noise and also knocking.

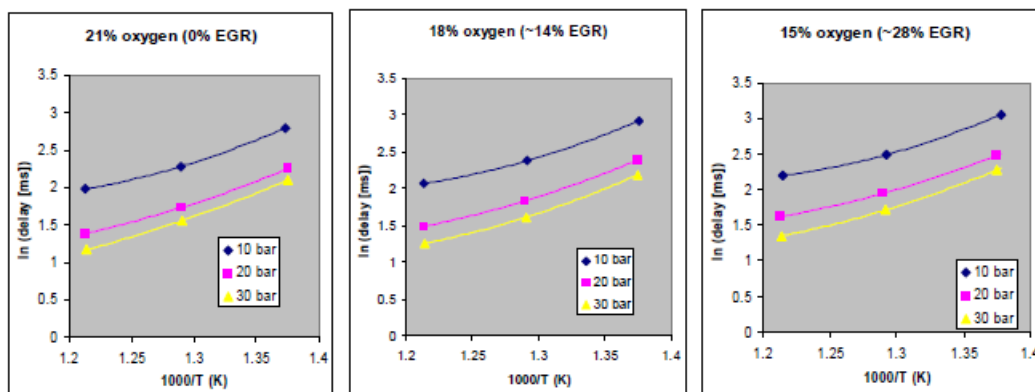


Figure 2.17 Effect of EGR on ignition delay for n-heptane fuel (Taylor 2006).

Knocking, as discussed in Section 2.2.9, is due to the instability in combustion phasing. Unstable combustion may cause knocking or misfiring (advanced or retarded ignition timing). EGR is able to retard the ignition timing and also to obtain higher loads, but too much retarded combustion causes misfiring especially for the fuel with longer burn duration (Dec 2009). The combustion phasing in HCCI engines is difficult to control at high loads because the stability limits between knocking and misfiring is narrow (Sjoberg *et al.* 2004). Maurya and Agarwal (2011) reported that the unstable combustion is due to high cycle-to-cycle variation and to overcome this, they used closed loop control to monitor the combustion phasing.

Olsson *et al.* (2002) in their study of compression ratio influence on the maximum load of an HCCI engine reported that the combustion-phasing stability is due to the coupling between chemical kinetics and thermal problems. The gas temperature during combustion is influenced by the wall temperature or heat transfer rate, which affects

the ignition timing. The instability in combustion becomes more severe at high loads, where the unstable combustion causes advanced or retarded combustion, as shown in Figure 2.18. They employed hydrogen addition to control the ignition timing. The mass fraction of hydrogen was increased in order to advance the ignition. Once the wall temperature was substantially increased, the hydrogen amount was then reduced to keep the stability limit under control. Thus, a closed-loop control for the ignition timing was achieved by monitoring the wall temperature (heat transfer rate) and the rate of hydrogen addition, in addition to the inlet temperature and fuel composition.

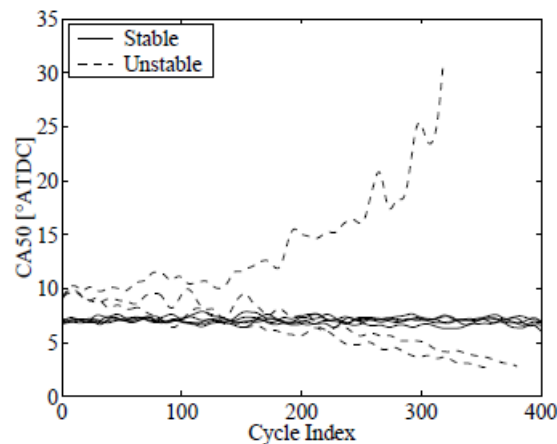


Figure 2.18 Ignition timing stability captured over time-lapse (Olsson *et al.* 2002).

2.5.6 Heat Transfer Model

The heat transfer model plays an important role in combustion: it affects ignition timing; combustion duration; formation of CO, UHC and NO_x; and the rate of in-cylinder pressure and temperature rise, which is correlated to knock (Hou *et al.* 2010; Komninos & Kosmadakis 2011). The influence of the heat loss through the combustion walls could be added in any of the numerical models discussed earlier. Some of the most commonly used heat transfer models are those devised by Anand, Woschni, Prandtl, Assanis and Hohenberg (Jia, Xie & Peng 2008; Reitz & Han 1997; Soyhan *et al.* 2009) and readers are advised to look at the work by Soyhan *et al.* (2009), which explains the heat transfer equations by Assanis, Woschni and Hohenberg. From the study by Soyhan *et al.* (2009), the Hohenberg model performs best in comparison

with the Woschni and Assanis models: it predicted the in-cylinder pressure closest to the experiment, as shown in Figure 2.19.

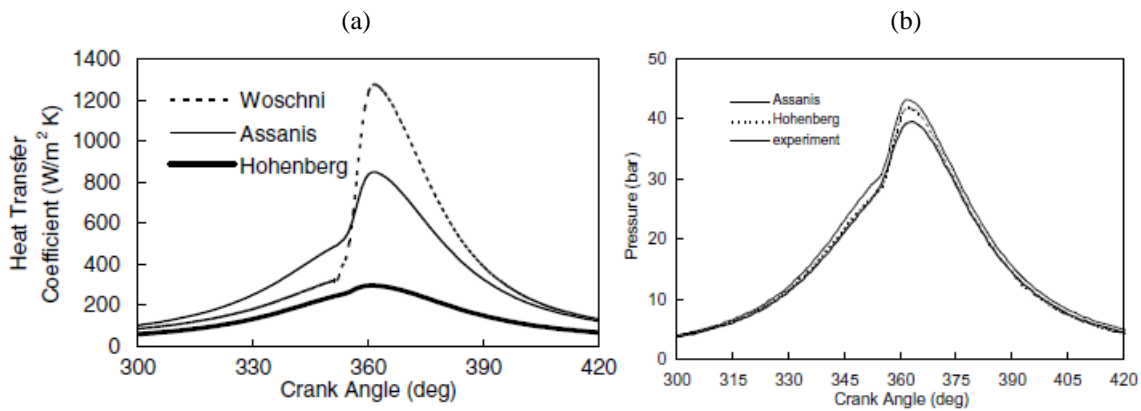


Figure 2.19 Heat transfer model comparison with experiment, (a) heat transfer coefficient, (b) in-cylinder temperature difference, reproduced from (Soyhan *et al.* 2009).

2.5.7 Turbulence Models: RANS vs. LES

Turbulent flow occurs at high Reynolds numbers and, according to Tennekes and Lumley (1972), the nature of the turbulence can be characterized as “irregularity, diffusivity, three-dimensional vorticity fluctuations, large Reynolds number and continuum phenomenon (continuous in space and time)”. Currently there is no exact solution for most turbulent flows and this has led to the creation of turbulence models, where the useful method to analyse the equation of motion is using statistical techniques (Cant & Mastorakos 2008; Peters 2000). The simplest statistical technique is to consider the average of flow variables over time.

Reynolds-Averaged Navier-Stokes (RANS) turbulence models are used in transient fluid flows, whereby the flow variables are decomposed into average and fluctuating quantities over regions in physical space that are of the order of the integral length scale (Peters 2000). Different classes of RANS models exist: zero-equation models, one-equation models, two-equation models and stress-equation models (Alfonsi 2009). RANS models have their disadvantages, whereby: 1) they are not able to properly predict simple free-shear layers and are known to be inadequate in complex flows (Alfonsi 2009; Girimaji 2006); 2) they are unable to capture dynamically evolving fine-scale vortical and scalar structures due to turbulence model induced

dissipation on the in-cylinder unsteady mixing process (Sone & Menon 2003). Celik, Yavuz and Smirnov (2001) reported that the k- ϵ model performs poorly when applied to IC engines, with the predictions being less accurate than desired.

In HCCI engines, a piston-crown design is important to create turbulent behaviour inside the combustion chamber. A study by Kong *et al.* (2003) found that the square-bowl piston generates higher turbulence levels and results in a longer combustion duration, where the turbulence affects the combustion through its influence on the wall heat transfer and property transport. This is supported by Aceves *et al.* (2004) with their experimental data, where the square-bowl piston resulted in a longer combustion duration but with higher UHC and CO emissions and lower combustion efficiency as a result of the thicker boundary layer. Therefore, one has to pay particular attention when designing the piston-crown to achieve the desired combustion behaviour. Another study by Kong and Reitz (2002) revealed that including the turbulent mixing effects gave better predictions for in-cylinder pressure compared to the chemistry alone, as shown in Figure 2.20. The link between chemistry and mixing effects with turbulence models is illustrated in Figure 2.21.

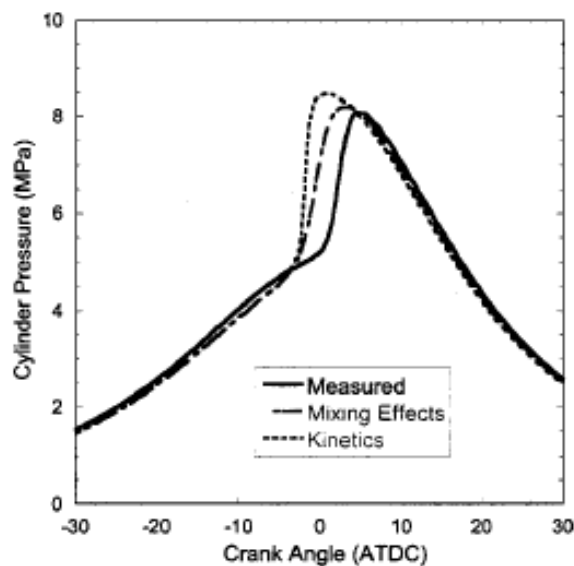


Figure 2.20 The in-cylinder pressure comparison for experiment, modelling with chemical kinetics only and modelling with both chemical kinetics and turbulent mixing, reproduced from (Kong & Reitz 2002).

Chapter 2

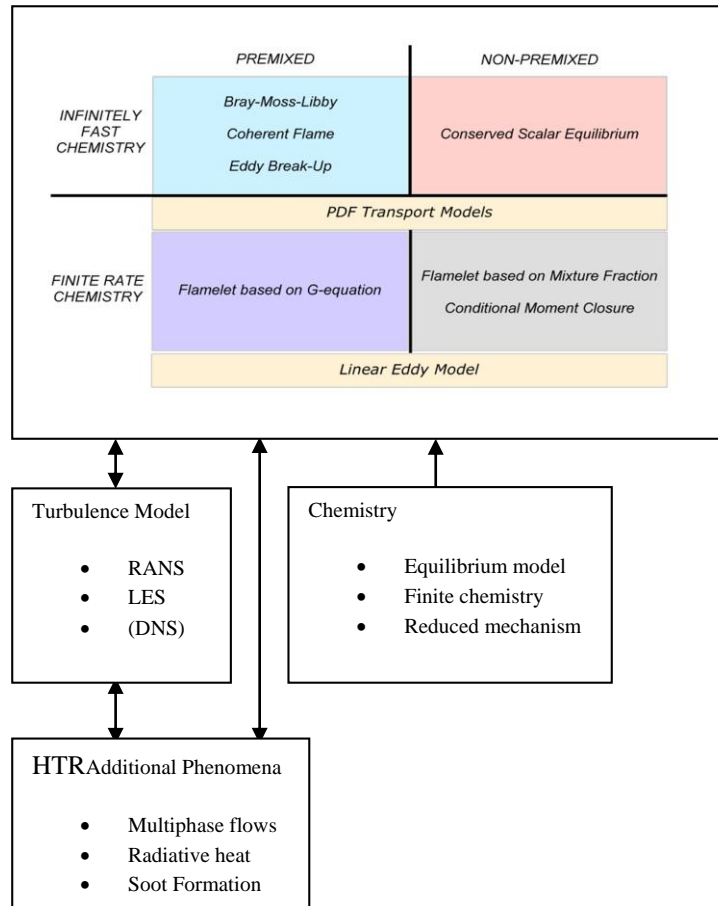


Figure 2.21 Illustration of an overall model for transient simulations (*Combustion* 2009; Janicka & Sadiki 2005; Peters 2000).

Large Eddy Simulation (LES), on the other hand, is a turbulence model that computes more turbulent length scales than RANS, with the turbulent energy within the inertial sub-range separated into resolved large-scale eddies and unresolved small-scale eddies. Resolved large-scale eddies are computed directly by the discretized equations, while small-scale unresolved eddies, which contain only a small fraction of the turbulent kinetic energy, are modelled through subgrid scale models. LES equations are obtained by appropriate filtering of the Navier-Stokes equations and the energy equations over a three-dimensional space (Celik, Yavuz & Smirnov 2001). In complex flows for nonreactive and reactive system studies, LES generally predicts the scalar mixing process and dissipation rates with considerably improved accuracy compared to RANS (Pitsch 2006). It offers a more realistic representation of the in-cylinder turbulent flow and delivers accurate predictions for non-premixed combustion (Haworth 1999; Janicka & Sadiki 2005).

However, LES has difficulties in the near-wall region, where the mesh should be fine enough to compute a correct shear stress (Benarafa *et al.* 2006; Janicka & Sadiki 2005). Furthermore, results from LES may introduce serious errors into simulations due to both aliasing and truncation errors of low-order schemes, which can degrade LES computations (Peters 2000). LES requires greater mesh refinement compared to RANS as the LES models the small-scale eddies, which increases the computational cost. However, mesh or time-step refinement in RANS improves the numerical accuracy, but does not improve the scales that are resolved.

A hybrid approach between RANS and LES has been created in order to resolve the disadvantages of these two models. Alfonsi (2009) has categorized this approach into zonal decomposition, nonlinear disturbance equations and universal modelling. Benarafa *et al.* (2006) in their study on the hybrid approach, which they called RANS/LES coupling, shows that this approach seems to correctly force the averaged LES velocity to reach the correct steady RANS velocity field even at high Reynolds numbers. The fluctuations are globally improved despite the use of very coarse meshes.

Another approach which is similar to the hybrid RANS-LES model is called Detached Eddy Simulation (DES). DES, which is already included in commercial CFD software packages, implements the RANS approach near the wall region, while using the LES technique in the outer detached eddies. The main objective of using this technique is to avoid using high resolution in the near-wall region and, therefore, reduce computational cost. Instead, algebraic boundary-layer models (which have proven to be very successful in the RANS context) are implemented.

2.5.8 Mixing Models for Non-premixed Combustion

Turbulent mixing will take place when there is inhomogeneity in the mixture and depends on the geometry of the piston-crown. Fuels and oxidizers are required to be mixed at molecular levels to initiate combustion, while the molecular mixing will take place at the interface between small eddies (Peters 2000; Pitsch 2006). This process

will heavily involve the chemical reactions, which accelerate the diffusion process by creating strong gradients through the removal or creation of the species.

The Probability Density Function (PDF) (Pope 1985) method offers a good advantage in modelling turbulent reactive flows, where it has the ability to capture strong turbulence-chemistry interactions in the mixing models, such as Euclidean Minimum Spanning Tree (EMST), Interaction by Exchange with the Mean (IEM), or the Modified Curl's (MC) (Haworth 2010). The EMST (Subramaniam & Pope 1998) mixing model is designed to overcome shortcomings of simpler turbulent mixing models, and was successful in diffusion flame tests (Mitarai, Riley & Kosaly 2005; Subramaniam & Pope 1998). The problem with simpler models is that the mixing occurs between particles across the reaction zone, which is not local. The EMST model only allows the particles to mix between their immediate neighbours in composition space. The model was constructed by connecting particles to form branches of trees over the time step. The particles enter or leave the cell according to their velocity. Each of the particles has its own age property and this determines whether the particle belongs to the mixing or non-mixing state. If the particle age property is positive, it belongs to the mixing state, while it does not if the age property is zero or negative. The EMST is formed on the mixing state and changes discontinuously in time due to the particles entering or leaving the mixing state.

Mitarai, Riley and Kosaly (2005) conducted a performance comparison between EMST, IEM (Villermaux & Devillon 1972) and MC (Janicka, Kolbe & Kollmann 1979) mixing models in RANS and LES environments and found the EMST mixing model yielded significantly better results than the IEM and MC mixing models. It was found that the EMST mixing model performs better in an LES environment than in a RANS environment. This is because of the ability of LES to resolve finer scales compared to RANS and therefore particle interactions are over finer scales (Bisetti & Chen 2005). The EMST mixing model has also successfully predicted the appearance and disappearance of cold particles in LES, where it has failed in RANS. A study of turbulence and chemistry interaction performed by Bisetti and Chen (2005) showed that the EMST in the LES environment performed better than the IEM and MC in predicting the temperature conditioned on the mixture fraction, as shown in Figure 2.22.

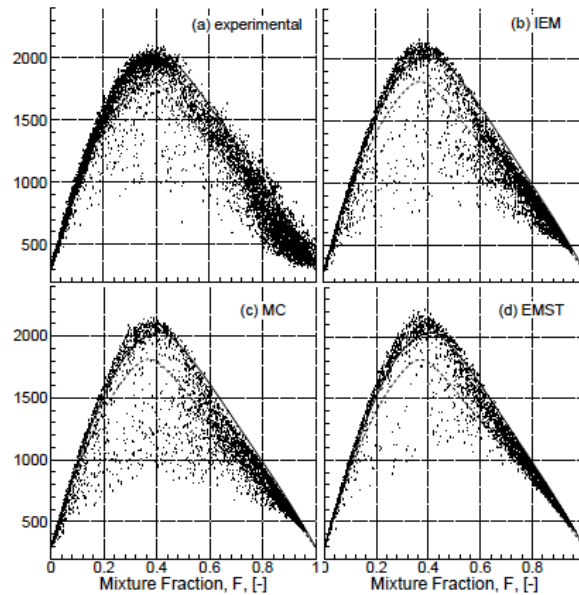


Figure 2.22 Scatter plots of temperature versus mixture fraction from experiment and simulations using LES, a) experimental data, b) IEM, c) MC and d) EMST. All figures reproduced from (Bisetti & Chen 2005).

Bisetti *et al.* (2008) studied turbulence and chemistry interactions in HCCI engines using the same models as Mitarai, Riley and Kosaly (2005). They found that the EMST mixing model performed better than the other mixing models. They noted that the LES simulation gives a promising step in HCCI engine modelling under high levels of stratification.

However, the PDF model is hard to solve because it has many dimensions: one for each chemical species in a particular set of chemical reactions. Therefore, it will end up with n dimensions for n chemical species and if there are m nodes per dimension, the total number of nodes will be m^n , resulting in an enormous computational cost, which is why it is always solved stochastically.

The Conditional Moment Closure (CMC) (Bilger 1993) model, on the other hand, was designed to handle turbulence-chemistry interactions, where large chemical mechanisms can be used at modest computational cost. The conditional fluctuations of the reactive components are to be ignored when calculating the chemical source term for first-order CMC: the value is significantly smaller than the unconditional fluctuations (Schroll 2009). Bushe and Steiner (1999) implemented the CMC model in the LES environment for non-premixed turbulent reacting flows. They noted that

the resolution constraints were reduced because the chemical reactions are resolved in the mixing space. However, the CMC model has a disadvantage in modelling the properties' fluctuations since it has only one conditioning variable (Klimenko & Pope 2003).

The MMC model (Klimenko & Pope 2003) was designed to solve the difficulties faced by the PDF method and the CMC model. It combines the precepts of PDF modelling (in modelling the major species) and CMC (for the minor species) while treating the complete set of dependent variables equally (Klimenko & Pope 2003). The major species are solved by mapping them to a set of prescribed reference variables (often standard Gaussian in the conventional description), while fluctuations of minor species are either ignored (conditional MMC) or treated with conventional mixing models (probabilistic MMC) (Cleary, M. J. & Kronenburg, A. 2007). The MMC model has been investigated in a number of studies such as homogeneous and inhomogeneous combustion, and non-premixed and partially premixed flames (Cleary, M. & Kronenburg, A. 2007; Cleary & Klimenko 2009; Cleary *et al.* 2009; Cleary, M. J. & Kronenburg, A. 2007; Vogiatzaki, Cleary, *et al.* 2009; Vogiatzaki, Kronenburg, *et al.* 2009; Wandel & Klimenko 2005; Wandel & Lindstedt 2009).

A study of MMC in a homogeneous turbulence shows that the model is capable of predicting the bimodal distribution of sensible enthalpy in near stoichiometric mixture when compared with DNS data (Cleary & Klimenko 2011). This is in contrast with the presumed β -PDF model where the model is incapable of predicting such distribution between arbitrary minimum and maximum sample space limits. The MMC model has also been investigated in inhomogeneous turbulence, where the MMC model has been coupled with RANS turbulence model, with the binomial Langevin model and LES. The results show that the MMC model is able to produce high-quality and efficient simulations (Cleary & Klimenko 2011).

An investigation of MMC studying the same case as Mitarai, Riley & Kosaly (2005) reported that the model is capable of predicting the mean temperature rise with reasonable fidelity and follows the temperature history at stoichiometric mixture fraction better than the other models (Wandel & Klimenko 2005), as shown in Figure 2.23. A study by Cleary and Kronenburg (2007) for the MMC model in turbulent

diffusion flames shows an improved accuracy in predicting local extinction compared to the CMC model by accounting for multiple timescales across the spectrum. CMC utilises an average timescale to model the fast and slow processes. Vogiatzaki *et al.* (2009) tested the MMC model for inhomogeneous reactive flows in turbulent jet diffusion flames. The model was constructed using a one-dimensional reference space with mixture fraction used as a basis for the reference variable. They found that the temperature was predicted well compared to the experiment at all locations. In addition, Vogiatzaki *et al.* (2009) mentioned that the MMC model could be easily included in an LES turbulent model. This was done by Cleary *et al.* (2009) where they used the MMC model with an LES scheme for turbulent diffusion flames. The LES model was used to solve for the turbulent velocity field and the reference mixture fraction, while the stochastic MMC model solved the reactive scalars. They concluded that the conditional averages of temperature and species were in good agreement with the experiment.

Another advantages of using the MMC model (Vaishnavi & Kronenburg 2010; Vogiatzaki, Cleary, *et al.* 2009) are: 1. the simplicity of modelling the MMC diffusion coefficients against other models; 2. conditional scalar dissipation rate appears in closed form; and 3. no need to presume the mixture fraction PDF because it is computed from the modelling of the relationship between mixture fraction and reference variable. However, there is difficulty in modelling the MMC where the model cannot generate fluctuations around the conditional mean for the joint PDF, and an additional transport equation is necessary to impose the conditional fluctuations (Kronenburg & Cleary 2008). In other words, the MMC method looks to be a promising step in developing a mixing model for HCCI engines.

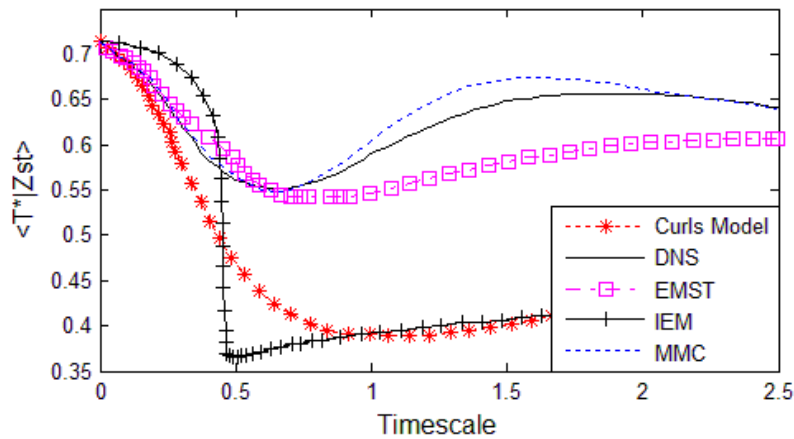


Figure 2.23 Temperature at stoichiometric mixture fraction for various mixing models (Mitarai, Riley & Kosaly 2005; Wandel & Klimenko 2005).

2.6 Conditional Moment Closure (CMC) Model in HCCI Engines

Even though the MMC mixing model has shown a promising result in simulating the mixing behaviour, CMC was chosen in this thesis as a starting point to couple the mixing model with a zero-dimensional single-zone model for HCCI engines. The CMC mixing model performance has been studied extensively by many researchers, especially in the area of a jet flame (Kim & Huh 2004; Navarro-Martinez & Kronenburg 2009; Navarro-Martinez & Rigopoulos 2011; Patwardhan *et al.* 2009; Roomina & Bilger 2001). However, applying the CMC model to the engine simulation is relatively new, where most applications use CFD to obtain the flow field (De Paola *et al.* 2008; Seo *et al.* 2010; Wright *et al.* 2005). The usage of CMC in a zero-dimensional single-zone model is new in the literature. A zero-dimensional environment was selected due to its faster computing time and ease of coding. An assumption has been made in modelling the CMC, where the conditional fluctuations of reactive scalars are negligibly small. This is because the use of port fuel injection reduces the inhomogeneity of the mixture. This has led to the use of simple first-order closure for the conditional chemical reaction rates. The combination of CMC and the zero-dimensional model is expected to produce good accuracy in the results, with reduced simulation time as a consequence of using the zero-dimensional model. The difference between zero-, two- and three-dimensional CMC models is shown in Figure 2.25, where the result for the zero-dimensional CMC model is in good agreement with

the experiment. The intention of this study is to use the CMC model in a zero-dimensional single-zone environment to study the combustion behaviour in an HCCI engine.

2.6.1 CMC Modelling in Zero-Dimensional Simulations

Usage of the CMC model in a zero-dimensional environment has been investigated by Kwon *et al.* (2011), where they studied the combustion and emissions of a diesel engine using skeletal reaction mechanisms. A direct-injection diesel engine was simulated in a zero-dimensional environment, where the entire engine cycle was modelled based on the energy equation of the first law of thermodynamics. The fuel injection was modelled using a multi-zone spray penetration model, where the fuel injection was divided into ten radial zones. They reported that the result for the pressure trace shows reasonable agreement between simulation and experiment, as shown in Figure 2.24. This is a good indication that the CMC model could be used in a zero-dimensional environment. However, the approach in this thesis for the zero-dimensional simulation is slightly different, where the fuel is injected at the inlet manifold instead of direct injection. Therefore, there is no multi-zone spray model to be used.

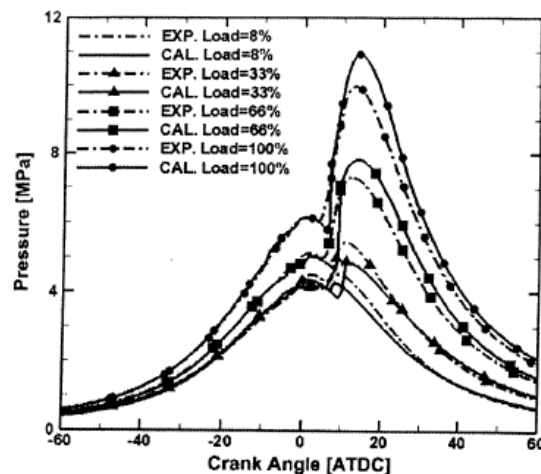


Figure 2.24 Result for in-cylinder pressure at 1000 rpm between simulation and experiment, as reported by Kwon *et al.* (2011).

2.6.2 CMC Modelling in Multi-Dimensional Simulations

Most multi-dimensional simulations use CFD for the computations at the expense of computing resources. A separate code has to be written to couple the CMC mixing model with the CFD software package. The CFD will solve the flow field parameters, e.g. mean pressure, pressure rate of change, turbulence parameters, variance and mean of the mixture fraction. Then, all these parameters will be used by the CMC mixing model to compute the temperature and species mass fractions due to the chemical reaction by weighting with presumed β -function PDF. The computed values will be returned to CFD for the next time step computation. This is called full two-way coupling, as reported by Wright (2005).

A multi-dimensional simulation of a diesel engine coupled with the CMC model has been studied by De Paola *et al.* (2008). A commercialised CFD software package (STAR-CD) was used in the study and the result was then compared with a single-cylinder diesel engine. Heat transfer to the cylinder wall was added to the CMC mixing model and evaluated using the CFD solver. They concluded that the predicted in-cylinder pressure traces are in good agreement with the experiment, as shown in Figure 2.25.

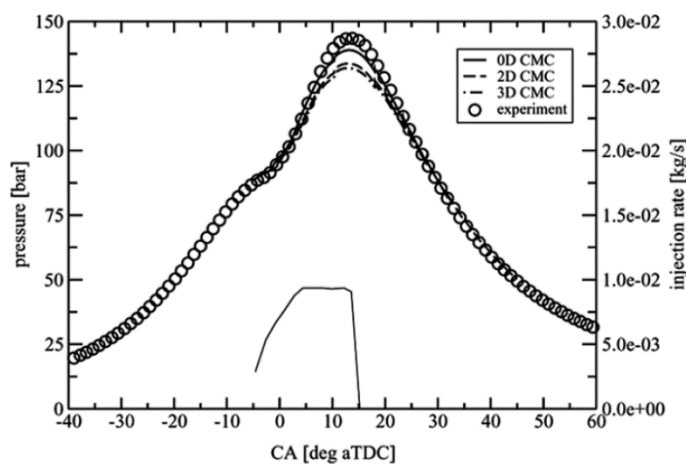


Figure 2.25 In-cylinder pressure comparison between CMC model using CFD and experiment, reproduced from (De Paola *et al.* 2008).

Seo *et al.* (2010) have also studied the CMC model in a multi-dimensional environment. They investigated the combustion behaviour for a diesel engine in partial HCCI mode with split injections (a pair of sequential injections: first injection at -57.5°CA ATDC and second injection at 7.5°CA ATDC). In this case, they used KIVA3V as a CFD solver and coupled with the CMC model using a separate script. A heat transfer model was then added to the CMC equation with a different approach, i.e. the heat loss coefficient was determined using Woschni's experimental correlation. They reported that the in-cylinder pressure traces are in reasonable agreement between the experiment and the simulation.

Therefore, it could be concluded that the CMC model in multi-dimensional simulations is capable of producing good results, with the ability of predicting the flame structure.

2.7 Conclusion

Many studies show the HCCI engine has low NO_x emissions, soot and particulates. The HCCI engine can achieve a higher or similar BTE compared to CI engines by using a high CR engine configuration. One of the advantages of the HCCI engine is that it does not suffer from throttling losses, which also improves the BTE. A higher BTE helps in reducing the fuel consumption of the engine and it might be able to match the fuel consumption of a hybrid engine. However, HCCI engines still have unresolved issues, which are ignition control, knocking and high levels of unburned HC and CO emissions. Further studies have to be performed in order to solve these remaining issues. To achieve this, the numerical method shows a great advantage over experiments to simulate the combustion behaviour in terms of cost and time. To this end, a simulation model has to be developed to investigate the behaviour and, once completed, it has to be validated against experiments.

The multi-zone numerical method combined with advanced turbulent mixing models shows promising results, compared with the single-zone model. CFD offers greater accuracy than the multi-zone model at the expense of computational cost. However,

one could easily implement the LES or DES model with CFD. The DES model will be useful in the near future, where it combines the LES and RANS models together with improved accuracy using the former where needed and improved computational efforts using the latter where possible. A mixing model has been developed to study the mixing behaviour at molecular levels. The performance of EMST, MC and IEM models was compared and the result showed that the EMST model performed best. A study of the CMC model showed that it has the ability to capture all phases of combustion, i.e. ignition, flame propagation and a diffusion flame (Mastorakos 2010). A CMC model in an LES environment has been investigated and it shows that the model has the capability to predict extinction and ignition phenomena (Bushe & Steiner 1999). The MMC model is created by combining the advantages of the CMC and PDF models. In this thesis, the CMC model was chosen and combined with zero-dimensional modelling, as discussed in Section 2.6.

There are several methods to achieve HCCI configurations through experiments. Using a direct injection system seems to require few modifications, but care is required with the associated disadvantages. If port injection is to be used, one might have to install the atomizer and heater in the inlet port, which leads to additional costs. The main objective of the HCCI engine is to achieve low emissions levels with efficiency similar or better to that of a CI engine. Therefore, an optimized experimental method would be able to solve the HCCI engine problems, with the help of simulations.

Chapter 3

TURBULENCE MODELLING BACKGROUND

3.1 Introduction

A computer simulation, in general, has a strong influence in today's research activities, but because they are only models of reality, they must be validated against experimental data. Once the numerical analysis has been validated, the simulation could be used for further research, which would reduce many experimental costs. Recently, the emissions regulations in automotive sectors have become more stringent and, therefore, more effort is required to obtain less polluting engines. The research and development (R&D) cost would increase substantially if all efforts relied solely on experiments. Thus, research efficiency must be improved. This could be achieved by using computer simulations to predict experimental results, which has the advantage of reducing the R&D time with relatively low computation costs.

HCCI combustion occurs when the correct composition of oxidisers and fuels is present in the combustion chamber. It is important to investigate mixing between oxidisers and fuels in more detail, which could improve the knowledge of mixing due to turbulent flows. Numerical investigations are truly important in current research, where they could improve research productivity in the near future. This chapter will briefly explain the current models used in simulations of turbulence. The chapter begins with fundamental governing equations in Section 3.2, followed by chemical reaction mechanisms and statistical descriptions in Sections 3.3 and 3.4 respectively. Next, turbulence modelling is discussed in Section 3.5, before closing with a conclusion in Section 3.6.

3.2 Conservation Equations

3.2.1 Mass

The conservation of mass is represented by

$$\frac{\partial \rho}{\partial t} + \nabla \cdot (\rho \mathbf{V}) = 0 \quad (3.1)$$

The first term is the rate of change of density and the second term is the convective transport, where \mathbf{V} is the velocity and ρ is the density.

3.2.2 Momentum

The conservation of linear momentum equation is represented by:

$$\frac{\partial \rho \mathbf{V}}{\partial t} + \nabla \cdot (\rho \mathbf{V} \mathbf{V}) = -\nabla p + \nabla \cdot \boldsymbol{\tau} + \rho \mathbf{g} \quad (3.2)$$

The first term on the left hand side (LHS) is the local rate of change, and the second term is convection of momentum, while the first two terms on the right hand side (RHS) represent pressure gradient and molecular transport due to viscous forces, respectively. The last term on the RHS is the body forces due to buoyancy. The viscous stress tensor $\boldsymbol{\tau}$, is represented by

$$\boldsymbol{\tau} = \mu \left(2\mathbf{S} - \frac{2}{3} \boldsymbol{\delta} \nabla \cdot \mathbf{V} \right) \quad (3.3)$$

$$\mathbf{S} = \frac{1}{2} (\nabla \mathbf{V} + \nabla \mathbf{V}^T) \quad (3.4)$$

and \mathbf{S} is the strain rate tensor, where μ is the dynamic viscosity, $\nabla \mathbf{V}$ is the velocity gradient and $\nabla \mathbf{V}^T$ is the transpose of the velocity gradient.

3.2.3 Species

The balance equation for the mass fraction, Y , of species i is represented by

$$\rho \frac{\partial Y_i}{\partial t} + \rho \mathbf{V} \cdot \nabla Y_i = \nabla \cdot (\rho D_i \nabla Y_i) + \rho \dot{\omega}_i \quad (i = 1, 2, \dots, n) \quad (3.5)$$

where D_i is the mass diffusivity, $\dot{\omega}_i$ is the mass reaction rate of the species per unit volume and summation over repeated indices is not intended. The first term on the LHS is the rate of change of species mass fraction and the second term is convection. The first term on the RHS is the molecular diffusivity and the last one is the source term.

For simplicity, all mass diffusivities, D_i , are assumed to be proportional to the thermal diffusivity, κ , and the Lewis number, Le , is constant

$$\kappa = \frac{\lambda}{\rho c_p}, \quad Le = \frac{\lambda}{\rho c_p D_i} = \frac{\kappa}{D_i} \quad (3.6)$$

In equation (3.6), λ is the thermal conductivity and c_p is the specific heat capacity at constant pressure of the mixture.

3.2.4 Energy

In a mixture, the enthalpy, h , is the mass-weighted sum of the specific enthalpies h_i of species i ,

$$h = \sum_{i=1}^n Y_i h_i \quad (3.7)$$

and similarly for c_p ,

$$c_p = \sum_{i=1}^n Y_i (c_p)_i \quad (3.8)$$

Chapter 3

The enthalpy of an ideal gas at a temperature T can be decomposed into enthalpy of formation, $h_{i,ref}$, and sensible enthalpy, h_s , so that $h(T) = h_{i,ref} + h_s(T)$. This equation can be rewritten in its differential form as

$$\frac{dh}{dt} = \sum_{i=1}^n h_i \frac{dY_i}{dt} + c_p \frac{dT}{dt} \quad (3.9)$$

where, for an ideal gas, h depends only on the temperature. Then, the enthalpy balance equation can be derived from the first law of thermodynamics (Williams 1985)

$$\rho \frac{\partial h}{\partial t} + \rho \mathbf{V} \cdot \nabla h = \frac{\partial p}{\partial t} + \mathbf{V} \cdot \nabla p - \nabla \cdot \mathbf{j}_q + q_R \quad (3.10)$$

Equation (3.10) has been simplified by ignoring frictional heating due to low speed flows. The term $\mathbf{V} \cdot \nabla p$ can also be ignored for small Mach numbers. The rate of change in pressure $\partial p / \partial t$ is retained for engine applications. The heat flux term is denoted by \mathbf{j}_q , while the source term due to radiation heat transfer, q_R , can be ignored in HCCI engines (Chang *et al.* 2004; Soyhan *et al.* 2009).

3.3 Chemical Reactions

The last term in equation (3.5) is the source term due to chemical reactions, which accounts for destruction and creation of species i . A complete description of combustion reactions involves a highly complex chemical system, which must be modelled. If there are N possible species in the system, with the i th species in the j th reaction, the general chemical reaction can be written as



Chapter 3

where \mathcal{X}_i represents the chemical formula of species i , L is the number of elementary reactions, while ν'_{ij} and ν''_{ij} are the stoichiometric coefficients of the reactants and products respectively. Forward and backward reaction constants, k_{fj} and k_{bj} , are modelled by the temperature-dependent Arrhenius form,

$$k(T) = A \exp\left(-\frac{E_A}{R_u T}\right) \quad (3.12)$$

where A is the pre-exponential factor, E_A is the activation energy and R_u is the universal gas constant.

The net production rate of all chemical reactions, or the source term $\dot{\omega}_i$, which is the mass of species i produced per unit volume and unit time, is

$$\dot{\omega}_i = MW_i \sum_{j=1}^L \nu_{ij} q_j \quad (i = 1, 2, \dots, N) \quad (3.13)$$

with

$$\nu_{ij} = (\nu''_{ij} - \nu'_{ij}) \quad (3.14)$$

and

$$q_j = k_{fj} \prod_{i=1}^N \left(\frac{\rho Y_i}{MW_i}\right)^{\nu'_{ij}} - k_{bj} \prod_{i=1}^N \left(\frac{\rho Y_i}{MW_i}\right)^{\nu''_{ij}} \quad (3.15)$$

where q is the rate-of-progress variable and MW_i is the molecular weight of species i . Chemical species with strong bonds require extra energy to break the chemical bonds. The extra energy is supplied by the so-called catalyst, where the catalytic molecule or the third body remains unaffected by the reaction. An example of this reaction is represented by



where “M” is the catalyst, or the third-body species. The rate-of-progress variable of this reaction is obtained using

$$q_j = [M]_j \left(k_{fj} \prod_{i=1}^N \left(\frac{\rho Y_i}{MW_i} \right)^{\nu'_{ij}} - k_{bj} \prod_{i=1}^N \left(\frac{\rho Y_i}{MW_i} \right)^{\nu''_{ij}} \right) \quad (3.17)$$

The third body concentration, $[M]$, in equation (3.17) is

$$[M]_j = \sum_{i=1}^N [X_i] = \frac{p}{RT} \quad (3.18)$$

assuming that all the third-body species behave the same way.

3.4 PDF and Statistical Descriptions

Random methods are generally used in turbulent processes to describe the fluctuating velocity and scalar fields in terms of their statistical distributions. As a starting point, let φ be a random variable and η its sample space variable. The random variable φ can take any value within its sample space, where the sample space is defined as the space of all possible realizations of the random variable. It is assumed that $\varphi \in [\eta_{\min}, \eta_{\max}]$ and $-\infty < \eta < \infty$.

The cumulative probability $\mathcal{P}_\varphi(\eta)$ is defined as the total probability for any value $\varphi < \eta$:

$$\mathcal{P}_\varphi(\eta) = \text{prob}(\varphi < \eta) \quad (3.19)$$

and the probability of φ within a range $\eta_{\min} \leq \varphi < \eta_{\max}$ is represented by

$$\text{prob}(\eta_{\min} \leq \varphi < \eta_{\max}) = \mathcal{P}_\varphi(\eta_{\max}) - \mathcal{P}_\varphi(\eta_{\min}) \quad (3.20)$$

Now, the Probability Density Function (PDF) is defined as

$$P_\varphi = \frac{d\mathcal{P}_\varphi(\eta)}{d\eta} \quad (3.21)$$

The PDF is non-negative and the probability of finding φ in the whole of its sample space $\eta_{min} \leq \varphi < \eta_{max}$ is

$$\int_{\eta_{min}}^{\eta_{max}} P_\varphi d\eta = 1 \quad (3.22)$$

Such a statement indicates that the probability is certain (i.e. unity probability) and serves as a normalising condition if the PDF is determined numerically. Once P_φ is known, the first moment of φ can be defined as

$$\langle \varphi \rangle = \int_{\eta_{min}}^{\eta_{max}} \varphi(\eta) P_\varphi d\eta \quad (3.23)$$

Here, the first moment represents the average or mean value of φ , with the $\langle \bullet \rangle$ symbol. Then, the second central moment is defined as

$$\langle (\varphi - \bar{\varphi})^2 \rangle = \int_{\eta_{min}}^{\eta_{max}} (\eta - \langle \varphi \rangle)^2 P_\varphi d\eta \quad (3.24)$$

which is called the variance.

The moments of a random scalar can be explicitly calculated using its PDF. However, the calculation of PDF is often computationally expensive or insufficient information is known to be able to determine it. To overcome this, presumed functions for single PDF are often used (e.g. Gaussian-type or β -function PDF), which is parameterized on the mean and variance of a variable.

3.5 Turbulence Modelling

One of the characteristics of turbulent flows is the existence of eddies of different length scale. The eddies are developed when a high Reynolds number flow experiences

shear layer instabilities before being transformed into many eddies. According to Kolmogorov's 1941 theory for homogeneous isotropic turbulence, the kinetic energy from large-scale eddies will be transferred to the small-scale eddies before being dissipated at the small-scale eddies through viscous dissipation. These eddies can be categorised as large scale, integral scale, inertial sub-range and viscous sub-range. Figure 3.1 shows the turbulent kinetic energy spectrum, where the wavenumber k is the inverse of a length scale. The well-known $k^{-5/3}$ law is used for the kinetic energy spectrum in the inertial sub-range. The maximum turbulent kinetic energy is contained in the integral scale eddies, then decreases following the $k^{-5/3}$ law in the inertial sub-range. The energy decreases exponentially in the viscous sub-range due to viscous effects.

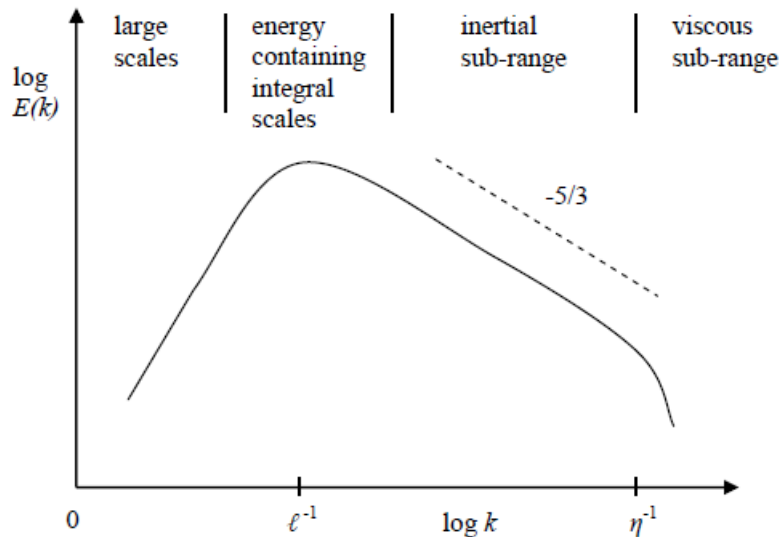


Figure 3.1 Turbulent kinetic energy spectrum as a function of the wavenumber, reproduced from (Peters 2000).

Direct numerical simulation (DNS) is necessary to resolve all the spatial and temporal scales present in the flow with high accuracy (Sengupta & Mashayek 2008). It solves the Navier-Stokes equations using a fine mesh. However, DNS is computationally expensive to use with current computing power for engineering-scale problems. To overcome this limitation, a number of turbulence modelling approaches have been developed, so that the solution for different turbulent flow regimes can be obtained within a reasonable time and cost.

3.5.1 Averaging Techniques

Averaging is used to filter small-scale fluctuations in turbulent flows because it is not feasible to consider in detail all of the small scales in flows. It could be done by decomposing instantaneous quantities into mean and fluctuating quantities. This section describes two methods of averaging, which are Reynolds and Favre averaging.

3.5.1.1 Reynolds Averaging

Reynolds averaging refers to averaging a variable in time. Let a mean of a random variable be

$$\bar{\varphi}(x, t) = \frac{1}{N} \sum_{i=1}^N \varphi(x_i, t) \quad (3.25)$$

where N is the sample size. A variable φ can be decomposed into a slowly varying mean and rapidly varying turbulent fluctuation components

$$\varphi(x, t) = \bar{\varphi}(x, t) + \varphi'(x, t) \quad (3.26)$$

with the assumption that the mean is constant over the period of averaging. By definition $\overline{\varphi'}(x, t) = 0$ and, for instance, using Reynolds averaging in equation (3.1) produces,

$$\frac{\partial \bar{\rho}}{\partial t} + \nabla \cdot (\bar{\rho} \bar{\mathbf{V}}) = 0 \quad (3.27)$$

3.5.1.2 Favre Averaging

Favre averaging is used to separate turbulent fluctuation from the mean flow when there is a fluctuation in density, especially in a compressible flow. A density-weighted average (Favre 1969) is defined as

$$\tilde{\varphi} = \frac{\overline{\rho\varphi}}{\bar{\rho}} \quad (3.28)$$

with Favre decomposition

$$\varphi(x, t) = \tilde{\varphi}(x, t) + \varphi''(x, t) \quad (3.29)$$

Double prime superscript is used to distinguish between Reynolds and Favre averaging. It should be noted that

$$\overline{\varphi'}(x, t) = 0 \quad \text{but} \quad \overline{\varphi''}(x, t) \neq 0 \quad (3.30)$$

However,

$$\overline{\rho\varphi''}(x, t) = 0 \quad \text{and} \quad \overline{\rho\tilde{\varphi}} = \bar{\rho}\tilde{\varphi} = \overline{\rho\varphi} \quad (3.31)$$

By introducing Reynolds decomposition for ρ and p , and Favre decomposition for u and h as

$$\rho = \bar{\rho} + \rho' \quad p = \bar{p} + p' \quad (3.32)$$

$$u = \tilde{u} + u'' \quad h = \tilde{h} + h'' \quad (3.33)$$

The Favre averaged mass, momentum, species and energy conservation equations then become

$$\frac{\partial \bar{\rho}}{\partial t} + \nabla \cdot (\bar{\rho}\tilde{\mathbf{V}}) = 0 \quad (3.34)$$

$$\frac{\partial \bar{\rho}\tilde{\mathbf{V}}}{\partial t} + \nabla \cdot (\bar{\rho}\tilde{\mathbf{V}}\tilde{\mathbf{V}}) = -\nabla \bar{p} + \nabla \cdot \bar{\boldsymbol{\tau}} - \nabla \cdot (\bar{\rho}\widetilde{\mathbf{V}''\mathbf{V}''}) + \bar{\rho}g \quad (3.35)$$

$$\frac{\partial (\bar{\rho}\tilde{Y}_i)}{\partial t} + \bar{\rho}\tilde{\mathbf{V}} \cdot \nabla \tilde{Y}_i = \nabla \cdot (\bar{\rho}D_i \nabla Y_i - \bar{\rho}\widetilde{\mathbf{V}''_i Y''_i}) + \bar{\omega}_i \quad (3.36)$$

$$(i = 1, 2, \dots, n)$$

$$\begin{aligned} & \frac{\partial (\bar{\rho}\tilde{h})}{\partial t} + \nabla \cdot (\bar{\rho}\tilde{\mathbf{V}}\tilde{h}) \\ &= -\nabla \cdot (\bar{\rho}\widetilde{\mathbf{V}''h''}) + \frac{\partial \bar{p}}{\partial t} + \tilde{\mathbf{V}} \cdot \nabla p + \bar{\boldsymbol{\tau}} : \nabla \tilde{\mathbf{V}} - \nabla \cdot \bar{J}_q + \bar{q}_R \end{aligned} \quad (3.37)$$

Additional terms arising from the averaging are Reynolds stress ($\bar{\rho}\widetilde{\mathbf{V}''\mathbf{V}''}$) in equation (3.35), velocity-scalar co-variances ($\bar{\rho}\widetilde{\mathbf{V}''_i Y''_i}$) in equation (3.36), and enthalpy fluxes

$(\overline{\rho V'' h''})$ in equation (3.37). These terms, including the chemical source term $(\overline{\dot{\omega}_i})$ in equation (3.36), are known as the closure problem of moment methods, which require modelling. The modelling of these terms will not be discussed in detail in this thesis because they are not used in zero-dimensional modelling.

3.5.2 Turbulence Models

The averaged conservation equations are not closed until the unknown quantities are modelled. The zero-, one- and two-equation models are presented briefly in this section. They will not be discussed in detail and serve as a background to turbulence modelling.

3.5.2.1 Zero-equation models

Zero-equation models, also called algebraic turbulence models, are the simplest of the turbulence models because the closure of the shear stress term is in algebraic form. It does not require any partial differential equation (PDE) that describes the turbulent fluxes and can be calculated directly from the flow variables. In this model, the mixing length theory of Prandtl is usually used (Pope 2000). The Reynolds stress is modelled as

$$\overline{\rho V'' V''} = \nu_t \left(\frac{\partial V}{\partial y} \right) \quad (3.38)$$

where ν_t is the eddy viscosity. The mixing length model of Prandtl for two-dimensional flows is represented by

$$\nu_t = l_m^2 \left(\frac{\partial V}{\partial y} \right) = \frac{\mu_t}{\rho} \quad (3.39)$$

where μ_t is the turbulent viscosity, y is the coordinate normal to the wall and l_m is the mixing length. The problem with this model is that l_m is unknown and must be determined. This model has good predictions in free shear and boundary layer flows. However, it is incapable of capturing many flow details such as separation and recirculation (Pope 2000).

3.5.2.2 One-equation models

In one-equation models, an additional PDE (transport equation) is required to solve the turbulent kinetic energy and the turbulent length scale is obtained from an algebraic equation. The unknowns are expressed as a function of turbulent kinetic energy as

$$\bar{\rho} \frac{\partial \tilde{k}}{\partial t} + \bar{\rho} \tilde{\mathbf{V}} \cdot \nabla \tilde{k} = \nabla \cdot \left(\frac{\bar{\rho} \nu_T}{\sigma_k} \nabla \tilde{k} \right) - \bar{\rho} \widetilde{\mathbf{V}'' \mathbf{V}''} : \nabla \tilde{\mathbf{V}} - \bar{\rho} \tilde{\varepsilon} \quad (3.40)$$

The first term on the LHS is the local rate of change, and the second term is the convection. On the RHS, the first term is the turbulent transport, the second one turbulent production and the last term is turbulent dissipation. The constant $\sigma_k = 1.0$ is generally used (Peters 2000). The Reynolds stress in equation (3.40) is usually modelled using eddy viscosity hypothesis:

$$-\bar{\rho} \widetilde{\mathbf{V}'' \mathbf{V}''} = \bar{\rho} \nu_t \left[2\tilde{S} - \frac{2}{3} \boldsymbol{\delta} \nabla \cdot \tilde{\mathbf{V}} \right] - \frac{2}{3} \boldsymbol{\delta} \bar{\rho} \tilde{k} \quad (3.41)$$

where $\boldsymbol{\delta}$ is the Kronecker delta. The kinematic eddy viscosity ν_t can be modelled using the Favre average turbulent kinetic energy, \tilde{k} , and its dissipation, $\tilde{\varepsilon}$, as

$$\nu_t = c_\mu \frac{\tilde{k}^2}{\tilde{\varepsilon}}, \quad \text{with } c_\mu = 0.09 \quad (3.42)$$

The dissipation rate is modelled as follows,

$$\tilde{\varepsilon} = \frac{C_D \tilde{k}^{\frac{3}{2}}}{l_m} \quad (3.43)$$

where C_D is an empirical constant. This model still requires a prescribed length scale to be fitted with a given flow, and it is not possible to determine this scale in many types of flow. The only advantage over the zero-equation model is that the turbulent kinetic energy is calculated.

3.5.2.3 Two-equation models

In this model, two transport equations are derived for two scalars, e.g. the turbulent kinetic energy, k , and dissipation rate, ε . The k - ε model is the most widely used due to its completeness and simplicity, and it is incorporated in most commercial CFD codes (Pope 2000). Once this model is solved, a length scale ($l = k^{3/2}/\varepsilon$), a timescale ($\tau = k/\varepsilon$) and an eddy viscosity in equation (3.37) can be computed, and l_m is no longer required. It consists of k given by equation (3.40) and ε with similar form as

$$\bar{\rho} \frac{\partial \tilde{\varepsilon}}{\partial t} + \bar{\rho} \tilde{V} \cdot \nabla \tilde{\varepsilon} = \nabla \cdot \left(\frac{\bar{\rho} \nu_T}{\sigma_\varepsilon} \nabla \tilde{\varepsilon} \right) - c_{\varepsilon 1} \bar{\rho} \frac{\tilde{\varepsilon}}{\tilde{k}} \widetilde{V''V''} : \nabla \tilde{V} - c_{\varepsilon 2} \bar{\rho} \frac{\tilde{\varepsilon}^2}{\tilde{k}} \quad (3.44)$$

The constants are generally set as $\sigma_\varepsilon = 1.3$, $c_{\varepsilon 1} = 1.44$ and $c_{\varepsilon 2} = 1.92$. This model is usually acceptable for simple flows, but can be inaccurate for complex flows, where the inaccuracies come from the turbulent viscosity hypothesis and from the ε -equation (Kim 2004; Pope 2000).

3.5.3 Turbulent Reacting Flows

3.5.3.1 Dissipation and Scalar Transport

Another unclosed term appears in equation (3.36) and equation (3.37), which are reactive scalars in the form of $\widetilde{V''Y''}_i$ and $\widetilde{V''h''}$. Considering ψ represents the reactive scalars for the mass fraction and enthalpy, the unclosed term may be written as $\widetilde{V''\psi''}$. Generally, the transport term containing molecular diffusivity, D_i , can be ignored in high Reynolds numbers. The scalar can then be modelled as

$$\widetilde{V''\psi''} = -D_t \nabla \tilde{\psi}_i \quad \text{and} \quad D_t = \frac{\nu_t}{Sc_t} \quad (3.45)$$

where D_t is the turbulent diffusivity and Sc_t is the Schmidt number. The variance can be obtained by subtracting equation (3.36) from equation (3.5) and ignoring the mean of molecular diffusive flux,

$$\begin{aligned} \bar{\rho} \frac{\partial \widetilde{\psi_i'^2}}{\partial t} + \bar{\rho} \widetilde{\mathbf{V}} \cdot \nabla \widetilde{\psi_i'^2} = & -\nabla \cdot (\bar{\rho} \widetilde{\mathbf{V}'' \psi_i''^2}) + 2\bar{\rho} (-\widetilde{\mathbf{V}'' \psi_i''}) \cdot \nabla \widetilde{\psi}_i - \bar{\rho} \widetilde{\chi}_i \\ & + 2\bar{\rho} \widetilde{\psi_i'' \dot{\omega}_i''} \end{aligned} \quad (3.46)$$

The first term on the RHS is the turbulent transport term, the second one the production of scalar fluctuation, the third term is the scalar dissipation and the last one covariance of the reactive scalar with the chemical source term. For a non-reacting case, the scalar dissipation is conventionally modelled as

$$\widetilde{\chi}_i = C_D \frac{\bar{\epsilon}}{k} \widetilde{\psi_i'^2} \quad (3.47)$$

where C_D is a constant which is often set to 2.0 (Peters 2000).

3.5.3.2 Mixture Fraction

Mixture fraction is an important quantity to describe non-premixed combustion, where can be used in determining the flame surface (Peters 2000) and is denoted as Z in this thesis. Note that the behaviour at the stoichiometric mixture fraction is very important in combustion, but the behaviour at a range of mixture fractions is found to be critical in this study. It is defined as the ratio of mass originating from the fuel stream to the sum of mass in the system

$$Z = \frac{m_F}{m_F + m_O} \quad (3.48)$$

where m_F is the mass from the fuels and m_O is the mass from the oxidisers. The mixture fraction is normalized to 0 in the oxidiser stream and 1 in the fuel stream. Considering a two-feed system containing fuel in one stream and oxygen in the other

stream, the mass fraction of fuel Y_F and oxygen Y_{O_2} is related to the mixture fraction as

$$Z = \frac{\nu Y_F - Y_{O_2} + Y_{O_2,2}}{\nu Y_{F,1} + Y_{O_2,2}} \quad (3.49)$$

where ν is the stoichiometric oxygen-to-fuel mass ratio, $Y_{F,1}$ is the mass fraction of fuel in the fuel stream and $Y_{O_2,2}$ represents the mass fraction of oxygen in the oxidiser stream.

3.5.4 Turbulent Combustion Models

This section discusses the turbulent combustion models available for non-premixed combustion. A comprehensive overview of present turbulent approaches is presented by Veynante and Vervisch (2002).

3.5.4.1 Eddy Break-Up

Eddy break-up is an attempt to provide a closure for the chemical source term based on the work from Spalding (1971), and it is available in most CFD software packages. In non-premixed combustion with fast chemistry, the model uses turbulent mixing as the rate controlling parameter, with the assumption that the reactions are completed at the moment of mixing. The turbulent mean reaction rate of products is defined as

$$\overline{\dot{\omega}_P} = \rho C_{EBU} \frac{\varepsilon}{k} \left(\overline{Y_P''^2} \right)^{\frac{1}{2}} \quad (3.50)$$

where C_{EBU} is the Eddy Break-Up constant and $\overline{Y_P''^2}$ is the variance of the product mass fraction. The variance can be modelled as

$$\overline{Y_P''^2} \cong \overline{Y_P} (1 - \overline{Y_P}) \quad (3.51)$$

The model was later modified by Bilger (1976), where for non-premixed combustion, the PDF of mixture fraction Z at a point \mathbf{x} and time t has to be defined. The mean fuel consumption rate is expressed as

$$\overline{\dot{\omega}_F} = -\frac{1}{2}\bar{\rho}\frac{Y_{F,1}}{1-Z_{st}}\tilde{\chi}_{st}\tilde{P}_Z(Z_{st}) \quad (3.52)$$

In equation (3.52), $Y_{F,1}$ is the fuel mass fraction in the fuel stream, $\tilde{\chi}_{st}$ is the scalar dissipation rate at the stoichiometric condition and $\tilde{P}_Z(Z_{st})$ is the probability density function at the stoichiometric mixture fraction. However, this model tends to overestimate the reaction rate especially in the highly strained region, where the ratio ε/k is large (Veynante & Vervisch 2002).

3.5.4.2 Flamelet Models

Flamelets are a wrinkled sheet of thin reactive-diffusive layers where the reaction occurs (Peters 2000). If the layer is thin compared to the smallest turbulent eddies, the flame can be treated as laminar. The flamelet equations are based on the mixture fraction using the scalar dissipation rate for the mixing process. The model has the advantage of including both finite-rate chemistry and the influence of the local mixture fraction gradients (Pitsch, Chen & Peters 1998).

The flamelet equation for the reactive scalars is defined as

$$\rho \frac{\partial \psi_i}{\partial t} = \frac{\rho}{2} \chi \frac{\partial^2 \psi_i}{\partial Z^2} + \dot{\omega}_i \quad (3.53)$$

and the temperature equation as (Barths *et al.* 2000)

$$\begin{aligned} \rho \frac{\partial T}{\partial t} = & \rho \frac{\chi}{2} \frac{\partial^2 T}{\partial Z^2} + \rho \frac{\chi}{2C_p} \frac{\partial T}{\partial Z} \frac{\partial C_p}{\partial Z} \\ & + \sum_{i=1}^n \rho \frac{\chi}{2Le_i} \frac{C_{p_i}}{C_p} \frac{\partial Y_i}{\partial Z} \frac{\partial T}{\partial Z} - \frac{1}{C_p} \sum_{i=1}^n h_i \dot{\omega}_i + \frac{1}{C_p} \frac{\partial p}{\partial t} \end{aligned} \quad (3.54)$$

where the instantaneous scalar dissipation rate is computed as

$$\chi = 2D|\nabla Z|^2 \quad (3.55)$$

The transport equation of the mixture fraction is

$$\rho \frac{\partial Z}{\partial t} + \rho \mathbf{V} \cdot \nabla Z = \nabla \cdot (\rho D \nabla Z) \quad (3.56)$$

From equation (3.53), it can be seen that the reactive scalars, ψ_i , depend on the mixture fraction and the scalar dissipation rate. To obtain mean values of ψ_i , it is necessary to solve the PDF transport equation, where the mean values are obtained using equation (3.23), as represented by

$$\tilde{\psi}_i = \int_0^1 \tilde{P}_Z \tilde{\psi}_i(\eta) d\eta \quad (3.57)$$

A study by Pitsch, Chen and Peters (1998) on unsteady flamelet modelling of turbulent hydrogen-air diffusion flames showed that the transient effects can be ignored for predictions of major species. However, the flamelet model is not valid for a flame with local extinction and re-ignition, where the variations of scalar dissipation rate are significant (Veynante & Vervisch 2002).

A flamelet model has also been used in engine simulations. A study by Keum, Im and Assanis (2012) on the use of the flamelet model for a CI engine reported that the model satisfactorily describes the physical and chemical processes for spray injection conditions. Mittal, Cook and Pitsch (2012) studied the two-dimensional flamelet model with different mixture and thermal inhomogeneities for CI and HCCI engines. The study, which used CFD, reported that the two-dimensional flamelet model performs well in both CI and HCCI engines in the presence of charge stratification.

3.5.4.3 Presumed PDF Methods

Presumed PDF methods are used to represent a set of parameters with a pre-determined PDF, instead of solving a full PDF equation directly. It is computationally efficient by assuming that the involved scalars are statistically independent of each other. The most commonly used are β -function PDF and clipped Gaussian PDF. The mean mixture fraction and its variance are the parameters that are required to determine the shape of a presumed PDF. The conserved scalar transport equation of the Favre mean mixture fraction is

$$\frac{\partial(\bar{\rho}\tilde{Z})}{\partial t} + \nabla \cdot (\bar{\rho}\tilde{V}\tilde{Z}) = \nabla \cdot (\bar{\rho}D\nabla\tilde{Z}) \quad (3.58)$$

and its variance, $\widetilde{Z''^2}$,

$$\frac{\partial(\bar{\rho}\widetilde{Z''^2})}{\partial t} + \nabla \cdot (\bar{\rho}\tilde{V}\widetilde{Z''^2}) = \nabla \cdot (\bar{\rho}D\nabla\widetilde{Z''^2}) + 2\bar{\rho}D(\nabla\tilde{Z})^2 - \bar{\rho}\tilde{\chi} \quad (3.59)$$

where the mean scalar dissipation rate can be modelled in a similar fashion as equation (3.47) for the non-reacting case. The constant, C_D , in equation (3.47) is increased with the increasing of Reynolds number (Peters 2000) and Kim (2004) reported that C_D is large for fast mixing. The value of C_D used in this thesis is case-specific and will be specified later.

3.6 Conclusion

This chapter has briefly discussed the conservation equations and models related to turbulent flows. The equations are presented in a multi-dimensional form, similarly to all the turbulence equations.

A brief description of moment methods is discussed, followed by the difference between Reynolds and Favre averaging, with Favre averaging used for the rest of the equations. The chemical reactions present the most challenging closure problem, where they consume most of the computing resources. There are challenges ahead for using detailed chemical mechanism with current turbulent combustion models. However, they will not be discussed in this thesis.

The non-premixed combustion, also called diffusion flames, uses two important parameters, which are the mean mixture fraction and variance. These two quantities will be extensively used in CMC equations. This equation (CMC), together with the simplification of the turbulent equations in a zero-dimensional environment, will be presented in the next chapter.

Chapter 3

Chapter 4

NUMERICAL MODELS

4.1 Introduction

Modelling the combustion in an IC engine has received increasing attention from researchers worldwide. Models have become widely available in many commercial CFD packages, such as Ansys Fluent, Kiva-3V and STAR-CD. They can be categorised as:

1. Zero-dimensional models: time is the only independent variable used in the combustion model.
2. Quasi-dimensional models: uses zero-dimensional model for the fluid mechanics, with an additional separate model for turbulent combustion to account for the inhomogeneities in the system.
3. Multi-dimensional model: this model solves the conservation equations in three dimensions.

A multi-dimensional model requires substantial computational time as compared to zero- and quasi-dimensional models, which are a simplified version of a multi-dimensional model. Thus, the use of simplified models with the addition of turbulent sub-models becomes increasingly important because of its advantages in computational time and resources. A quasi-dimensional model used in this thesis was initially developed by Assanis and Heywood (1986). This thesis uses the term zero-dimensional instead of quasi-dimensional model because the simulation environment is based on a zero-dimensional model. However, some changes have been made, so that the model uses different heat release rate and valve motion models for the zero-dimensional simulation and added chemical reaction mechanisms, followed by the

CMC mixing model later on. This chapter describes the equations used in the zero- and quasi-dimensional single-zone model, and also the CMC formulations.

4.2 Single-Zone Model

The single-zone model assumes that the mixture of air and fuel in the combustion chamber is mixed homogeneously before combustion occurs. The mixing process of the HCCI engine in this study begins in the inlet manifold. Thus, the CMC mixing starts from the inlet manifold, where the fuel and air are in a non-premixed condition. The engine modelling starts with a zero-dimensional model, before being updated to a quasi-dimensional model with the addition of a turbulence model. The CMC mixing model was then added after the quasi-dimensional model.

4.2.1 Zero-Dimensional Modelling

A zero-dimensional model uses time as the independent variable to model the combustion in the chamber. In this study, time can be represented by θ , which is the CA, because θ monotonically increases with time. In the next sub-sections, the equations used to model the zero-dimensional environment for a single-cylinder engine are discussed. The MATLAB code was developed based on these equations.

4.2.1.1 Engine Parameters

The engine movements are defined from the engine parameters, which have to be defined before employing the energy equation of the first law of thermodynamics in the zero-dimensional model. Figure 4.1 shows the geometry of the piston and crank mechanisms.

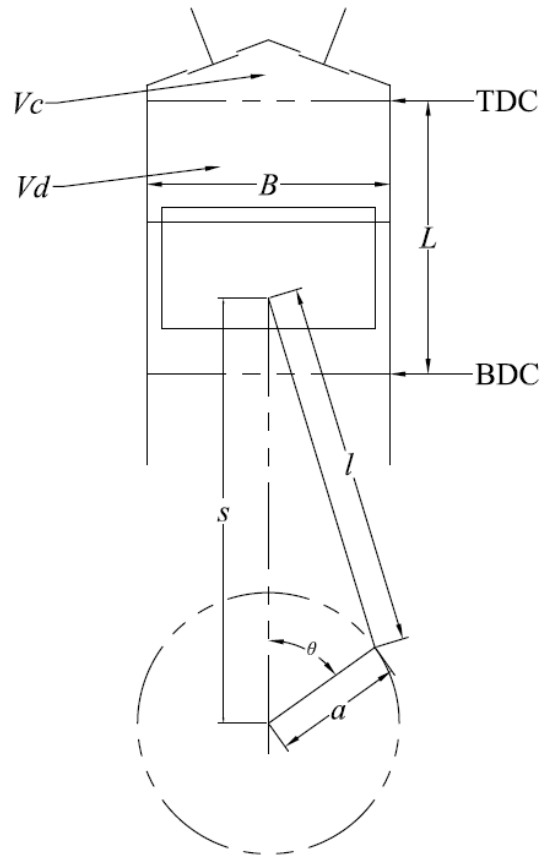


Figure 4.1 Engine geometry of the piston and crank mechanisms.

The crank radius, a , is defined as half the stroke length, L

$$a = \frac{L}{2} \quad (4.1)$$

and the ratio of connecting rod length to crank radius is given by

$$R = \frac{l}{a} \quad (4.2)$$

The rotational speed of the engine is

$$\omega = \frac{2\pi N}{60} \quad (4.3)$$

Chapter 4

where N is the engine speed in rotations per minute (RPM). For a flat piston crown, the area is given by

$$A_p = \frac{\pi B^2}{4} \quad (4.4)$$

where B represents the bore diameter of the engine. When the piston is at TDC, the clearance volume is

$$\mathcal{V}_c = \frac{\mathcal{V}_d}{(R_c - 1)} \quad (4.5)$$

where \mathcal{V}_d is the displacement volume and R_c is the compression ratio, which are given as

$$\mathcal{V}_d = A_p L \quad (4.6)$$

$$R_c = \frac{\text{maximum cylinder volume}}{\text{minimum cylinder volume}} = \frac{\mathcal{V}_d + \mathcal{V}_c}{\mathcal{V}_c} \quad (4.7)$$

From these parameters, the instantaneous piston speed can be obtained

$$S_p = \frac{\pi}{2} \bar{S}_p \sin\theta \left(1 + \frac{\cos\theta}{\sqrt{R_c^2 - \sin^2\theta}} \right) \quad (4.8)$$

where \bar{S}_p is the mean piston speed, defined as

$$\bar{S}_p = \frac{2LN}{60} \quad (4.9)$$

The instantaneous piston speed S_p is zero at the beginning of the stroke and approaches its maximum at the middle of the stroke. It goes to zero again at the end of the stroke, as shown in Figure 4.2.

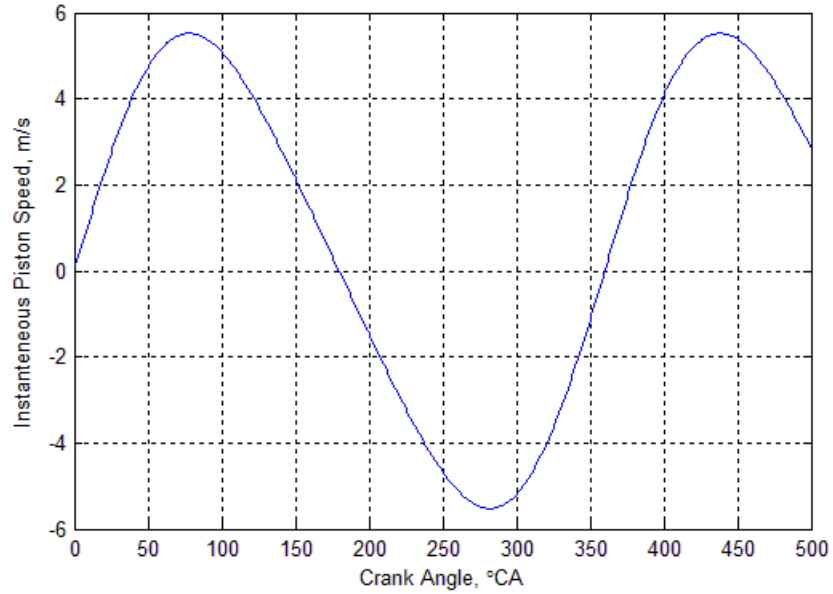


Figure 4.2 Instantaneous piston speed: zero at TDC and BDC, maximum at the middle of the stroke.

Then, the instantaneous cylinder volume at any crank angle location can be determined from

$$\mathcal{V} = \mathcal{V}_c + A_p(l + a - s) \quad (4.10)$$

where s is the distance between crank axis and piston pin axis, which is given by

$$s = a \cos \theta + \sqrt{(l^2 - a^2 \sin^2 \theta)} \quad (4.11)$$

After manipulation of equations (4.10) and (4.11), the instantaneous cylinder volume is

$$\mathcal{V} = \mathcal{V}_c \left[1 + \frac{R_c - 1}{2} (R + 1 - \cos \theta - \sqrt{R^2 - \sin^2 \theta}) \right] \quad (4.12)$$

with the rate of change of volume

$$\frac{d\mathcal{V}}{d\theta} = \mathcal{V}_c \left[\frac{R_c - 1}{2} (\sin \theta) \left(\frac{1 + \cos \theta}{\sqrt{R^2 - \sin^2 \theta}} \right) \right] \quad (4.13)$$

Cylinder volume is an important parameter because it determines the piston work in the energy equation.

4.2.1.2 Valve Geometry

Valve geometry is an important parameter to be considered because the mixing begins in the inlet manifold and it determines the mass flow rate to the combustion chamber. In general engine configurations, the valve head is circular with a slightly different diameter between inlet and exhaust valves. Typical valve geometry for most engines is shown in Figure 4.3.

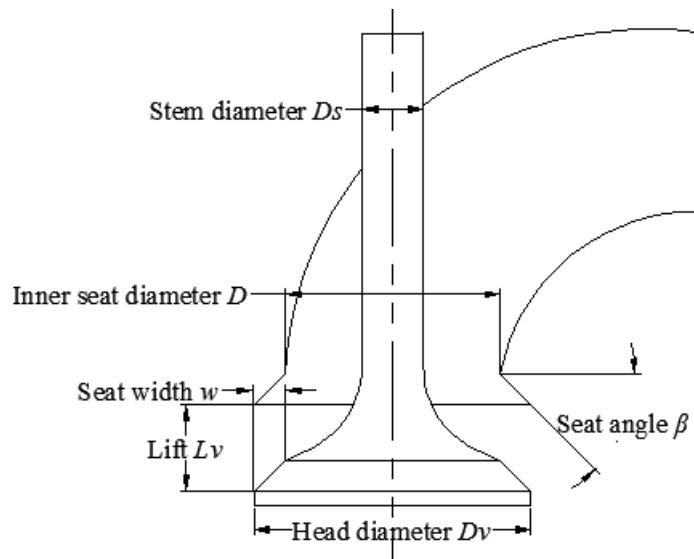


Figure 4.3 Valve geometry for most engines with parameters defining the valve.

Based on Heywood's definition (Heywood 1988) on valve configurations for most engines, the valve head diameter is taken as

$$D_v = 1.1D \quad (4.14)$$

where D is the inner seat diameter, as shown in Figure 4.3. Then, the valve seat width is

$$S_w = D_v - D \quad (4.15)$$

with the valve stem diameter defined as

$$D_s = 0.2D \quad (4.16)$$

In order to determine the mass flow rate of the mixture to the combustion chamber, the valve lift profile has to be defined. The valve lift profile is determined by using the desired maximum valve lift L_v and half-event angle c . The half-event angle is defined as half of the total valve opening duration. The profile as a function of crank angle (Assanis & Polishak 1990) is then given by

$$y = L_v + C_2\theta^2 + C_w\theta^w + C_q\theta^q + C_r\theta^r + C_s\theta^s \quad (4.17)$$

where w, q, r and s are constants to match the desired valve lift curve, which are selected as $w = 6, q = 8, r = 10$ and $s = 12$. The coefficients C_w, C_q, C_r and C_s are

$$C_2 = \frac{-wqrsL_v}{[(w-2)(q-2)(r-2)(s-2)c^2]} \quad (4.18)$$

$$C_w = \frac{2qrsL_v}{[(w-2)(q-w)(r-w)(s-w)c^w]} \quad (4.19)$$

$$C_q = \frac{-2wrsL_v}{[(q-2)(q-w)(r-q)(s-q)c^q]} \quad (4.20)$$

$$C_r = \frac{2wqsL_v}{[(r-2)(r-w)(r-q)(s-r)c^r]} \quad (4.21)$$

$$C_s = \frac{-2wqrL_v}{[(s-2)(s-w)(s-q)(s-r)c^s]} \quad (4.22)$$

Using equation (4.17), a typical valve lift profile with tappet mechanism (mechanical lifters) is illustrated in Figure 4.4. Once the valve lift is known, the effective valve open area can be obtained. In this case, the effective valve open area is taken as its curtain area, which is given by

$$A_c = \pi D_v L_v \quad (4.23)$$

Figure 4.4 shows a typical profile of valve lift for poppet valves with mechanical lifters. Generally, larger valve sizes (or more valves per cylinder) give higher maximum air flow in and out of the chamber.

Chapter 4

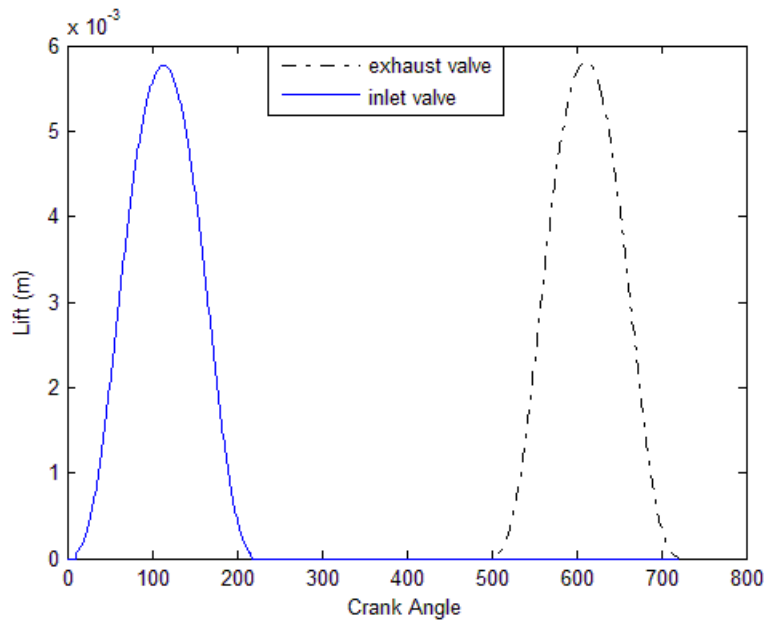


Figure 4.4 Valve lift profile for typical poppet valves with mechanical lifters.

The mass flow rate to the combustion chamber can be obtained by using the equation of compressible flow through a flow restriction (Heywood 1988). The equation includes the real gas flow effects with discharge coefficient C_d obtained from the experiments. In principle, the mass flows in or out of the combustion chamber when there is a pressure difference between the chamber and ports. The equation is separated into two cases: choked and subsonic flows. For choked flow, the following conditions are obeyed:

$$\left(p_T/p_0 \leq \left[\frac{2}{\gamma + 1} \right]^{1/\gamma-1} \right)$$

$$\dot{m}_{in} = \frac{C_d A_c p_0}{\sqrt{RT_0}} \sqrt{\gamma} \left[\frac{2}{\gamma + 1} \right]^{\gamma+1/2(\gamma-1)} \quad (4.24)$$

while for subsonic flow,

$$\left(p_T/p_0 > \left[\frac{2}{\gamma + 1} \right]^{1/\gamma-1} \right)$$

$$\dot{m}_{in} = \frac{C_d A_c p_0}{\sqrt{RT_0}} \left(\frac{p_T}{p_0}\right)^{1/\gamma} \left\{ \frac{2\gamma}{\gamma-1} \left[1 - \left(\frac{p_T}{p_0}\right)^{\gamma-1/\gamma} \right] \right\}^{1/2} \quad (4.25)$$

where p_T , p_0 , T_0 and γ are the downstream static pressure, upstream stagnation pressure, upstream stagnation temperature and ratio of specific heats, respectively. These equations, (4.24) and (4.25), are a function of gas properties, valve geometry and thermodynamics states upstream and downstream of the valves. For flow into the combustion chamber, p_0 is the intake port pressure and p_T is the cylinder pressure. On the other hand, p_0 is the cylinder pressure and p_T is the exhaust port pressure for the flow out of the combustion chamber. The value C_d is obtained experimentally from Stiesch (2003) and interpolated for the whole valve lift event as shown in Figure 4.5.

Once the mass flow rate is determined, it will be used in the energy equation and also to obtain the total mass in the combustion chamber. The next section will discuss the conservation equations used in the zero-dimensional model, which is a simplified version of the multi-dimensional model.

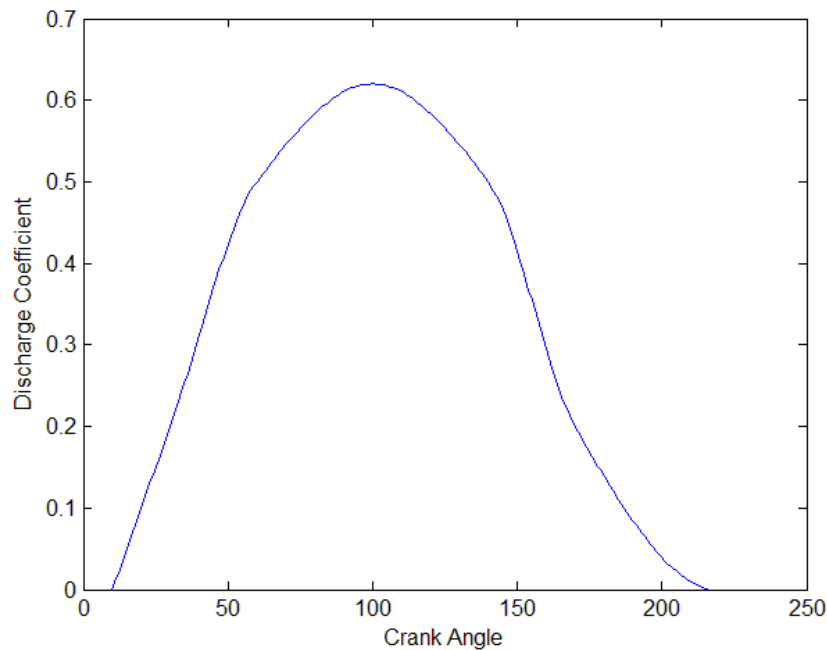


Figure 4.5 Discharge coefficient for one valve event

4.2.1.3 Conservation of Mass

The combustion chamber is assumed to be the control volume of the system, where it has mass transfer in and out of the system through the intake and exhaust valves. Thus, the mass in the system obeys

$$\frac{dm}{dt} = \sum_j \dot{m}_j \quad (4.26)$$

where j is the number of flows in (\dot{m}_j positive) or out of the system and m is the total mass in the system.

4.2.1.4 Conservation of Species

Conservation of species is used to determine the evolution of species inside the combustion chamber due to the chemical reactions. The rate of change of the mass fraction of species i is given by

$$\frac{dY_i}{dt} + \frac{(Y_i - Y_{i_{in}})\dot{m}}{\bar{\rho}\mathcal{V}} = \dot{\omega}_i \quad (4.27)$$

where $Y_{i_{in}}$ is the inlet mass fraction and $\dot{\omega}_i$ is the mass reaction rate of the species i .

4.2.1.5 Conservation of Energy

The first law of thermodynamics equation in differential form is used to model the combustion in the zero-dimensional single-zone model. The control volume of the combustion chamber is assumed to be an open thermodynamics system, by ignoring the changes in potential energy. The derivation of the first law of thermodynamics for engine simulations is described extensively by Assanis and Heywood (1986). In differential form, the first law of thermodynamics equation is

$$\frac{dU}{dt} = \frac{dQ_h}{dt} - \frac{dW}{dt} + \sum_j \frac{dH_j}{dt} \quad (4.28)$$

where U is the internal energy, Q_h is the heat transfer, W is the work and H_j is the enthalpy of flows entering or leaving the system. By using the definition of each term, equation (4.28) then becomes

$$\frac{d(mu)}{dt} = \frac{dQ_h}{dt} - p \frac{dV}{dt} + \sum_j h_j \frac{dm_j}{dt} \quad (4.29)$$

After manipulating equation (4.29), the final equation for the temperature change in the zero-dimensional single-zone model is given by

$$\begin{aligned} \frac{dT}{dt} = \frac{1}{C_A} \left[\sum_i \left[\left(\frac{p\nu}{R} R_i - h_i \right) \frac{dY_i}{dt} \right] \right. \\ \left. - \frac{C_B}{m} \frac{dm}{dt} + \frac{1}{m} \left(\frac{dQ_h}{dt} - p \frac{dV}{dt} + \sum_j \dot{m}_j h_j \right) \right] \end{aligned} \quad (4.30)$$

where C_A and C_B are defined as

$$C_A = \bar{c}_p - \frac{p\nu}{T} \quad (4.31)$$

$$C_B = h - p\nu \quad (4.32)$$

The derivation of equation (4.30) is given in Appendix A. Once the temperature is obtained from equation (4.30), the in-cylinder pressure is determined by using the ideal gas law

$$p = \frac{\rho R_u T}{\overline{W}_{mw}} \quad (4.33)$$

where R_u is the universal gas constant and \overline{W}_{mw} is the mean molecular weight of the mixture.

4.2.1.6 Heat Loss Model in Zero-Dimensional Model

Heat transfer from the combustion chamber to the cylinder wall occurs by convection and radiation. In HCCI engines, radiation heat transfer is negligible because its effect is very small, due to low soot and low temperature combustion (Bengtsson, Gafvert & Strandh 2004; Chang *et al.* 2004): therefore it is ignored (Soyhan *et al.* 2009). The convective heat transfer was modelled to match the experimental results so that the in-cylinder gas motion can be predicted (Stone 1999). The convective heat transfer rate can be described by Newton's law of cooling (Stiesch 2003), as

$$\frac{dQ_h}{dt} = h_c A_w (T - T_w) \quad (4.34)$$

where h_c is the heat transfer coefficient, A_w is the wall area and T_w is the wall temperature. The wall area is the sum of the piston, cylinder head and cylinder wall area, which is

$$A_w = \frac{\pi}{4} B^2 + \left(\frac{\pi}{4} B^2 + \frac{4V_c}{B} \right) + \left[\left(\pi B \frac{L}{2} \right) \left(R + 1 - \cos\theta - \sqrt{R^2 - \sin^2\theta} \right) \right] \quad (4.35)$$

In zero-dimensional modelling, an empirical sub-model is used for the heat transfer coefficient, where the model does not contain any physical or chemical principles. Instead, the model attempts to reproduce the characteristics of heat loss obtained from experiments (Stiesch 2003). In this thesis, the heat transfer coefficient is modelled using the modified Woschni (Chang *et al.* 2004) correlation, which has been calibrated in an HCCI engine mode. The details of the correlation are discussed in Section 5.3.2.

4.2.2 Quasi-Dimensional Modelling

Quasi-dimensional modelling requires a separate turbulent model. In this study, a simplified form of the k - ϵ turbulence model was used. The heat loss is no longer modelled; instead, the turbulence models were used to predict the behaviour of the heat release rate by the combustion products.

4.2.2.1 Turbulence Models

An energy cascade method by Mansouri, Heywood and Radhakrishnan (1982) was used to model the turbulence. It is called the energy cascade method because the mean kinetic energy, K , (due to the mean velocity of the fluid) enters the cylinder through the intake valve and is converted to the turbulent kinetic energy, k , (the strength of turbulence in the flow) via turbulent dissipation, (ε). The turbulent kinetic energy is then converted into heat by viscous dissipation. These are represented by the following differential equations:

$$\frac{dK}{dt} = \frac{1}{2}\dot{m}_{in}V_{in}^2 - P - K\frac{\dot{m}_{ex}}{m} \quad (4.36)$$

$$\frac{dk}{dt} = P - \varepsilon - k\frac{\dot{m}_{ex}}{m} + RDT \quad (4.37)$$

where \dot{m}_{in} is the mass flow rate of the inlet flow, V_{in} is the inlet velocity to the cylinder, P is the production term, \dot{m}_{ex} is the exhaust mass flow rate and RDT is the Rapid Distortion Theory term. The turbulence dissipation rate is then given by

$$\varepsilon = \frac{mv'^3}{l_m} = \frac{m}{l_m} \left(\frac{2k}{3m} \right)^{\frac{3}{2}} \quad (4.38)$$

assuming that the turbulence is isotropic. In equation (4.38), v' is the turbulent intensity and l_m is the characteristic length scale, which is assumed to be the instantaneous combustion chamber height, subject to the restriction that it is less than half of the cylinder bore (Agarwal *et al.* 1998).

RDT is the turbulence amplification rate due to rapid distortion during compression and combustion processes, which is modelled by

$$RDT = \frac{2}{3} \left(\frac{k}{\rho} \right) \left(\frac{d\rho}{dt} \right) \quad (4.39)$$

The production term, on the other hand, uses the assumption that the turbulence is generated in the boundary layer over a flat plate

$$P = \mu_t \left(\frac{\partial V}{\partial y} \right)^2 \approx 0.3307 C_\beta \left(\frac{K}{L} \right) \left(\frac{k}{m} \right)^{\frac{1}{2}} \quad (4.40)$$

where C_β is an adjustable constant. The value of C_β is chosen as 1, following the calibration from Agarwal *et al.* (1998). Once the turbulence is modelled, it will be used to determine the mixture velocity in the combustion chamber, which is then converted to the heat loss due to combustion.

4.2.2.2 Heat Loss Model in Quasi-Dimensional Model

The convective heat transfer in the quasi-dimensional model is obtained by using the same heat loss equation as in equation (4.34). However, the heat transfer coefficient is obtained from the Nusselt-Reynolds number correlation as

$$h_c = \frac{\text{Nu} \gamma_T}{l_m} \quad (4.41)$$

where Nu is the Nusselt number and γ_T is the thermal conductivity of the mixture. The Nusselt number is given by

$$\text{Nu} = \theta \text{Re}^d \quad (4.42)$$

where θ and d are the adjustable constants to fit the experimental data. The suggested values are (Assanis & Heywood 1986)

$$\begin{aligned} \theta &= 0.035 - 0.13 \\ d &= 0.7 - 0.8 \end{aligned} \quad (4.43)$$

Then, the Reynolds number is obtained based on the steady turbulent flow in a pipe as

$$\text{Re} = \frac{\rho V_m l_m}{\mu} \quad (4.44)$$

where μ is the dynamic viscosity and V_m is the characteristic velocity given by

$$V_m = \sqrt{\left[V_f^2 + v'^2 + \left(\frac{S_p}{2} \right)^2 \right]} \quad (4.45)$$

where V_f is the mean flow velocity. The characteristic velocity in equation (4.45) is due to the contribution of mean kinetic energy, turbulent kinetic energy and the piston motion.

4.3 Mixing Model: Conditional Moment Closure

4.3.1 Conditional Transport Equations

The CMC transport equations solve the conditional means of reactive scalars and temperature. The mass fraction of species i , Y_i , is chosen as the reactive scalars and in non-premixed combustion, the reactive scalars is conditionally averaged with respect to the conserved scalar, Z , which is the mixture fraction. This is because the turbulent fluctuations of reactive scalars are strongly dependent on the fluctuations of the mixture fraction. The conditional mean of the mass fraction, Y_i , and the temperature, T , are then defined as

$$Q_i(\eta; \mathbf{x}, t) \equiv \langle Y_i(\mathbf{x}, t) | \eta = Z \rangle \quad (4.46)$$

$$Q_T(\eta; \mathbf{x}, t) \equiv \langle T(\mathbf{x}, t) | \eta = Z \rangle \quad (4.47)$$

where Q_i is the conditional mean of reactive scalars, Q_T is the conditional temperature and η is the sample space variable for the mixture fraction, Z , at location \mathbf{x} and time t . The operator

$$\langle \bullet | Z(\mathbf{x}, t) = \eta \rangle \quad (4.48)$$

denotes the conditional averaging subject to the condition on the right of the vertical bar. The instantaneous mass fraction, Y , and temperature, T , can be decomposed into a conditional mean and conditional fluctuation as

$$Y_i(\mathbf{x}, t) = Q_i(\eta; \mathbf{x}, t) + Y_i''(\mathbf{x}, t) \quad (4.49)$$

$$T(\mathbf{x}, t) = Q_T(\eta; \mathbf{x}, t) + T''(\mathbf{x}, t) \quad (4.50)$$

where Y_i'' and T'' are the conditional fluctuations with respect to the conditional mean mass fraction and conditional mean temperature, respectively. Differentiating equation (4.49) and (4.50) with respect to time gives (Klimenko & Bilger 1999)

$$\frac{\partial Y_i}{\partial t} = \frac{\partial Q_i}{\partial t} + \frac{\partial Q_i}{\partial \eta} \frac{\partial Z}{\partial t} + \frac{\partial Y_i''}{\partial t} \quad (4.51)$$

$$\frac{\partial T}{\partial t} = \frac{\partial Q_T}{\partial t} + \frac{\partial Q_T}{\partial \eta} \frac{\partial Z}{\partial t} + \frac{\partial T''}{\partial t} \quad (4.52)$$

and with respect to the location is

$$\nabla Y_i = \nabla Q_i + \frac{\partial Q_i}{\partial \eta} \nabla Z + \nabla Y_i'' \quad (4.53)$$

$$\nabla T = \nabla Q_T + \frac{\partial Q_T}{\partial \eta} \nabla Z + \nabla T'' \quad (4.54)$$

4.3.1.1 Conditional Mass Fraction

To obtain the transport equation for the conditional mass fraction, the molecular diffusive flux in equation (3.5) is substituted to equation (4.53) and leads to

$$\begin{aligned} \nabla \cdot (\rho D_i \nabla Y_i) &= \nabla \cdot (\rho D_i \nabla Q_i) + \frac{\partial Q_i}{\partial \eta} \nabla \cdot (\rho D_i \nabla Z) + \rho D_i (\nabla Z)^2 \frac{\partial^2 Q_i}{\partial \eta^2} \\ &+ \rho D_i \nabla Z \cdot \nabla \frac{\partial Q_i}{\partial \eta} + \nabla \cdot (\rho D_i \nabla Y_i'') \end{aligned} \quad (4.55)$$

Substituting equations (4.51), (4.53) and (4.55) into equation (3.5) gives

$$\begin{aligned} \rho \frac{\partial Q_i}{\partial t} + \rho \mathbf{V} \cdot \nabla Q_i &= \rho N \frac{\partial^2 Q_i}{\partial \eta^2} + \rho D_i \nabla Z \nabla \frac{\partial Q_i}{\partial \eta} + \nabla(\rho D_i \nabla Q_i) \\ &+ \nabla(\rho D_i \nabla Y_i'') - \rho \frac{\partial Y_i''}{\partial t} - \rho(\mathbf{V} \cdot \nabla Y_i'') + \rho \dot{\omega} \end{aligned} \quad (4.56)$$

where N is the scalar dissipation rate, which is denoted as $N \equiv D_i(\nabla Z)^2$. Taking the conditional expectation of equation (4.56), conditional on $Z(\mathbf{x}, t) = \eta$, yields

$$\rho_\eta \frac{\partial Q_i}{\partial t} + \rho_\eta \langle \mathbf{V} | \eta \rangle \cdot \nabla Q_i = \rho_\eta \langle N | \eta \rangle \frac{\partial^2 Q_i}{\partial \eta^2} + \rho_\eta \langle \dot{\omega} | \eta \rangle + e_Q + e_Y \quad (4.57)$$

with

$$e_Q = \langle \nabla(\rho D_i \nabla Q_i) + \rho D_i \nabla Z \nabla \frac{\partial Q_i}{\partial \eta} | Z(\mathbf{x}, t) = \eta \rangle \quad (4.58)$$

$$e_Y = - \langle \rho \frac{\partial Y_i''}{\partial t} + \rho(\mathbf{V} \cdot \nabla Y_i'') - \nabla(D_i \rho \nabla Y_i'') | Z(\mathbf{x}, t) = \eta \rangle \quad (4.59)$$

Equation (4.57) represents a multi-dimensional CMC equation in the unclosed form for Q , where $\rho_\eta \equiv \langle \rho | \eta \rangle$ and the conditional fluctuations of density are ignored. According to Klimenko and Bilger (1999), e_Q in equation (4.58) is small when the Reynolds number is large. Thus, this term can be ignored. Also, following the closure hypothesis, e_Y in equation (4.59) can be modelled as

$$e_Y = - \frac{\nabla \cdot [\rho_\eta \langle \mathbf{V}'' Y_i'' | \eta \rangle P_z(\eta)]}{P_z(\eta)} \quad (4.60)$$

Therefore, equation (4.57) can be rewritten as

$$\begin{aligned} \rho_\eta \frac{\partial Q_i}{\partial t} + \rho_\eta \langle \mathbf{V} | \eta \rangle \cdot \nabla Q_i \\ = \rho_\eta \langle N | \eta \rangle \frac{\partial^2 Q_i}{\partial \eta^2} + \rho_\eta \langle \dot{\omega} | \eta \rangle - \frac{\nabla \cdot [\rho_\eta \langle \mathbf{V}'' Y_i'' | \eta \rangle P_z(\eta)]}{P_z(\eta)} \end{aligned} \quad (4.61)$$

The last term on the LHS is the convection term. The first term on the RHS corresponds to diffusion in conserved scalar space and is affected by the scalar dissipation rate. The

second term on the RHS is the conditional expectation of the chemical source term and the last term represents spatial diffusion. Equation (4.61) is the unconservative form of the CMC equation and the conditional covariance in the spatial diffusion term is usually ignored, while $\langle N|\eta \rangle$ must satisfy the conserved scalar PDF transport equation

$$\frac{\partial P_z(\eta)\rho_\eta}{\partial t} + \nabla(\langle \mathbf{V}|\eta \rangle P_z(\eta)\rho_\eta) + \frac{\partial^2 \langle N|\eta \rangle P_z(\eta)\rho_\eta}{\partial \eta^2} = 0 \quad (4.62)$$

The unconservative CMC equation can be transformed to its conservative form by multiplying equation (4.61) by $P_z(\eta)$ and equation (4.62) by Q_i and adding to give

$$\begin{aligned} & \frac{\partial Q_i P_z(\eta)\rho_\eta}{\partial t} + \nabla(\langle \mathbf{V}|\eta \rangle \mathbf{Q}_i P_z(\eta)\rho_\eta) \\ & = \langle \dot{\omega}|\eta \rangle P_z(\eta)\rho_\eta + \frac{\partial}{\partial \eta} \left(\langle N|\eta \rangle P_z(\eta)\rho_\eta \frac{\partial Q_i}{\partial \eta} - \frac{\partial \langle N|\eta \rangle P_z(\eta)\rho_\eta Q_i}{\partial \eta} \right) \end{aligned} \quad (4.63)$$

For homogeneous CMC, which was used in the study, the combustion chamber is modelled as an Incompletely Stirred Reactor (ISR) (Kwon *et al.* 2011) with varying Probability Density Function (PDF).

$$\begin{aligned} & \frac{\partial Q_i P_z(\eta)\rho_\eta}{\partial t} + \nabla(\bar{\rho} \langle \mathbf{V}|\eta \rangle \mathbf{Q}_i \tilde{P}_z(\eta)) \\ & = \bar{\rho} \langle \dot{\omega}|\eta \rangle P_z(\eta) - \frac{\partial^2 \bar{\rho} \langle N|\eta \rangle \tilde{P}_z(\eta) Q_i}{\partial \eta^2} + 2 \frac{\partial}{\partial \eta} \left(\bar{\rho} \tilde{P}_z(\eta) \langle N|\eta \rangle \frac{\partial Q_i}{\partial \eta} \right) \end{aligned} \quad (4.64)$$

where the Favre PDF is introduced:

$$\tilde{P}_z(\eta) = \frac{\langle \rho|\eta \rangle P_z(\eta)}{\bar{\rho}}$$

Taking the volume integral of equation (4.64) and applying the flux divergence theorem to the convective term produces:

$$\begin{aligned}
 & \iiint_{\mathcal{V}} \frac{\partial Q_i \tilde{P}_z(\eta) \rho_\eta}{\partial t} d\mathcal{V} + \iint_{S_{out}} (\bar{\rho} \langle \mathbf{V} | \eta \rangle Q_i \tilde{P}_z(\eta))_{out} dS \\
 & \quad - \iint_{S_{in}} (\bar{\rho} \langle \mathbf{V} | \eta \rangle Q_i \tilde{P}_z(\eta))_{in} dS \\
 & = \iiint_{\mathcal{V}} \bar{\rho} \langle \dot{\omega} | \eta \rangle \tilde{P}_z(\eta) d\mathcal{V} - \iiint_{\mathcal{V}} \frac{\partial^2 \bar{\rho} \langle N | \eta \rangle \tilde{P}_z(\eta) Q_i}{\partial \eta^2} d\mathcal{V} \\
 & \quad + \iiint_{\mathcal{V}} 2 \frac{\partial}{\partial \eta} (\bar{\rho} \tilde{P}_z(\eta) \langle N | \eta \rangle \frac{\partial Q_i}{\partial \eta}) d\mathcal{V}
 \end{aligned} \tag{4.65}$$

where S_{out} is the cross-sectional area of the chamber and S_{in} includes both oxidiser and fuel inlets. The conditional expectations of the reactive scalars ($\dot{\omega}$, Q_i) are uniform inside the core of the chamber and can be moved outside of the integrals in equation (4.65) to yield

$$\begin{aligned}
 & \frac{\partial Q_i \iiint_{\mathcal{V}} \tilde{P}_z(\eta) \rho_\eta d\mathcal{V}}{\partial t} + Q_{out} \iint_{S_{out}} (\bar{\rho} \langle \mathbf{V} | \eta \rangle \tilde{P}_z(\eta))_{out} dS \\
 & \quad - Q_{in} \iint_{S_{in}} (\bar{\rho} \langle \mathbf{V} | \eta \rangle \tilde{P}_z(\eta))_{in} dS \\
 & = \langle \dot{\omega} | \eta \rangle \iiint_{\mathcal{V}} \bar{\rho} \tilde{P}_z(\eta) d\mathcal{V} - \frac{\partial^2 Q_i \iiint_{\mathcal{V}} 2 \bar{\rho} \tilde{P}_z(\eta) \langle N | \eta \rangle d\mathcal{V}}{\partial \eta^2} \\
 & \quad + \frac{\partial^2 Q_i}{\partial \eta^2} \iiint_{\mathcal{V}} \bar{\rho} \tilde{P}_z(\eta) \langle N | \eta \rangle d\mathcal{V}
 \end{aligned} \tag{4.66}$$

By using the following definitions for certain integrals:

$$P_{io}^* = \frac{1}{\dot{m}} \iint_S \bar{\rho} \langle \mathbf{V} | \eta \rangle \tilde{P}_z(\eta) dS \tag{4.67}$$

$$\rho^{**} = \frac{1}{\mathcal{V}} \iiint_{\mathcal{V}} \bar{\rho} d\mathcal{V} \tag{4.68}$$

$$P_z^{**} = \frac{1}{\rho^{**} \mathcal{V}} \iiint_{\mathcal{V}} \bar{\rho} \tilde{P}_z(\eta) d\mathcal{V} \tag{4.69}$$

$$N^{**} = \frac{1}{\rho^{**} P_z^{**} \mathcal{V}} \iiint_{\mathcal{V}} \bar{\rho} \tilde{P}_z(\eta) \langle N|\eta \rangle d\mathcal{V} \quad (4.70)$$

Equation (4.66) can then be written as

$$\begin{aligned} \tau \frac{\partial P_z^{**} Q_i}{\partial t} + (Q_{out} P_{out}^* - Q_{in} P_{in}^*) \\ = \tau \left(P_z^{**} \langle \dot{\omega}|\eta \rangle + 2 \frac{\partial}{\partial \eta} \left(P_z^{**} N^{**} \frac{\partial Q_i}{\partial \eta} \right) - \frac{\partial^2 P_z^{**} N^{**} Q_i}{\partial \eta^2} \right) \end{aligned} \quad (4.71)$$

where τ is the residence time, given by

$$\tau = \frac{\rho^{**} \mathcal{V}}{\dot{m}} \quad (4.72)$$

In deriving equation (4.66), two assumptions have been made: 1) the conditional expectations of reactive scalars are uniform inside the core; and 2) the outlet composition of Q is the same as that within the volume, thus $Q_{out} = Q_i$. Integrating the PDF transport equation (4.62) in a similar fashion and using the definitions of equations (4.67)-(4.70), yields

$$\tau \frac{\partial P_z^{**}}{\partial t} + (P_{out}^* - P_{in}^*) = -\tau \frac{\partial^2 P_z^{**} N^{**}}{\partial \eta^2} \quad (4.73)$$

Equation (4.73) is multiplied by Q_i and subtracting from equation (4.71) gives

$$\tau P_z^{**} \frac{\partial Q_i}{\partial t} + (Q_i - Q_{in}) P_{in}^* = \tau \left(P_z^{**} \langle \dot{\omega}|\eta \rangle + P_z^{**} N^{**} \frac{\partial^2 Q_i}{\partial \eta^2} \right) \quad (4.74)$$

For the unsteady ISR, equation (4.74) can be written as

$$\frac{\partial Q_i}{\partial t} + \frac{(Q_i - Q_{in}) P_{in}^*}{\tau P_z} = \langle N|\eta \rangle \frac{\partial^2 Q_i}{\partial \eta^2} + \langle \dot{\omega}|\eta \rangle \quad (4.75)$$

where \dot{m}_{in} as the denominator in τ is the mass flow rate into the system, Q_{in} is the inlet reactive scalar and P_{in}^* is the inlet averaged PDF. The mass flow rate, \dot{m}_{in} , is a

function of time depending on the inlet valve opening and closing, and it becomes zero when the valve is closed. The importance of considering the gas exchange process is that the in-cylinder temperature and pressure at IVC can be obtained accurately by using actual inlet conditions. Hence, no assumptions need to be made in obtaining the in-cylinder properties at IVC. Equation (4.75) is the CMC equation used for the HCCI engine simulation, which will be attached to the zero-dimensional model environment. Then, the mean mass fraction of the i th species can be obtained as

$$\bar{Y}_i = \int_0^1 Q_i(\eta) P_z(\eta) d\eta \quad (4.76)$$

4.3.1.2 Conditional Enthalpy Equation

The enthalpy, h , of a mixture, as in equation (3.9), is a function of species mass fraction, Y_i , and temperature, T , as given by

$$h = h(Y_1, Y_2, \dots, Y_n, T) = \sum_i Y_i \left[(h_0)_i + \int_{T_0}^T (c_p)_i dT \right] \quad (4.77)$$

where $(h_0)_i$ is the enthalpy of formation, specified from a standard state. Following the form in equation (3.10) and Klimenko and Bilger (1999), the CMC equation for $Q_h \equiv \langle h | \eta \rangle$ is given by

$$\begin{aligned} & \frac{\partial Q_h}{\partial t} + \langle \mathbf{V} | \eta \rangle \cdot \nabla Q_h \\ & = \langle N | \eta \rangle \frac{\partial^2 Q_h}{\partial \eta^2} + \left\langle \frac{1}{\rho_\eta} \frac{\partial p}{\partial t} \middle| \eta \right\rangle - \langle W_{RAD} | \eta \rangle - \frac{\nabla \cdot [\rho_\eta \langle \mathbf{V}'' h'' | \eta \rangle P_z(\eta)]}{P_z(\eta) \rho_\eta} \end{aligned} \quad (4.78)$$

where W_{RAD} is the heat loss rate per unit mass due to radiation. The term $\partial p / \partial t$ in equation (4.78) is important for combustion simulation for IC engines (Seo *et al.* 2010).

Equation (4.78) (the unconservative conditional enthalpy equation) is transformed to its conservative form and the ISR model is then derived in a similar fashion to equation (4.75). The heat loss due to radiation is ignored for HCCI engine simulations and the

term is replaced with the heat loss due to convection (De Paola *et al.* 2008; Kwon *et al.* 2011; Seo *et al.* 2010). Equation (4.78) then becomes

$$\frac{\partial Q_h}{\partial t} + \frac{(Q_h - Q_{in})P_{in}^*}{\tau P_z} = \langle N|\eta \rangle \frac{\partial^2 Q_h}{\partial \eta^2} + \left\langle \frac{1}{\rho_\eta} \frac{\partial p}{\partial t} \middle| \eta \right\rangle - \left[h_c(Q_T - T_w) \frac{A_w}{m} \right] \quad (4.79)$$

The heat transfer coefficient, h_c , is modelled according to Section 4.2.1.6 based on the mean in-cylinder temperature. The heat loss in equation (4.79) is determined using, Q_T the conditional temperature, which is obtained from equation (4.77). ρ_η in the second term of RHS of equation (4.79) was obtained based on $\langle T|\eta \rangle$ using the ideal gas law, while $\partial p/\partial t$ was obtained based on the difference of the mean in-cylinder pressure between the current and previous time step. In this case, $\langle \rho \rangle$ must satisfy $\langle \rho \rangle = \int_0^1 \rho_\eta P_z(\eta) d\eta$ and $\langle T \rangle = \int_0^1 \langle T|\eta \rangle P_z(\eta) d\eta$, where $\langle T \rangle$ is given by the energy equation from the zero-dimensional model. A comparison of the mean and the integral of the conditional mean shows they are identical within computational error.

4.3.2 Sub-models for the Unclosed Terms

Sub-models are required to close all terms in the CMC equations. The simplification of the CMC equations for the zero-dimensional simulation obviates the need for models for the conditional velocity, $\langle \mathbf{V}|\eta \rangle$, in the convection term and conditional turbulent flux, $\langle \mathbf{V}'' Y_i''|\eta \rangle$, in the spatial diffusion term. Thus, the terms required to be modelled in this case are the conditional scalar dissipation rate $\langle N|\eta \rangle$, the presumed PDF $P_z(\eta)$ and the conditional chemical source term $\langle \dot{\omega}|\eta \rangle$.

4.3.2.1 Conditional Scalar Dissipation

The conditional scalar dissipation rate measures the magnitude of turbulent mixing in the mixture fraction space. It appears in the transport equations for both conditional species mass fraction, equation (4.75), and conditional enthalpy, equation (4.79). The model used for conditional scalar dissipation rate in this thesis is the Amplitude Mapping Closure (AMC), which has been used in other engine simulations (De Paola

et al. 2008; Kwon *et al.* 2011; Seo *et al.* 2010). The AMC model (Obrien & Jiang 1991) is given by

$$\langle N|\eta \rangle = \frac{\bar{\chi}G(\eta)}{2 \int_0^1 G(\eta)P_z(\eta)d\eta} \quad (4.80)$$

$$G(\eta) = \exp(-2[\text{erf}^{-1}(2\eta - 1)]^2)$$

where erf is the error function. The mean scalar dissipation rate, $\bar{\chi}$, is obtained from equation (3.47), where the turbulent quantities ε and k are computed using equations (4.37) and (4.38).

4.3.2.2 Presumed PDF

The PDF of the mixture fraction is modelled using a presumed β -function PDF. This model is a function of the first two moments: mean mixture fraction \tilde{Z} and mixture fraction variance \tilde{Z}''^2 . A β -function PDF is commonly used in multi-dimensional CMC engine simulations (De Paola *et al.* 2008; Seo *et al.* 2010; Wright *et al.* 2005) and takes the form

$$P_z(\eta) = \frac{(Z)^{\alpha-1}(1-Z)^{\beta-1}}{\Gamma(\alpha)\Gamma(\beta)} \Gamma(\alpha + \beta) \quad (4.81)$$

$$\alpha = \tilde{Z}\gamma, \quad \beta = (1 - \tilde{Z})\gamma, \quad \gamma = \frac{\tilde{Z}(1 - \tilde{Z})}{\tilde{Z}''^2} \quad (4.82)$$

where Γ is the gamma function. The mean mixture fraction and its variance are given in equations (3.58) and (3.59), respectively. With the assumption of using ISR, the mean mixture fraction is

$$\frac{\partial(\bar{\rho}\tilde{Z})}{\partial t} + \nabla \cdot (\bar{\rho}\tilde{V}\tilde{Z}) = \nabla \cdot (\bar{\rho}D\nabla\tilde{Z}) \quad (4.83)$$

Taking the volume integral and applying the flux divergence theorem to the convective term yields

$$\begin{aligned} \iiint_{\mathcal{V}} \frac{\partial(\bar{\rho}\tilde{Z})}{\partial t} d\mathcal{V} + \iint_{S_{out}} (\bar{\rho}\mathbf{V}\tilde{Z})_{out} dS - \iint_{S_{in}} (\bar{\rho}\mathbf{V}\tilde{Z})_{in} dS \\ = \iiint_{\mathcal{V}} \nabla \cdot (\bar{\rho}D\nabla\tilde{Z}) d\mathcal{V} \end{aligned} \quad (4.84)$$

\tilde{Z} is uniform inside the core and can be moved outside the integrals, while the gradient of \tilde{Z} is zero. Equation (4.84) then becomes

$$\frac{\partial\tilde{Z}}{\partial t} \iiint_{\mathcal{V}} \bar{\rho} d\mathcal{V} + \tilde{Z}_{out} \iint_{S_{out}} (\bar{\rho}\mathbf{V})_{out} dS - \tilde{Z}_{in} \iint_{S_{in}} (\bar{\rho}\mathbf{V})_{in} dS = 0 \quad (4.85)$$

By using the following definitions for the above integrals

$$\dot{m} = \iint_S (\bar{\rho}\mathbf{V}) dS \quad (4.86)$$

$$\rho^{**} = \frac{1}{\mathcal{V}} \iiint_{\mathcal{V}} \bar{\rho} d\mathcal{V} \quad (4.87)$$

yields

$$\bar{\rho}\mathcal{V} \frac{\partial\tilde{Z}}{\partial t} + (\tilde{Z}_{out} - \tilde{Z}_{in})\dot{m} = 0 \quad (4.88)$$

Using the same assumption from the derivation of equation (4.75), $\tilde{Z}_{out} = \tilde{Z}$ and rearranging equation (4.88) gives the mean mixture fraction equation for the zero-dimensional model

$$\frac{\partial\tilde{Z}}{\partial t} + \frac{(\tilde{Z} - \tilde{Z}_{in})\dot{m}}{\bar{\rho}\mathcal{V}} = 0 \quad (4.89)$$

The initial condition of the mean mixture fraction, \bar{Z}_0 , can be obtained from

$$\bar{Z}_0 = \frac{Y_F}{Y_F + Y_O} \quad (4.90)$$

In equation (4.90), Y_F and Y_O are the mass fraction for fuel and oxidiser respectively. This equation can be expressed as a function of equivalence ratio by dividing every term in equation (4.90) with Y_O and then with $(Y_F/Y_O)_{st}$, where subscript st is the stoichiometric condition, to give

$$\bar{Z}_0 = \frac{\left(\frac{Y_F}{Y_O}\right) / \left(\frac{Y_F}{Y_O}\right)_{st}}{\left[\left(\frac{Y_F}{Y_O}\right) / \left(\frac{Y_F}{Y_O}\right)_{st}\right] + \left[1 / \left(\frac{Y_F}{Y_O}\right)_{st}\right]} \quad (4.91)$$

By using the definition of equivalence ratio,

$$\phi = \frac{Y_F/Y_O}{(Y_F/Y_O)_{st}} \quad (4.92)$$

equation (4.91) then becomes

$$\bar{Z}_0 = \frac{\phi}{\phi + AFR_{st}} \quad (4.93)$$

where AFR_{st} is the air-to-fuel ratio at the stoichiometric condition.

The transport equation for the mixture fraction variance can be derived in a similar fashion to equation (4.89), which gives

$$\frac{\partial \widetilde{Z''^2}}{\partial t} + \frac{\left(\widetilde{Z''^2} - \widetilde{Z''_in^2}\right) \dot{m}}{\bar{\rho} \mathcal{V}} = -\tilde{\chi} \quad (4.94)$$

where the initial condition of the mixture fraction variance in the chamber is $\widetilde{Z''_0^2} = 0$. Equation (3.47) was used to determine the mean scalar dissipation rate $\tilde{\chi}$ in equation (4.94). The initial condition of the inlet mixture fraction variance was obtained based on $\widetilde{Z''_in^2} = Y_F(1 - Y_F)$. These values (the initial conditions) were used to obtain the

mixture fraction variance in the chamber and in the inlet port. It was assumed that there was no turbulent decay in the inlet manifold (the mixture fraction variance and kinetic energy were kept constant) because the fuel injector is located close to the inlet port. A mass-weighted average was then used to obtain the variance in the chamber after IVO, which implements the second term of equation (4.94). Another method was also used to obtain the initial condition of the inlet mixture fraction variance, which is using $\overline{Z_{in0}''^2} = \int_0^Z (Z - \bar{Z})^2 P_Z dZ$. A comparison between those equations was made and yields almost identical result.

4.3.2.3 Chemical Source Term

The chemical source term of the conditional reaction rate in equation (4.75) is modelled using the standard first-order CMC closure (Seo *et al.* 2010; Wright *et al.* 2005):

$$\langle \dot{\omega} | \eta \rangle \approx \dot{\omega}_i(Q_i, \dots, Q_n, Q_h, p) \quad (4.95)$$

It is only a function of the conditional mean mass fraction, conditional enthalpy and pressure: the conditional fluctuations are not included. The reaction rate is obtained from an open source chemical kinetics software package, Cantera.

4.3.2.4 Other sub-models

Another sub-model in the CMC equation that needs to be closed is

$$\left\langle \frac{1}{\rho_\eta} \frac{\partial p}{\partial t} \middle| \eta \right\rangle = \frac{1}{\langle \rho | \eta \rangle} \frac{\partial \bar{p}}{\partial t} \quad (4.96)$$

where the in-cylinder pressure is assumed to be homogeneous for the whole chamber in each CA step, and thus there is no variation of pressure in the mixture fraction space. Density, however, is not the same, where it is affected by the conditional temperature and mass fraction, as given by

Chapter 4

$$\langle \rho | \eta \rangle = \frac{\bar{p} W_{mw\eta}}{R_u Q_T} \quad (4.97)$$

where

$$W_{mw\eta} = \left(\sum_{i=1}^n \frac{Q_i}{W_{mwi}} \right)^{-1} \quad (4.98)$$

The thermodynamic quantities in equations (4.97) and (4.98) are also obtained from the Cantera chemical kinetics software package.

4.4 Implementation of CMC in Zero-Dimensional Model

4.4.1 Interfacing the Zero-Dimensional and CMC Codes

A combination of the CMC code with a zero-dimensional single-zone model was implemented following the method applied for CMC with multi-dimensional model (Kim & Huh 2002; Mastorakos & Wright 2003; Wright *et al.* 2009). The diagram of how the combined model works is shown in Figure 4.6. The zero-dimensional model solves the energy equation from equation (4.30). Then, the zero-dimensional model is used to determine the mean pressure in the chamber, as well as the following parameters: pressure rate of change $\partial p/\partial t$, the turbulent quantities (\tilde{k} and $\tilde{\varepsilon}$) and mean and conditional scalar dissipation rate, $\tilde{\chi}$ and $\langle N|\eta \rangle$ respectively. The pressure rate of change is obtained as discussed in Section 4.3.1.2. Cantera was used to determine the chemical reaction rate based on the current crank angle step at a constant volume. All these equations (conditional mass fraction and enthalpy and chemical source term) were solved simultaneously. Conditional temperature, Q_T , can then be obtained once the equation (4.79) is solved.

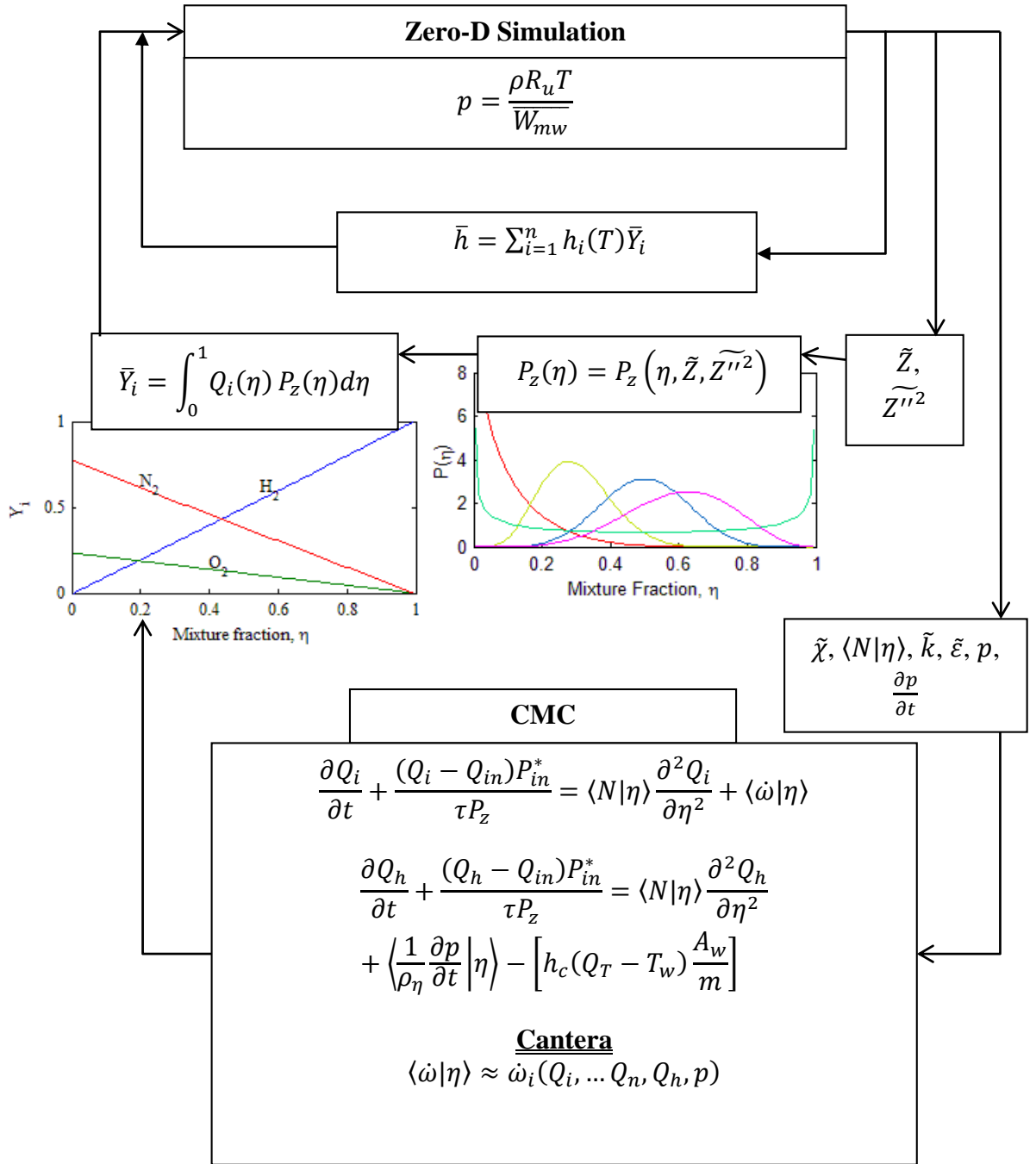


Figure 4.6 Coupling between CMC and zero-dimensional single-zone model.

At the beginning of the simulation, where the intake valve is in the closed position, only the zero-dimensional model is used without CMC mixing. This is due to the absence of mixing activity in the chamber, which contains only air: the fuel is introduced to the chamber when the intake valve is open. Once the intake valve is opened, the CMC mixing calculation begins. The effect of residuals are neglected in this study because the effect is very small for non-overlapped valves. Fiveland and

Assanis (2002) reported that the residual gas will be diluted back to a fresh mixture state during the intake process. Liu and Chen (2009) in their zero-dimensional modelling study also neglected the effect of burnt residuals. The effect of residuals can be considered if there is a big overlap between exhaust and intake valves and when the simulation is run for two or three engine cycles. Then, the temperature, pressure, conditional and mean mass fraction, conditional enthalpy and all the turbulent parameters between the intake manifold and combustion chamber are to be calculated. The CMC model will obtain pressure, pressure rate of change and the turbulent parameters from the zero-dimensional model. Equation (4.76) is used to obtain the mean quantities for the conditional mass fraction and enthalpy. These quantities are returned to the zero-dimensional model, which subsequently advances to the next time-step.

4.4.2 Numerical Solutions

This section discusses the numerical solution for the zero-dimensional model and the CMC equation. In the zero-dimensional model, a flow chart on how the code works is discussed. The discretisation involved in solving the CMC equation is also presented.

4.4.2.1 Zero-Dimensional Solution

A zero-dimensional model solves the first law of thermodynamics equations, as presented in equation (4.30). The numerical solution for the temperature change is straightforward because the equation is in the form of a first-order Ordinary Differential Equation (ODE). The equation was rearranged so that the change in temperature is on the LHS. Then, a stiff solver was used to solve equations (4.27) and (4.30) simultaneously. A flow chart of the model is presented in Figure 4.7.

The model was coded so that the simulation runs based on the value of CA, instead of the pre-defined process with pre-defined combustion, as done by Shaver *et al.* (2003), Bengtsson, Gafvert and Strandh (2004), Canova *et al.* (2005) and Killingsworth *et al.* (2006). A pre-defined or segregated process is where the simulation code is divided

according to the engine cycle: intake, compression, power and exhaust. Each cycle will use a different set of equations to obtain temperature or pressure change across the CA, which is based on the ideal gas law equation. Then, the ignition occurs based on the pre-defined ignition location with an estimated combustion duration, where the ignition delay has been measured according to the experiment. There is no detailed chemical reaction involved. For the simulation based on the value of CA, it uses the energy equation for the entire engine cycle to solve the temperature change in the chamber with detailed chemical reactions involved. This method gives an advantage in predicting the chemical reaction behaviour along the CA step, because the chemical reactions fully control the HCCI engines.

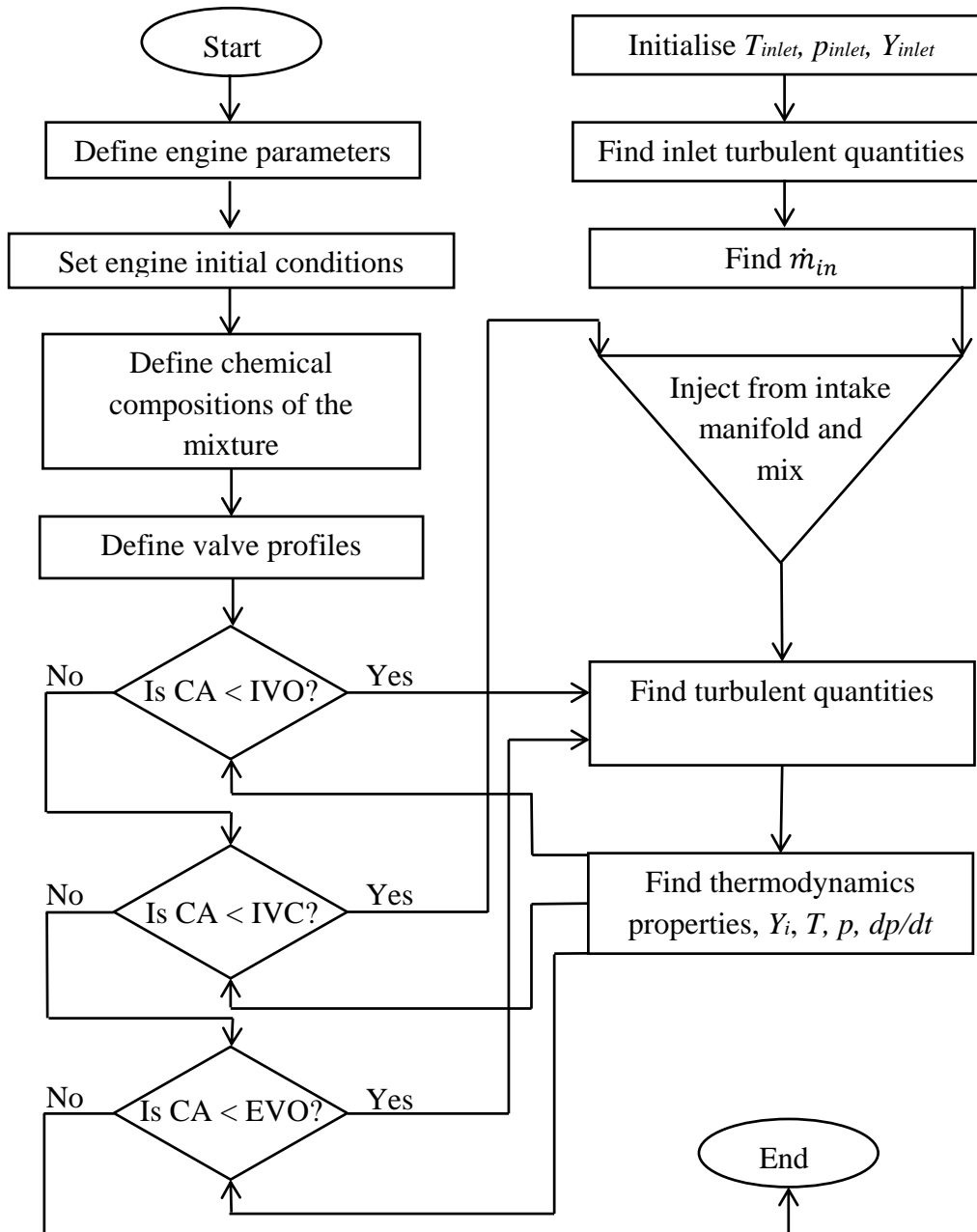


Figure 4.7 A flow chart for zero-dimensional single-zone model simulation

At the beginning of the simulation, the engine parameters and initial operating condition were defined, which were based on the experimental data. Then, the mixture composition in the combustion chamber and inlet manifold was initialised. It was assumed that the initial composition in the combustion chamber before IVO consists of only air and a mixture of air and fuel is introduced after the IVO. A typical valve profile was determined based on equation (4.17), which was used to represent the valve motion and also to get the inlet mass flow rate, \dot{m}_{in} .

The simulation began from 0°C, where the piston was at TDC, and finished at EVO. The entire simulation consists of three parts: before IVO, before IVC and before EVO, as shown in Figure 4.7. For the first part, the piston was in downward motion and the air was expanded before being mixed with the intake mixture. Once the intake valve was opened (second part), the air in the combustion chamber was mixed with the intake mixture. In this process, the mass was added to the combustion chamber based on equation (4.26). The cylinder volume was expanding and it is expected that the mixture temperature was decreasing at this stage. The final part is where the main combustion occurred, which was after IVC and before EVO. At this stage, the piston was in upward motion after IVC, compressing the gas mixture. The chemical kinetics plays an important role here as it will determine the start of combustion. Once the piston passes the TDC mark, it will be in downward motion again, expanding the mixture and the simulation stops at EVO. The simulation solves the energy and species equations, along with the turbulent transport equations for the entire process. Therefore, this technique has eliminated the segregated process as usually done in zero-dimensional modelling. Segregated process is where the simulation is divided into four parts in one engine cycle: intake, compression, expansion and exhaust. Thus, the simulation uses four different sets of equations to cater for each process. In this study, the simulation uses only one set of equations for all the processes. This ensures the in-cylinder properties are consistent from one process to another.

4.4.2.2 CMC Solution

A zero-dimensional CMC is used, which is zero-dimensional in physical space but dependent on the conserved scalar space. The CMC equation is stiff because of the presence of the chemical reactions, and thus a stiff solver is necessary to solve the equations. The CMC equations contain several partial differential equations (PDEs). To solve the CMC equations, the PDE is transformed into a number of ordinary differential equations (ODEs), in the form of $dy/dt = f(t, y)$. A fractional step method was then employed and a stiff ODE solver can be used to solve separately the stiff chemical reactions. The equation (4.75) for conditional mass fraction is separated as

$$\frac{\partial Q_i^{(1)}}{\partial t} = \langle N|\eta \rangle \frac{\partial^2 Q_i}{\partial \eta^2} \quad (4.99)$$

$$\frac{\partial Q_i^{(2)}}{\partial t} = \langle \dot{\omega}|\eta \rangle - \frac{(Q_i^{(1)} - Q_{in})P_{in}^*}{\tau P_z} \quad (4.100)$$

Similarly, equation (4.79) for conditional enthalpy is separated as the following:

$$\frac{\partial Q_h^{(1)}}{\partial t} = \langle N|\eta \rangle \frac{\partial^2 Q_h}{\partial \eta^2} \quad (4.101)$$

$$\frac{\partial Q_h^{(2)}}{\partial t} = \left\langle \frac{1}{\rho_\eta} \frac{\partial p}{\partial t} \middle| \eta \right\rangle - \left[h_c (Q_T^{(1)} - T_w) \frac{A_w}{m} \right] - \frac{(Q_h^{(1)} - Q_{in})P_{in}^*}{\tau P_z} \quad (4.102)$$

Equations (4.99) and (4.101) were solved using the implicit finite difference method (IFDM). The numerical implementation of the IFDM was second-order in mixture-fraction space and utilised an LU decomposition before back-substituting to determine the intermediate value, $Q^{(1)}$, that was the initial condition for solving equations (4.100) and (4.102). It can also be solved using the explicit finite difference method (EFDM), which has a simpler algorithm compared with IFDM. However, EFDM has a numerical stability issue, where the error at any stage of the computation could be amplified (Chapra & Canale 2006). The Courant-Friedrichs-Lewy (CFL) criterion must be satisfied, where the method is both convergent and conditionally stable when $CFL \leq 0.5$ (Carnahan, Luther & Wilkes 1969). For IFDM scheme, the method is stable at any CFL value, which is called unconditionally stable. The CFL criterion is defined as

$$CFL = \frac{\max(N_\eta) \Delta t}{(\Delta \eta)^2} \quad (4.103)$$

The errors of the solution do not grow but oscillate if the $CFL \leq 1/2$. Furthermore, if CFL is set to be $\leq 1/4$, this will ensure the solution will not oscillate and when $CFL \leq 1/6$, the truncation error is minimised (Carnahan, Luther & Wilkes 1969; Chapra & Canale 2006). In this thesis, $CFL \leq 1/6$ was used to ensure minimised truncation error and the numerical computations became unstable when the CFL was not controlled.

The fundamental difference between EFDM and IFDM is shown in Figure 4.8. For EFDM, the spatial derivative is estimated at time level t , giving it a single unknown to be solved explicitly, which is Q_{η}^{t+1} . IFDM, on the other hand, approximates the spatial derivatives at the advanced time level, $t+1$. Thus, when a discretised term is substituted back into its original PDE, it has several unknowns to be solved simultaneously. Even though IFDM has a complicated algorithm, it overcomes the stability issue from EFDM (Chapra & Canale 2006).

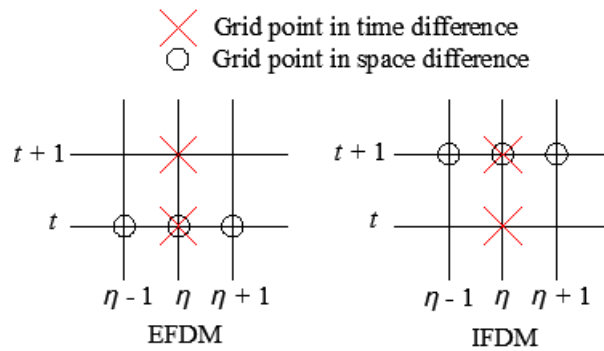


Figure 4.8 The fundamental difference between EFDM and IFDM (Chapra & Canale 2006).

Equations (4.99) and (4.101) can then be discretised using central finite-differences with second order accuracy as

$$\frac{Q_{\eta}^{t+1} - Q_{\eta}^t}{\Delta t} = \langle N|\eta \rangle \left[\frac{Q_{\eta+1}^{t+1} - 2Q_{\eta}^{t+1} + Q_{\eta-1}^{t+1}}{(\Delta\eta)^2} \right] \quad (4.104)$$

Rearranging equation (4.104) gives

$$Q_{\eta}^{t+1} - Q_{\eta}^t = \xi (Q_{\eta+1}^{t+1} - 2Q_{\eta}^{t+1} + Q_{\eta-1}^{t+1}) \quad (4.105)$$

where ξ is given by

$$\xi = \langle N|\eta \rangle \frac{\Delta t}{(\Delta\eta)^2} \quad (4.106)$$

Equation (4.105) is rearranged so that the reactive scalars at current time-step is on the RHS

$$-\xi Q_{\eta+1}^{t+1} + (1 + 2\xi)Q_{\eta}^{t+1} - \xi Q_{\eta-1}^{t+1} = Q_{\eta}^t \quad (4.107)$$

For n number of CMC bins, equation (4.107) can be transformed into a matrix form as

$$\begin{bmatrix} 1 & 0 & 0 & 0 & 0 \\ e_2 & f_2 & g_2 & 0 & 0 \\ 0 & \ddots & \ddots & \ddots & 0 \\ 0 & 0 & e_{n-1} & f_{n-1} & g_{n-1} \\ 0 & 0 & 0 & 0 & 1 \end{bmatrix} \begin{Bmatrix} Q_1^1 \\ Q_2^1 \\ \vdots \\ Q_{n-1}^1 \\ Q_n^1 \end{Bmatrix} = \begin{Bmatrix} Q_1^0 \\ Q_2^0 \\ \vdots \\ Q_{n-1}^0 \\ Q_n^0 \end{Bmatrix} \quad (4.108)$$

Where, $f = (1 + 2\xi)$ and $e = g = -\xi$. Then, equation (4.108) can be solved using the LU decomposition method, followed by back substitution. Once equation (4.108) was solved, a stiff solver was used to solve the remaining equations (4.100) and (4.102) simultaneously.

4.4.2.3 Chemical Kinetics Mechanism: Cantera

The chemical source term in equation (4.75) is the net production rate of the i th chemical species. Equation (4.100) was solved sequentially after equation (4.108), where the net production rate is obtained from Cantera (Goodwin 2003). Cantera is also used to evaluate the other properties such as thermodynamic and transport properties. Cantera is an open source software package for chemical kinetics mechanism and is widely used (Andrae 2011; Lee & Jeung 2009; Totton, Shirley & Kraft 2011; Votsmeier 2009). New researchers could easily adopt Cantera for their research needs given the software's capability to integrate with MATLAB, Fortran and Python languages.

The chemical kinetics mechanism files can be obtained in Chemkin format, where the file will then be converted to a Cantera-readable file. The use of a chemical reaction mechanism enables the study of the chemical species interaction, where the interaction is influenced by the temperature, pressure and species mass fraction. Furthermore, the chemical reaction mechanism would be able to give a better understanding in the combustion study.

4.4.3 Boundary Conditions

Boundary conditions for the simulation are discussed in this section, while the initial conditions for each different case will be discussed in different chapters, since they are case-specific. This section will discuss the boundary conditions of the CMC model, where the conditions is similar for each different test. For n number of bins of the CMC model, as depicted in Figure 4.9, the boundary was set at the first and last bins. For the first bin, it was filled with pure air in atmospheric quantity (O_2 is 21% of the mole fraction and N_2 is 79%), for both intake and combustion chamber. On the other hand, the n th bin was filled with fuel ($Y = 1$) at $\eta = 1$. This type of boundary condition was chosen because of the assumption that the fuel and air remain as distinct volumes until mixing is almost complete. The dissociation effect of changing the species can be neglected during the intake and compression processes, as suggested by Heywood (1988), because the dissociation occurs at a sufficiently high temperature. The temperature at the beginning of the simulation is low (less than 1000 K). The boundary conditions for the conditional enthalpy transport equation were set based on the values of the temperature and pressure at the start of each time step. Hence, this boundary varies over time (as the piston moves). Then, the mixing state in each bin is controlled by the CMC transport equations.

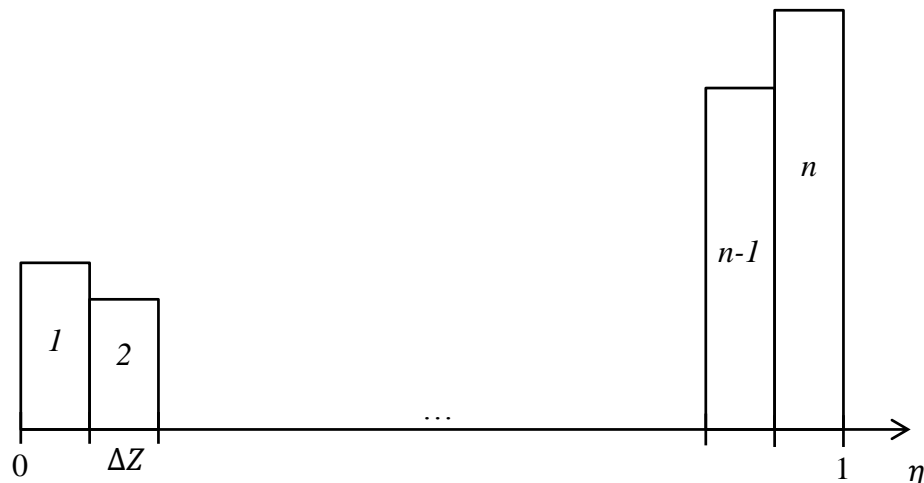


Figure 4.9 Bin configuration of the CMC model

The boundary condition of the β -function PDF is also set at the first and last bins. For the first bin, the β -function PDF is as follows,

$$P_{z_1} = \frac{\text{CDF}_\beta[(\eta = \Delta Z), \alpha, \beta]}{\Delta Z} \quad (4.109)$$

while for the last bin, the β -function PDF is given by

$$P_{z_n} = \frac{1 - \text{CDF}_\beta[(\eta = 1 - \Delta Z), \alpha, \beta]}{\Delta Z} \quad (4.110)$$

where $\text{CDF}_\beta(X, A, B)$ is the β -function cumulative distribution function at a location X given the corresponding parameter A and B , which are governed by the \tilde{Z} and Z''^2 , which were set according to the AFR of the test condition. By definition, the CDF is

$$\text{CDF} = \int P_z(\eta) d\eta \quad (4.111)$$

Equations (4.109) and (4.110) are used because a discrete representation of a β -function PDF cannot capture the full probability contained in the tails when the PDF at the bounds tends to infinity: this deficiency grows with increasing bin size. By capturing the full probability contained in the boundary bins, the integral of the PDF throughout the entire domain is 1.

4.5 Conclusion

This chapter has discussed the methodology used in developing the simulation model. It begins with the single-zone zero-dimensional model, where the model assumed that the entire combustion chamber is homogeneous. Then, the model was further improved to a quasi-dimensional model with the addition of the turbulence model: the energy cascade method was used. In the quasi-dimensional model, the heat loss to the cylinder wall was influenced by the turbulence model, instead of using a pre-defined

Chapter 4

heat loss model. Both models for zero- and quasi-dimensional models employed a chemical reaction mechanism, where the properties of the species was obtained from the Cantera software package with a MATLAB interface.

After that, a formulation for the CMC with zero-dimensional model was discussed, together with its sub-models for the unclosed terms. Then, the CMC was combined with the zero-dimensional model, where the interface between the CMC and zero-dimensional model was discussed in Section 4.4.1. The solution to the model was also discussed, along with its boundary conditions.

Chapter 4

Chapter 5

VALIDATION OF CMC MODELS

5.1 Introduction

This chapter will validate the zero-dimensional and CMC models against the experimental data from the literature. The ability of the model to predict the in-cylinder pressure over a range of engine conditions, including intake temperature, AFR and compression ratio is also discussed. Two experimental data sets were used for validation purposes: one is the HCCI engine fuelled with diesel and the other with gasoline. Because two types of engine configurations were used, the models used two different types of chemical reaction mechanism to model the fuels. This is to ensure that the model works in both engine conditions.

This chapter consists of two parts. Part 1 will discuss the validation of the models against the experimental data using diesel, which covers up to Section 5.5. Section 5.1 concludes with the chemical reaction mechanism used for both models, followed by the experimental data of the engine in Section 5.2. Section 5.3 validates the zero-dimensional model against the experiment, which also discusses the heat loss model to be used in an HCCI engine. The validation of the combined model of the CMC and zero-dimensional together with its performance against different engine parameters will be discussed in Sections 5.4 and 5.5 respectively. Part 2, discusses the validation of the combined model against the experiment using gasoline fuel, and contains two sections. Section 5.6 discusses the engine details used for the validation and Section 5.7 discusses the validation work. The chapter ends with the conclusion in Section 5.8.

5.1.1 Chemical Reactions Mechanism for n-Heptane

A chemical reaction mechanism is used to solve the chemical reactions during combustion. For diesel fuelled HCCI engines, a reduced *n*-heptane mechanism (Seiser *et al.* 2000) was used to simulate the diesel combustion. This was chosen because *n*-heptane's chemical properties are similar to those of conventional diesel in terms of the cetane number (Maroteaux & Noel 2006). In addition, *n*-heptane as a diesel surrogate fuel has been widely used by many researchers (Hernandez *et al.* 2008; Pitz & Mueller 2011; Westbrook, Pitz & Curran 2006). The mechanism consists of 160 species and 770 elementary reactions. The mechanism was then used in the Cantera chemical kinetics software package (Goodwin 2003) to obtain the chemical properties and reactions mechanisms.

5.1.2 Chemical Reactions Mechanism for Gasoline

Commercial grade gasoline consists of a blend of many chemical species (Westbrook *et al.* 2009). Most of the gasoline contents are distilled from crude oil, which is then upgraded in the refinery to improve the octane rating by blending with other chemicals (Pitz *et al.* 2007). The content of gasoline in the market varies from one brand to another, in order to meet a stringent regulations regarding fuel volatility, octane number, stability and other product quality parameters (Chevron 1996; Pitz *et al.* 2007). In this study, a reduced gasoline mechanism was used as a surrogate fuel for gasoline, which was developed by Chalmers University of Technology (Golovitchev 2003). The hundreds of hydrocarbons in gasoline are represented by the blends of *n*-paraffins, *iso*-paraffins and aromatics, where they are modelled using *n*-heptane, *iso*-octane and toluene, respectively (Lee, Kim & Min 2011). Thus the mechanism used in this study was chosen to have the blends of 54% *iso*-octane, 24% toluene and 22% *n*-heptane by liquid volume, because this composition has been validated as having a similar ignition delay time compared with commercial gasoline (Lee, Kim & Min 2011; Lee & Min 2009). The selected reduced mechanism consists of 119 species and 621 reactions. More detailed gasoline mechanisms are available in the literature, such as those developed by Mehl *et al.* (Mehl, Chen, *et al.* 2011; Mehl, Pitz, *et al.* 2011).

In the past, the gasoline surrogate was only modelled using *iso*-octane, *n*-heptane or a mix of the two (Curran *et al.* 1998, 2002; Pitz *et al.* 2007). The gasoline surrogate has only more recently been modelled using a more complicated mechanism as discussed above. Hence it is necessary to validate the gasoline surrogate. Unlike *n*-heptane, which many people already use as a diesel surrogate fuel in diesel HCCI engines, a gasoline reduced mechanism is quite new in the literature. The validation for the reduced gasoline mechanism is shown in Figure 5.1, where the ignition delay time for the reduced gasoline mechanism is in agreement with a more detailed mechanism. The detailed mechanism used in the validation consists of 874 species and 3796 elementary reactions, while 119 species and 621 reactions are used in the reduced mechanism. The validation was completed at stoichiometric conditions and pressure of 1 MPa. The equivalence ratio used in the validation is almost similar to the experiment in this study using a gasoline fuelled HCCI engine. The ignition delay time for both mechanisms agrees well with the experiment. A reduced mechanism was chosen in this study because according to the validation in Figure 5.1, the ignition delay time is comparable to a more detailed mechanism. By using reduced mechanism, the computational resources can be minimised without sacrificing the ignition delay time accuracy.

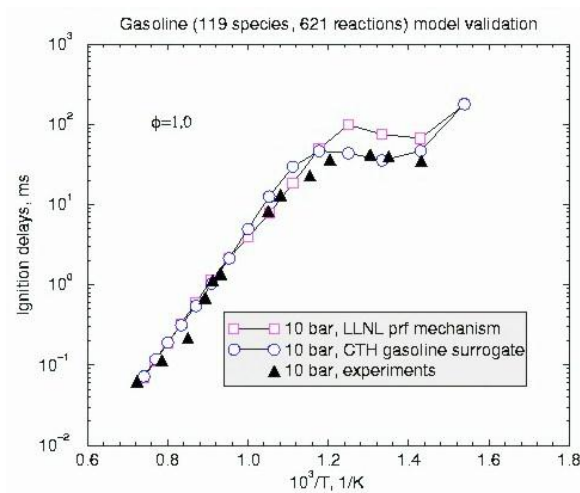


Figure 5.1 A validation for reduced gasoline mechanism used in this study (Golovitchev 2003). LLNL prf is a detailed gasoline mechanism from Lawrence Livermore National Laboratory. CTH is a reduced gasoline mechanism from Chalmers University of Technology.

PART 1: DIESEL HCCI

5.2 Experimental Data

Part 1 of this chapter discusses the validation of CMC and zero-dimensional models against the experiment of a diesel fuelled HCCI engine. The experimental data from Guo *et al.* (Guo *et al.* 2010) was used as a validation tool, where the diesel was port injected at the intake manifold. Then the intake temperature was increased to 40°C or 313K. The details of the engine used in this study is shown in Table 5.1.

Table 5.1 Engine parameters used in the simulation of a diesel fuelled HCCI engine (Guo *et al.* 2010)

Cylinder bore	82.55 mm
Stroke	114.3 mm
Connecting rod length	254 mm
Compression ratio	10
Engine speed	900 rpm
Inlet pressure	95 kPa
Inlet valve open (IVO)	10°CA ATDC
Inlet valve closed (IVC)	36°CA ABDC
Exhaust valve open (EVO)	40°CA BBDC
Exhaust valve closed (EVC)	5°CA ATDC
Wall Temperature (K)	530
AFR	50

5.3 Zero-Dimensional Single-Zone Model

This section will discuss the validation of the zero-dimensional single-zone model without CMC. The difference in the models for the heat transfer coefficient, h_c , used in equation (4.34) is also discussed, where all coefficient models (Woschni, modified Woschni and Hohenberg) have been widely used in the HCCI engine simulation (Bengtsson, Gafvert & Strandh 2004; Chang *et al.* 2004; Guo *et al.* 2010; Komninou & Kosmadakis 2011; Kwon *et al.* 2011; Seo *et al.* 2010; Soyhan *et al.* 2009). Thus, the performance of those heat transfer coefficient models used in the area of HCCI engines was investigated in order to match with the zero-dimensional environment in this study.

5.3.1 Validation

The diesel in this study was injected at the intake manifold and the mixing effect must be taken into consideration. For the zero-dimensional model, the intake air temperature was set 20K higher than the actual temperature to account for the mixing effects (Guo *et al.* 2010). A different study also stated that the intake temperature for a single-zone model has to be increased up to 30K, while up to about 10K for a multi-zone model (Bunting *et al.* 2008). The assumption of uniform wall temperature for the entire engine cycle, uniform in-cylinder temperature and pressure, and a potential limitation of the chemical chemistry as well may contribute to the adjustment of the intake temperature (Guo *et al.* 2010). The wall temperature for this case, on the other hand, was estimated at 530 K, which is in reasonable agreement with 500 K from De Paola *et al.* (2008) using a diesel setup. Further justification for wall temperature selection will be discussed in Section 5.4.1. The wall temperature value was obtained by comparing the simulation result with experiment, where the intake temperature was set according to Guo *et al.* (2010). In this study for the zero-dimensional model using *n*-heptane, the intake temperature was increased to 333K from the actual experimental intake temperature of 313K.

The result is compared with the experiment, as shown in Figure 5.2, where it is also compared with another zero-dimensional single-zone model from Guo *et al.* (2010). The results show that both zero-dimensional models predict higher in-cylinder pressure compared to the experiment, with the zero-dimensional model from Guo *et al.* (2010) over-predicting by a greater amount. The predicted maximum in-cylinder pressure is evidently slightly higher than that of the experiment due to the limitation of the zero-dimensional model, where the entire combustion chamber is assumed to be homogenous. Overall, the combustion phasing is in good agreement with the experimental data, demonstrating that the zero-dimensional single-zone model can be used in HCCI engine simulations.

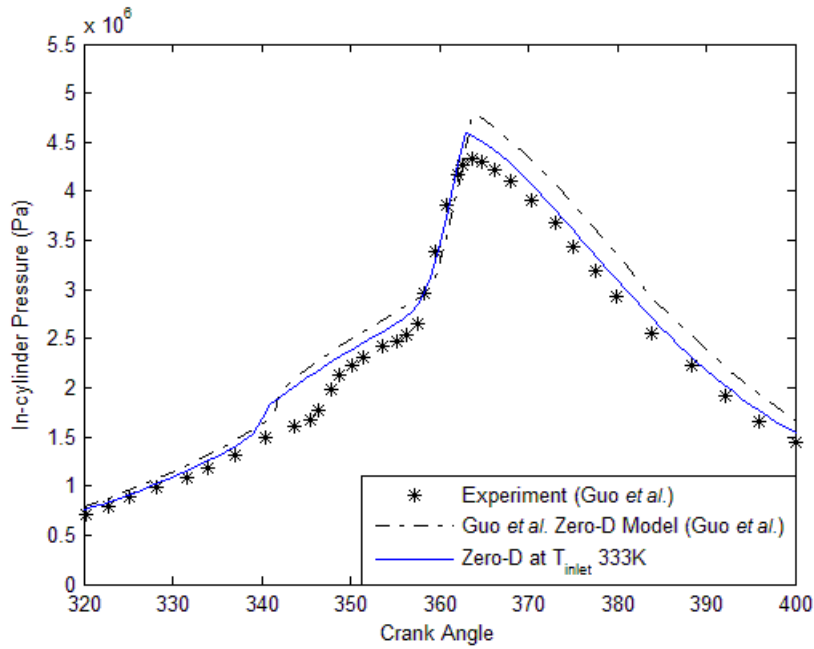


Figure 5.2 Comparison between zero-dimensional model (with modified Woschni heat transfer coefficient model) with experimental data and another single-zone model (Guo *et al.* 2010). CR=10.0, N=900 rpm, $T_{in}=40^{\circ}\text{C}$, $P_{in}=95$ kPa, AFR=50.

5.3.2 Heat Transfer Coefficient Models

In equation (4.34), a heat transfer coefficient model, h_c , is used in the zero-dimensional single-zone model, where the coefficient model attempts to reproduce the heat loss obtained from experiments. The effects of different heat transfer coefficient models are discussed, where the models used are the Woschni correlation (Bengtsson, Gafvert & Strandh 2004; Woschni 1967), modified Woschni correlation for HCCI engines (Chang *et al.* 2004), and Hohenberg correlation (Hohenberg 1979; Sanli *et al.* 2008; Zeng & Assanis 1989).

The Woschni heat transfer coefficient uses bore, B , as the characteristic length and mean piston speed, \overline{S}_p , as the characteristic velocity:

$$h_c = 129.8B^{-0.2}p^{0.8}T^{-0.55}(2.28\overline{S}_p)^{0.8} \quad (\text{W/m}^2\text{K}) \quad (5.1)$$

A modified Woschni correlation has been developed for HCCI engines where the measurements of the heat flux were taken in the piston crown and cylinder head areas (Chang *et al.* 2004). The equation then becomes

$$h_c = \alpha_{scaling} L^{-0.2} p^{0.8} T^{-0.73} (v_{tuned})^{0.8} \quad (\text{W/m}^2\text{K}) \quad (5.2)$$

where the characteristic velocity v_{tuned} is

$$v_{tuned} = C_1 \overline{S_p} + \frac{C_2}{6} \frac{\mathcal{V}_d T_r}{P_r \mathcal{V}_r} (p - p_{mot}) \quad (5.3)$$

The modified Woschni equation uses the instantaneous chamber height, L , as the characteristic length scale; the temperature exponent is changed to 0.73, and $\alpha_{scaling}$ is the scaling factor to fit the experimental data. In equation (5.3), $C_1 = 2.28$ and $C_2 = 0.00324$ are constants, \mathcal{V}_d is the displacement volume, subscript r is the reference condition, and p_{mot} is the motoring pressure: the cylinder pressure without combustion.

The Hohenberg correlation, on the other hand, includes some modifications to the Woschni equation, where it uses instantaneous cylinder volume instead of bore. In addition to that, the characteristic velocity is replaced with the effective gas velocity, and the temperature exponent has also changed. The Hohenberg correlation is

$$h_c = 130 p^{0.8} T^{-0.4} \mathcal{V}^{-0.06} (\overline{S_p} + 1.4)^{0.8} \quad (\text{W/m}^2\text{K}) \quad (5.4)$$

In equations (5.1), (5.2) and (5.4), SI units are used for all variables (B in m, T in K, \mathcal{V} in m^3 , S_p and v in m/s) except for p , the instantaneous in-cylinder pressure, which is in bars. The difference in heat transfer correlations leads to varying predictions regarding heat loss. Therefore, the combustion behaviour is also changed with different heat coefficients. The changes become significant in HCCI engines, where chemical kinetics plays a major role in combustion.

The in-cylinder pressure is predicted differently when using different heat transfer coefficient models, as shown in Figure 5.3 (left). Both the Woschni and Hohenberg models over-predicted the combustion phasing by having an advanced ignition about 5°CA earlier than the experiment did. The modified Woschni equation, on the other

hand, agreed well with the experiment despite having a slightly higher maximum in-cylinder pressure compared with the experiment.

In a diesel HCCI engine, the fuel has a characteristic of two-stage ignition, which are low temperature reaction (LTR) and high temperature reaction (HTR) (Kim & Lee 2007; Neely, Sasaki & Leet 2004). LTR, also called the cool flame phenomenon, occurs at a temperature below the auto-ignition temperature. The LTR region was found to be advanced by about 10°CA compared to the experiment for all heat transfer coefficient models. The LTR region occurred at approximately 800K, which is the same as reported by Kim and Lee (2007), where they studied experimentally the effect of narrow spray angle of a diesel fuelled HCCI engine. The HTR region, on the other hand, begins at about 1000K, as shown in Figure 5.3 (right). This is in agreement with other studies (experimentally and numerically), where the HTR region began at about 900–1050K (Epping *et al.* 2002; Kim & Lee 2007; Zheng *et al.* 2001) .

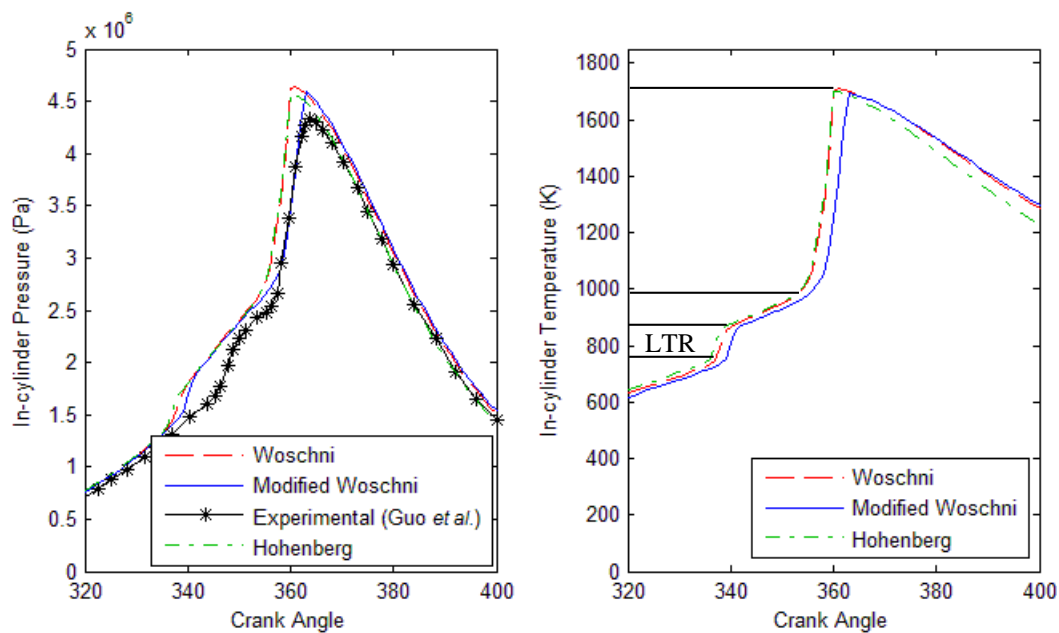


Figure 5.3 Combustion phasing for different heat transfer coefficient models showing high temperature region (HTR) and low temperature region (LTR). In-cylinder pressure on the left and temperature on the right for different heat transfer coefficient models.

5.3.2.1 Heat Fluxes

The history of the heat loss, dQ_h/dt and the heat transfer coefficient, h_c among all models is shown in Figure 5.4, where the maximum values of the heat transfer coefficient vary from 303 to 880 W/m²K. The difference in this value is due to a difference in the scaling factor, velocity characteristic, and temperature exponent. The Hohenberg equation has the highest value of the heat transfer coefficient, which causes it to have the highest heat loss, as in Figure 5.4 (left).

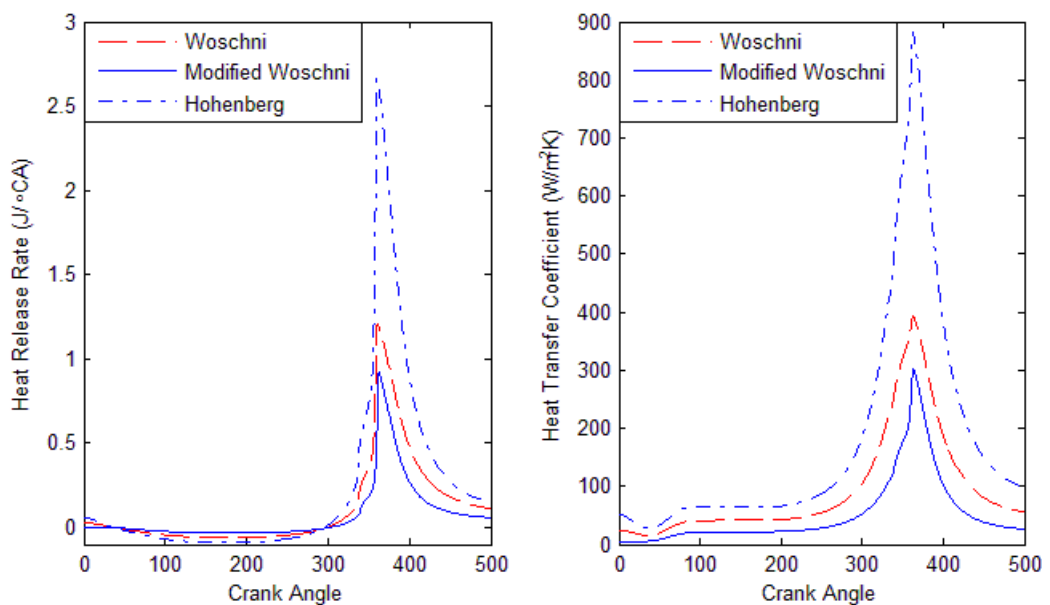


Figure 5.4 Heat release rate (left) and heat transfer coefficient (right) comparison among Woschni, modified Woschni and Hohenberg models.

The heat transfer coefficient traces were changed when the same scaling factor ($\alpha_{scaling}=194.7$) was used for all models, as shown in Figure 5.5. The Hohenberg correlation has the highest heat transfer coefficient compared with the other two models as a result of the difference in the temperature exponent used in the model. The heat flux decreases when the piston is in a downward motion, and during the intake process, the heat flux is minimal. This indicates that the heat loss is minimal due to a small different between in-cylinder and wall temperatures during the intake process. However, the heat flux increases when the piston is in the compression process. A high heat transfer coefficient causes too much heat loss to the cylinder wall, and this shows

that the Hohenberg model causes too much energy to be wasted when the piston is at TDC. Therefore, a high scaling factor is not suitable for the Hohenberg model.

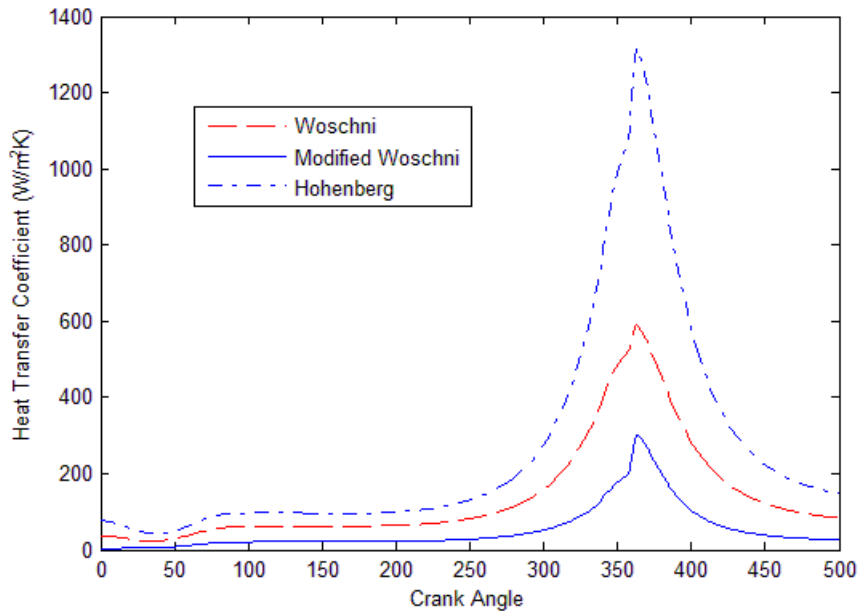


Figure 5.5 Comparison of heat transfer coefficient with same scaling factor.

Improper characteristic velocity causes incorrect heat loss to the cylinder wall as well. The piston is in a downward and upward motion, so the piston's instantaneous velocity is not the same across the crank angle ranges. The instantaneous piston speed is at its minimum when the piston is at TDC and BDC, and it is at its maximum when the piston is in the middle of the stroke. Therefore, in this case, the characteristic velocity could be different across the stroke range. However, the Voschni and Hohenberg models assume that the characteristic velocity is constant for all of the crank angle ranges, as shown in Figure 5.6. The modified Voschni equation, on the other hand, uses a different approach, where the characteristic velocity varies across the engine cycle.

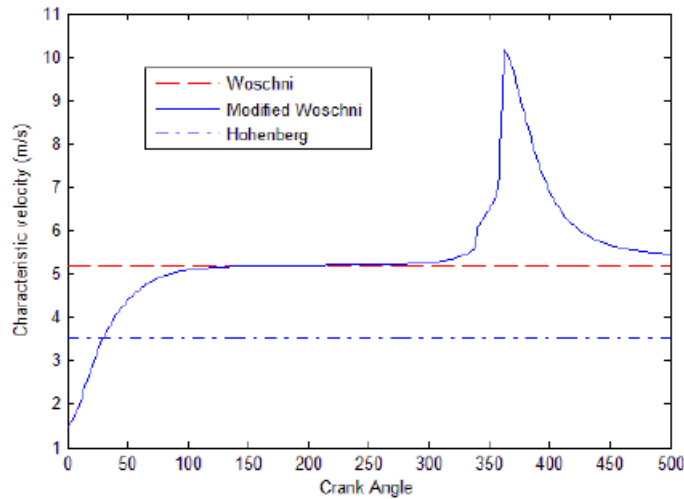


Figure 5.6 Comparison of characteristic velocity between the Woschni, modified Woschni, and Hohenberg models.

5.3.2.2 Heat Transfer Behaviour of Different AFR

A diesel HCCI engine operates in a lean condition, where the actual AFR is greater than the stoichiometric AFR of 14.5. In a high-load operation, the AFR is reduced toward the rich zone, while the AFR is higher when the engine is in a low load. Heat loss effects for all models were tested with varying AFRs. Both the Woschni and Hohenberg models yielded slightly lower in-cylinder pressure compared with the modified Woschni equation for both different AFRs, as shown in Figure 5.7.

The LTR region is advanced for both the Woschni and Hohenberg models and subsequently for the main combustion (HTR) region. A high heat transfer coefficient for the Woschni and Hohenberg models, as shown in Figure 5.8, leads to more energy loss from the combustion chamber. The modified Woschni equation agreed well with the experiment, which produced a more accurate result compared with the other two models and could be used for further analysis of HCCI engines. More tuning is required for Woschni and Hohenberg models in order to achieve a desirable result. Therefore, a modified Woschni equation for the convection heat loss was used for the rest of the simulations.

Chapter 5

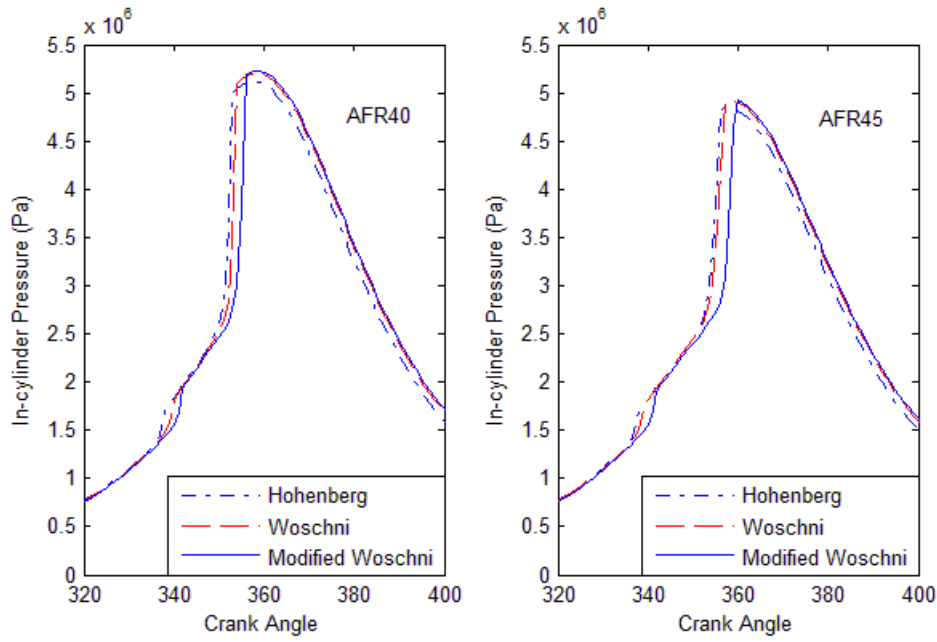


Figure 5.7 In-cylinder pressure comparison with different AFRs and different heat transfer coefficient models, CR=10.0, N=900 rpm, $T_{in}=40^{\circ}\text{C}$, $P_{in}=95\text{ kPa}$.

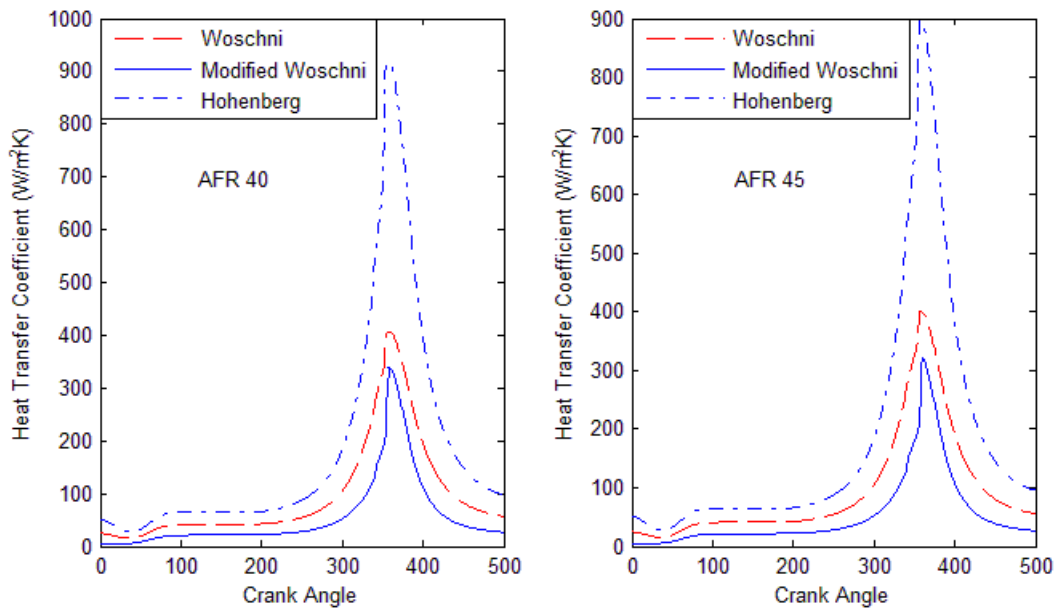


Figure 5.8 Heat release rate comparison with varying AFRs and different heat transfer coefficient models, CR=10.0, N=900 rpm, $T_{in}=40^{\circ}\text{C}$, $P_{in}=95\text{ kPa}$.

5.4 CMC with Zero-Dimensional Model

This section will discuss the performance of the combined model between CMC and zero-dimensional models in a diesel fuelled HCCI engine. The combined model in this thesis is called CMC, while the standalone zero-dimensional model without CMC is called zero-dimensional. A comparison of the CMC with the experiment and zero-dimensional model is discussed. The turbulent behaviour in the chamber is also discussed and then followed by the characteristics of the CMC model.

5.4.1 Boundary and Initial Conditions

In this study, the boundary condition for air (in mole fraction) was set to 79% nitrogen (N_2) and 21% oxygen (O_2) at $\eta = 0$ and 0% for both N_2 and O_2 at $\eta = 1$. These correspond to conditional mass fractions of $\langle Q_{N_2} | \eta = 0 \rangle = 0.7671$, $\langle Q_{O_2} | \eta = 0 \rangle = 0.2329$ and $\langle Q_{N_2} | \eta = 1 \rangle = 0$, $\langle Q_{O_2} | \eta = 1 \rangle = 0$. For the fuel, the mass fraction is $\langle Q_{C_7H_{16}} | \eta = 0 \rangle = 0$ and $\langle Q_{C_7H_{16}} | \eta = 1 \rangle = 1$. The mass fraction of the mixture was then initialised in the intake manifold by using linear interpolation between $\eta = 0$ and $\eta = 1$, as shown in Figure 5.9 (the frozen limit). The initial conditions for \bar{Z}_0 and $\overline{Z''_0^2}$ at the inlet valve are, 0.0196 and 0.0192 respectively. On the other hand, both \bar{Z}_0 and $\overline{Z''_0^2}$ in the chamber are 0. As for the inlet pressure and temperature, the initial conditions are $P_0 = 95$ kPa and $T_0 = 313$ K.

The wall temperature, T_w was set to be 530K for a CI engine (Zheng, Zhang & Zhang 2005). However, the wall temperature used in the numerical studies varies from one engine to another (Jia, Xie & Peng 2008; Komninos, Hountalas & Kouremenos 2004; Komninos, Hountalas & Kouremenos 2005; Soyhan *et al.* 2009; Wang, Z. *et al.* 2006; Zheng, Zhang & Zhang 2005), where the wall temperature ranges from 293K (Barroso, Escher & Boulouchos 2005) to approximately 800K (Soyhan *et al.* 2009). The exhaust temperature and pressure were approximated at 1000K and 101.3kPa, respectively (Heywood 1988), where the approximated value is close to measurement of a diesel engine (Zhou, Zhou & Clelland 2006).

At the beginning of the simulation, where CA is less than IVO, the mixture composition in the chamber was assumed to be only air with no fuel. The fuel is being introduced into the chamber during the IVO period, where the fuel quantity is based on the AFR used in the experiment.

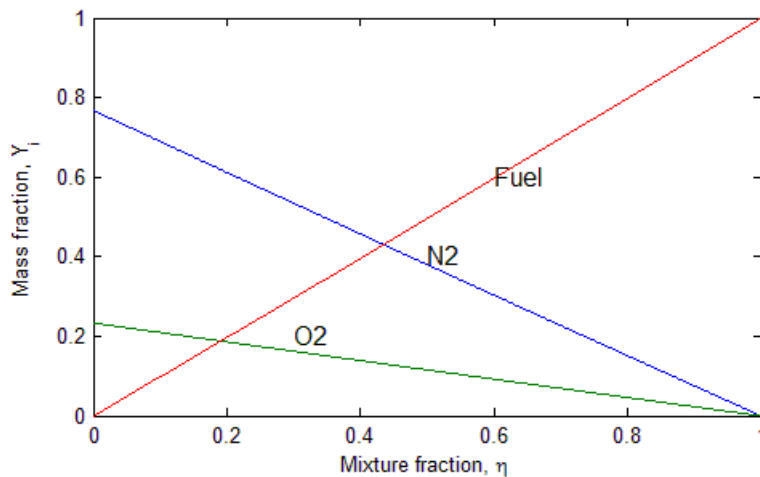


Figure 5.9 Initial condition of the air-fuel mixture in the intake manifold.

5.4.2 Comparison with Experiment

The CMC with zero-dimensional model was studied using the same engine operating conditions as discussed in Section 5.2. The result shown in Figure 5.10 is a comparison between the experiment (Guo *et al.* 2010), the zero-dimensional model from Guo *et al.* (2010), the zero-dimensional model without CMC and CMC with zero-dimensional model. The result shows that the CMC with zero-dimensional model is in good agreement with the experiment. The model predicted the LTR and HTR points close to those found in the experiment. However, the model predicts lower in-cylinder peak pressure. This behaviour is similar to that observed when modelling a zero-dimensional CMC in a diesel engine, where the result was improved when implementing CMC in a multi-dimensional simulation (Figure 5.11) (Wright 2005). The lower in-cylinder peak pressure could be due to the low number of CMC bins, homogenous assumptions of the combustion chamber temperature and pressure,

constant wall temperature for the whole engine cycle or the limitations of the reduced chemical kinetics mechanism.

The advantage of using CMC in a zero-dimensional model in this study is that the model does not require the increase in intake air temperature that a zero-dimensional model needs. Instead, the model uses the actual experimental intake temperature, which is 313K. The result shown in Figure 5.10 was using the intake temperature of 313K for CMC compared to 333K for zero-dimensional alone, where both of them yield a very similar HTR point.

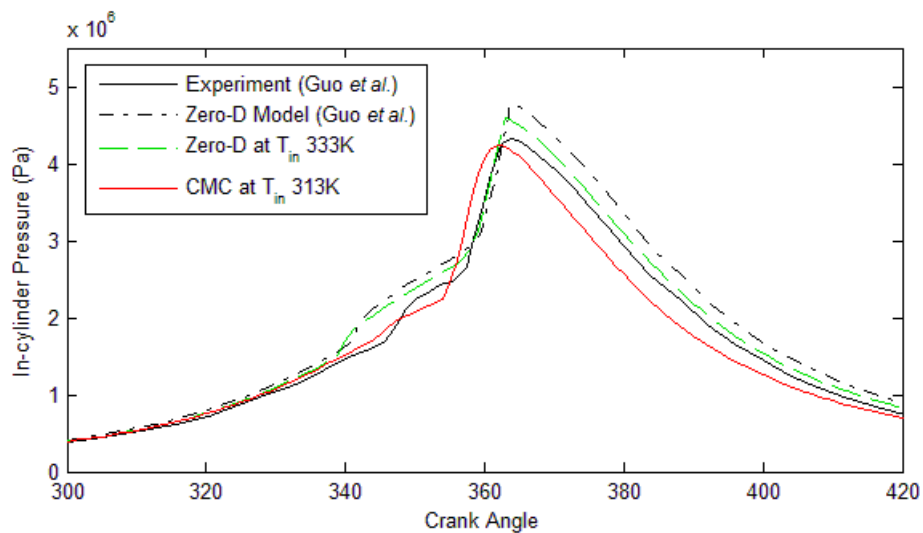


Figure 5.10 Comparison of the in-cylinder pressure between experiment (Guo *et al.* 2010), zero-dimensional model from Guo *et al.* (2010), zero-dimensional model without CMC and CMC with zero-dimensional model.

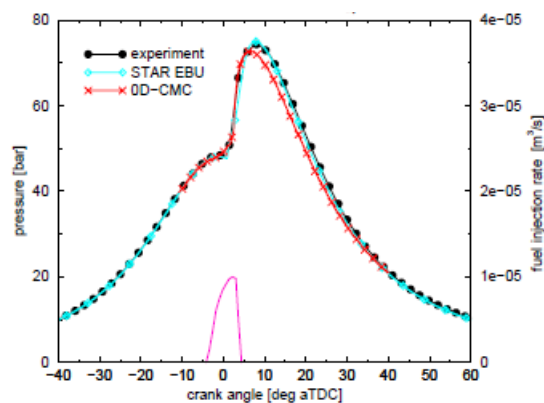


Figure 5.11 Zero-dimensional CMC and a multi-dimensional simulation (STAR EBU) compared with experiment (Wright 2005)

To test the sensitivity of the intake temperature, Figure 5.12 shows the CMC model with the same intake temperature as the zero-dimensional model, which is 333K: the combustion is advanced by about 10°CA. This is expected from actual engine operation: combustion is advanced when the intake temperature increases. The zero-dimensional model, on the other hand, predicted that auto-ignition failed to occur when the intake temperature was set to be the same as the experimental data. Thus, it is necessary to fine tune the intake temperature before the zero-dimensional model can be used, while the CMC model can be used without any artificial alteration of the input parameters. The CMC model in a zero-dimensional simulation predicts the timing of key events with a known under-prediction of pressure, thus this model can be used for further analysis.

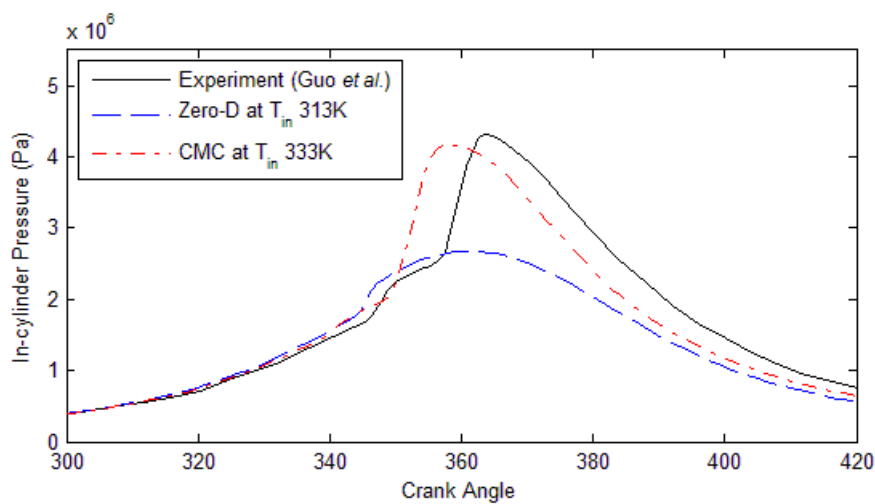


Figure 5.12 Combustion behaviours when the intake temperature was changed for both models.

5.4.3 Turbulence Interactions

A turbulence model was used in modelling the CMC and is important to understand the turbulence behaviour in the chamber. Low in-cylinder pressure when using CMC compared to zero-dimensional alone could be due to the turbulence effects in the combustion chamber. In the zero-dimensional model, the mixture was assumed to be homogenous and therefore no turbulence effect was involved. The CMC model, on the other hand, uses a turbulence model to account for the molecular mixing rate, where

the mixing rate is proportionally related to the ratio of turbulent dissipation rate and turbulent kinetic energy. Thus, in the CMC model, combustion is influenced by the turbulence-chemistry interactions.

Because the engine was simulated from the IVO, the turbulence effects due to the fluid flowing through the intake valve must be taken into consideration. The intake mass flow rate and piston speed pattern across the entire CA are shown in Figure 5.13, where the flow rate is at its maximum when the valve is nearly at the maximum opening. At this condition, the mixture flows in faster. Hence, the mean kinetic energy increases and reached the peak at approximately the maximum intake valve opening, as shown in Figure 5.14. Then, the mean kinetic energy is gradually decreasing when the intake valve is closing and the decrease rate is faster when the piston is approaching TDC in the compression stroke. The turbulent kinetic energy and dissipation rate begin to increase when the mean kinetic energy is decreasing.

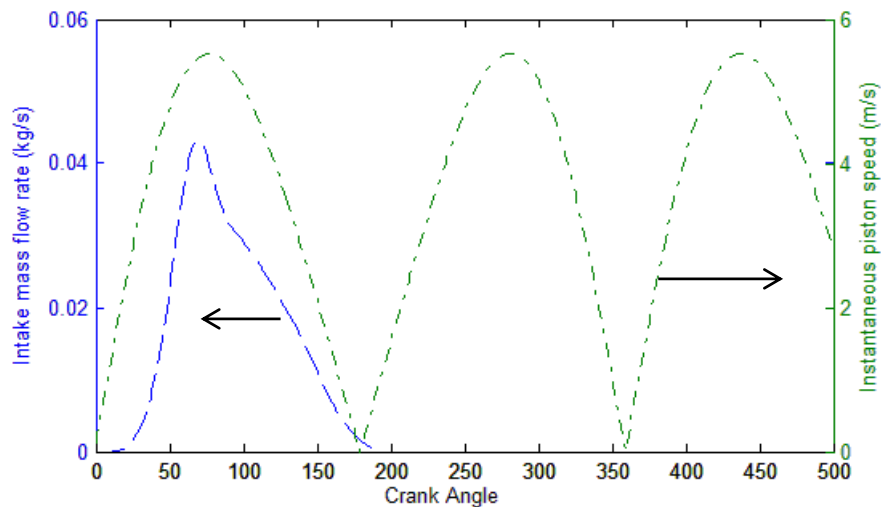


Figure 5.13 Intake mass flow rate and piston speed pattern for the simulated engine. CR=10.0, N=900 rpm, $T_{in}=40^{\circ}\text{C}$, $P_{in}=95\text{ kPa}$, AFR=50

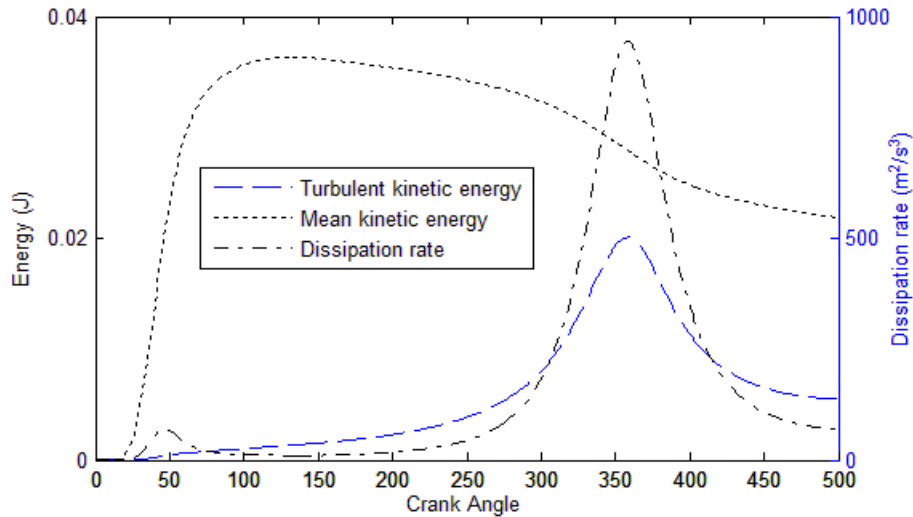


Figure 5.14 The difference in mean kinetic energy, turbulent kinetic energy and turbulent dissipation rate across the crank angle cycle.

The energy cascade method used in the turbulent model converts the mean kinetic energy to the turbulent kinetic energy via turbulent dissipation. The loss in mean kinetic energy is described by the increase of the turbulent kinetic energy, which shows the conversion between those energies. The turbulent kinetic energy is increased during the compression stroke because of the effect of RDT in the turbulence model. According to Borgnakke, Arpaci and Tabaczynski (1980), the RDT effect can generate turbulence during compression due to the compressibility effect. Hence, the turbulent kinetic energy is at its maximum at the end of the compression stroke. The turbulence starts to decay when the piston is in the power stroke. The effect of turbulence would justify the molecular mixing rate in the CMC model, which will be discussed in the next section.

5.4.4 CMC Characteristics

5.4.4.1 Independence Test: Effects of Different C_D

The value of C_D in equation (3.47) is case-specific and according to Kim (2004), this constant should be large enough to reproduce fast mixing. Thus, this constant will be tested for each of the different engine models. For the *n*-heptane fuelled HCCI engine, the test was using the engine setup by Guo *et al.* (2010) and the number of bins of the

CMC model was set to 100 to reduce the time taken to complete the test. Figure 5.15 shows the in-cylinder pressure trace between the experiment and CMC model with varying C_D , where $C_D = 2.5$ shows a better result compared to 2.0 and 3.0. When $C_D = 3.0$, the in-cylinder peak pressure is slightly lower than $C_D = 2.5$. $C_D = 2.0$ shows the lowest in-cylinder peak pressure. This is because different value of C_D affects the scalar variance, where the variance decreases when C_D is increased, as shown in Figure 5.16 (right). This is because the mean scalar dissipation rate (SDR), which governs the mixing rate in the mixture, is proportional to C_D . The mean SDR is the highest for the highest C_D value until the significantly reduced variance reverses this behaviour, as shown in Figure 5.16 (left), when the combustion is about to occur after 300°CA . Hence, a different level of mixing rate will then affect the in-cylinder pressure. The comparison between Figure 5.15 and Figure 5.16 also shows that there is an optimal value for C_D to achieve optimal combustion phasing that is close to the experiment, where C_D directly affects the mixing rate in the mixture. When comparing the oxidisers and fuel behaviour over the entire simulation, as shown in Figure 5.17, $C_D = 2.0$ yields inconsistent O_2 consumption during the main combustion, while $C_D = 3.0$ shows a slight increase in N_2 when the simulation is nearly finished. Thus, $C_D = 2.5$ for the *n*-heptane case was chosen for the study and can be used for further analysis.

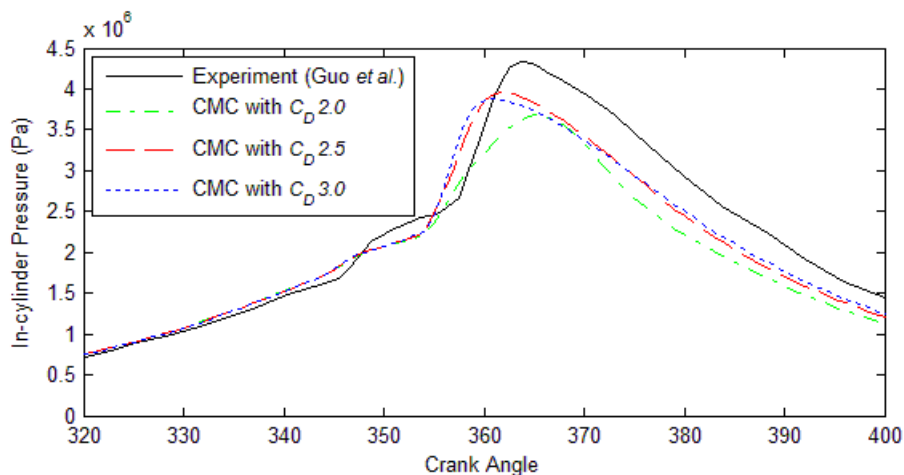


Figure 5.15 In-cylinder pressure comparison between experiment and CMC model with varying C_D .

Chapter 5

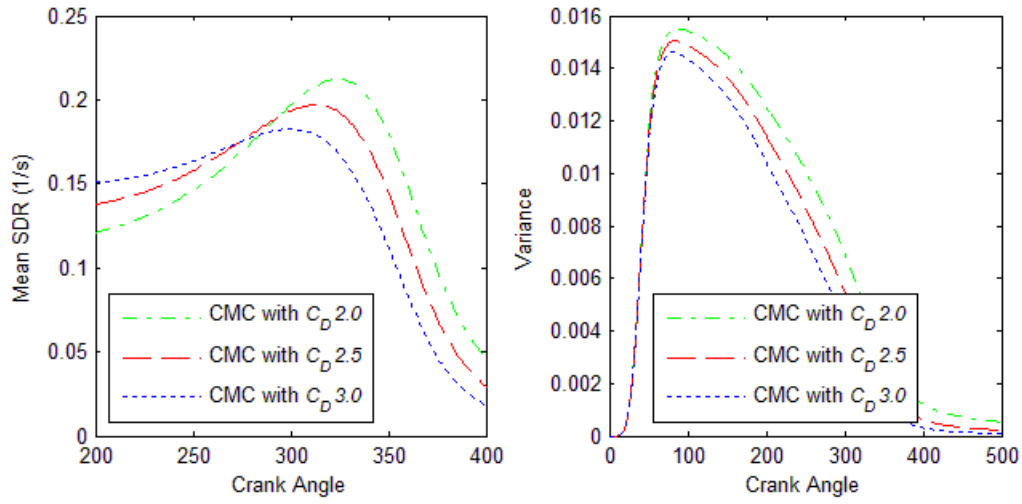


Figure 5.16 Effects of varying C_D on the mean SDR (left) and mixture fraction variance (right).

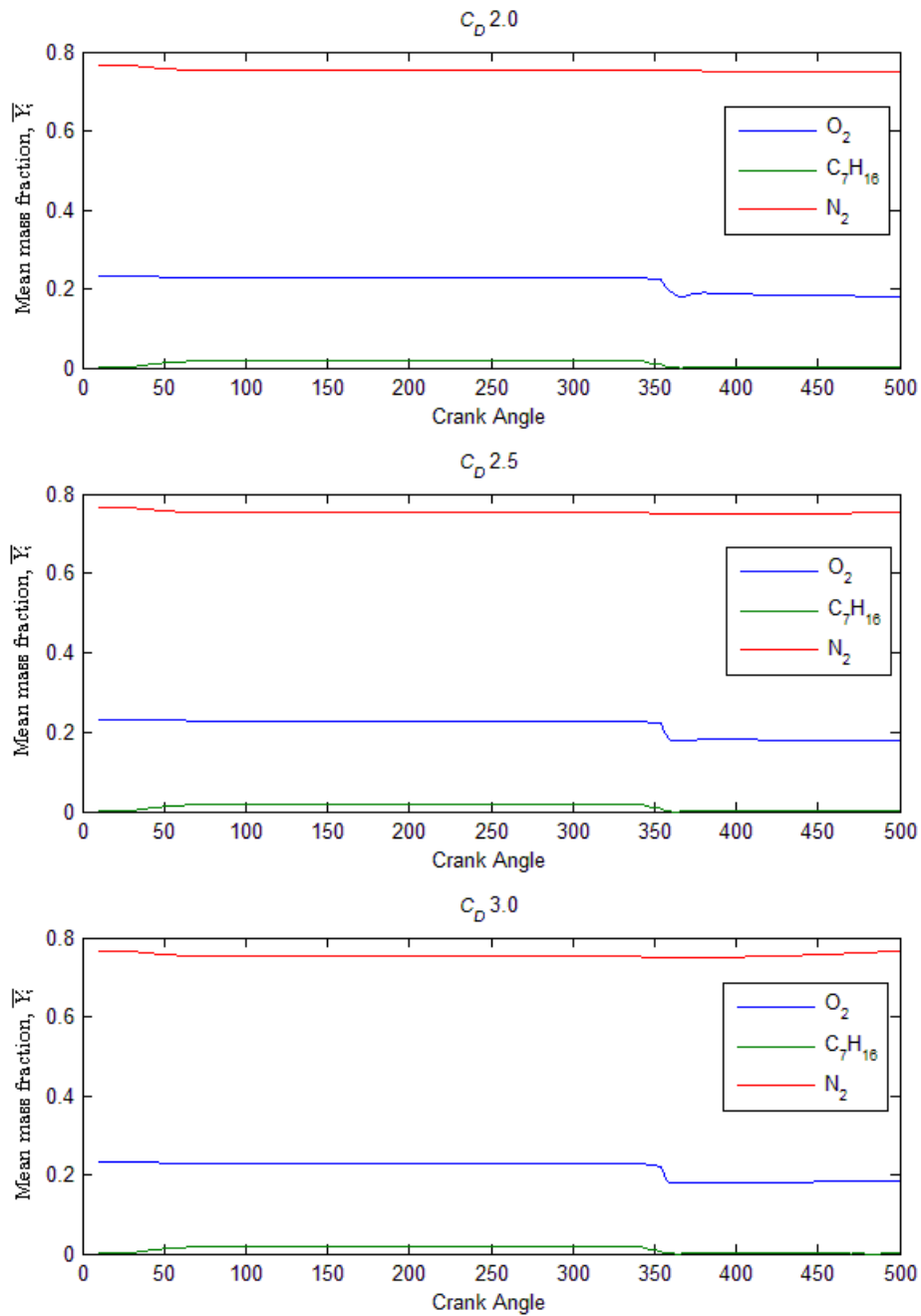


Figure 5.17 Oxidiser and fuel behaviour for the entire simulation with varying C_D

5.4.4.2 Grid Independence Test: Number of Bins of the CMC Model

The number of bins (as shown in Figure 4.9) of the CMC model is important so that the CMC model has enough resolution to account for the chemical reaction in η -space around Z_{mean} . The stoichiometric mixture fraction is $Z_{stoic} = 0.0622$ and the mean mixture fraction used for comparison with the experiment is $Z_{mean} = 0.0188$. Figure

5.18 shows the comparison of the CMC model with different numbers of bins compared with the experiment. Because the Z_{mean} is small, the CMC model with 100 bins is not enough to accurately resolve the details around the mean mixture fraction space. The CMC model with 100 bins yielded the lowest in-cylinder peak pressure compared to others.

The in-cylinder peak pressure increases with the increased number of bins, as shown in Figure 5.19. However, the time taken to complete the test with increasing numbers of bins is also increased. For comparison, the 100 bins CMC model took about one day on a mainstream 2013 computer, two days for 150 bins, three days for 200 bins, four days for 300 bins and almost five days for 500 bins. There was a big jump in in-cylinder peak pressure when more than 100 bins was used, with 150 bins yielding slightly lower than the experiment while 200 bins and above showed slightly higher peak pressure. The results show that at least 150 bins are enough to resolve the details around the mean mixture fraction space. Thus, 150 bins of the CMC model were used for the rest of the analysis for the *n*-heptane case.

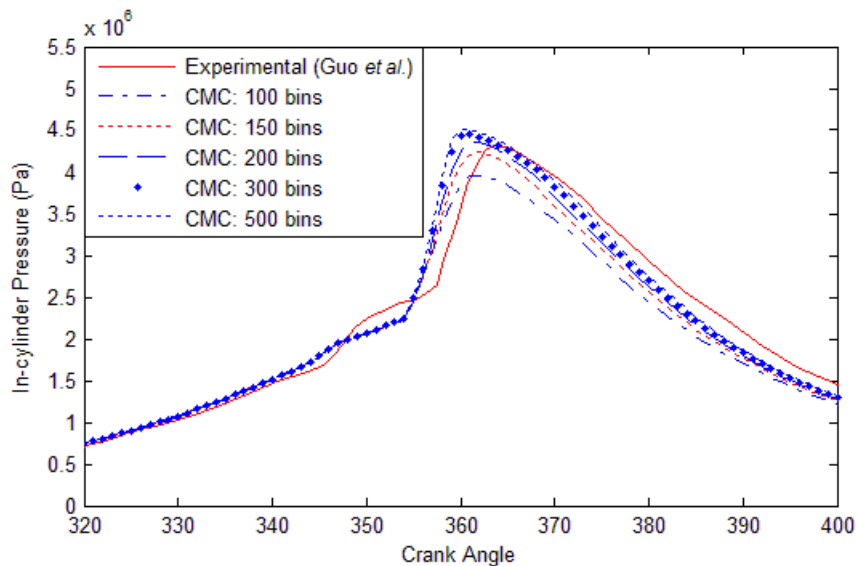


Figure 5.18 Comparison between CMC model and experiment with varying number of bins.

Even though the 200 bins model shows close in-cylinder peak pressure compared to the experiment, 150 bins provides a balance between numerical accuracy and computational efficiency. A slightly lower in-cylinder peak pressure compared with the experiment is similar to results using zero-dimensional CMC coupled with multi-

dimensional CFD, as in Figure 5.11 (Wright 2005). Therefore, the 150 bins CMC model for the *n*-heptane case is sufficient when time and accuracy are taken into consideration and the result for fewer bins is expected to improve if the model runs in a multi-dimensional simulation.

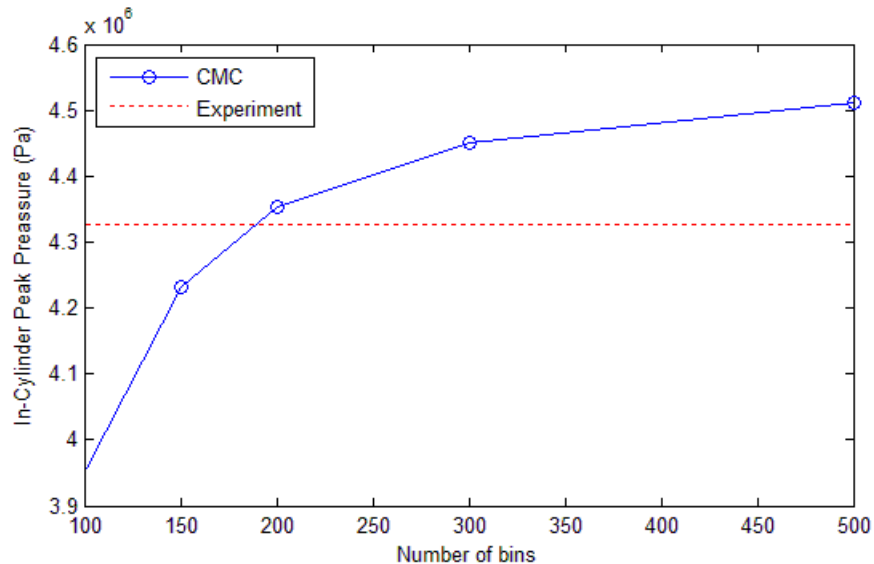


Figure 5.19 Peak pressure comparison between experiment and varying number of bins of the CMC model.

5.4.4.3 Scalar Dissipation Rate

The scalar dissipation rate measures the mixing rate at a molecular level. The mixing rate is high when there is inhomogeneity in the mixture. This is shown in Figure 5.20 for direct injected diesel in a multi-dimensional CMC by Seo *et al.* (2010), where the mixing rate is increased abruptly during the injection period. In contrast to this study, the mean mixing rate is very low, which is below 0.3/s as shown in Figure 5.21. Because the fuel was port injected, the mean mixing rate is at its maximum during the intake stroke, which is 0.27/s, before decreasing again when the intake valve is closing. The mixing rate begins to increase again in the compression stroke, because turbulence is generated at this stage as shown in Figure 5.14. Then, the mixing rate is reduced when combustion is about to occur: the mixture is not completely homogeneous even though after the combustion occurred, as shown in Figure 5.21. The result shown here indicates that a high turbulence generation rate causes a high mixing rate.

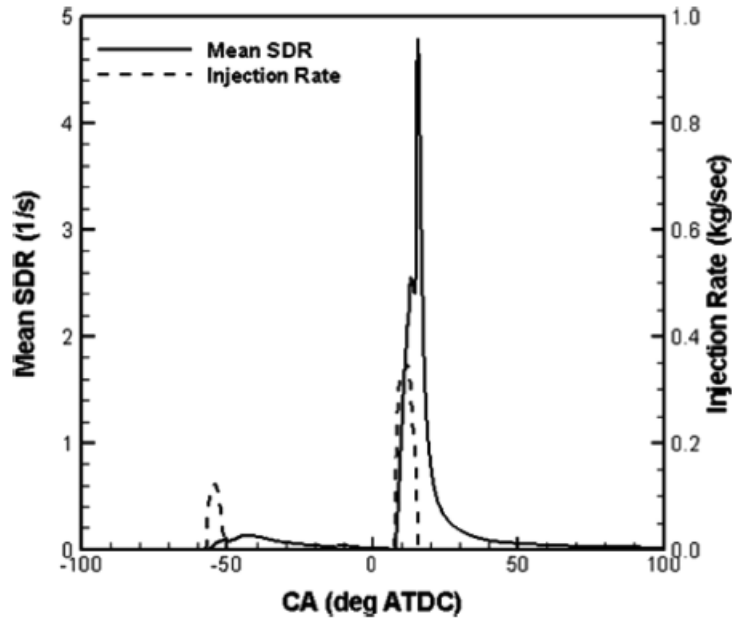


Figure 5.20 Mean SDR for direct-injected diesel in a multi-dimensional CMC model (Seo *et al.* 2010).

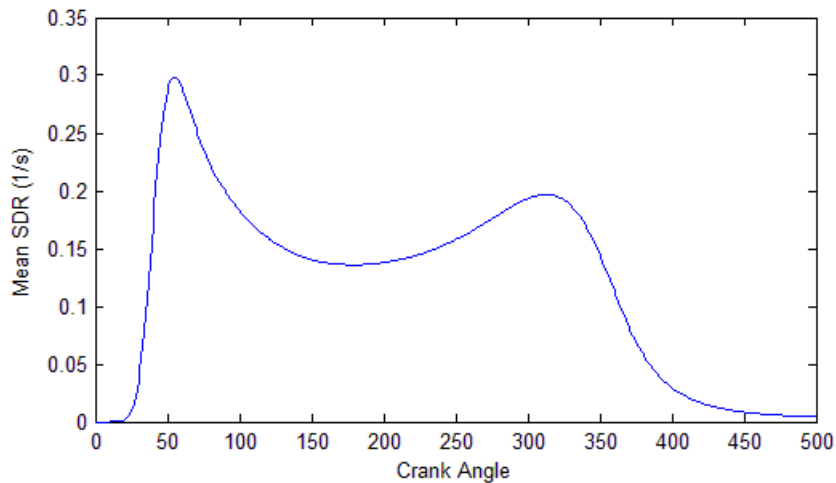


Figure 5.21 Mean scalar dissipation rate for port injected diesel of CMC with zero-dimensional model.

A low mixing rate in this study when compared with Figure 5.20 is due to the assumption that the in-cylinder pressure is homogeneous and the fuel was injected in the intake manifold instead of being direct injected. The direct injection method contributes to the turbulence generation in the chamber and also creates a high inhomogeneity in the mixture. Thus, port injection methods reduce the turbulence, where the turbulence is generated due to the piston motion and fluid through the valves. Therefore, the effect of turbulence in a homogeneous mixture is low. The result is in agreement with the study from Aceves *et al.* (2000), where turbulence has a minor direct effect on HCCI combustion.

5.4.4.4 Chemical Reactions

The chemical reactions are considered in equation (4.75) as a chemical source term of the CMC equations, where they affect the mass fractions and temperature in the combustion chamber. The temperature and mass fractions change as a result of the chemical energy being released during combustion. In HCCI engines, the combustion is necessary to model with a chemical kinetics mechanism rather than a pre-defined ignition point (Assanis & Heywood 1986; Bengtsson, Gafvert & Strandh 2004; Shaver *et al.* 2005) because chemical kinetics fully control the combustion.

Figure 5.22 shows the mean mass fraction over the CA locations for the entire simulation. The fuel (C_7H_{16}) is being added to the combustion chamber after IVO and its mass fraction begins to increase and becomes constant after the specified AFR is attained. The result shows that no chemical reaction occurred until after $340^\circ CA$. Once the combustion started at approximately $345^\circ CA$, the oxygen and fuel were consumed and the amount of CO_2 increased. The characteristics of LTR and HTR are also observed by having two-stage reductions in Y_{O_2} , where LTR is shown by a small reduction in Y_{O_2} while HTR is shown with a sudden drop. A two-stage reaction of *n*-heptane is also reported in the literature (Curran *et al.* 1998; Maroteaux & Noel 2006; Mehl, Curran, *et al.* 2009).

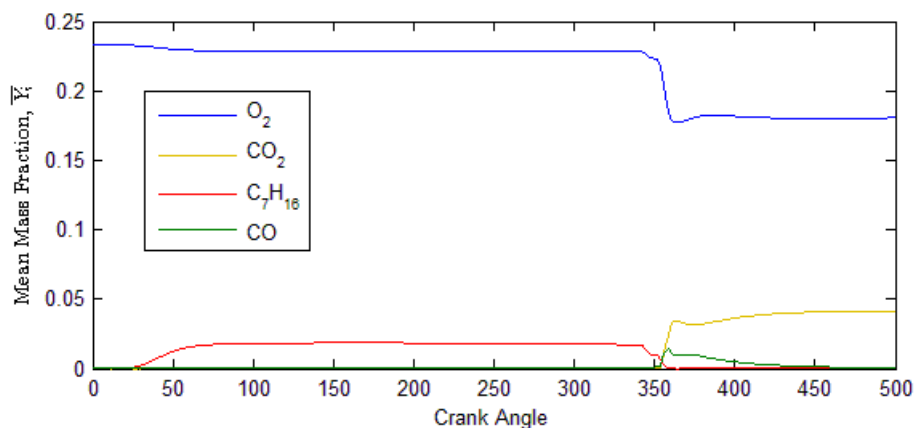
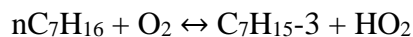
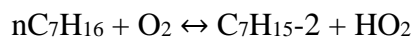


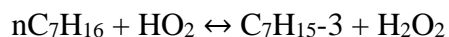
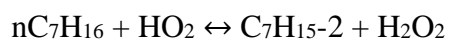
Figure 5.22 Mean mass fraction for the entire simulation, which shows the mean mass fraction of O_2 , H_2O_2 , CO_2 , C_7H_{16} and CO .

The details of the species mass fraction change during the combustion event is shown in Figure 5.23, where the in-cylinder temperature trace is also shown to indicate at

which temperature the changes occur. These species (H, OH, H₂O₂, CH₂O and HO₂) are selected during the combustion because they are the most important for driving the ignition process (Aceves *et al.* 2000; Zheng & Yao 2007; Zheng & Yao 2006), while C₇H₁₆ and O₂ are the main reactants and CO and CO₂ are the combustion by-products. NO_x is not included in the chosen chemical kinetics mechanism. Maroteaux and Noel (2006) reported that the H₂O₂ decomposition occurs at the time of auto-ignition and a similar trend is observed in Figure 5.23 (B), where the amount of H₂O₂ increases when LTR is started. Radicals H₂O₂ and HO₂ (Figure 5.23 (C)) are related to LTR, where they reached the peak near the point of the main combustion (Aceves *et al.* 2000). The LTR occurs when the in-cylinder temperature is between 850K and 1000K (Aceves *et al.* 2000; Curran *et al.* 1998; Maroteaux & Noel 2006), as can be seen in Figure 5.23, where *n*-heptane and O₂ begin to decrease at approximately 850K followed by H₂O₂ decomposition. Almost half of the fuel is consumed during LTR and intermediate species such as H₂O₂, HO₂ and CH₂O are generated. The main initial reactions during LTR are represented by (Zheng & Yao 2006)

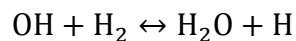


which show the H-atom is abstracted from the fuel molecule and generates an *n*-heptyl radical. The O₂ addition in the above reactions is the most important path for low temperature branching (Zheng & Yao 2006). The increase in HO₂ radical can be seen in Figure 5.23 (C) during the start of LTR. The HO₂ radicals will then react with fuel molecules to generate hydrogen peroxide (H₂O₂)

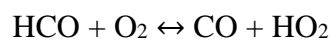
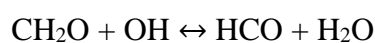


The H₂O₂ plays an important role during HTR. The accumulation process of HO₂ followed by H₂O₂ is shown in Figure 5.23 (B) and Figure 5.23 (C), where HO₂ radicals reach the first peak at the start of LTR and H₂O₂ reaches its peak at the end of the LTR process. Due to the large amounts of HO₂, the H₂O₂ is mainly generated from HO₂ + HO₂ ↔ H₂O₂ + O₂ and then consumed by H₂O₂(+M) ↔ OH + OH(+M) to form OH radicals.

In general, the combustion occurs when the amount of H_2O_2 starts to accumulate during the LTR process and decomposes to form a significant amount of hydroxyl (OH) radicals: two OH radicals are produced for each H_2O_2 . The decomposition rate becomes very rapid when the in-cylinder temperature reaches 900-1000K (Maroteaux & Noel 2006) and the amount of OH also increases rapidly, as in Figure 5.23 (B). The results observed in Figure 5.23 show that the main combustion starts at about 354°CA and the remaining amounts of O_2 and C_7H_{16} are decreasing when the H_2O_2 is decomposed. During the decomposition of H_2O_2 , the amount of OH and H radicals are increasing and reach the peak by the time the H_2O_2 is fully decomposed, which is consistent with Aceves *et al.* (2000). The OH radicals react with the remaining fuel molecules producing water and heat, which increases the temperature during the combustion event. These radicals (H and OH) are at their maximum when the fuel molecules are fully consumed at the maximum in-cylinder temperature. The production and destruction activities of OH radicals are briefly shown below (Aceves *et al.* 2000; Roomina & Bilger 2001):

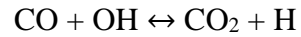


The OH radicals are observed to have two peaks, which are during LTR and HTR. The amount of OH produced during LTR is very small; hence the fuel is only consumed a little. The radicals H and OH are then reduced after the combustion and according to Aceves *et al.* (2000), the radical H is consumed during high temperature combustion (1100-1800K). The intermediate species CH_2O plays an important role in the transition from LTR to HTR. The CH_2O is consumed as soon as the HTR begins to form CO. OH radicals will abstract an H-atom from CH_2O to generate HCO radicals and HCO will be converted to CO as



Chapter 5

The oxidation of CO occurs during the HTR, where the oxidation process releases a significant portion of energy at high temperature (Zheng & Yao 2006). The reaction for CO consumption is given by



The amounts of CO and CO₂ are increased as a result of the combustion products. Heywood (1988) reported that the amount of CO is increased rapidly to a maximum value in the flame zone and this behaviour can be seen in Figure 5.23(D), where the value of CO is increased to a peak value during the main combustion.

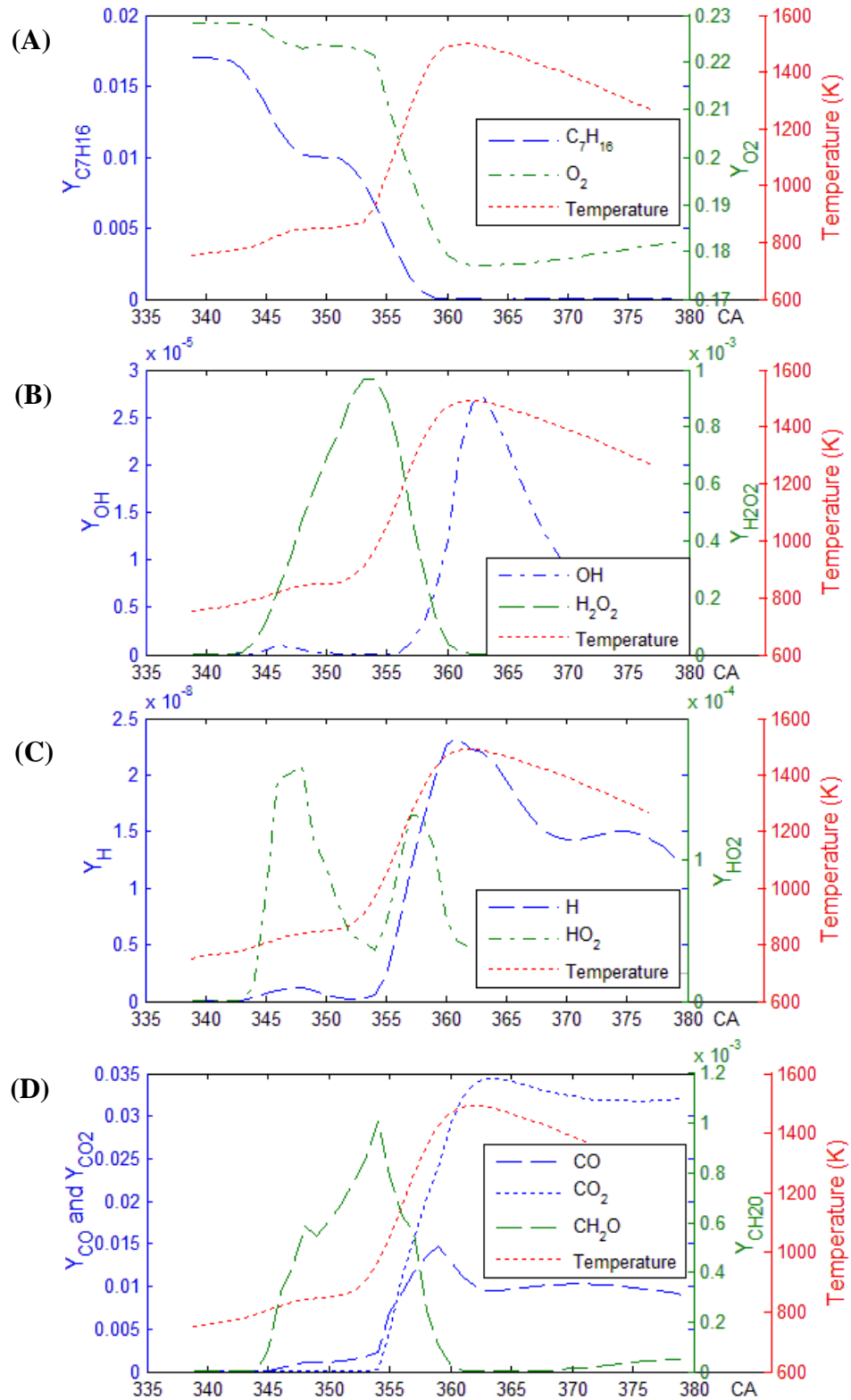


Figure 5.23 Mean mass fractions behaviour during combustion event compared with in-cylinder temperature trace, A: C_7H_{16} and O_2 , B: OH and H_2O_2 , C: H and HO_2 , D: CO and CO_2 .

When studying the combustion behaviour in the mixture fraction space of the CMC model, the result shows that the combustion started in the lean side of mixture fraction space and propagated towards the rich side. Then the combustion shifted back to stoichiometric conditions during HTR. The stoichiometric mixture fraction for *n*-heptane is 0.0622. Figure 5.24 shows the PDF of mixture fraction (modelled as a β -function PDF), where most of the mixture has been dominated by air towards the combustion (PDF \approx 0 at $Z=1$). This shows that the mixture has not mixed homogeneously. There is a visible change when the combustion is finished (Figure 5.24 D), which indicates that the mixture continues to mix, even though it does not reach perfect homogeneity. This is shown in Figure 5.16, where some inhomogeneity still exists in the mixture (variance > 0) after the combustion. The first stage of ignition (LTR) occurs in the lean side of mixture fraction space and propagates towards the rich region. The HTR occurs in the rich mixture and propagates towards the lean side, where the propagation from the rich to lean mixture can be seen at 355°C. This behaviour is shown in Figure 5.27 for OH radicals, where OH plays an important role during combustion. The amount of OH increases first in the lean mixture before propagating to the rich region during the LTR process. Then, the chemical reactions continue, causing the peak OH radicals to shift back towards stoichiometric conditions at 355°C, which is the HTR region. The amount of OH increases steadily at stoichiometric conditions during the main combustion event (HTR) before being consumed, as shown in Figure 5.27 (D). The combustion behaviour can also be seen from the generation of CO₂, which is a by-product of the combustion. The CO₂ is generated at the lean mixture and propagates towards the rich side during LTR process. Then the CO₂ shifts back, with an increase at the stoichiometric condition at HTR. Figure 5.25 to Figure 5.30 show the conditional mean mass fraction for reactive scalars (C₇H₁₆, O₂, OH, H₂O₂, CO and CO₂) during the combustion event from LTR to HTR. The LTR starts at 345°C with *n*-heptane being slowly consumed from the lean side of the mixture fraction space and moves to the rich region. Note that the LTR region is generally shown in images (A) and (B) while images (C) and (D) show the main combustion of the HTR region.

From Figure 5.28, the result shows that the H₂O₂ is rapidly accumulating on the lean side of η during LTR. The H₂O₂ is slowly decomposed and forms a small amount of OH radicals. These OH radicals are slowly consumed by *n*-heptane, where the

consumption of *n*-heptane propagates to the rich region and the *n*-heptane is not fully consumed at the lean mixture. Once the HTR starts at about 354°CA, the remaining *n*-heptane at lean mixture is rapidly consumed. The same occurs for O₂, where the O₂ is fully consumed around the stoichiometric mixture. This can be seen by the rapid decomposition of H₂O₂ during HTR and OH reaching the peak at the stoichiometric mixture fraction when the in-cylinder temperature is at its maximum. The mass fractions of CO and CO₂ are also slowly increasing from LTR to HTR, where CO₂ has its maximum at the stoichiometric mixture fraction. The behaviour of the OH mass fraction profile is in agreement with Bolla *et al.* (2013) running diesel spray simulation using multi-dimensional CMC, where the OH mass fraction profiles peak at the stoichiometric mixture fraction. This indicates that the main combustion occurs at the stoichiometric mixture fraction.

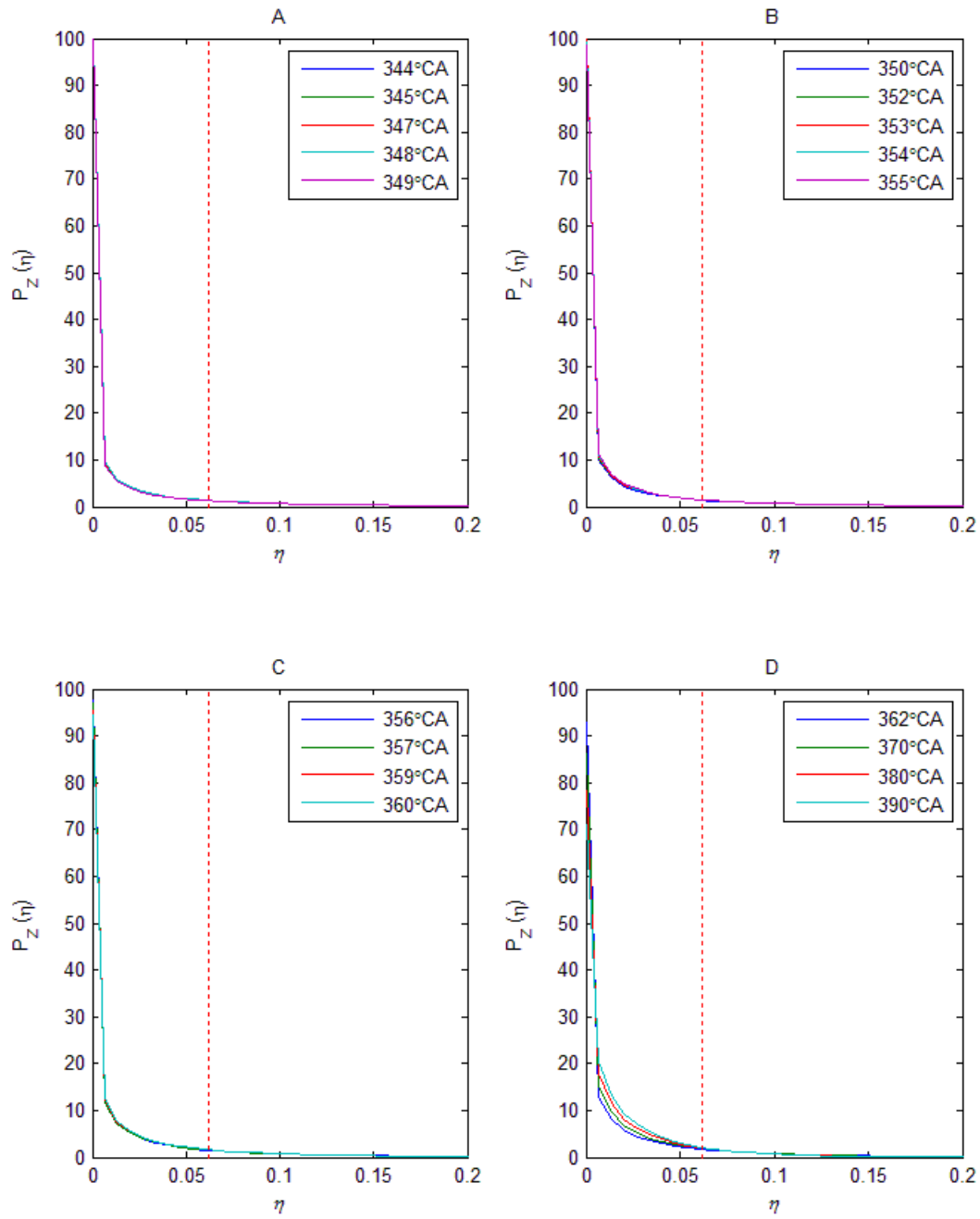


Figure 5.24 PDF of mixture fraction during the combustion event.

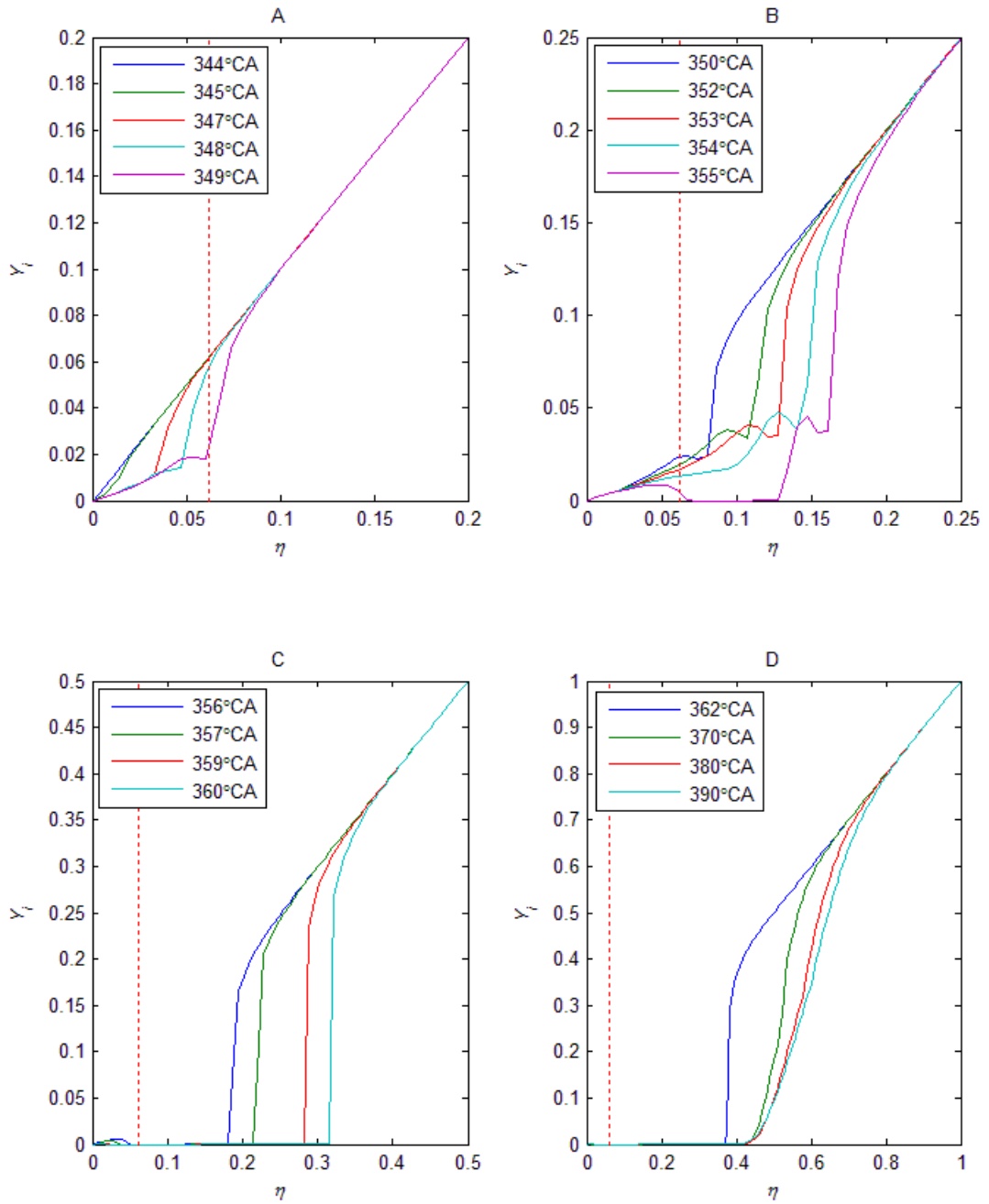


Figure 5.25 Conditional mass fraction of n -heptane (C_7H_{16}) during combustion with varying CA. The x-axis range is slowly increased from image A-D because the ignition started at the lean side before propagating to the rich side of the mixture fraction space. The dotted red line shows the location of the stoichiometric mixture fraction.

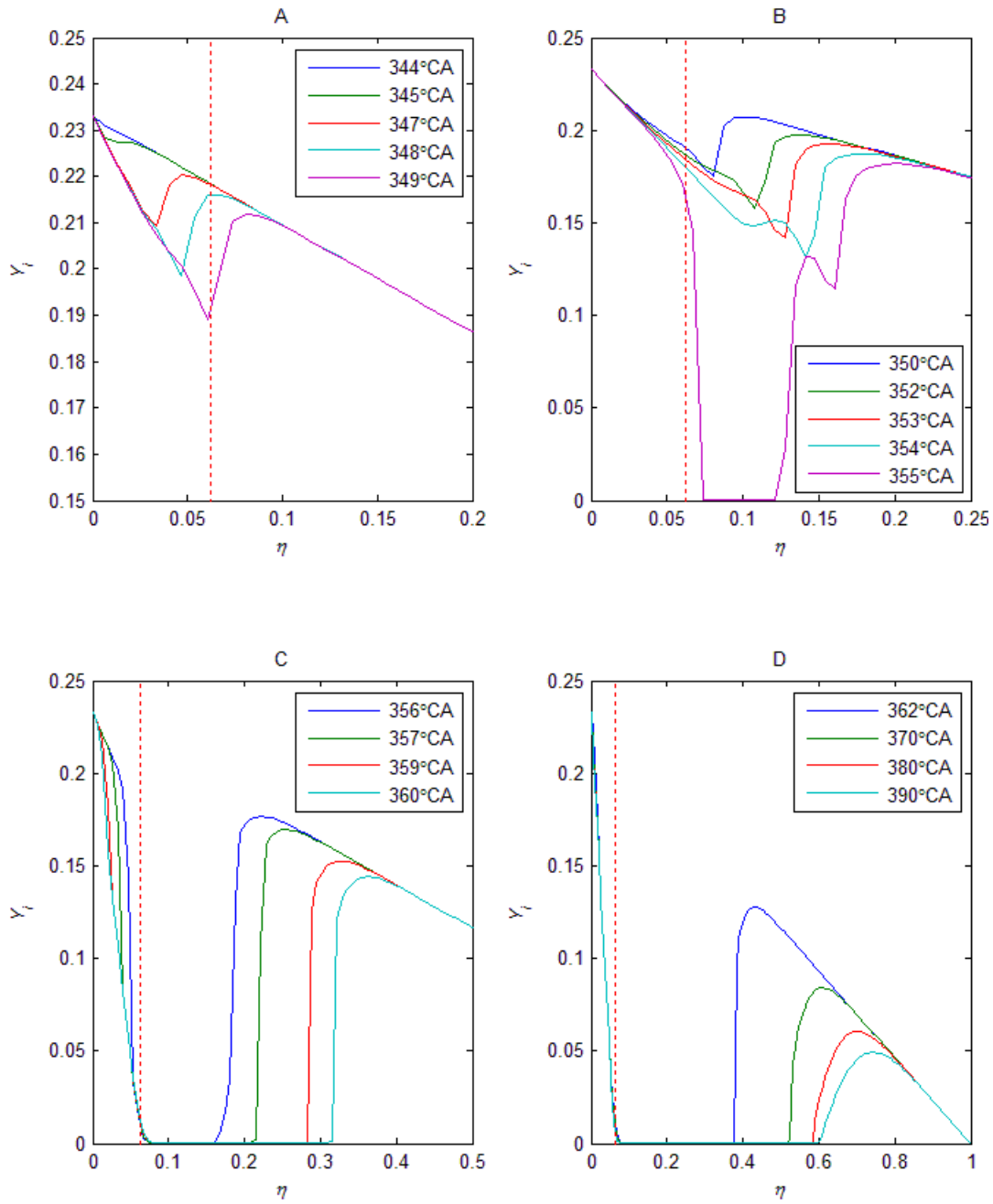


Figure 5.26 Conditional mass fraction of oxygen (O_2) during combustion with varying CA. The x-axis range is slowly increased from image A-D because the ignition started at the lean side before propagating to the rich side of the mixture fraction space. The dotted red line shows the location of the stoichiometric mixture fraction.

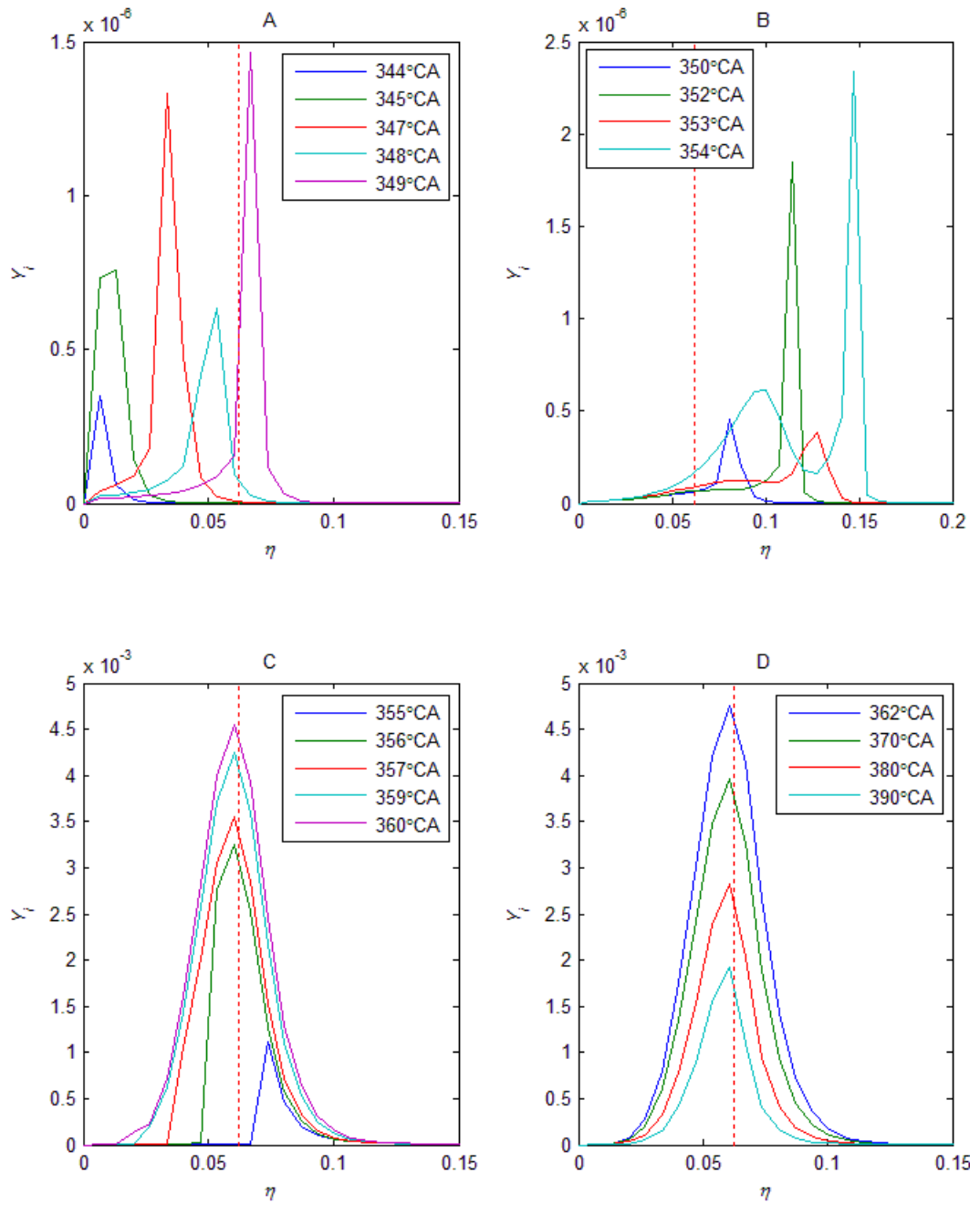


Figure 5.27 Conditional mass fraction of hydroxyl (OH) radical during combustion with varying CA. The dotted red line shows the location of the stoichiometric mixture fraction.

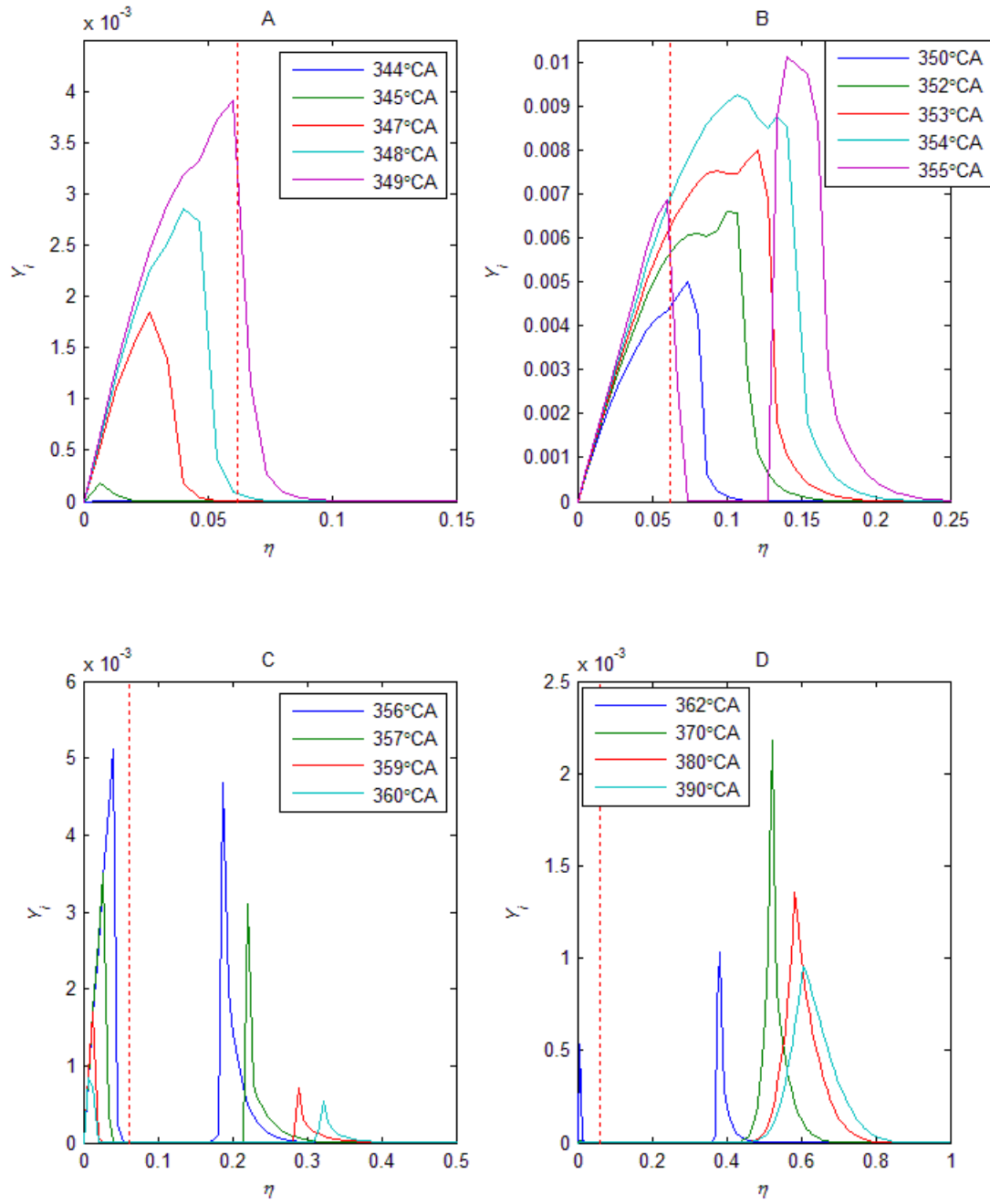


Figure 5.28 Conditional mass fraction of hydrogen peroxide (H_2O_2) during combustion with varying CA. The x-axis range is slowly increased from image A-D because the ignition started at the lean side before propagating to the rich side of the mixture fraction space. The dotted red line shows the location of the stoichiometric mixture fraction.

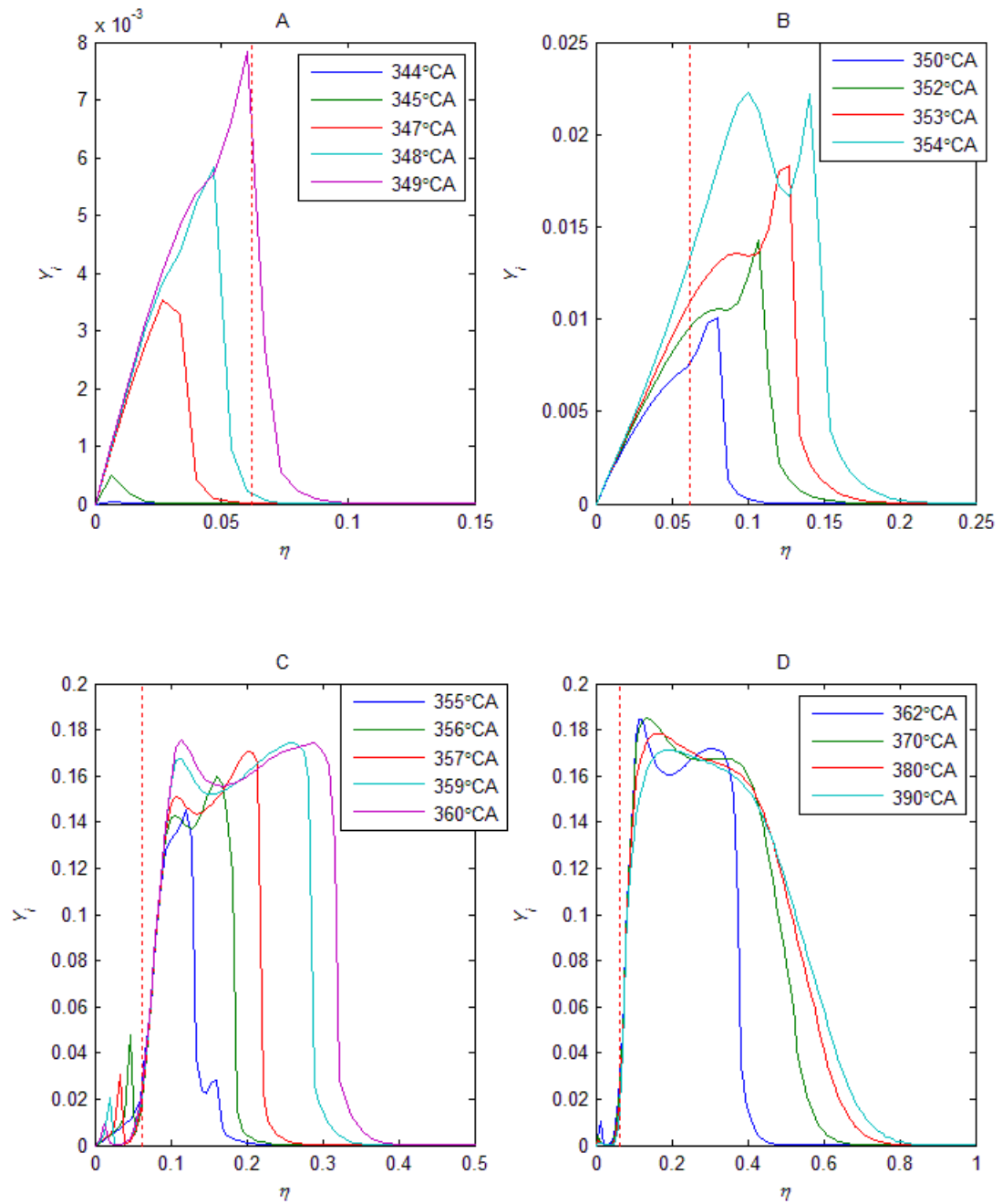


Figure 5.29 Conditional mass fraction of carbon monoxide (CO) during combustion with varying CA. The x-axis range is slowly increased from image A-D because the ignition started at the lean side before propagating to the rich side of the mixture fraction space. The dotted red line shows the location of the stoichiometric mixture fraction.

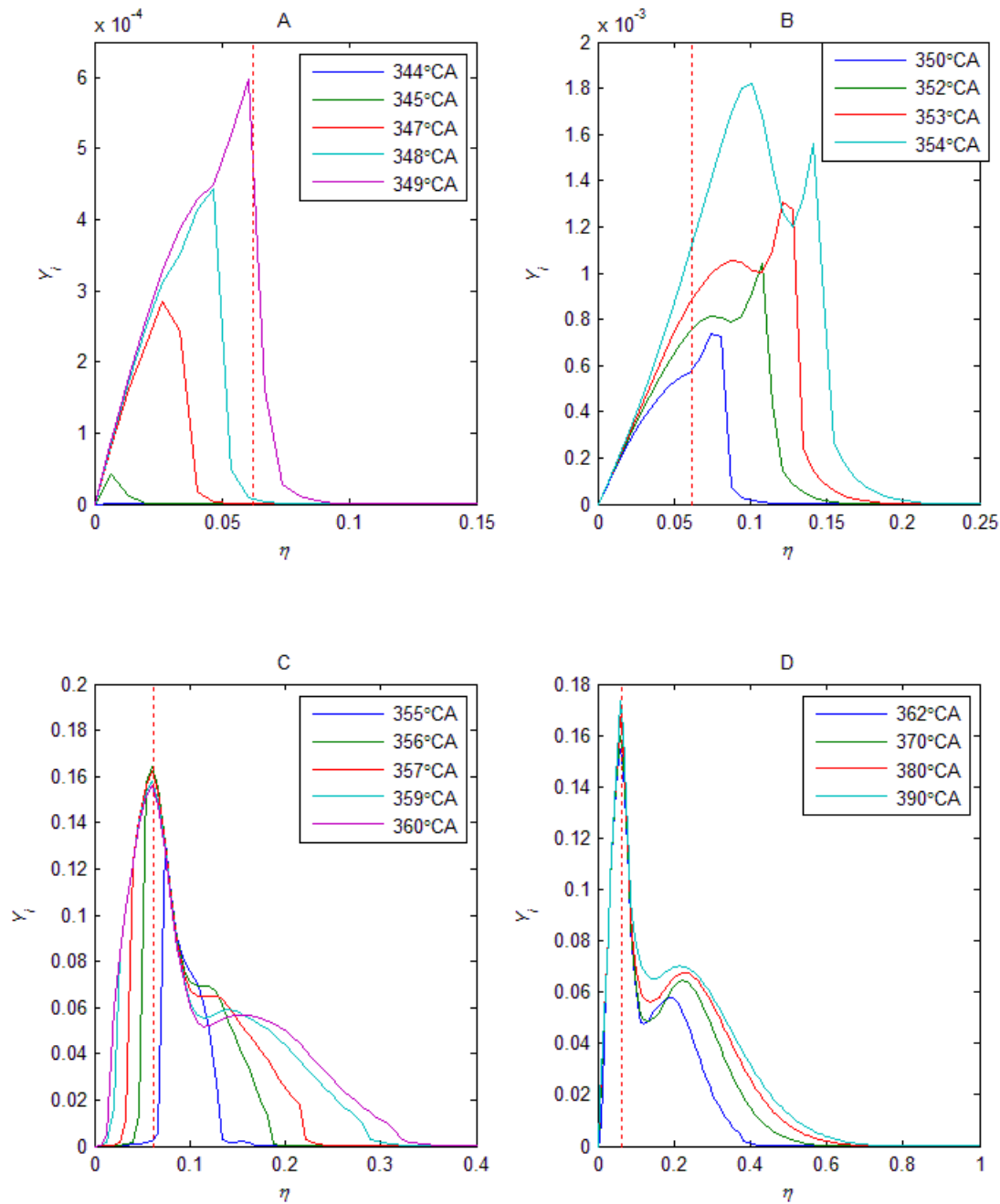


Figure 5.30 Conditional mass fraction of carbon dioxide (CO_2) during combustion with varying CA. The x-axis range is slowly increased from image A-D because the ignition started at the lean side before propagating to the rich side of the mixture fraction space. The dotted red line shows the location of the stoichiometric mixture fraction.

5.4.4.5 Conditional Temperature

The conditional temperature profile is used to investigate the evolution of in-cylinder temperature in η -space over the CA step. Figure 5.31 shows the conditional temperature profile for the same image configurations of the LTR and HTR events as

in Figure 5.25 to Figure 5.30. The temperature increases from the lean side of η -space and propagates towards the rich region. During LTR, the temperature propagates until approximately $\eta = 0.16$. The temperature profile shows a double-peak at the beginning of HTR (355°CA), where the small peak can be seen to form at 348°CA and slowly dominates until 354°CA: the small peak lies in the LTR region. Then, the second peak (the higher peak) occurs at 355°CA and the small peak diminishes from this point onwards. This shows that the small peak is not present in the HTR region. However, this double-peak profile is not evident when using gasoline, as discussed in section 5.6. This behaviour is also due to the chemical reaction mechanisms being used in this study, where skeletal, reduced or detailed mechanisms would have different behaviours (Bolla *et al.* 2013). The use of a zero-dimensional study would also give a different performance due to homogeneity assumption, where most of the CMC studies in the engine research were performed using multi-dimensional simulations (Bolla *et al.* 2013; De Paola *et al.* 2008; Seo *et al.* 2010; Wright 2005; Wright *et al.* 2005).

Once the HTR occurred, the temperature rapidly increased towards the stoichiometric mixture fraction and reached the peak at that condition. This indicates that the heat is released at the stoichiometric mixture fraction, where the conditional temperature is at maximum at 362°CA before decreasing again when the piston is moving towards BDC. The high temperature zone slowly propagates to the rich region when the peak temperature is decreasing in the process of reaching chemical equilibrium. The conditional temperature peaks at the stoichiometric mixture fraction in agreement with multi-dimensional CMC simulations (De Paola *et al.* 2008; Seo *et al.* 2010), as it is expected to be. Thus, further study can be performed using a zero-dimensional CMC approach.

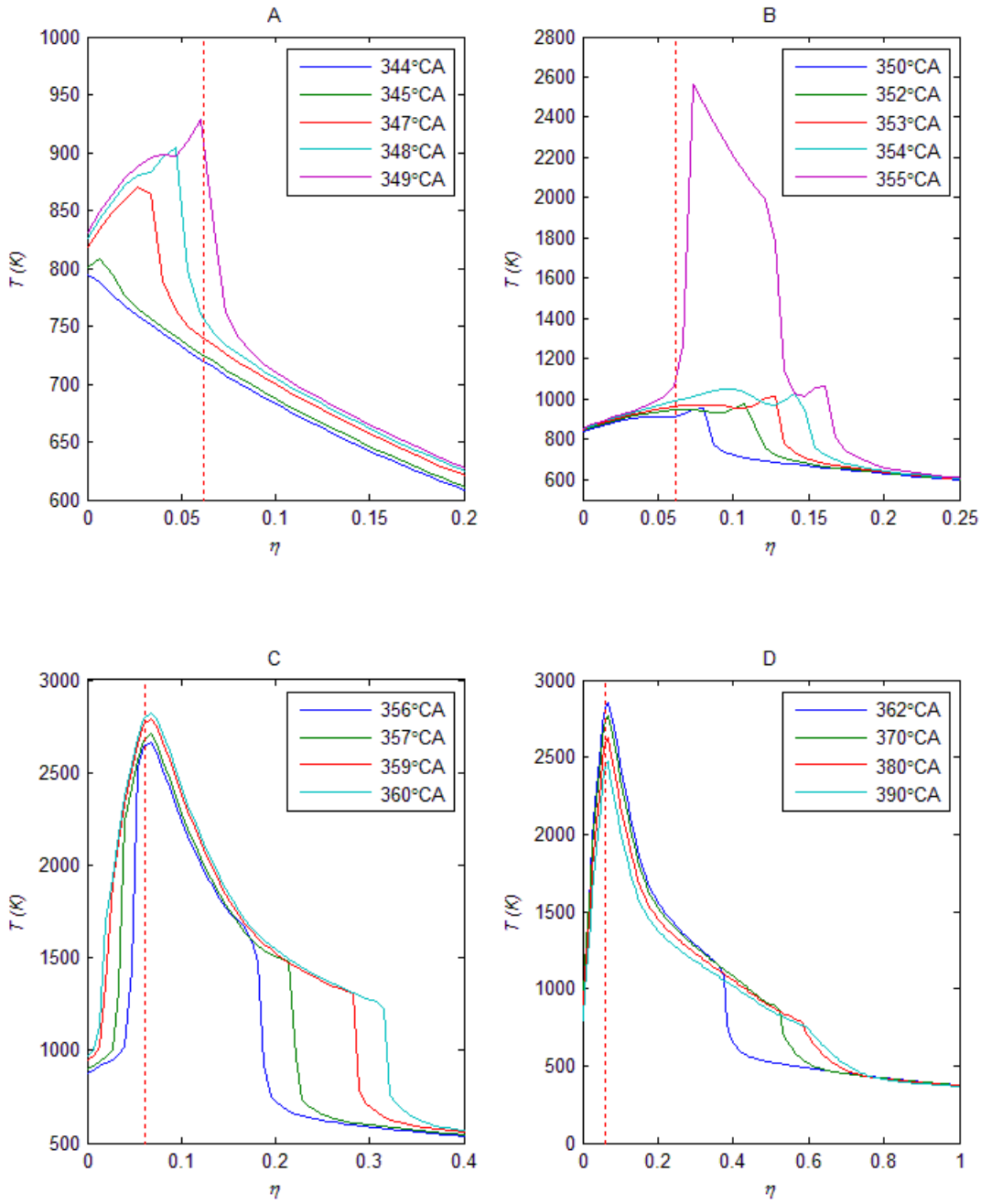


Figure 5.31 Conditional temperature during combustion with varying CA. The x-axis range is slowly increased from image A-D because the ignition started at the lean side before propagating to the rich side of the mixture fraction space. The dotted red line shows the location of the stoichiometric mixture fraction.

5.5 Behaviour of CMC and Zero-D

This section will discuss the parametric study between a zero-dimensional model and a combination of CMC with zero-dimensional model. The parameters investigated are the effect of intake air temperature, effect of air-to-fuel (AFR) ratio and the predicted effect of hydrogen addition to a diesel HCCI engine.

5.5.1 Effect of Intake Temperature

Intake air temperature is an important factor for controlling the auto-ignition timing of HCCI engines. Different fuels have different auto-ignition points and some of them require pre-heating to achieve good combustion. If methane or natural gas is used as a fuel, the intake air temperature has to be set to at least 400K to achieve appropriate ignition (Morsy 2007). Therefore, the intake temperature will affect the auto-ignition point for other fuels as well and increasing the intake temperature will reduce the ignition delay.

Figure 5.32 and Figure 5.33 show that the auto-ignition timing can be advanced once the intake temperature is increased for both CMC and zero-dimensional models. Results from the current simulation were compared with experimental results (Guo *et al.* 2010) in Figure 5.33 to validate the model over different operating temperatures. The usage of the CMC model improves the result compared to the zero-dimensional model alone. For an intake temperature of 25°C, the CMC model is in agreement with the experiment with marginally lower peak pressure for HTR and much lower pressure for LTR. The zero-dimensional model, on the other hand, has retarded combustion and higher peak pressure even though the intake temperature has been increased to 20°C higher than the actual temperature. For an intake temperature of 57°C, both the CMC and zero-dimensional models have advanced combustion, where the peak pressure of the CMC model is slightly higher than the experiment and the zero-dimensional model higher still.

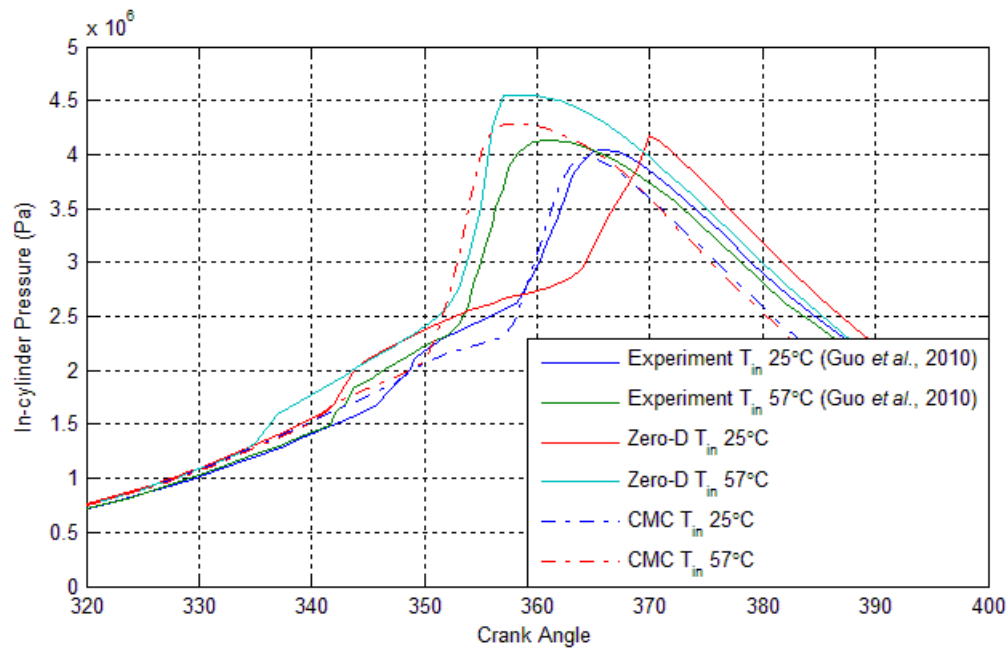


Figure 5.32 A comparison between experiment, zero-dimensional model and CMC model with various intake air temperatures.

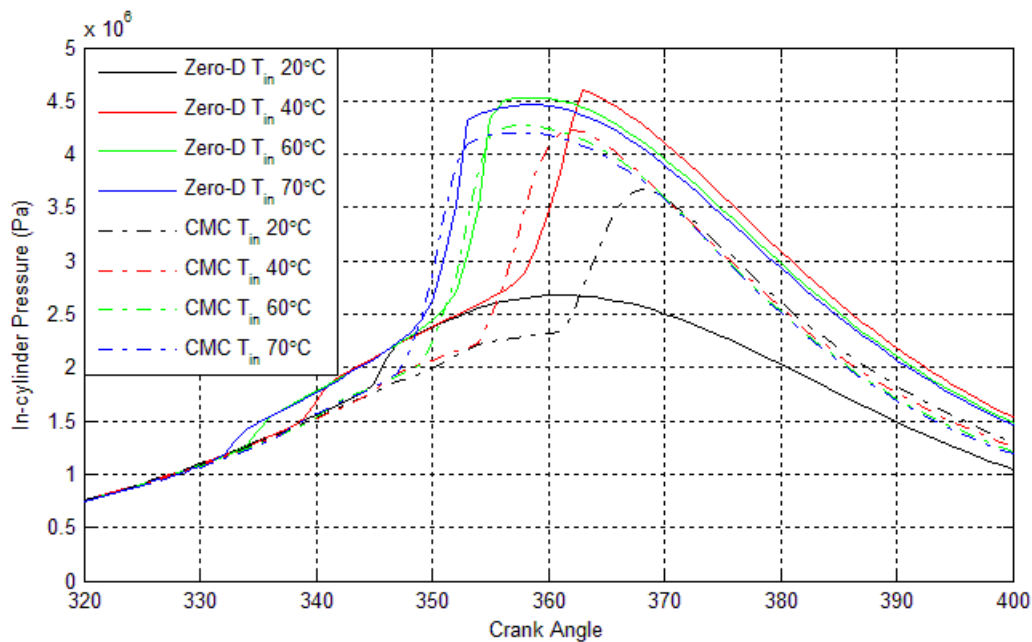


Figure 5.33 The effect of different intake air temperatures on in-cylinder pressure trace between zero-dimensional and CMC models.

A performance comparison between the CMC and zero-dimensional models is shown in Figure 5.33. The result shows that both models have very similar ignition points for intake temperatures of 60°C and 70°C. When the intake temperature is reduced, the zero-dimensional model has retarded combustion for an intake temperature of 40°C and no combustion at 20°C. The peak pressure for the CMC model is always lower

than for the zero-dimensional model. In all cases, the intake temperature for the zero-dimensional model was set 20°C higher than for the CMC model. The deficiency in the zero-dimensional model is due to the assumption that the combustion is homogeneous, no turbulence effect was considered in the combustion chamber and there was a constant combustion chamber wall temperature for the whole engine cycle. In practice, temperature, pressure and mixture inhomogeneities exist in the chamber (Guo *et al.* 2010). The deficiency may also be due to the potential limitation (slightly different auto-ignition point compared to the detailed mechanism) of the reduced chemical kinetics mechanism. All these assumptions contribute to the artificial increase in intake temperature. It was found that the temperature for the ignition point (start of HTR) or start of combustion (SOC) for the zero-dimensional model is always higher than the CMC model, as shown in Figure 5.34. If the temperature was not increased and was set to be the same as the actual temperature, the combustion did not occur (Figure 5.12). This shows that the single-zone zero-dimensional model requires more energy due to the assumptions discussed above. In the CMC model, the combustion was affected by the turbulence-chemistry interactions. The main combustion in the CMC model occurs at stoichiometric conditions given the right operating temperature, but this is initiated by reactions at a range of mixture fractions, which is not captured in the single-zone zero-dimensional model. Thus, the ignition occurs once the composition gains enough energy from the chemistry interaction. For lean combustion, the temperature started to increase in the lean mixture fraction space before propagating to the rich side and peaking at the stoichiometric condition, as discussed in Section 5.4.4.5. In the zero-dimensional model, combustion can only occur at the lean mixture fraction of the composition, and so there is no possibility for strong chemical reactions around the stoichiometric mixture fraction. This deficiency in the rate of releasing chemical energy has to be substituted by thermal energy in the form of an artificially-increased intake temperature. Thus, the result shows that the CMC model has better performance compared to the zero-dimensional model for varying the intake air temperature.

An increase in air intake temperature will not affect the in-cylinder peak pressure significantly. However, it does affect the ignition timing. The ignition point is advanced when the intake temperature increases, as shown in Figure 5.34, where the start of HTR was chosen as the ignition point (Shahbakhti & Koch 2008). Note the

trend as the intake temperature increases: the predicted in-cylinder peak pressure starts to decrease (Figure 5.35) even though the auto-ignition is advanced (Figure 5.34). This trend is also observed in the experiment (Guo *et al.* 2010). This is a good option for control because of the low increase in in-cylinder peak pressure: high peak pressures and advanced auto-ignition will create knocking. Also note that because CMC allows reactions in the vicinity of stoichiometric conditions, the temperature at start of combustion (SOC) can be lower (Figure 5.34) due to the higher rate of chemical energy being released promoting combustion.

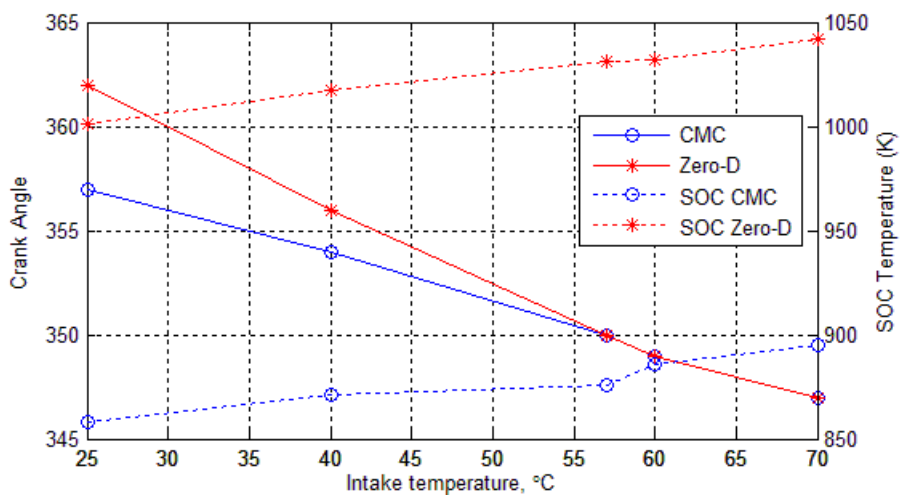


Figure 5.34 Effect of varying intake air temperature on ignition timing and start of combustion (SOC) temperature for CMC and zero-dimensional models.

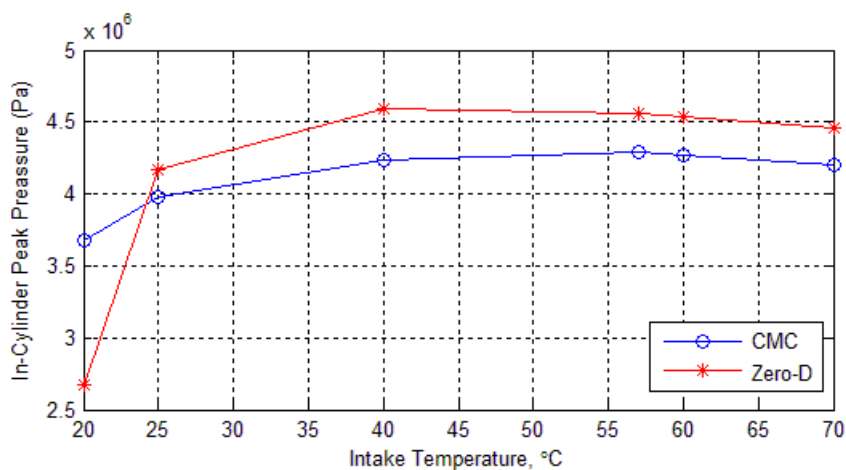


Figure 5.35 In-cylinder peak pressure comparison between CMC and zero-dimensional models with varying intake air temperature.

5.5.2 Effect of Air-to-Fuel Ratio (AFR)

The AFR is a measure of how much fuel and air is being consumed in the combustion chamber; HCCI engines operate with lean mixtures ($AFR_{actual} > AFR_{stoic}$). Figure 5.36 shows the validation of different AFR between the CMC and zero-dimensional models compared to the experiment, again showing good agreement.

Figure 5.37 shows the predicted result of increasing the equivalence ratio: an increase in the in-cylinder peak pressure and advancement of the auto-ignition timing can be observed for the zero-dimensional model. The CMC model, however, shows a limitation, where the ignition point is almost identical for all cases with varying AFR even though the in-cylinder peak pressure increases when the AFR moves towards the rich mixture. The limitation is possibly due to the implementation of the zero-dimensional model with CMC, where the mixture could be close to the lower flammability limit. This requires further investigation to confirm the cause. The formulation for conditional quantities of a homogeneous CMC model is reduced to reaction-diffusion in conserved scalar space with no physical space dependence. CMC is reported to produce a better result when implemented in a multi-dimensional simulation (Wright 2005). Thus, implementing a CMC model in a zero-dimensional simulation has some advantages but also some limitations.

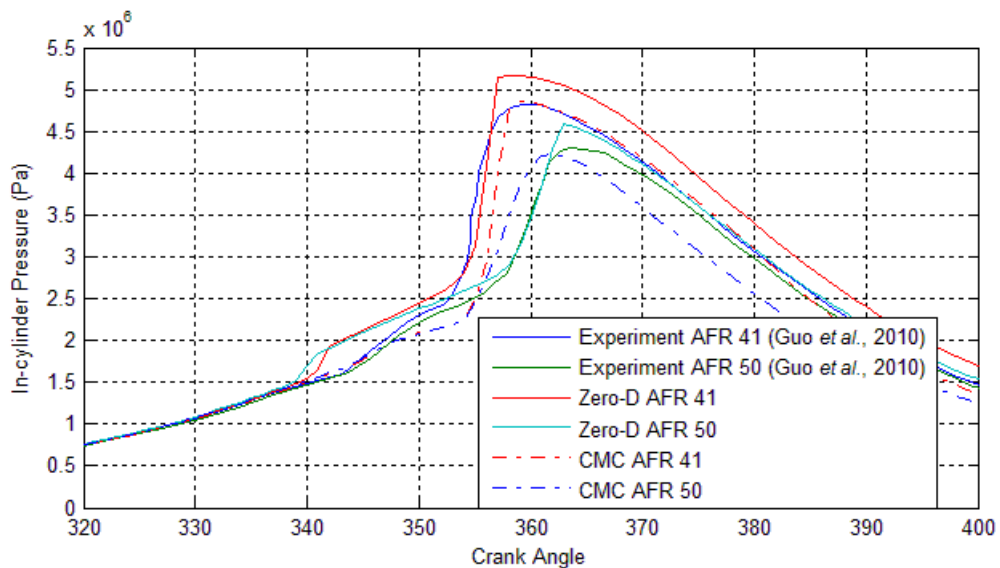


Figure 5.36 A comparison between experiment, zero-dimensional and CMC models with various AFR.

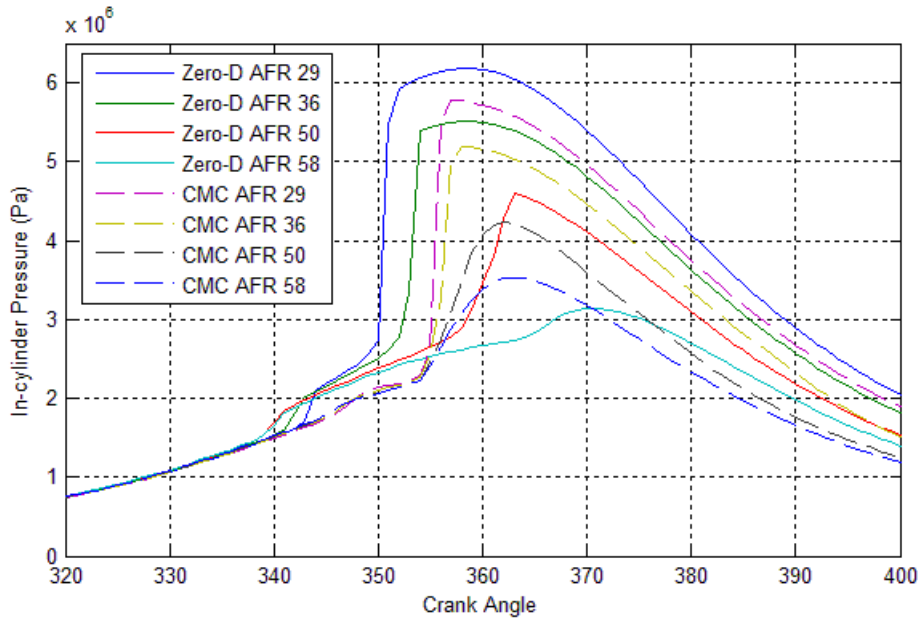


Figure 5.37 The effect of different AFR on in-cylinder pressure trace between zero-dimensional and CMC models, where the stoichiometric AFR for *n*-heptane is 15.1.

Figure 5.38 shows the in-cylinder peak pressure trend with the change of AFR. The in-cylinder peak pressure trend keeps increasing when the AFR is reduced towards the rich mixture, which will possibly create knocking. In addition, the start of LTR is retarded, as shown in Figure 5.37, when the AFR is reducing. Therefore, careful tuning (especially for AFR) is needed to adapt to dynamic engine loads.

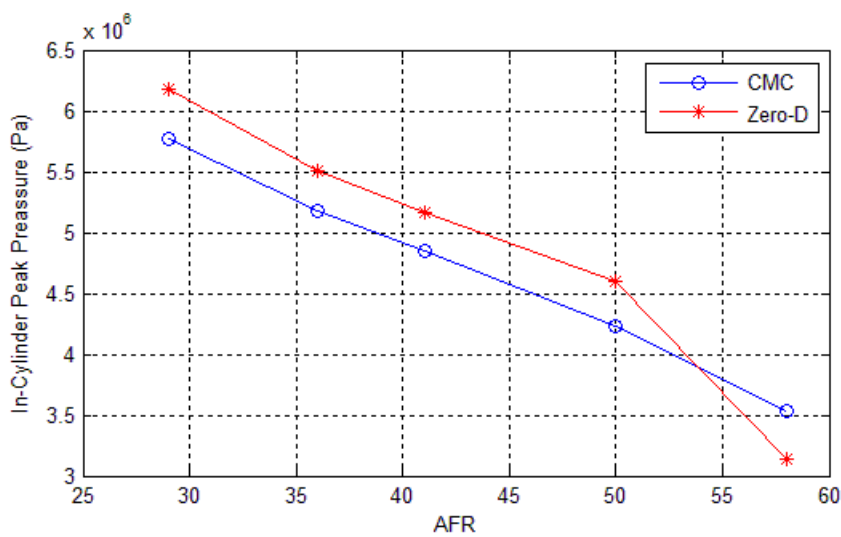


Figure 5.38 In-cylinder peak pressure comparison between CMC and zero-dimensional models with varying AFR.

PART 2: GASOLINE HCCI

5.6 Experimental Data

Part 2 of this chapter will discuss the validation of CMC and zero-dimensional models against a gasoline fuelled HCCI engine. The experimental data of the engine from Bunting *et al.* (2008) was used as a validation tool, where the engine was run in HCCI mode with port atomisation of fuel. The focus of the study by Bunting *et al.* (2008) was on the emission characteristics of the engine. Thus the in-cylinder pressure data of the engine was taken from Puduppakkam *et al.* (2009), where they studied the effect of different gasoline chemical kinetics models using the same engine configuration. The engine details used for validation are shown in Table 5.2. Note the wall temperature used for this case, which is 353 K, is different compared to a diesel fuelled HCCI engine. This is consistent with Komninos and Kosmadakis (2011) where a gasoline fuelled engine has a lower wall temperature compared to diesel.

Table 5.2 Engine parameters used in the simulation of a gasoline fuelled HCCI engine (Bunting *et al.* 2008)

Cylinder bore	97 mm
Stroke	70 mm
Connecting rod length	110.42 mm
Compression ratio	14.5
Engine speed	1800 rpm
Inlet pressure	101.3 kPa
Inlet valve open (IVO)	350°CA ATDC
Inlet valve closed (IVC)	578°CA ATDC
Exhaust valve open (EVO)	139°CA ATDC
Exhaust valve closed (EVC)	380°CA ATDC
Wall Temperature	353 K
AFR	35.9

5.7 CMC with Zero-Dimensional Model Validation

Just like the *n*-heptane case, the zero-dimensional model required the intake temperature for the gasoline case to be set higher than the actual to account for the mixing effect. For the gasoline case, the intake temperature for the zero-dimensional

model was set 7K higher than the actual to achieve a good result, smaller than that for the *n*-heptane case (20K). The increase in intake air temperature for the zero-dimensional model is expected due to the limitations of the model. When the intake temperature was set to be the same as the actual, the zero-dimensional model showed a retarded combustion by 2°CA, as shown in Figure 5.39. The in-cylinder peak pressure is marginally lower than the experiment. A 10K higher intake temperature yields a slightly advanced combustion by 1°CA with slightly higher peak pressure. The results show that a zero-dimensional model requires tuning of the intake temperature to achieve a good agreement with the experiment.

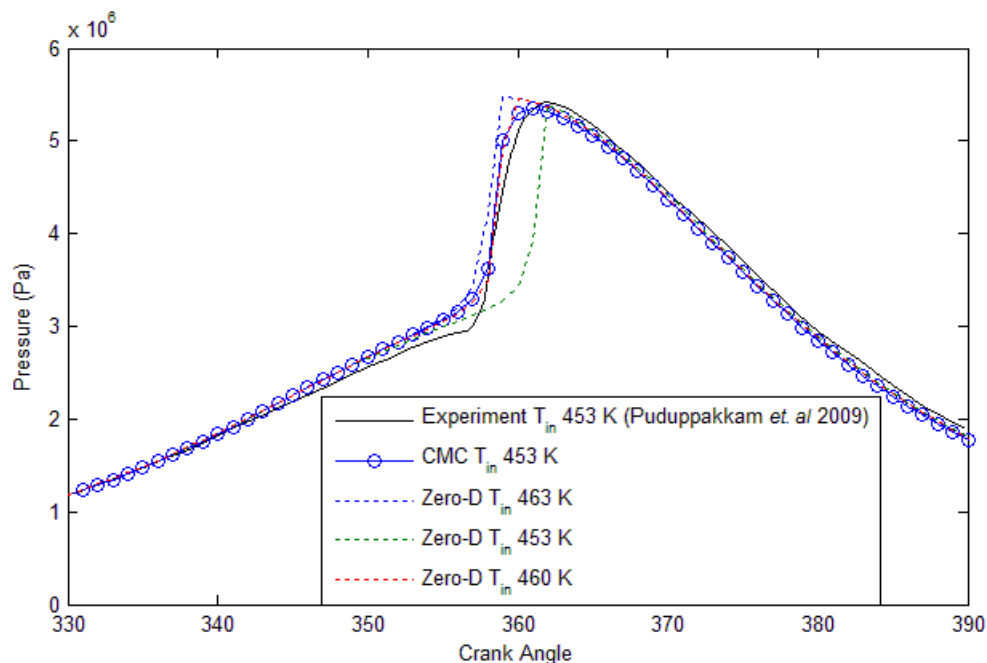


Figure 5.39 In-cylinder pressure comparison between the experiment (Puduppakkam *et al.* 2009), the CMC and zero-dimensional models, where the zero-dimensional model was tested with different intake temperatures.

The CMC with zero-dimensional model, on the other hand, is in very good agreement with the experiment. The intake temperature was set to be the same as in the experiment and the model yields a slightly lower in-cylinder peak pressure. Note that the in-cylinder pressure trace is smooth over the peak and has no sharp edges like the zero-dimensional model has. This shows that a combination of CMC with zero-dimensional model reduces the instantaneous rise in in-cylinder pressure, which overcomes one of the disadvantages of a zero-dimensional model: it exhibits a short burn duration (Morsy 2007). Also, with a combination of these models, the actual

intake temperature of the engine can be used without any tuning. Therefore, a CMC with zero-dimensional model shows an advantage over the single-zone zero-dimensional model and can be used for further analysis.

5.7.1 Independence Test

The independence test will investigate the performance of the number of bins of the CMC model and the constant C_D . The CMC result in Figure 5.39 was tested with 150 CMC bins. A comparison between 100 and 150 bins is shown in Figure 5.40 and compared with the experiment. The CMC model with 100 bins seems to be insufficient to resolve the details around the mean mixture fraction space. The mean mixture fraction for this study is $Z_{mean} = 0.0271$ while the stoichiometric mixture fraction is $Z_{stoic} = 0.0637$. The mean is relatively low, hence a higher number of bins is required to resolve the details in that region of the mixture fraction space. The CMC with 100 bins shows a lower in-cylinder peak pressure and when the number of bins increased to 150, the in-cylinder peak pressure improved, which is close to the experiment. Thus, 150 bins for the CMC model are used for the validation and further study.

When comparing the constant C_D , the value used in this case is different compared to the *n*-heptane case. A difference in the engine model lead to a difference in the mixing coefficient, where the engine design also influenced the mixing rate in the combustion chamber. The value used for C_D in the validation is 2.0 as implemented by other researchers. Figure 5.41 shows the effect of varying C_D on in-cylinder pressure. High C_D increases the scalar dissipation rate during the intake process, as shown in Figure 5.42 (left). This results in a smaller variance as shown in Figure 5.42 (right), where the variance diminishes faster when the piston is moving towards TDC. The fuel amount reduces with higher C_D , which results in a lower in-cylinder peak pressure. Thus, a proper C_D has to be chosen, as also reported by Kim (2004), to achieve better agreement with in-cylinder pressure.

Even though the results for $C_D = 1.5$ show a good agreement with in-cylinder pressure compared to the experiment, there is a slight inconsistency in O_2 consumption during the main combustion event, as shown in Figure 5.43. Also, the N_2 is slightly increased when the simulation is nearly finished. This shows that there is a small instability when using a smaller C_D value. When C_D was set to 1.0, the O_2 consumption inconsistency becomes even worse during combustion where its amount is increasing after 30°CA . Thus, $C_D = 2.0$ shows a good result in chemistry computation, where the in-cylinder pressure is improved when the number of CMC bins is increased.

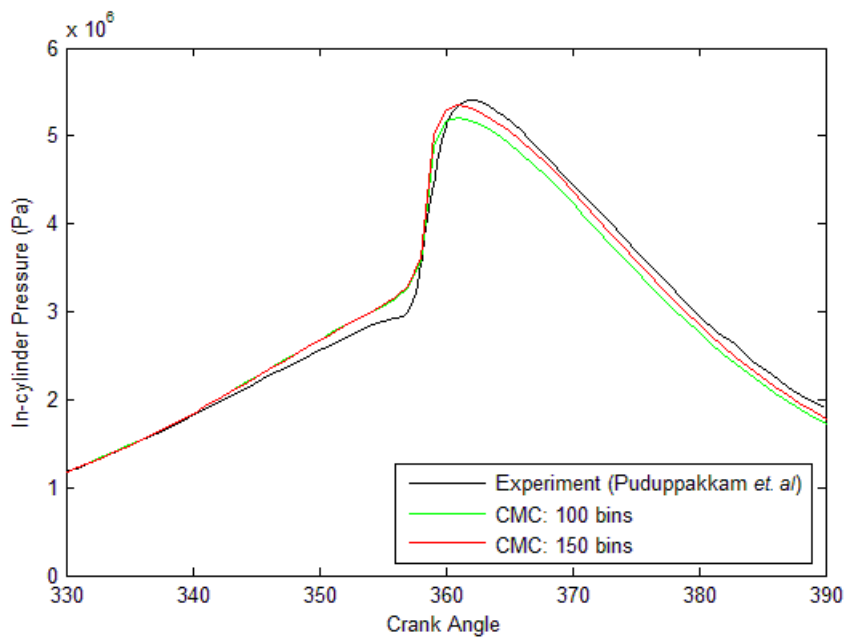


Figure 5.40 A comparison between the CMC model and the experiment, where the CMC model varies with 100 and 150 bins.

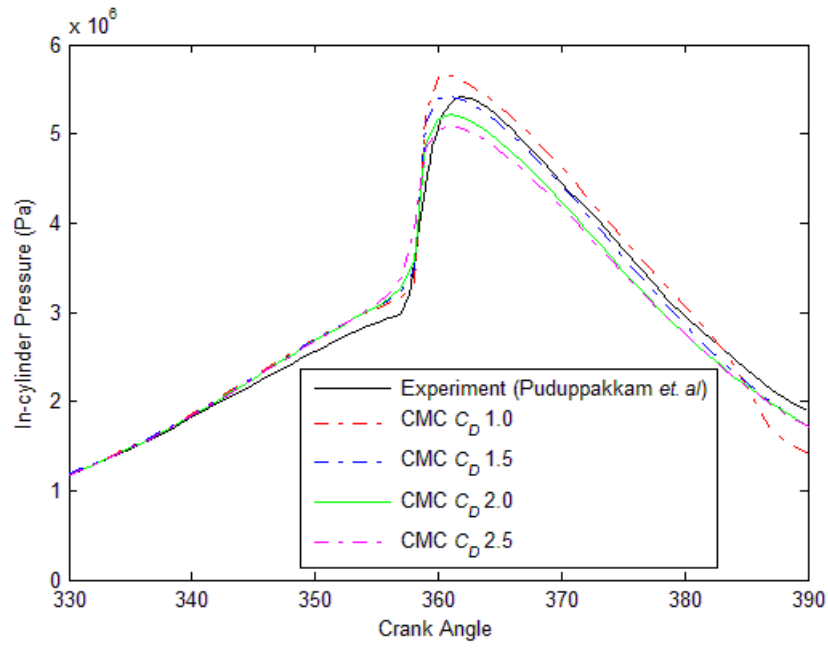


Figure 5.41 A comparison of constant of C_D used in the gasoline study and compared with the experiment.

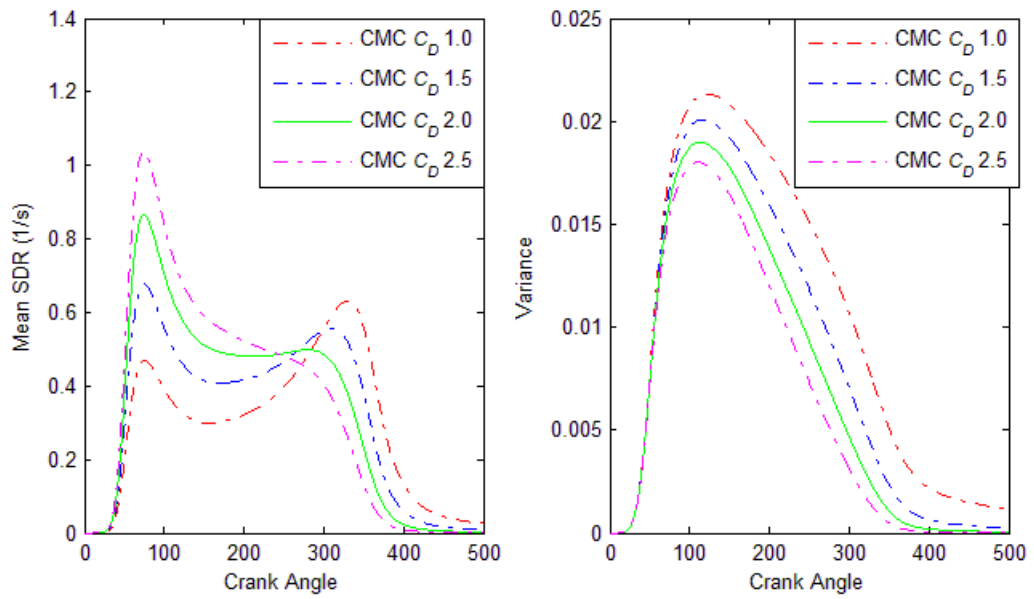


Figure 5.42 Global mean SDR (left) and variance (right) comparison over the entire simulation with varying C_D .

Chapter 5

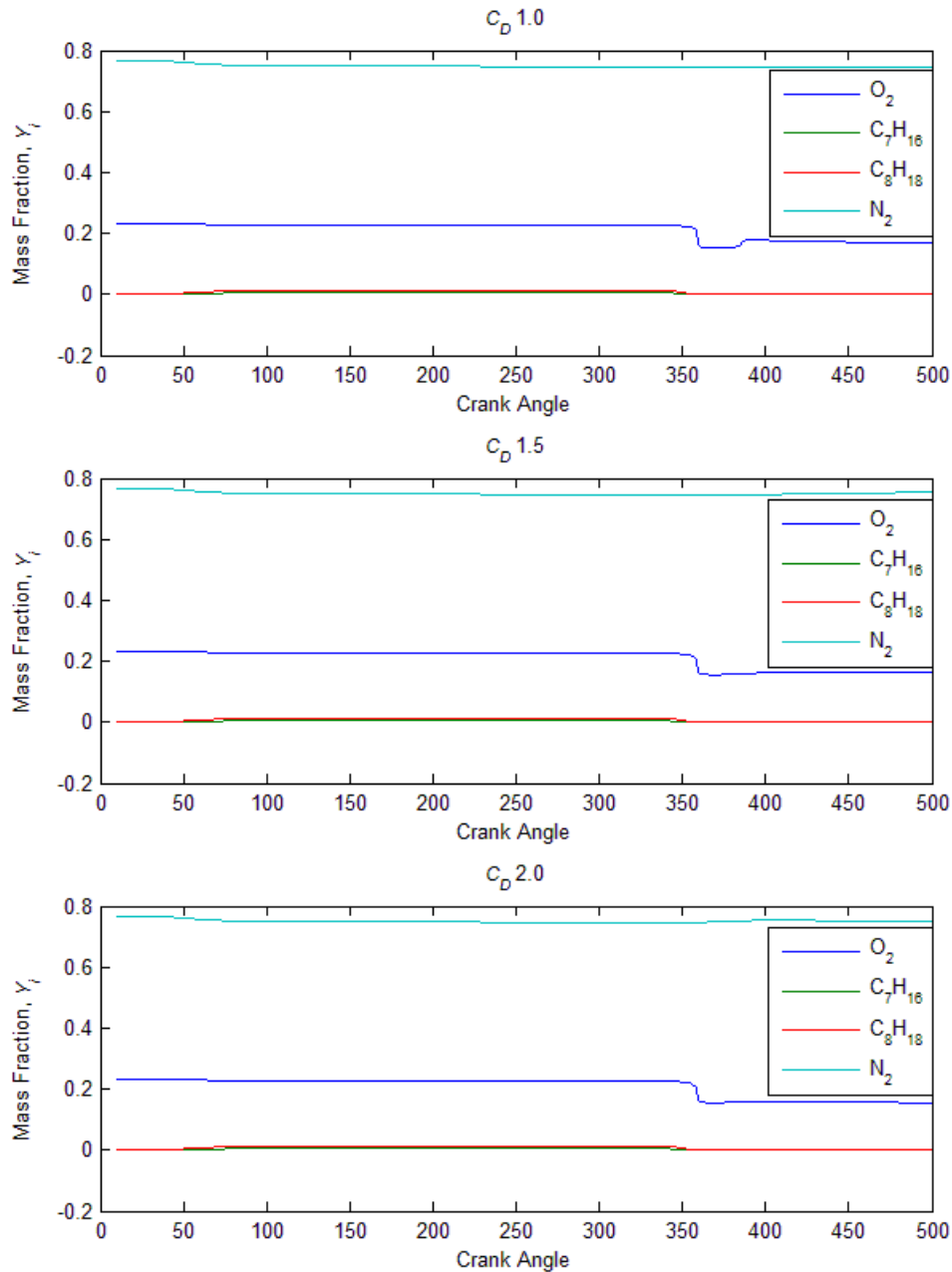


Figure 5.43 Oxidisers and fuels behaviour for the entire simulation with varying C_D .

5.7.2 Chemical Reactions

The chemical kinetics mechanism for gasoline fuel in this study was discussed in section 5.1.2, where it has a blend between *n*-heptane (C_7H_{16}), *iso*-octane (C_8H_{18}) and toluene (C_7H_8). The chemical reactions slowly occurred at approximately $335^\circ CA$ before the main combustion. Unlike the *n*-heptane case, the gasoline fuel exhibits a

single-stage ignition, as shown in Figure 5.44, where the figure shows the result of fuels' (C_7H_{16} , C_8H_{18} , C_7H_8) and oxidisers' (N_2 , O_2) mean mass fraction over the CA step for the entire simulation. A single-stage ignition for gasoline fuel is consistent with Kim, Kim and Lee (2004), where they reported that the combustion of a premixed gasoline HCCI engine can be controlled using the premixed ratio of the EGR rate and exhibits a single-stage ignition. In the experiment of a gasoline HCCI engine in this study (discussed in Chapter 8), the combustion in the HCCI engine was controlled by varying the intake temperature using heating without EGR.

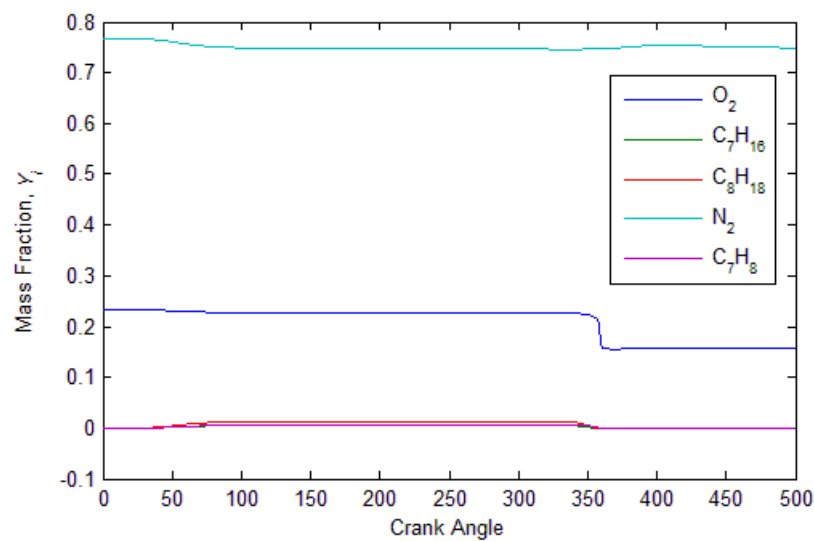


Figure 5.44 Mean mass fraction for the entire simulation for fuels (C_7H_{16} , C_8H_{18} , C_7H_8) and oxidisers (N_2 , O_2)

As reported by Aceves *et al.* (2000) and Maroteaux and Noel (2006), the combustion is initiated by the accumulation of H_2O_2 and this behaviour can be seen in Figure 5.45. The H_2O_2 accumulates before the main combustion is about to occur and as the fuel is slowly being consumed after $340^\circ CA$. The H_2O_2 is fully decomposed to OH radicals as observed by the rapid increase in the amount of OH during the combustion. The results also show that the radicals HO_2 , OH and H only have one peak, unlike *n*-heptane's case whose radicals have a double-peak to account for LTR. This confirms that the gasoline only has single-stage ignition, as supported by Kim, Kim and Lee (2004).

Chapter 5

The amount of H_2O_2 is fully reduced to almost zero (fully decomposed) when the in-cylinder temperature reached its peak. The amount of OH radicals is drastically increased at approximately 357°CA , about 2°CA after the amount of H and HO_2 are rapidly increased. The in-cylinder temperature at which the rapid increase of H and HO_2 occurred is at approximately 1200K, which is also consistent with Aceves *et al.* (2000), where the consumption of H and HO_2 radicals occurred at a high temperature. In this case, those radicals (H and HO_2) are drastically reduced when the in-cylinder temperature reached the peak at about 1800K. At the same time, the amount of CO and CO_2 are also increased during the combustion, where the amount of CO_2 is much higher than that of CO. The amount of CO reduces after the combustion, showing that the CO is converted to CO_2 to achieve chemical equilibrium.

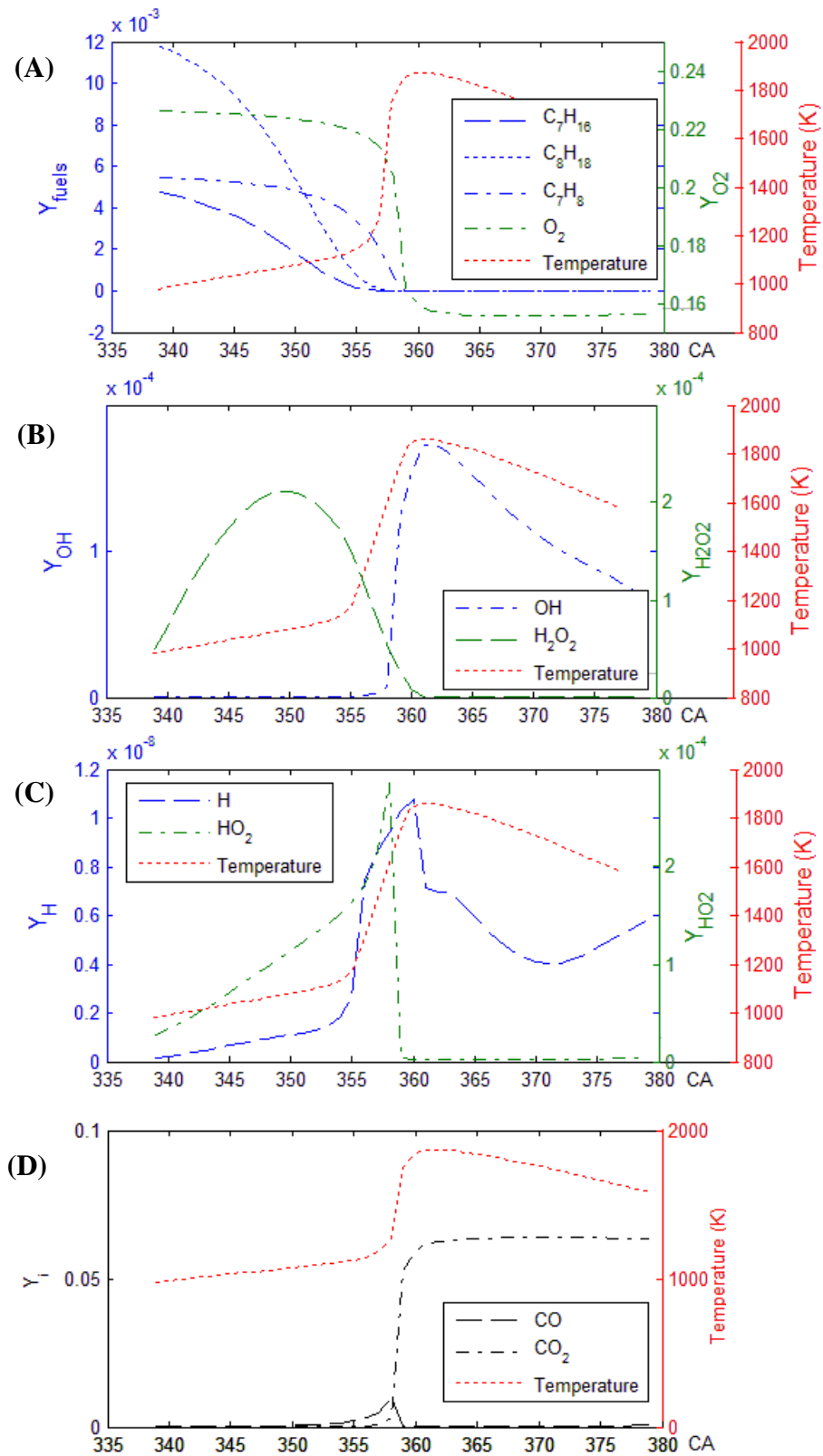


Figure 5.45 Mean mass fractions behaviour during the combustion event compared with in-cylinder temperature trace, A: C_7H_{16} , C_8H_{18} , C_7H_8 and O_2 , B: OH and H_2O_2 , C: H and HO_2 , D: CO and CO_2 .

5.7.3 Conditional Temperature

The conditional temperature for gasoline combustion is shown in Figure 5.46, where the results show the conditional temperature with varying CA steps during the combustion. The temperature starts to increase at the lean region of η -space, where $Z_{mean} = 0.0271$ and this can be observed at 357°CA and 358°CA. The Z locations of maximum temperature at 357°CA and 358°CA are 0.0269 and 0.0336 respectively. Then, the temperature increases towards the stoichiometric mixture fraction (De Paola *et al.* 2008; Seo *et al.* 2010) and reaches the peak at $Z = 0.0671$, which is close to the stoichiometric mixture fraction of 0.0637. After that, the temperature propagates towards the rich region of the η -space when the temperature is decreasing. Note that the conditional temperature profile only has one peak and confirms that the ignition for gasoline fuel is single-stage, as also reported by Kim, Kim and Lee (2004). This is in contrast with the *n*-heptane case, which has a secondary low peak during LTR, where the fuel has two-stage ignition. Thus, the gasoline mechanism with the CMC model can be used for further analysis.

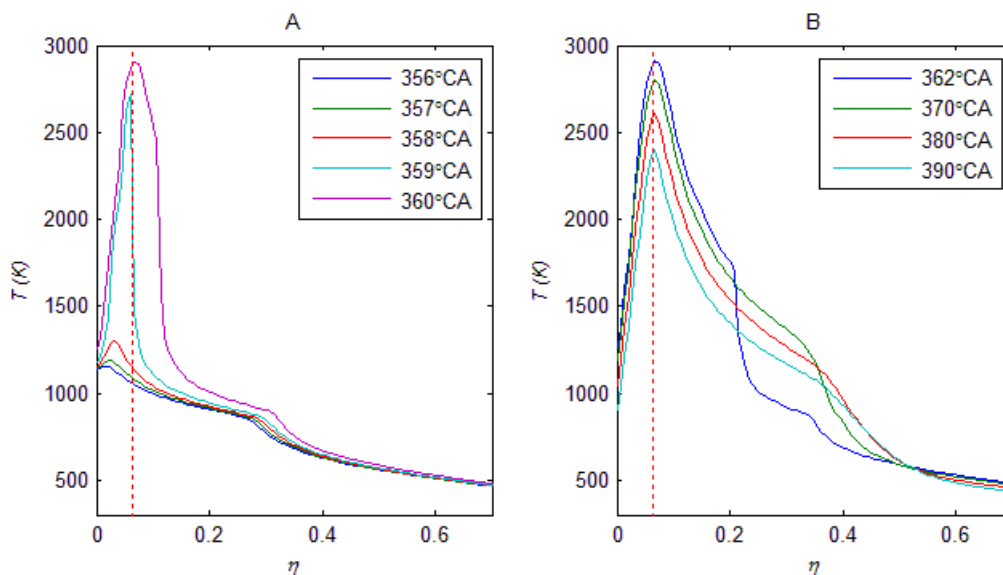


Figure 5.46 Conditional temperature for gasoline combustion with varying CA. The dotted red line shows the location of the stoichiometric mixture fraction.

5.8 Conclusion

This chapter has discussed the validation of the CMC and zero-dimensional models against experimental works from others. The validation covers the diesel and commercial gasoline fuels, where the diesel is represented by the *n*-heptane chemical reactions mechanism while the gasoline is a blend between *n*-heptane, *iso*-octane and toluene. Different heat transfer coefficient models were investigated so that the model is suitable for use with HCCI engines. In this case, a modified Woschni heat transfer coefficient was used for all simulations. Even though other models like Woschni and Hohenberg are also being used in HCCI engine models, the modified Woschni model shows better results because the equation was tuned according to the HCCI engine configuration.

For *n*-heptane's case, both the CMC and zero-dimensional models show good agreement with the experiment. The zero-dimensional model requires the intake temperature to be set 20°C higher than the actual to account for the mixing effects, while the CMC model does not need to tune the intake air temperature and can use the actual temperature. The CMC model shows better results than the zero-dimensional model in a validation test and also in the parametric study of varying intake temperature. However, the CMC model showed its limitation when AFR and hydrogen addition tests were performed. The limitation is due to the homogeneous equations of the CMC and zero-dimensional models, where the homogeneous model does not consider spatial variation.

The CMC and zero-dimensional models also show a good agreement with the experiment when a gasoline HCCI engine configurations are used. The CMC model shows a better result than the zero-dimensional alone without intake temperature tuning. However, a parametric study was not performed in this engine configuration. A parametric study for gasoline HCCI will be discussed in Chapter 8, where both models will be compared against the experimental data collected in this study.

Chapter 5

Chapter 6

EXPERIMENTAL METHODOLOGY

6.1 Introduction

A methodology employed to convert an SI engine to an HCCI engine is presented in this chapter. A single cylinder four-stroke SI engine was used in this work. Major modifications have been conducted to convert the engine to HCCI mode. The modification involves the engine management system, where an Electronic Control Unit (ECU) was added to the engine. The intake manifold was also modified to allow the installation of an air heater. A port fuel feeding system was replaced with an electronic fuel injection (EFI) system for safety reasons which will be discussed later in this chapter.

Many researchers have adopted the technique of using a high compression ratio for a gasoline HCCI engine (Dec & Yang 2010; Gerty & Heywood 2006; Koopmans & Denbratt 2001; Machrafi & Cavadias 2008; Yingnan *et al.* 2010). The advantage is that the engine will achieve diesel-like engine efficiency by employing a high compression ratio and lower emissions levels because of using gasoline as a fuel. However, the use of a low compression ratio (less than 12) in an HCCI engine with commercial grade gasoline fuel could cause deterioration in engine performance, which will be investigated in this study.

When operating an HCCI engine in a low compression ratio setup, *n*-Heptane is normally used (Charalambides 2006; Guo *et al.* 2010). The reason is that the *n*-heptane has the same characteristic as a diesel fuel in terms of its cetane number, which is susceptible to auto-ignition. Thus, HCCI mode would easily be achieved in a low compression ratio engine with a small increment in the intake air temperature; about 40-90°C (Guo *et al.* 2010).

Commercial grade gasoline, on the other hand, is unable to operate in HCCI mode in a low compression ratio engine with only a small increment in the intake air heating and without EGR. The transition point between SI and HCCI has to be achieved before switching to HCCI mode (Charalambides 2006; Dec & Yang 2010), where for a low compression ratio engine without EGR, the intake air temperature has to be at least 210°C (Charalambides 2006).

Therefore, a major modification has to be made for the single cylinder SI engine used in this study to achieve HCCI mode. In addition, most of the HCCI studies focus on the fundamental knowledge behind the combustion mechanism and also the techniques to improve the HCCI engines (Aceves *et al.* 2001; Aceves *et al.* 2000; Amneus *et al.* 1998; Dec & Yang 2010; Ganesh & Nagarajan 2010; Hyvonen, Haraldsson & Johansson 2003; Kawano *et al.* 2005; Kim & Lee 2006; Komninos 2009b; Komninos & Kosmadakis 2011; Sheppard, Tolegano & Woolley 2002). In this study, a side-by-side comparison of engine performance between SI and HCCI modes will be performed experimentally using the same engine configuration, because there is limited information in the literature.

This chapter discusses the experimental methodology, with Section 6.2 discussing the experimental apparatus, followed by the modification to an HCCI engine in Section 6.3. Then, the use of an Electronic Control Unit (ECU) is discussed in Section 6.4 and experimental techniques are discussed in Section 6.5. The chapter ends with a conclusion.

6.2 Experimental Apparatus

6.2.1 Engine Test Bed

The engine used in this study is a single cylinder Honda GX160 connected to a portable hydraulic dynamometer on a fixed test bed. The type of the engine is a four stroke engine with two-valve, flat crown piston, pull starter and is fully commercialised. The engine was originally in SI mode with a fixed compression ratio (CR) and is air-cooled. The valve is operated with a tappet mechanism and connected to the crank shaft via a gear system, as shown in Figure 6.1. The engine specification is presented in Table 6.1, where the rated power for the SI engine claimed by the manufacturer is 3.6 kW at 3600 rpm with 10.3 Nm of torque at 2500 rpm.

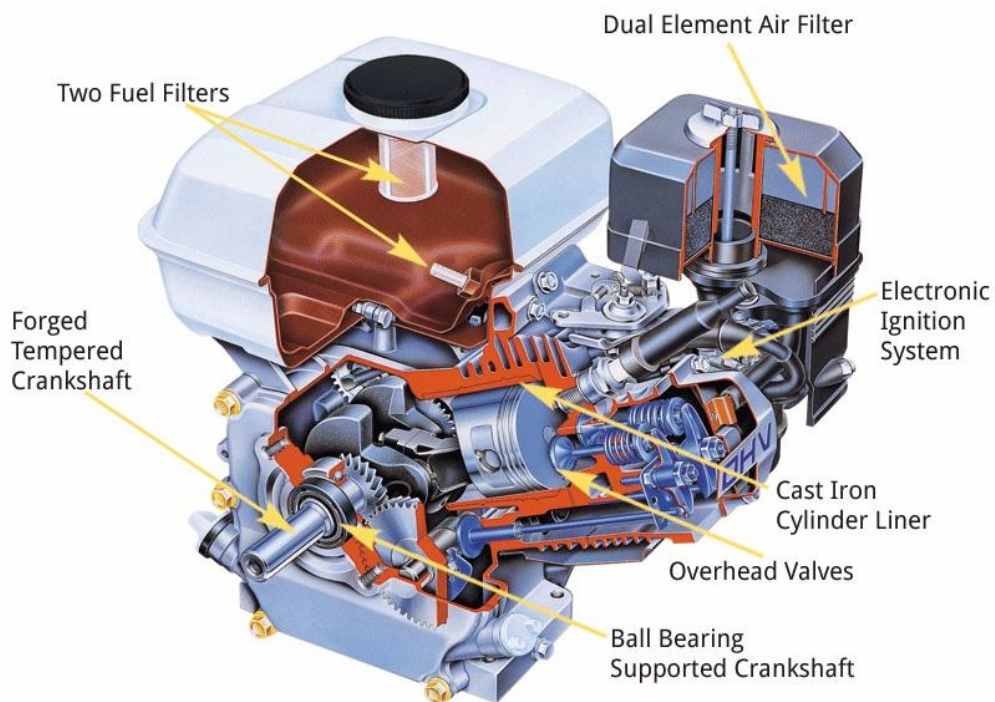


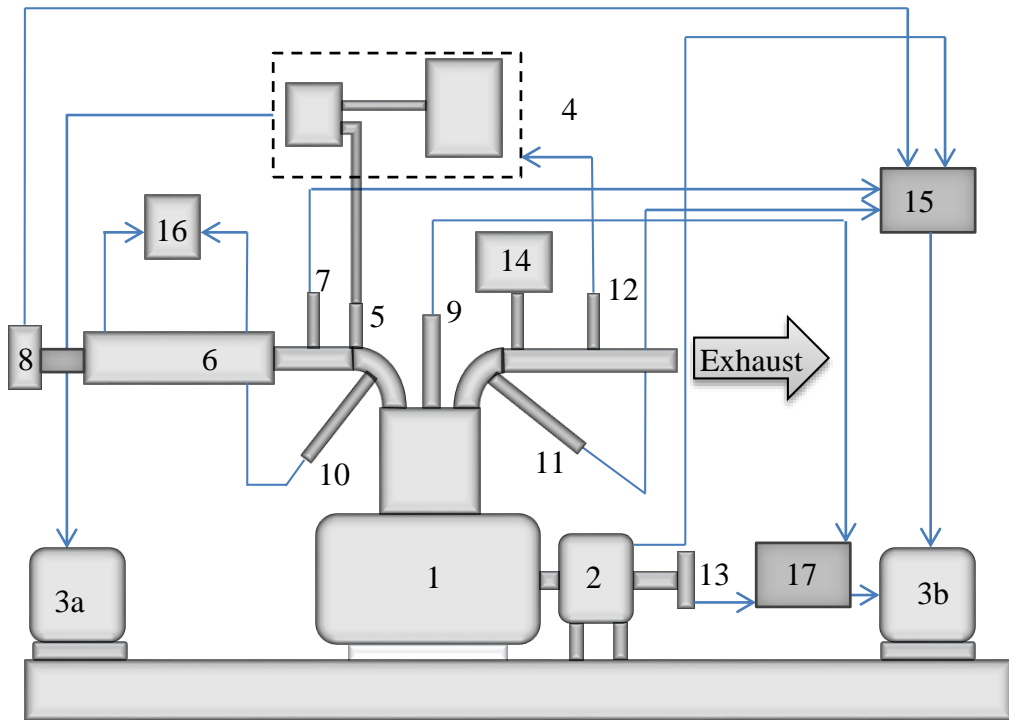
Figure 6.1 Cross-sectional view of the standard engine (Honda 2012).

Chapter 6

Table 6.1 Engine parameters used in this study

Engine Parameter	Honda GX160
Engine Type	Air-cooled 4-stroke overhead valve
Displacement	163 cc
Bore x stroke	68 x 45 mm
Compression ratio	9:1
Number of valves	2
Inlet valve diameter	24.9 mm
Inlet valve lift (max)	5.8 mm
Inlet valve open (°CA ATDC)	10.5
Inlet valve closed (°CA ATDC)	201
Exhaust valve diameter	23.9 mm
Exhaust valve lift (max)	5.8 mm
Exhaust valve open (°CA BTDC)	207
Exhaust valve closed (°CA ATDC)	12.5
Con-rod length	60.45 mm
Fuel	Gasoline RON91 unleaded
Rated power (kW)	3.6 at 3600 rpm
Rated torque (Nm)	10.3 at 2500 rpm

The experimental setup diagram is shown in Figure 6.2, where the engine was connected to various sensors and actuators. Two computers (PC) were used, as shown in the diagram and each PC recorded or monitored a different set of data. One PC was used to monitor or record the reading from the ECU and the other one for the dynamometer system, which has its own software. The pressure and encoder sensors were connected to the PC with the dynamometer system. Each of the sensors and actuators connected to the engine will be discussed in the following sections, as will the ECU details. A detailed experimental setup is shown in Figure 6.3, where the setup complied with all safety measures required by the university's safety body.



- | | |
|-----------------------------------|---|
| 1 Engine | 9 Pressure transducer |
| 2 Dynamometer | 10 Inlet temperature sensor |
| 3(a-b) PCs for data logger system | 11 Exhaust temperature |
| 4 ECU and Ignition systems | 12 Lambda sensor |
| 5 Fuel injector | 13 Rotary encoder |
| 6 Air inlet heater | 14 Exhaust gas analyser |
| 7 Inlet pressure sensor | 15 Data logger for the dynamometer system |
| 8 Airflow meter | 16 Temperature controller box |
| | 17 Data acquisition system |

Figure 6.2 Experimental setup diagram for an HCCI engine.



Figure 6.3 Engine setup in the engine laboratory.

6.2.2 Dynamometer

A portable water brake type dynamometer from Land and Sea was used in the study. The dynamometer model is DYNomite 5” with maximum power of 25 horsepower (Hp) at 4000 rpm, which is more than enough for the current engine. The dynamometer is connected to its own data logger and software, which can be used to measure power, torque and various sensor readings. Many sensors (including a weather station to determine atmospheric pressure, temperature and humidity) can be added to the system and the readings will be displayed on its software interface. In this study, only some sensors (inlet pressure, exhaust temperature and air flow meter) and actuators (load and throttle controllers) were connected to the dynamometer’s data logger system.

The dynamometer has a rotor inside the enclosure, which acts as a brake when water passes through. The water is controlled by an adjustable inlet valve and orifice. Increasing the water level will increase the rotor drag and thus apply more resistance to the engine. The dynamometer was controlled using an automatic controller, where the controller adjustment was made via the software. Figure 6.4 shows the dynamometer connected to the engine together with its automatic controller. The automatic controller was set up to have two sets of load increments, one with 5% increments for coarse tuning and the other with 1% increments for fine tuning.



Figure 6.4 The dynamometer connected to the engine (left) with its controller (right).

6.2.3 Instrumentations

6.2.3.1 Thermocouples and Pressure Sensors

Two thermocouples and three pressure sensors were used in this study. The thermocouples were used to measure the intake and exhaust temperatures, while two pressure sensors were used to measure the intake pressure and in-cylinder pressure. The intake and exhaust temperatures were measured using a K-type thermocouple. This type of thermocouple provides the widest operating temperature range, where the common range is between -270°C and 1250°C . The thermocouple for the intake air temperature was installed close to the intake port, as shown in Figure 6.5. The thermocouple reading was sent to the temperature controller box, which was used to control the mixing temperature in the intake manifold.

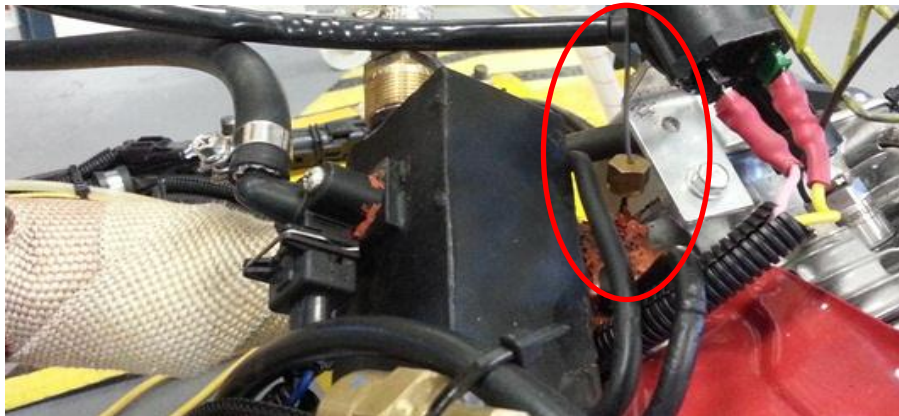


Figure 6.5 Intake temperature sensor location next to the intake port, as circled in red.

The exhaust temperature thermocouple was installed next to the exhaust port to give real time exhaust temperature reading with less heat loss to the environment. Figure 6.6 shows the location of the exhaust temperature sensor, which is close to the exhaust port. The sensor was connected to the Land and Sea data logger system, where the exhaust reading was monitored through its software.

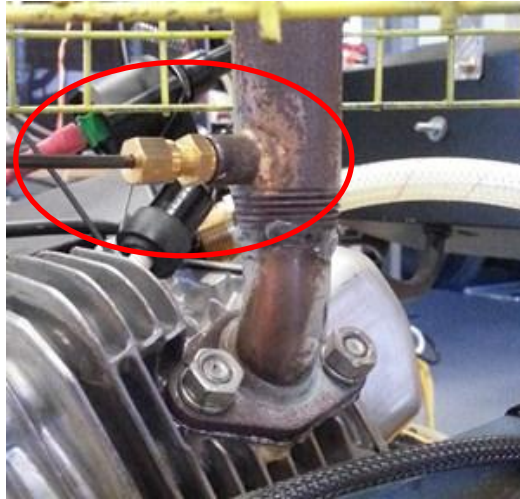


Figure 6.6 Exhaust temperature sensor was installed after the exhaust port, as circled in red.

The intake pressure, on the other hand, was measured using a pressure sensor, as shown in Figure 6.7 (left). The sensor has a measuring range between -82.74 kPa and 151.68 kPa. This type of sensor was chosen because no pressurising applied to the intake manifold. The intake manifold has a maximum pressure of 0.997 atm or 99.7 kPa at an altitude of about 600 m above sea level. The intake pressure reading was sent to the dynamometer's data logger system. Another intake pressure sensor, Figure 6.7 (right), was used to give the intake pressure reading to the Electronic Control Unit (ECU), where the sensor joins the ECU package.



Figure 6.7 Intake pressure sensors from Land and Sea (left) and for ECU (right)

For the in-cylinder pressure, the pressure transducer used was a spark plug type with model number 6118AFD35Q04 from Kistler. It has a measuring range from 0 MPa to 1.5 MPa. The transducer was connected to the Kistler SCP-Slim amplifier (type 5064) to amplify the signal before it was read by the data logger. In-house calibration was required to confirm the reading from the transducer even though the pressure transducer had been factory calibrated. The calibration technique is discussed in Appendix B.

6.2.3.2 Rotary Encoder

The rotary encoder was used to measure the engine speed and to recognize the location of top dead centre (TDC). The encoder was installed on the engine's Power Take-Off (PTO) shaft, which was connected after the dynamometer, as shown in Figure 6.4. The resolution of the encoder is 720 pulses per revolution, which records 1440 data points per engine cycle. The encoder was connected to a 5V DC power supply and the data logger from National Instruments was used to record the data.

6.2.3.3 Lambda Sensor

The lambda (λ) sensor comes with a digital display which uses a Bosch driver chip CJ125 and a Bosch LSU4.9 oxygen sensor. The Bosch LSU4.9 sensor is used to measure the exhaust gas oxygen, where the sensor type is a wideband λ sensor. The oxygen sensor used in this study has a wide range λ reading from 0.65 - ∞ and the fuel can be tuned based on the λ on the display. The sensor was installed further downstream from the exhaust port to avoid high temperature effects from the exhaust, which could damage the sensor. The display of the lambda sensor can be programmed to either show AFR or λ value.

6.2.3.4 Airflow Meter

The airflow meter used in this study is a low-inertia turbine type installed directly to the intake manifold, before the throttle body. The air will pass through, which will turn

the turbine. High turbine rotation shows a high air flow rate. The part number for the air flow meter is 430-803, which has an inlet diameter of three inches. The turbine has a measuring range of 1.7-85 m³/h. Figure 6.8 shows the air flow meter installed onto the inlet manifold in the L-shape due to space constraints.



Figure 6.8 Air flow meter connected to the inlet manifold before the throttle body.

6.2.3.5 Exhaust Gas Analyser

An exhaust gas analyser (model EMS 5002) was used to measure the concentration of O₂ (0-25%), CO (0-10%), CO₂ (0-20%), HC (0-2000 ppm) and NO_x (0-5000 ppm). AFR was also calculated when the gas analyser was connected to the dynamometer software on the PC. The exhaust gas analyser has an accuracy of 1% with a fast response time and is connected via a 12V DC connection.

6.2.4 Fuel Measurement

A 50 ml burette was used to measure the fuel consumption. The burette was connected to the fuel tank via a three-way valve. A ball valve was also used to open or close the fuel flow from the fuel tank. The ball valve was located before the three-way valve, at the bottom of the fuel tank, as shown in Figure 6.9. The ball valve was opened while the three-way valve handle was positioned towards the operator in order to fill the fuel into the burette. Once the fuel was about the same level as in the fuel tank, the ball

valve was closed and the three-way valve handle was left at its current position. In this position, the fuel flows straight to the fuel pump from the burette instead of the fuel tank. The measurement was taken five times at each operating condition and then averaged to reduce the parallax error.

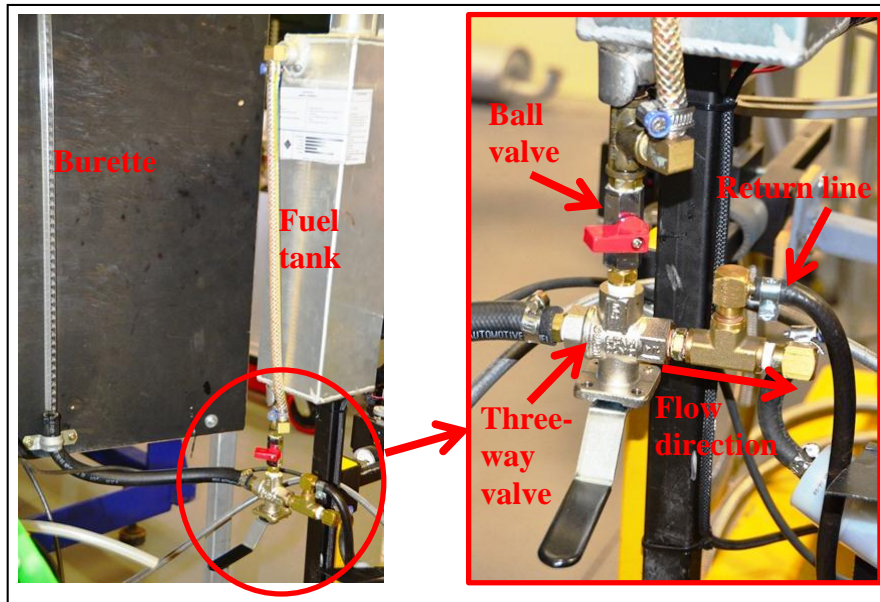


Figure 6.9 The burette and fuel tank were installed side-by-side (left) and an enlarged picture of the area circled in red contains the ball valve, three-way valve and fuel flow direction (right)

6.3 Modification to an HCCI Engine

HCCI mode can be achieved by using several techniques, such as increasing the air intake temperature and compression ratio, exhaust gas recirculating and negative valve overlap, as discussed in Chapter 2. Most of the engine configurations used in this study are fixed and there was not much room available for modifications considering time and cost. Because the engine has a fixed compression ratio, the easiest option available to achieve HCCI is to use a high air intake temperature. Thus, modification of the existing engine to operate in HCCI mode requires major changes in the air intake system.

Therefore, an air heater was chosen and installed in the intake system. To achieve this, the entire air intake system of the engine was modified, which will be discussed in the

following sub-sections. This change led to a modification of the other systems, including the fuel delivery system. The engine was then operated and evaluated based on its current unmodified compression ratio. The compression ratio was not modified, in order to reduce the modification work on the engine.

Safety issues were made a high priority when modifying the engine. Thorough safety identification was conducted between the laboratory and the safety auditor. The engine, surrounding, laboratory facilities and how to operate the engine were checked. The modification work was then performed according to the safety check.

6.3.1 Air Intake Heater

Installation of the air intake heater required the original air intake system and carburettor to be removed. The carburettor was replaced with an Electronic Fuel Injection (EFI) system. The intake manifold was redesigned to accommodate the heater and EFI. The EFI came with an Electronic Control Unit (ECU) and has its own fuel delivery system. The ECU is discussed in more detail in Section 6.4. The original fuel tank shown in Figure 6.1 was also removed. It was replaced with an in-house fuel tank as shown in Figure 6.9, which was easier to set up and keep away from any heat source.

The reason for replacing the carburettor with the EFI system was to remove any plastic parts in the air intake system. Hot air causes the plastic parts to melt. The fly valve in the carburettor has a plastic part in the middle of it and a failure occurred during the initial test. The plastic part melted when the air intake temperature reached 100°C, as shown circled in red in Figure 6.10. Due to this reason, the carburettor had to be replaced to ensure there were no plastic parts along the air intake system. Another reason for replacing the carburettor was to avoid the fuel in the small carburettor tank vaporising, as discussed in Section B.3.



Figure 6.10 Failure occurred on the plastic part of the fly valve of the carburettor due to the hot air, where the plastic part melted. The carburettor was then removed and replaced with an EFI.

Modification to an HCCI engine was started by choosing the right heater for the engine, which was achieved by installing a 2 kW heater in the air intake manifold. The required power of the heater was obtained based on the manufacturer's calculations. At the beginning, the maximum air intake flow rate has to be calculated, where the calculation assumes 100% volumetric efficiency (VE). Maximum VE gives the maximum air flow to the engine, as represented by

$$SCFM = \frac{V_a N}{3456} VE$$

where $SCFM$ is the air flow rate in standard cubic feet per minute and N is the engine speed in RPM. The maximum air flow should occur at the maximum engine speed and wide-open-throttle (WOT) condition. Thus, at $N = 3600$ rpm and $V_a = 9.7638$ in³, the maximum $SCFM$ is 10.17 ft³/min. Then, the power (in Watts) was obtained by using

$$P = \frac{SCFM(\Delta T)}{3}$$

where ΔT is the temperature difference in °F. The desired maximum intake temperature is 350°C and the room temperature during winter in the morning is about 15°C. This gives $\Delta T = 603$ °F. By using all these calculations, it can be seen that the

maximum required power for the heater would be 2044 W. Therefore, a 2 kW heater would be sufficient to heat the intake air given the calculation based on 100% VE , where the actual VE of the engine is less than that.

The heater is a flow-torch type using a 240 V single phase power supply. Two K-type thermocouples were pre-installed in the outlet of the heater. However, these thermocouples were not used because the location was too far from the intake port. The thermocouple used for the intake air temperature measurement and connected to the temperature controller box was discussed in Section 6.2.3.1. The heater has a maximum heating temperature of 755K at a maximum air flow rate of 195.4 m³/h. The minimum operating pressure was 0.0012 bar. Figure 6.11 shows the diagram of a modified air intake system, where the heater was installed downstream of the fuel injector.

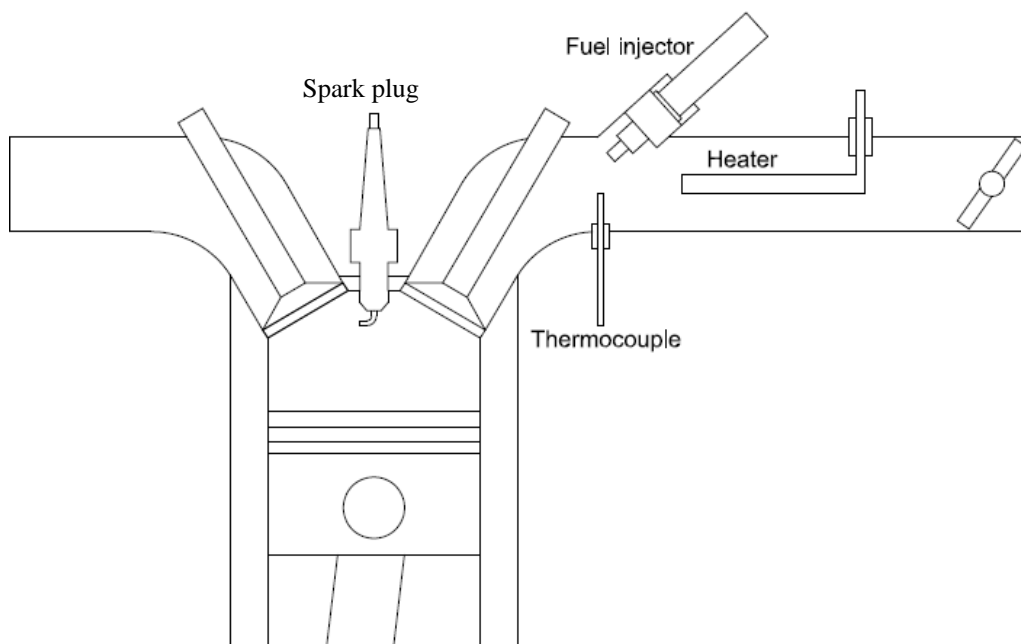


Figure 6.11 HCCI conversion by using a heater installed in the intake system.

A schematic diagram of the intake manifold modification to accommodate the heater is shown in Figure 6.12. The EFI is located at part number 4, which has a port to fit the EFI in and this part is close to the intake valve. Part number 5 and 6 are an adapter to connect to the throttle body, which has slightly smaller diameter. The heater is

located in between them and all these parts were fabricated by the university's mechanical workshop. The details of the drawing, which include all the dimensions, are attached in Appendix C.

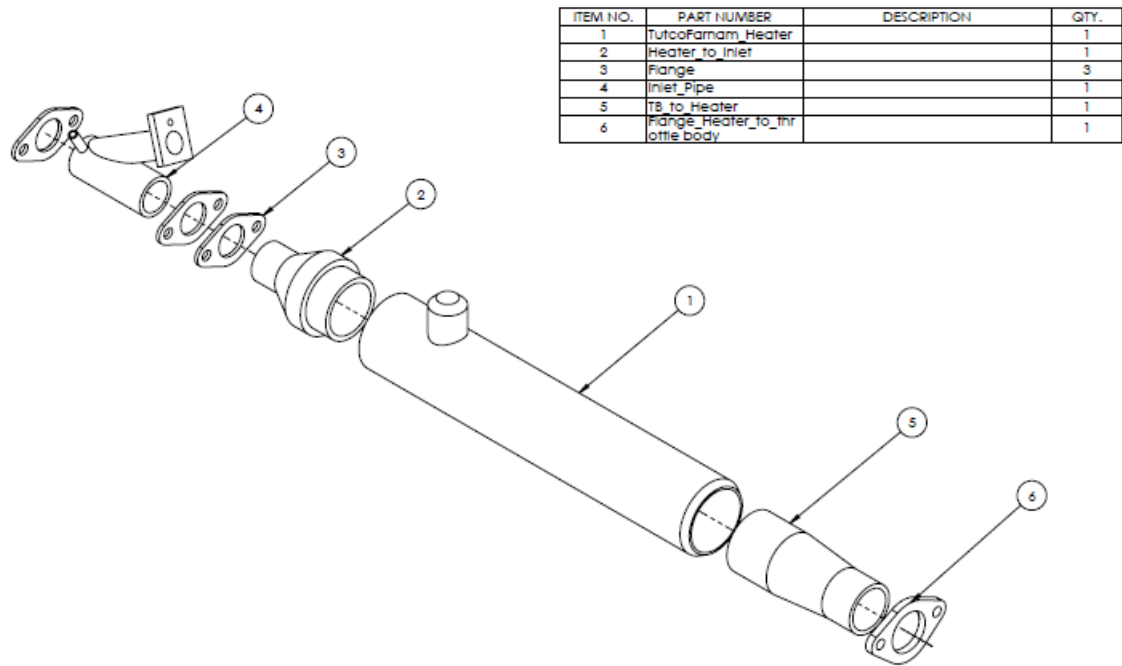


Figure 6.12 Engineering drawing shows the modification of the inlet manifold to install the heater

The physical location of the heater was fixed in the intake manifold, as shown in Figure 6.13, where the heater was installed in between the throttle body and the EFI. The heater was wrapped with a heat shield to ensure the heater body was not exposed to the environment (Figure 6.13 bottom). The temperature at the heater outlet was controlled by using the temperature controller, in a resolution of ± 1 °F. A high air intake temperature causes the port's wall (part number 4 in Figure 6.12) holding the EFI (which is made of steel) to be heated as well. Because the EFI has a plastic base with a rubber O-ring as a seal, the port's wall needs to be cooled down. Thus, a water jacket was installed around the EFI to ensure the EFI was always in a good condition, as shown in Figure 6.13 (bottom).

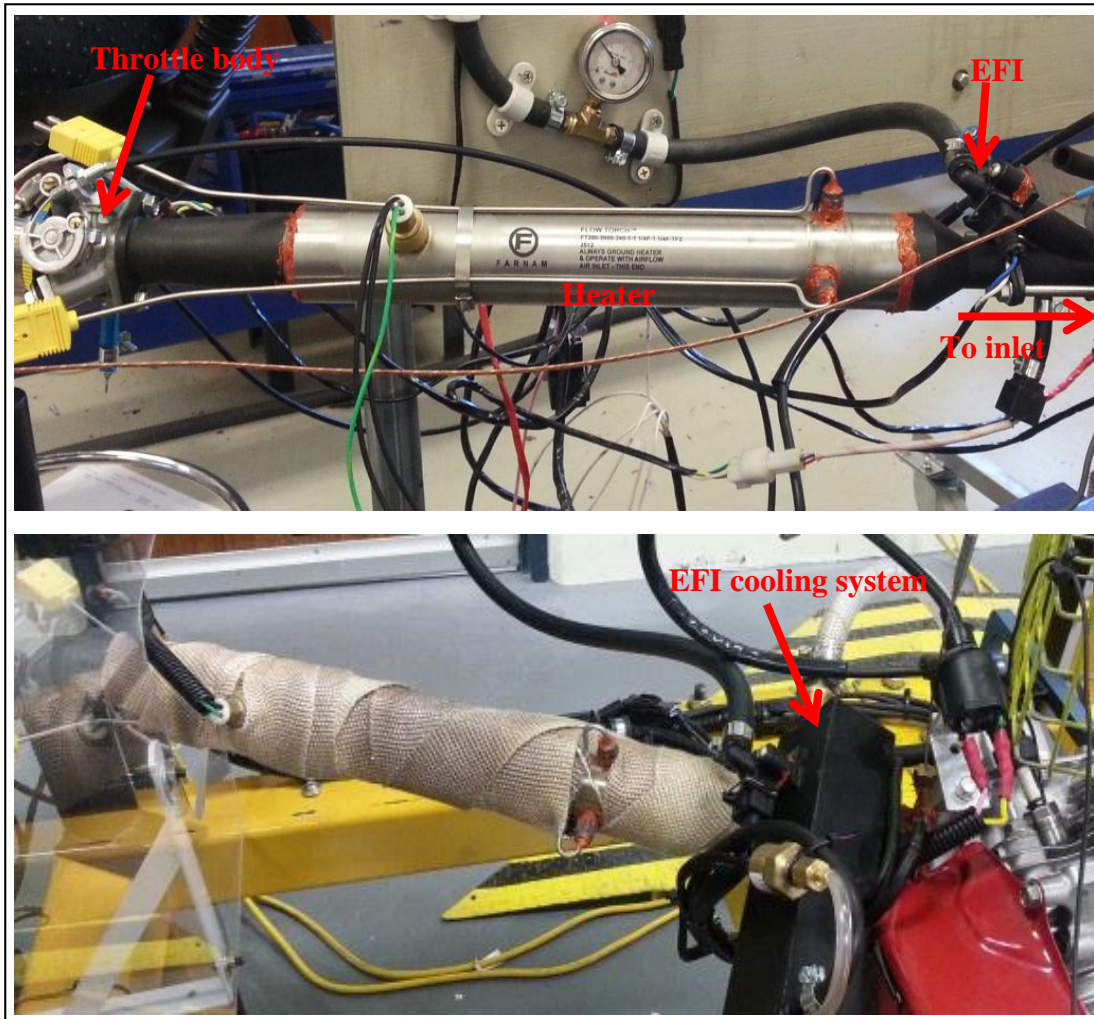


Figure 6.13 Top: The bare heater was installed in between the throttle body and the EFI in the inlet manifold. Bottom: The heater in the final setup with heat shield and also a water jacket installed around the EFI to prevent the plastic part from melting.

The EFI cooling system also helps to cool down the air used to measure the intake pressure. There were two intake pressure sensors used in the study; one of them connected to the ECU and the other one to the dynamometer software. The sensor connected to the ECU has a plastic base, which could melt if the air is too hot. Thus, the air used to measure the intake pressure has also been cooled down. An exploded view of the cooling system is shown in Figure 6.14, where there are two rolled tubes inside the water jacket to prevent hot air from reaching the pressure sensors. Those parts were also fabricated by the university's mechanical workshop. The details of the drawing are included in Appendix D.

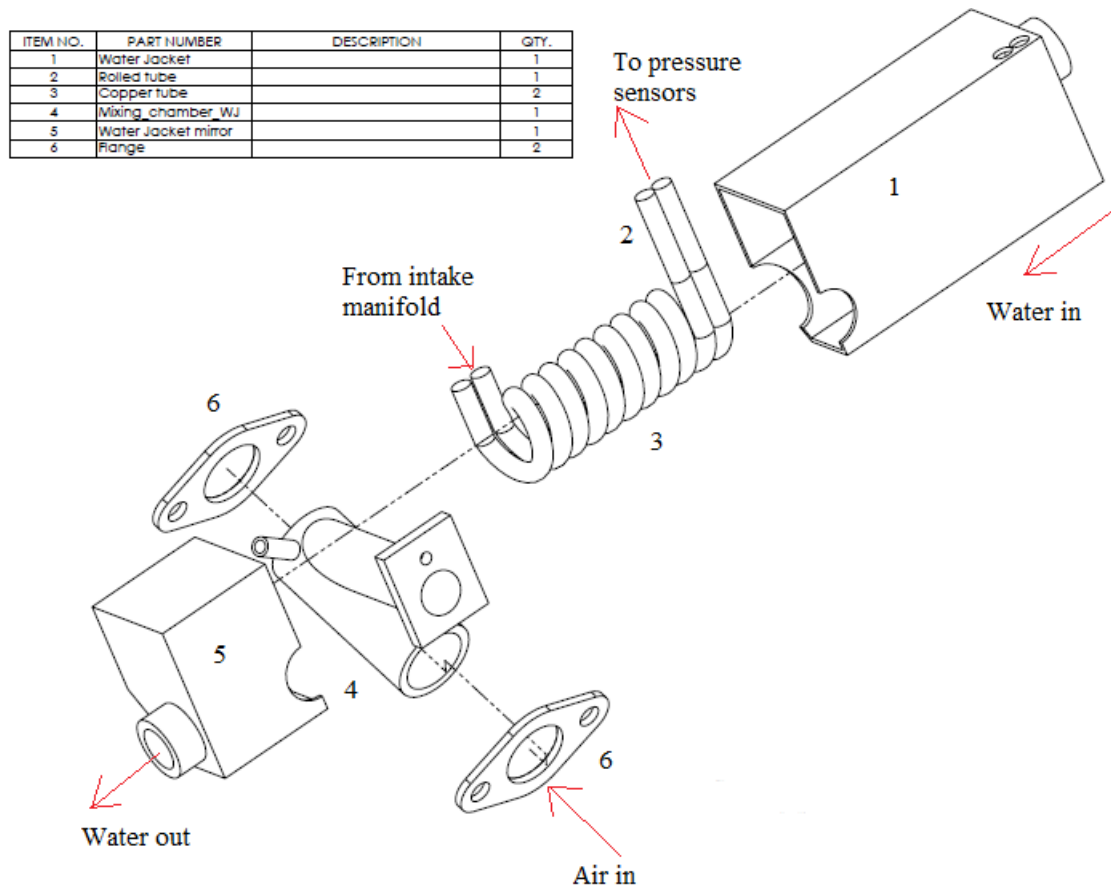


Figure 6.14 Exploded view of the water cooling system for the EFI and pressure sensors.

6.4 Electronic Control Unit (ECU)

The use of the EFI requires an ECU to be installed in order to control the fuel injection rate for precise fuel-air mixing. The ECU used in the study was a commercial type for motorbikes or any small size engines and can be re-programmed to suit the specific engine. The ECU and EFI have been pre-programmed according to the engine specification. Thus, a little more programming was required on the ECU to fine tune the engine operation to suit the current environment. The ECU was installed using the manual provided by Ecotrons (Ecotrons 2013) and the engine was tested after the installation was completed. Detailed information about the ECU is discussed in Appendix B.

6.4.1 ECU Program

Once the ECU installation was finished, the ECU required a little programming to adapt it to the current engine conditions and environment. To do this, ProCAL software version 7.2.4 from Ecotrons was used. This software communicates with the ECU via a Universal Serial Bus (USB) connection on the computer. Figure 6.15 shows the user interface of the software, where the software can also be used to monitor the readings from all sensors connected to the ECU. The data which can be displayed on the software, as shown by the dials, are the engine speed (RPM), manifold absolute pressure (MAP), throttle position sensor (TPS), engine temperature (ECT), intake air temperature (IAT), oxygen sensor (O2S), spark timing (SPARK) and fuel pulse-width of the injector (FUELPW1). The software can also be used to record all the ECU readings by pressing the record button.

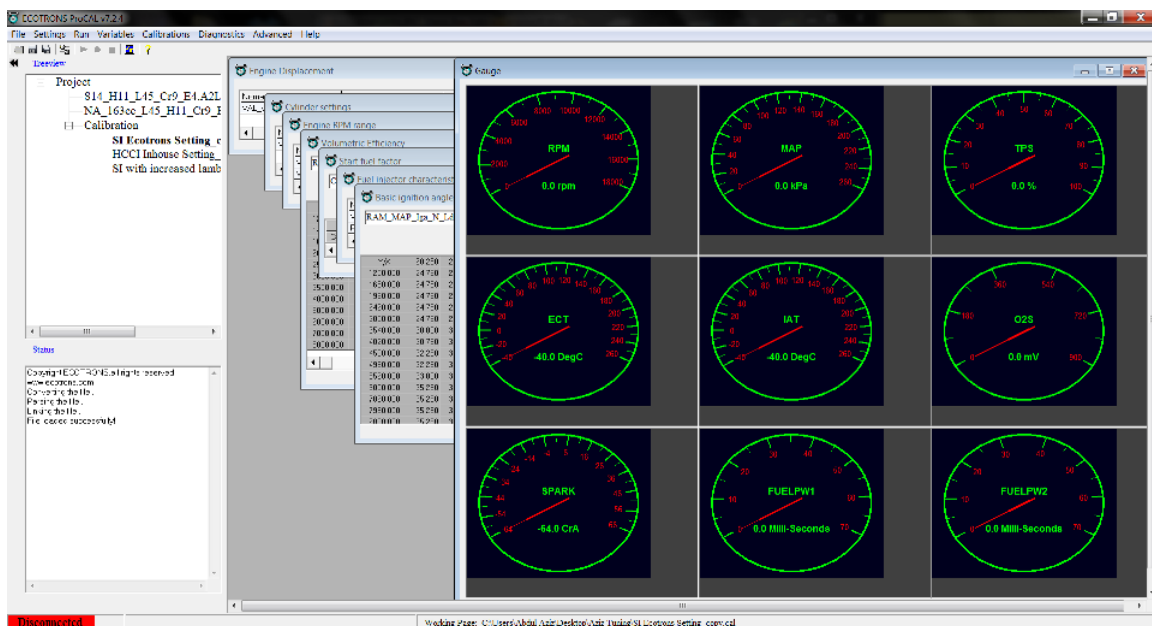


Figure 6.15 ProCAL version 7.2.4 user interface, which can show the readings from all the sensors connected to the ECU.

The engine capacity must be set correctly. To check this, one can click on Calibrations - System Parameters - Engine Displacement. A dialog box as shown in Figure 6.16 will pop up. The value can be changed according to the engine displacement size and in this case it was set to 163.

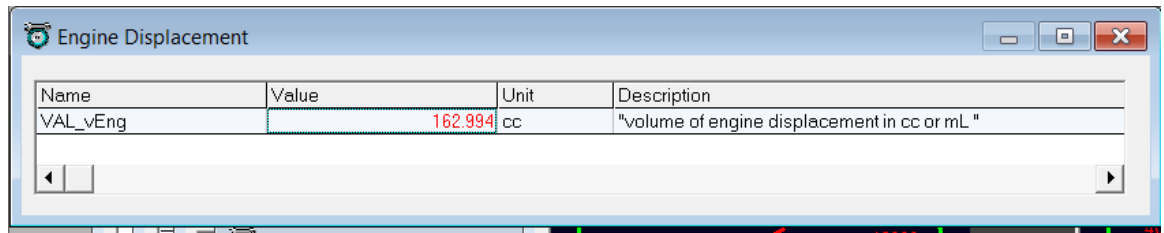


Figure 6.16 Engine displacement setting

The engine speed range also needs to be set correctly. The setting can be accessed via Calibrations - System Parameters - Engine RPM Range and a dialog box as shown in Figure 6.17 will pop up. The maximum value (3600) was set according to the engine specification from the manufacturer. Once the engine speed goes beyond the set point, the ECU will cut-off the EFI, thus leaving the engine speed at the maximum set value.

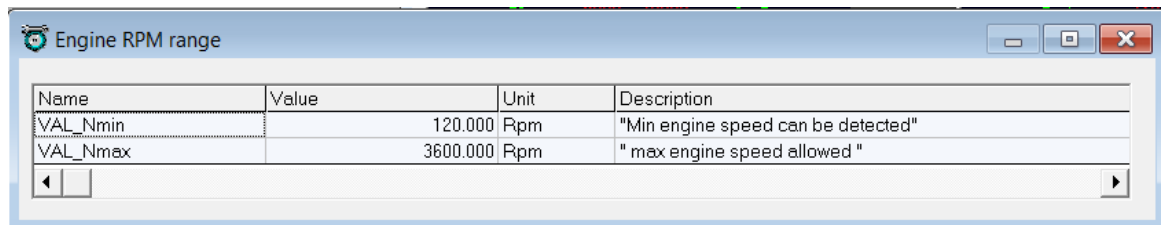


Figure 6.17 The setting for the maximum engine speed

The start fuel factor is an important tuning parameter in order to get the engine started. The start fuel factor varies from one engine to another. If the intake manifold has been modified substantially, the start fuel factor would be different from the one pre-set by Ecotrons. The start fuel factor works by multiplying the base fuel amount with the factor set as in Figure 6.18. The amount of fuel required to start the engine is increased and it is normal for the engine to run rich during the warming-up process. The colder the environment, the higher the fuel amount required to start the engine. The start fuel factor reduces to 1 as the engine temperature increases. Once the engine temperature has reached 90°C, the fuel amount is injected as normal based on the operating condition of the engine. The start fuel factor can be changed by clicking Calibrations - Fuel System - Start Fuel Factor on the ProCAL menu.

TmSta	-30.000	-25.000	-20.000	-15.000	-10.000	0.000	10.000	20.000	30.000	41.000	60.000	90.000
CUR_fCldSta_TmSta	25.000	20.000	16.000	13.000	10.000	8.500	5.500	4.500	3.000	3.000	1.500	1.000

Figure 6.18 Start fuel factor used for this engine

Once the above parameters have been set, advanced tuning is required to get the engine running in HCCI mode. The tuning required here is a set point (also called engine map) which determines the fuel amount to be injected at each operating condition. There are three methods that can be used for tuning: speed density, alpha-N and blended method (Ecotrons 2013). The speed density method uses the volumetric efficiency (VE) factor to determine how much fuel to be injected, which is dependent on engine speed and intake pressure. Alpha-N uses a load based system, where the load can tell the ECU how much fuel is needed for the desired air-to-fuel (AFR) ratio. Alpha-N depends on the engine speed and throttle position. The blended method is a combination of speed density and alpha-N, which has more accuracy. However, for low engine speeds (below 8000 rpm), the speed density method often gives good enough control and Ecotrons used this method for most of the engine calibrations (Ecotrons 2013). Thus, in this study, the speed density method was used for engine tuning, meaning the VE table needs to be examined.

Most of the programs have been pre-set by Ecotrons according to the engine specification. However, the ECU program that was pre-set by Ecotrons was based on the original engine setup and completed in isolation from the physical engine. The engine intake system has been substantially modified and due to this modification, the performance would therefore be different compared to the original setup. Because of this incomplete information, the engine might run unstably. Thus, the tuning step has to be completed to ensure the stability of the engine. The engine should be able to run smoothly once everything is set.

Chapter 6

To tune the VE table on the ProCAL software, VE should have been obtained by using information from the λ meter and the fuel injection pulse-width. The fuel injection pulse-width was used because it gives the exact amount of fuel injected into the intake manifold for one cycle. From that information, the mass of fuel can be obtained from:

$$m_f = I_C I_{PW}$$

where I_C is the injector characteristic (in kg/s) and I_{PW} is the injection pulse-width (in s) obtained from the ECU reading. The injector characteristic of the EFI is $80 g/min$, or $1.333 \times 10^{-3} kg/s$ as has been set in the program. By using λ definition:

$$\lambda = \frac{AFR_{actual}}{AFR_{stoic}}$$

where AFR_{stoic} is the stoichiometric air-to-fuel ratio which is taken to be 14.7 for gasoline and AFR_{actual} is the actual air-to-fuel ratio. The actual mass of air inducted into the chamber can be obtained using the information from the λ meter as:

$$m_a = \lambda m_f (AFR_{stoic})$$

Once the actual mass of air and fuel are obtained, the VE is determined using (Heywood 1988):

$$VE = \frac{m_a}{\rho_a \mathcal{V}_d}$$

For tuning purposes, VE at all operating points should have been obtained. The table can be accessed from the software by clicking Calibrations - Air System - Volumetric Efficiency. Then run the engine at one operating point, obtain the VE using the above relationship and change the value in the table if it is different from calculated. This step was repeated until all points were examined. To speed up the tuning process, an interpolation method between adjacent points can be used. The value in the table can be changed while the engine is running provided that the engine temperature has reached over $70^\circ C$. Figure 6.19 shows the engine map used in the study, where each point is dependent on the intake pressure (Y-axis) and engine speed (X-axis).

Volumetric Efficiency																
RAM_MAP_fVe_Map_N		X: Map, [hPa] "Intake manifold pressure measured with MAP sensor"														
		Y: N, [Rpm] "Engine speed in Rpm"														
		MAP_fVe_Map_N: [-] "Factor Volumetric Efficiency, dependent on pressure and engine speed"														
Y\X	300.000	350.000	400.000	430.000	460.000	500.000	550.000	600.000	650.000	700.000	750.000	800.000	850.000	900.000	970.000	1050.000
1200.000	0.4627	0.5093	0.5419	0.5756	0.5962	0.6118	0.6293	0.6440	0.6634	0.6849	0.6841	0.6774	0.6546	0.6348	0.6159	0.6059
1400.000	0.4837	0.5293	0.5619	0.5856	0.5992	0.6218	0.6453	0.6675	0.6807	0.6911	0.6941	0.6784	0.6562	0.6362	0.6180	0.6059
1650.000	0.5037	0.5483	0.5819	0.6056	0.6262	0.6418	0.6653	0.6835	0.6989	0.6976	0.7043	0.6812	0.6661	0.6581	0.6359	0.6159
2000.000	0.5237	0.5663	0.6019	0.6256	0.6462	0.6612	0.6853	0.7044	0.7137	0.7182	0.7161	0.6937	0.6758	0.6744	0.6491	0.6291
2500.000	0.5437	0.5863	0.6219	0.6456	0.6662	0.6818	0.7053	0.7273	0.7373	0.7484	0.7412	0.7204	0.7019	0.6888	0.6616	0.6480
3000.000	0.5639	0.6037	0.6441	0.6698	0.6892	0.7032	0.7232	0.7498	0.7674	0.7843	0.7742	0.7475	0.7350	0.7221	0.7069	0.6865
3500.000	0.5898	0.6246	0.6673	0.6825	0.7017	0.7260	0.7485	0.7608	0.7839	0.8051	0.7964	0.7726	0.7602	0.7463	0.7218	0.7061
4000.000	0.6041	0.6412	0.6857	0.7013	0.7258	0.7477	0.7647	0.7904	0.8223	0.8489	0.8293	0.8155	0.8052	0.7976	0.7607	0.7491
5000.000	0.6204	0.6667	0.7051	0.7278	0.7495	0.7629	0.7886	0.8264	0.8623	0.8889	0.8693	0.8410	0.8356	0.8249	0.8015	0.7814
6000.000	0.6471	0.6841	0.7218	0.7427	0.7684	0.7828	0.8156	0.8484	0.8923	0.9089	0.8893	0.8710	0.8656	0.8649	0.8423	0.8297
7000.000	0.6422	0.6848	0.7247	0.7418	0.7669	0.7828	0.8156	0.8554	0.8923	0.9089	0.8893	0.8710	0.8656	0.8649	0.8591	0.8297
8000.000	0.6473	0.6839	0.7258	0.7437	0.7669	0.7828	0.8156	0.8554	0.8923	0.9089	0.8893	0.8710	0.8656	0.8649	0.8591	0.8297

Figure 6.19 Engine map used for engine operating conditions

To ensure the engine is running smoothly, the table should be plotted in 3D and checked to see if there is a spike at any point. If a spike occurs, smooth the curve by changing the value in the table. This is important because a spike can cause the engine to run unstably. Figure 6.20 shows the engine map in 3D with a smooth curve. Once the ECU program was examined, the program was saved in the ECU by choosing 'Burn to ECU' from the ProCAL menu. The engine stability was then checked by running the engine at idle speed, part load, full load and wide-open-throttle (WOT).

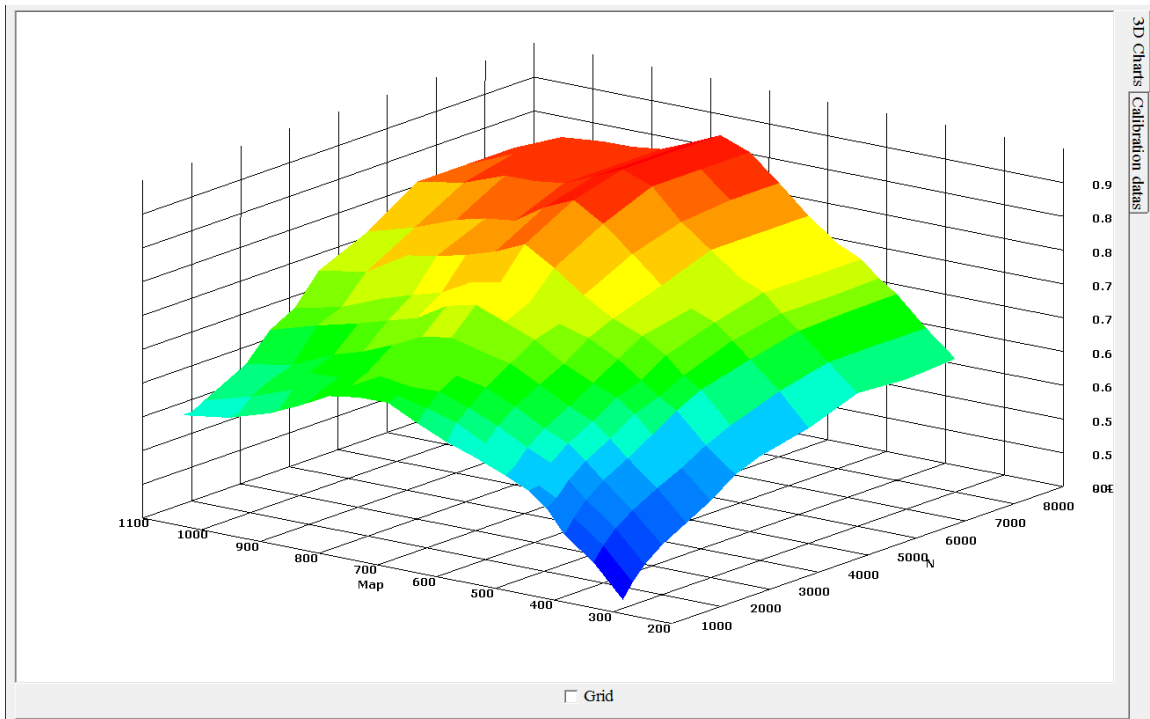


Figure 6.20 Engine map plotted in 3D to ensure there is no spike at any point.

6.5 Experimental Techniques

HCCI mode was achieved by using a high inlet temperature. To operate the engine, one should use the safe working procedure (SWP) created for this engine setup (the SWP is attached in Appendix E). The SWP was used as a reference for the step-by-step operation of the engine. The engine was run at 1500 rpm at 80% throttle opening: wide-open-throttle (WOT) or 100% opening causes the engine to run unstably at a high intake air temperature. HCCI mode was hard to achieve when the engine speed was running above 1500 rpm and the engine speed was also unstable beyond this point.

At the beginning, the engine was started in SI mode until the engine had warmed up. The engine speed was slowly increased above 2000 rpm with low load, about 30% of the SI engine's load. Once the engine speed was stable, the heater was then turned on. The intake air temperature was heated to at least 210°C due to the low compression ratio of the engine. In cold weather, the engine was difficult to switch from SI to HCCI mode at 210°C. To get the starting point, the air intake temperature had to be increased up to 310°C. The engine was run for about five more minutes before the intake air temperature gave a stable reading (no fluctuation). Then, the engine load was slowly increased by 1% increments until the transition point between SI to HCCI mode was achieved. The transition point could be observed when there was a ringing sound (or knocking) produced by the engine. After that, the spark plug can be turned off and the engine will operate in HCCI mode. The engine speed will reduce to 1500 rpm once the engine operates in HCCI mode.

Reducing the load will increase the engine speed but in an unstable condition. Increasing the load will stop the engine because the engine could not operate below 1500 rpm. In addition to that, the idle speed of the engine in SI mode is between 1500-2000 rpm. Thus, the engine will not work properly below 1500 rpm because the lowest speed of the engine is given by its idle speed characteristics. The experiment was started from the highest air intake temperature (310°C) to the lowest possible air intake temperature (210°C) in 10°C resolution. The lowest air intake temperature was selected as 210°C because the engine will stop working below this point. Sometimes the engine was also unstable at 210°C if the intake air temperature experienced small

Chapter 6

variations. The baseline data of the SI engine was created in order to compare the engine performance between SI and HCCI at the same operating condition, except for the air intake temperature the HCCI engine needs to work. The comparison will be discussed in the next chapter.

6.6 Conclusion

This chapter has discussed the experimental methodology used to achieve HCCI mode by using a commercially available four-stroke single-cylinder engine. The compression ratio of the engine is fixed, thus the HCCI mode can be achieved by heating the intake air. To achieve this, a 2 kW heater was installed in a modified air intake manifold. Also, the engine was using the EFI and ECU systems instead of the original carburettor due to safety reasons. Thus, a little bit of programming was required to install the ECU and, once completed, the engine can be operated in a closed-loop cycle: a wideband oxygen sensor was used to control the input parameters. A direct comparison between SI and HCCI engines will be discussed in Chapter 7.

Chapter 6

Chapter 7

EXPERIMENTAL PERFORMANCE STUDY OF A GASOLINE HCCI ENGINE

7.1 Introduction

The performance of a gasoline HCCI engine is discussed in this chapter and compared with the SI engine. The power curve of the SI engine will be developed before discussing the engine operating conditions. The HCCI engine performance (the in-cylinder pressure, engine power, fuel consumption, engine efficiency and emissions levels) will then be investigated and compared to the SI engine. The conclusion will complete the chapter.

7.2 Power Curve Comparison of SI Engine with Manufacturer Data

The power curve of the SI engine is compared against the manufacturer data because the air intake manifold of the engine has been substantially modified. The manufacturer data uses the original engine setup with a short air intake manifold coupled with a carburettor. The experimental setup, on the other hand, uses a long air intake manifold with an EFI. An ECU was also fitted to control the EFI. An ECU was not used in the old engine setup. Engine performance might vary depending on whether a short or long intake manifold is used. Figure 7.1 shows the difference between the manufacturer data and the experimental data for the engine power and torque. The engine power (Figure 7.1 top) for the experiment is slightly higher than the manufacturer data for the lower engine speed (below 3400 rpm). The maximum power,

however, is similar between the experiment and manufacturer data at the maximum engine speed, which is 3.5 kW at 3600 rpm.

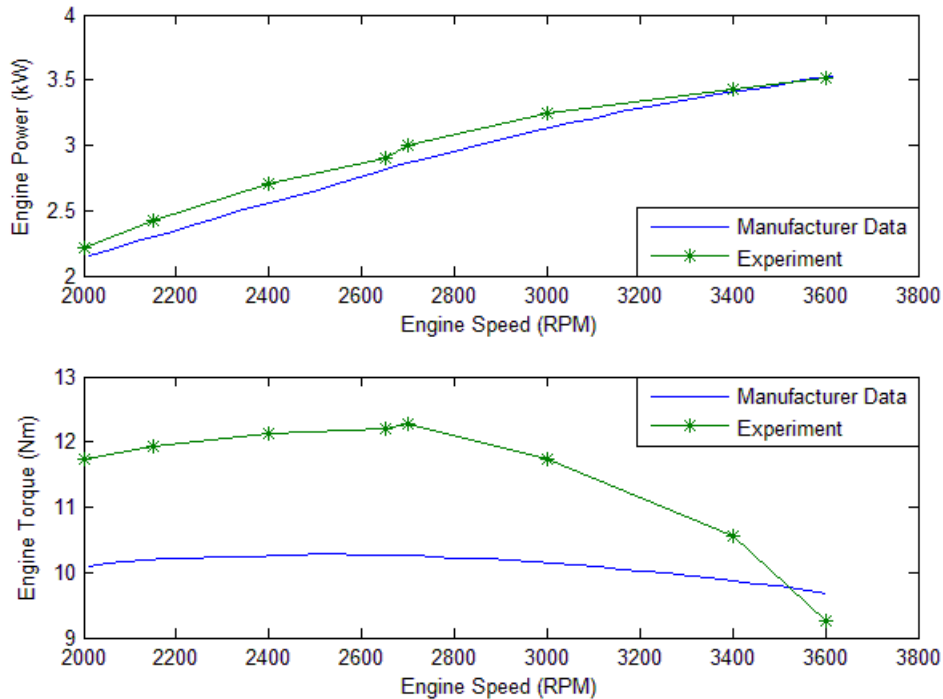


Figure 7.1 The comparison of SI engine power and torque between manufacturer data and experiment. Manufacturer uses carburettor with short intake manifold while experiment uses long intake manifold with EFI.

The engine torque, as shown in Figure 7.1 (bottom), has different behaviour between the manufacturer data and the experiment. The engine torque for the experiment is higher than the manufacturer data for the engine speed below 3400 rpm. The torque is then lower than the manufacturer data when the engine speed is maximum at 3600 rpm. The maximum engine torque for the experiment is 12.1 Nm at 2700 rpm, while the maximum engine torque from the manufacturer data is 10.3 Nm at 2500 rpm. A higher engine torque for the experiment is due to the long air intake manifold compared to the old engine setup from the manufacturer. A long intake manifold creates a pulsation effect at low engine speeds (Heywood 1988; Muller & Mich 1983). When the intake valve is closed, the air keeps moving in and hits the valve wall. This creates a piling effect and the air becomes slightly compressed. The compressed air then moves back and forward to form the pulsation effect. When the intake valve is open, the air is drawn into the combustion chamber, which creates a supercharging-like

effect. Thus, the torque is increased for the low engine speed, which explains the behaviour in Figure 7.1 (bottom).

In a modern automotive engine, higher engine torque is necessary at a low engine speed while higher engine power is required at a high engine speed. To achieve this, the engine uses an airflow module to change the length of the air intake manifold at the desired engine speed (Proton 2013), as shown in Figure 7.2. When the engine speed is low, the module uses a long air intake runner to get more torque. Once the engine achieves the desired high engine speed, the module will then bypass the long air intake and use a shorter air intake flow to get more engine power. This will enhance the engine performance at low and high engine speeds.

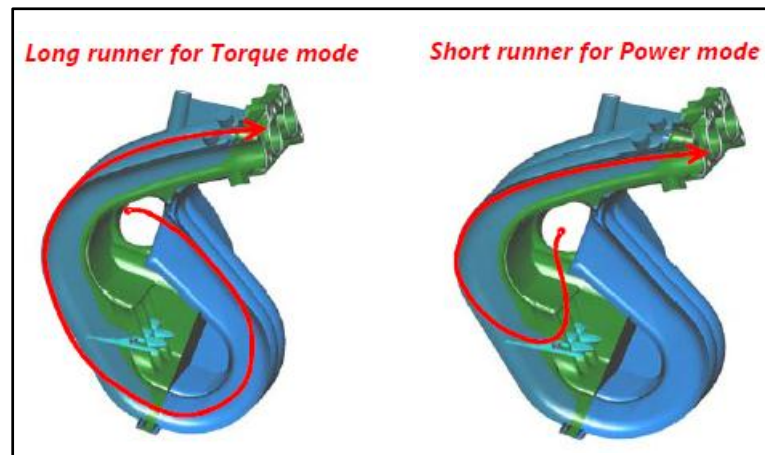


Figure 7.2 Airflow module used in the air intake manifold of modern engines to implement the effect of short or long air intake (Proton 2013).

7.3 Experimental Conditions

HCCI engines are reported to have difficulty starting in cold conditions (Kong & Reitz 2003; Soylu 2005). The air intake temperature has to be increased high enough to allow the HCCI operation. The engine was operated at a constant compression ratio of CR 9 and the λ was kept at near stoichiometric mixture of 1.1. Because the HCCI engine only operates in a stable condition at 1500 rpm and is unstable at a higher engine speed, the performance study will use an engine speed of 1500 rpm as a comparison point

between HCCI and SI modes. The engine speed was set to be constant so that a direct comparison can be made between the two modes of combustion. Three different cases were investigated: SI at its maximum load; SI at part load but similar power to HCCI; and HCCI at its maximum load. The engine operating conditions are shown in Table 7.1 and the details of the engine operations are discussed in Section 6.5. The λ was set the same for all the cases due to the limitation of the ECU, which cannot operate in a stable condition if the λ more the 1.1.

Table 7.1 Engine operating conditions

Case	Engine Speed (RPM)	Power Output (kW)	Lambda	CR	Load (%)
SI_1	1500	1.1	1.1	9	100
SI_2	1500	0.8	1.1	9	30
HCCI	1500	0.8	1.1	9	100

7.4 Engine Performance Comparison

7.4.1 In-Cylinder Pressure

The in-cylinder pressure can be used to monitor the combustion activities inside the combustion chamber. High in-cylinder pressure is useful when the engine requires more load and the in-cylinder pressure is low when the engine operates at no load. High or low in-cylinder pressure translates to high or low power produced by the engine. Figure 7.3 shows the in-cylinder pressure for the SI engine in this study between no load (Figure 7.3 left) and full load (Figure 7.3 right), where the TDC is at 360°CA. The idle engine speed is 1700 rpm (no load), 1500 rpm at full load and 6% throttle opening to get the desired engine speed. The in-cylinder pressure is very low (close to 0.7 MPa) when the engine is idle, where the in-cylinder pressure at full load is 4.37 MPa. The big in-cylinder pressure difference helps the engine to operate at a high load configuration in SI mode.

When the engine was switched to HCCI mode, the in-cylinder pressure sometimes became unstable, which created knocking. Knocking is not a desired behaviour because the engine will have a limited load range and long exposure to knocking would damage the engine. Verhelst and Wallner (2009) reported that knocking is caused by an instantaneous heat release rate due to spontaneous auto-ignition of the end gas condition which generates a high-amplitude pressure wave. Knocking phenomena limit the load range of an HCCI engine, where high load operations can easily initiate knock (Yap *et al.* 2006). In this study, the HCCI engine has knocking because the operating condition of λ is near stoichiometric condition.

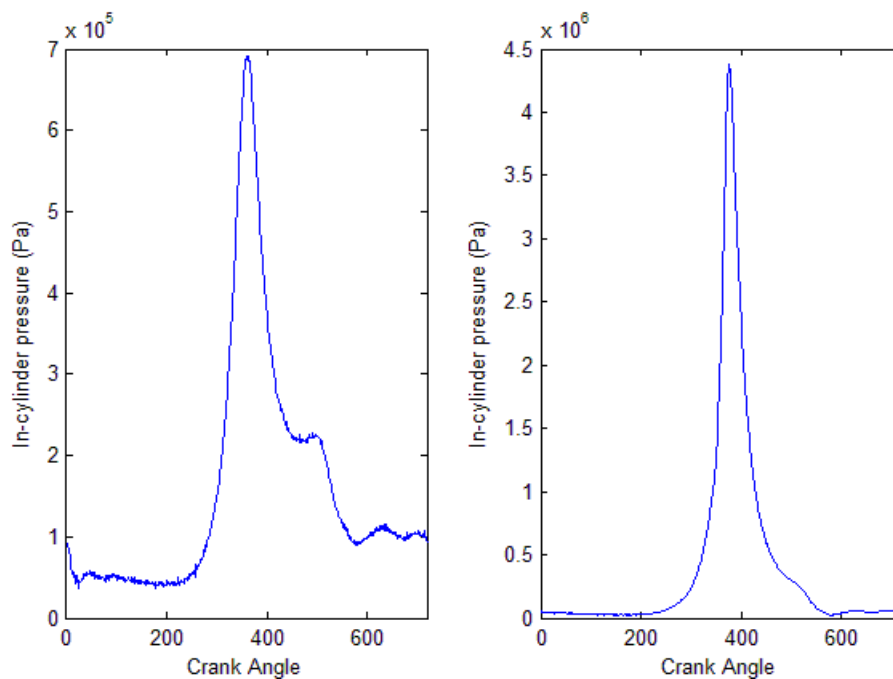


Figure 7.3 In-cylinder pressure comparison for SI mode in this study between no load (left) and full load (right).

The knock occurs when the combustion is advanced and a loud ‘pinging’ noise can be heard from the engine. Figure 7.4 shows the in-cylinder pressure behaviour when knocking occurs in the HCCI engine. The straight blue line in Figure 7.4 shows the TDC location at a position of 720th of the encoder reading where the encoder has 0.5°CA resolution. The combustion is advanced by almost 10°CA and the in-cylinder pressure reached the instantaneous peak at 6.41 MPa before TDC. The in-cylinder pressure has a rapid up and down motion before the pressure is uniform at 15°CA after TDC.

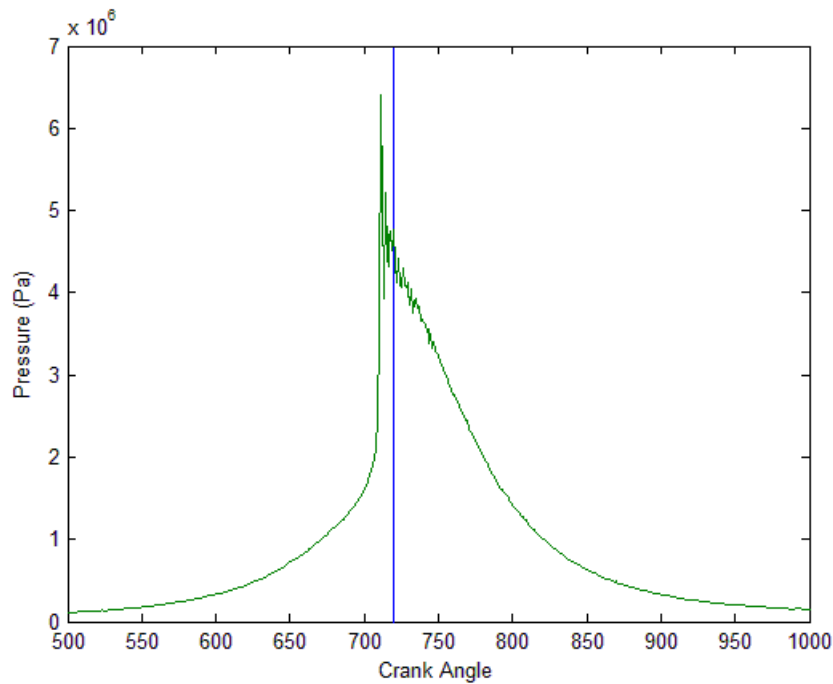


Figure 7.4 In-cylinder pressure for HCCI engine when knocking occurred. Straight blue line is the TDC location at 360°CA with encoder having a 0.5°CA resolution.

To reduce knocking in an HCCI engine, the engine should be operated in a lean condition, where the λ is about 2 in order to achieve a knock stability limit (John & Yang 2010). However, the λ in this study was kept at near stoichiometric condition so that a direct comparison can be made between SI and HCCI at the same engine speed and mixture condition. The engine was only run for a short time to keep the engine in good condition.

The in-cylinder pressure comparison between the SI and the HCCI engine is presented in Figure 7.5. The in-cylinder pressure condition of the HCCI engine was selected at a best case condition of 250°C intake temperature, when less knocking occurred. The in-cylinder pressure for the HCCI engine is higher than for the SI engine. The maximum pressure for the HCCI engine is 4.64 MPa and 4.37 MPa for the SI engine. Note that from the in-cylinder pressure diagram (Figure 7.5) the combustion event for the HCCI engine occurs in a short time. The in-cylinder pressure increases faster and reaches the peak in approximately 5°CA with the combustion starting at 365°CA. With the SI engine, the pressure increases steadily and the combustion is slower compared to the HCCI engine. The combustion event for the SI engine starts at approximately

357°CA before the pressure reaches the peak at 377°CA. Thus, the combustion event for the SI engine occurred in approximately 20°CA, which is four times slower than for the HCCI.

When the in-cylinder pressure is translated into the rate of change, the pressure increment rate for the HCCI engine is higher compared to the SI engine, as shown in Figure 7.6. This event shows that the in-cylinder pressure rise rate is very high during combustion. Hence, the combustion in the HCCI engine occurs instantaneously with a very fast combustion, as has been discussed by Rattanapaibule and Aung (2005) and Tomita (2004). Therefore, the HCCI combustion requires very well controlled operating conditions to achieve the desired in-cylinder pressure behaviour, otherwise knocking will take place.

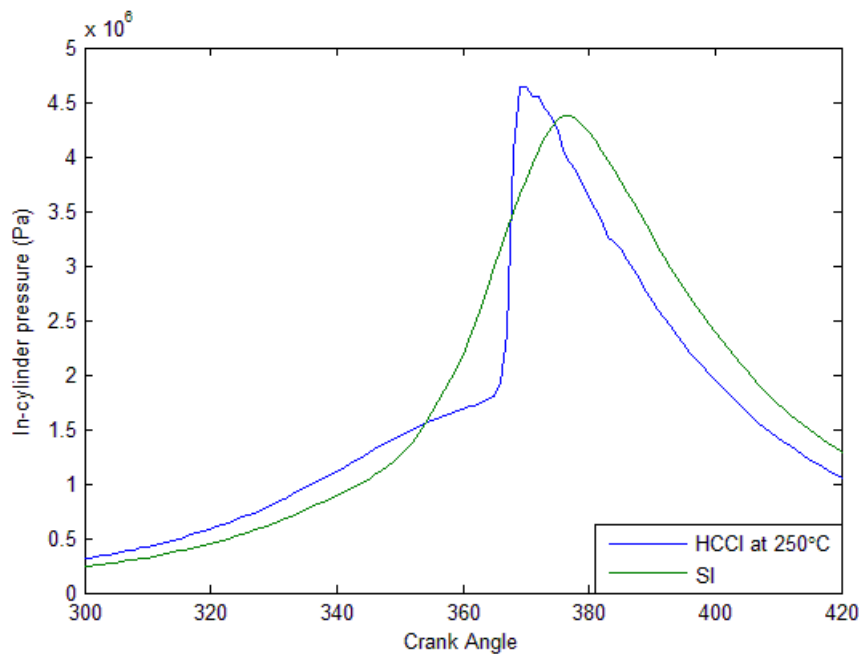


Figure 7.5 In-cylinder pressure comparison between SI and HCCI engines.

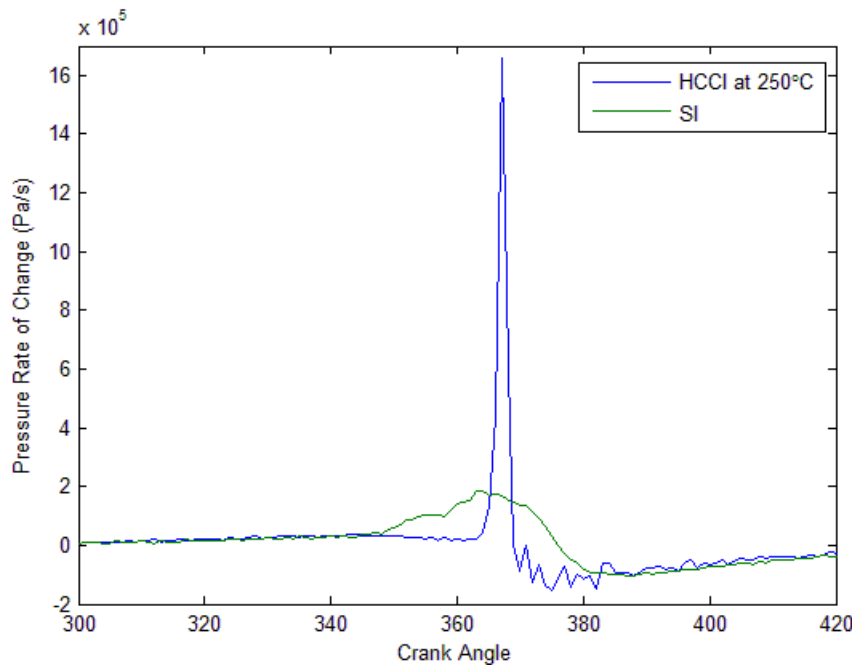


Figure 7.6 In-cylinder pressure rate of change comparison between SI and HCCI engines.

7.4.2 Engine Power

Engine power is a measure of the engine's ability to perform useful work over a period of time (Heywood 1988). The power absorbed by the dynamometer is a product of torque and angular speed; hence at a low engine speed the power produced by the engine is also low. In this study, the power produced by the engine was measured by using the dynamometer. A comparison in engine power was made and is shown in Figure 7.7, where it shows the engine power for the three different cases in this study (Figure 7.7 left) together with a recorded BMEP for each case (Figure 7.7 right). The maximum power for the SI engine is 1.1 kW at 1500 rpm (case SI_1) and 0.8 kW for the HCCI engine for all air intake temperatures. The SI engine was operated at full load (100%), while the HCCI engine only managed to operate at 35% of the SI engine's maximum load, which translates to a 27.3% power decrease over the SI engine. This is because the HCCI engine has difficulty in high load operations (Kong 2007). The 35% of the SI engine's maximum load represents the maximum load for the HCCI engine because the HCCI engine is unable to operate at higher loads. Thus, at an engine speed of 1500 rpm, the HCCI engine is suitable to operate in low load conditions.

A reduction in HCCI engine power was described in Figure 7.5, where the in-cylinder pressure trace experienced a rapid increase in pressure when combustion occurred. This, in turn, will reduce the area under the curve: meaning the work produced by the HCCI engine decreases. Integrating the in-cylinder pressure over the volume produces work $W = \int pdv$. Hence, the work produced by the HCCI and SI engines by using the in-cylinder pressure in Figure 7.5 is 109.94 J and 151.80 J respectively. Thus, the HCCI engine produces less work than its SI counterpart, which translates into low power.

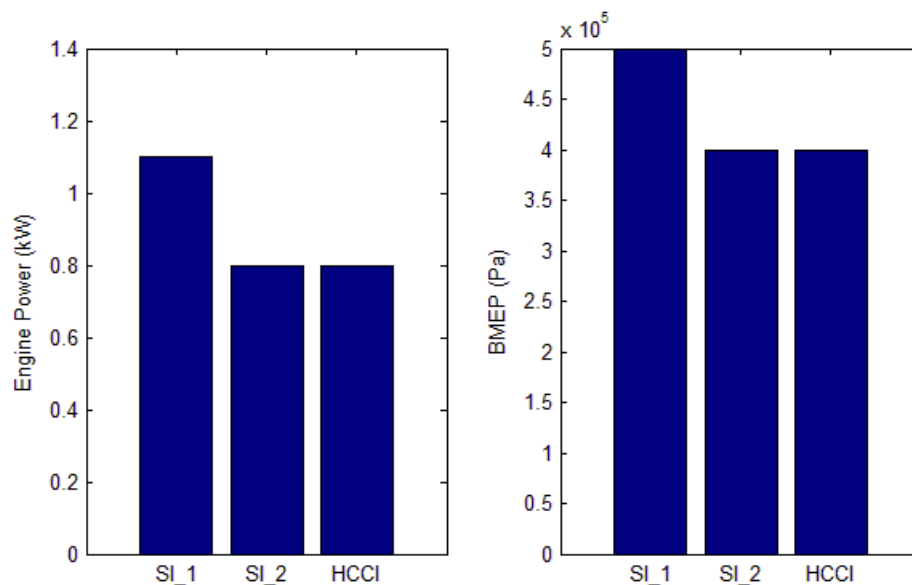


Figure 7.7 Engine power comparison between SI and HCCI modes

The lower power of the HCCI engine translates into a low BMEP, as shown in Figure 7.7 (right). SI_1 shows the highest BMEP of 0.5 MPa while the other two cases have BMEP of 0.4 MPa. SI_2 has the same BMEP as the HCCI mode because it was run on the same engine power so that a direct comparison could be made with the HCCI engine. BMEP shows the ability of the engine to perform high load operations. Typically, for a small engine the BMEP range is between 0.4 and 1 MPa (Heywood 1988). The maximum BMEP for the HCCI engine in this study is 0.4 MPa and it shows that the HCCI engine has a very limited load range and is not suitable for high load operations (Kong 2007; Nathan, Mallikarjuna & Ramesh 2010). However, the recorded BMEP for the HCCI engine in this study shows a better result compared to the 5-cylinder SAAB engine in HCCI mode, which has a maximum BMEP of 0.36

MPa (Hyvonen, Haraldsson & Johansson 2003). The HCCI engine in this study has a similar BMEP to the natural gas-diesel HCCI engine reported by Nathan, Mallikarjuna and Ramesh (2010). Therefore, the BMEP for the HCCI engine achieved in this study is in agreement with the literature, where the HCCI engine operates in a limited load range.

7.4.3 Fuel Consumption

The fuel consumption (FC) was measured using a method discussed in Chapter 6, where the FC indicates the fuel used by the engine over a certain period of time. Lower FC is a desired performance in today's world, where engine technology has been continuously improved to reduce the FC without sacrificing the engine power (Mehl, Faravelli, *et al.* 2009). The engine with low FC not only gives a fuel cost saving but also reduces the emissions levels as well (Ahn *et al.* 2002). Figure 7.8 shows the FC comparison between all cases of the engine test. The FC for the HCCI engine is shown at its minimum and maximum because the FC was measured across a range of intake air temperatures. The FC comparison for maximum load condition between the SI and HCCI engines shows that the SI engine has a higher FC with 0.32 kg/h (SI_1) while the HCCI engine recorded an improved FC with 0.24 kg/h at a minimum reading. When comparing the FC between the HCCI and SI engines for the same engine power, the SI engine shows a better result than the HCCI engine with an FC of 0.23 kg/h (SI_2). The results show that the HCCI engine, at maximum operating load condition, has up to 22.6% better FC than the SI engine, while for the same engine power, the SI engine shows a better result with 7.8% less FC than the HCCI engine.

The brake specific fuel consumption (BSFC) was used to measure how efficient the engine is in using the fuel to produce power. The BSFC is obtained by using

$$\text{BSFC} = \frac{\dot{m}_f}{P_e}$$

where \dot{m}_f is the fuel mass flow rate in kg/h and P_e is the engine power in kW which gives kg/kWh for the BSFC. A typical SI engine has a BSFC of about 0.27 kg/kWh and the lower it is, the better (Heywood 1988).

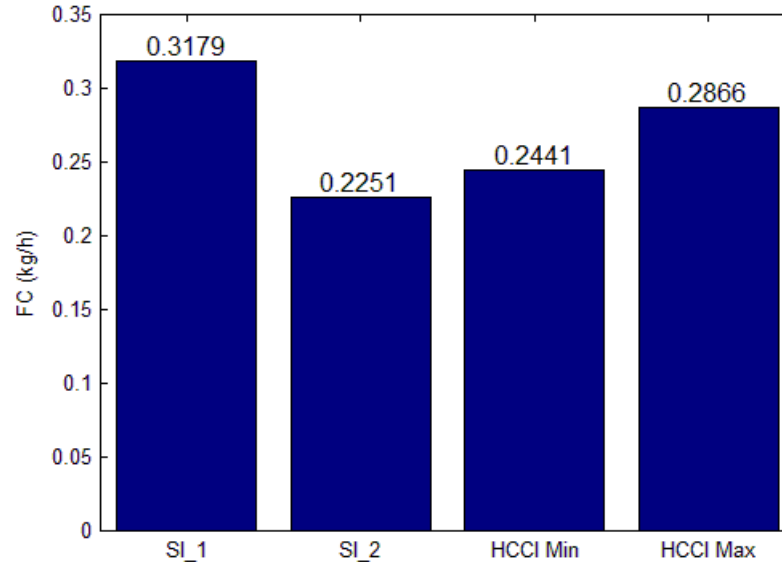


Figure 7.8 FC comparison between SI and HCCI engines, where the FC for the HCCI engine was recorded over a range of intake air temperatures and uses the minimum and maximum.

Figure 7.9 shows the BSFC for the HCCI engine over a range of intake air temperatures, where the BSFC varies for different air intake temperature. In Figure 7.9, intake air temperature was located on the x -axis because it is the control parameter (Antunes, Mikalsen & Roskilly 2008; Fiveland & Assanis 2000; Rattanapaibule & Aung 2005). When compared with the HCCI engine, the BSFC for SI (both cases) is better than the HCCI, as shown in Figure 7.10. The SI engine has the best BSFC at 0.28 kg/kWh, where the HCCI has a minimum BSFC of 0.30 kg/kWh. When the SI engine operates in a full load condition, the BSFC marginally increases to 0.29 kg/kWh. Thus, the HCCI engine has up to 4.3% lower BSFC than the SI engine at maximum load and 7.1% lower than the SI engine for the same engine power. This is because the power generated by the HCCI engine is 27.3% lower due to the low compression ratio of the engine. However, if the HCCI engine can achieve a lower BSFC than the SI engine, the HCCI engine would be a good option in the near future. The BSFC for the HCCI engine can be improved further by using other parameters to control the combustion such as high compression ratio, leaner mixture, exhaust gas recirculation etc.

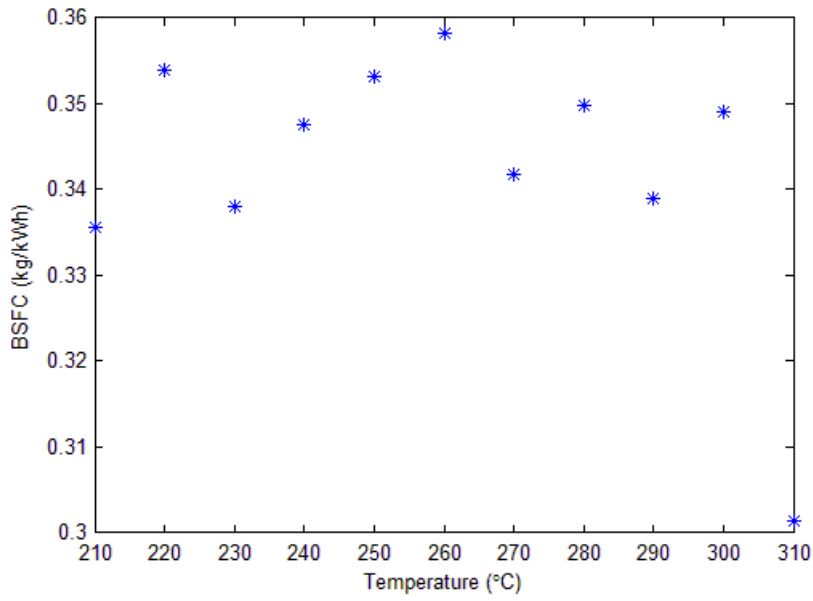


Figure 7.9 BSFC for the HCCI engine over a range of intake air temperatures

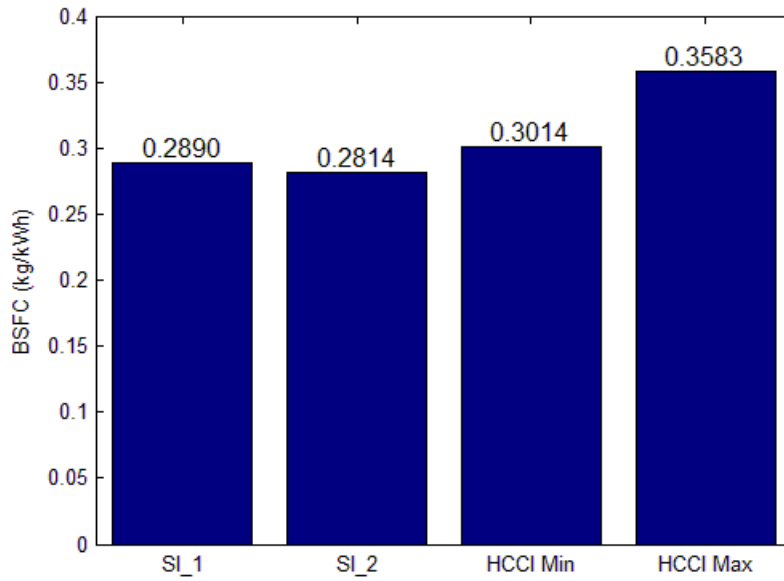


Figure 7.10 BSFC comparison between SI and HCCI engines with the HCCI engine using the minimum and maximum values over a range of intake air temperatures

7.4.4 Engine Efficiency

Engine efficiency measures the engine's ability to produce useful power given the amount of energy supplied by the fuel. The amount of energy supplied by the fuel is given by its heating value, Q_{HV} , where Q_{HV} for gasoline is taken to be 47300 kJ/kg. Then, the engine efficiency can be obtained by using

$$\eta_f = \frac{P_e}{\dot{m}_f Q_{HV}}$$

A typical engine efficiency for SI engines is between 20% and 25% (Heywood 2005; Meyer 2007), where the most common driving range falls into that efficiency region (Meyer 2007). Higher engine efficiency is good because the engine uses less fuel and produces more power. Hence, the engine with high efficiency has a lower fuel cost, which is good for long term usage. Figure 7.11 shows the HCCI engine efficiency for different intake air temperatures, where the engine has a minimum efficiency at temperatures between 240°C and 260°C. The engine efficiency starts to increase at the lower and higher ends of the intake air temperature range.

When the efficiency between the two modes of combustion is compared, the HCCI engine yields a lower efficiency than the SI engine. The SI engine has a maximum efficiency for case SI_2 of 27%, where the HCCI engine has an efficiency up to 25.3%. At a minimum condition, the HCCI engine yields 21.2% with 26.3% for the SI engine. Typically, a diesel engine has an efficiency of about 30% given a high compression ratio (Heywood 2005). However, diesel is not the focus in this chapter. The option to employ a high compression ratio in the HCCI engine is there in order to improve the HCCI engine efficiency. This is because, unlike the SI engine, the HCCI engine is able to operate at a high compression ratio with efficiencies similar to the CI engine (Christensen & Johansson 1998; Epping *et al.* 2002; Killingsworth *et al.* 2006; Mack, Aceves & Dibble 2009; William & Charles 2011). Therefore, given a small difference in engine efficiency between SI and HCCI engines at the same operating condition, the HCCI engine can produce a better result if more tuning is carried out.

Chapter 7

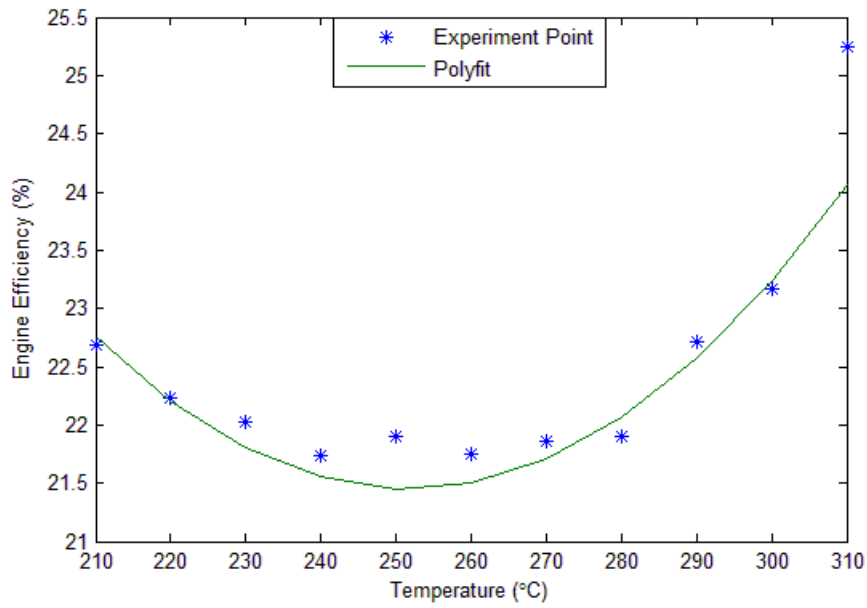


Figure 7.11 HCCI engine efficiency for a range of intake air temperatures.

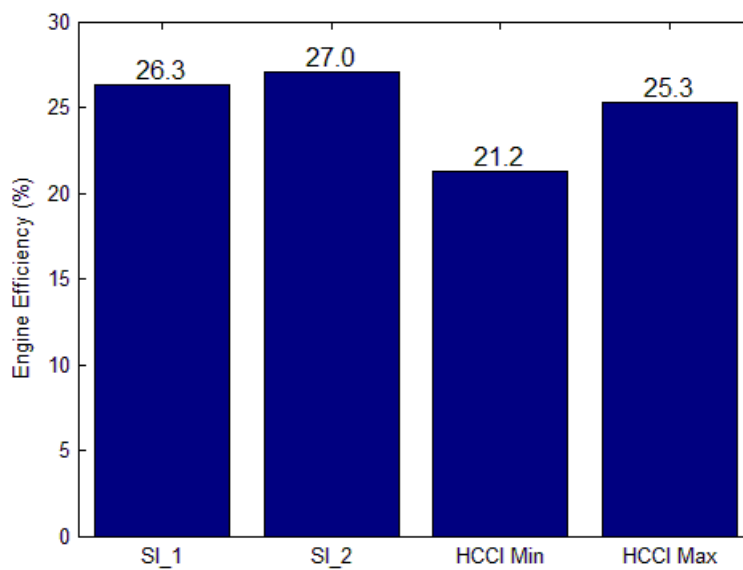


Figure 7.12 Engine efficiency comparison between SI and HCCI engines, where the HCCI engine has a minimum and maximum range for a set of air intake temperatures.

7.4.5 Emissions Levels

Limits on emissions levels are becoming more rigorous nowadays because regulatory bodies such as those in Europe, the United States (US) and Japan are imposing stringent vehicle emissions quality standards (EPA 2000; Popp 2004; Wesselink,

Buijsman & Annema 2006). HCCI engines claim to have low emissions levels of NO_x and particulate matters (Nathan, Mallikarjuna & Ramesh 2010) and high levels of unburned hydrocarbons (HC) and carbon monoxide (CO) (Kong *et al.* 2003; Nathan, Mallikarjuna & Ramesh 2010). However, the emissions levels vary from one engine to another and are dependent on the operating conditions of the engine, fuel quality and the engine design (Meca 1997; Rizvi 2009). Thus, the emissions levels from one engine cannot be directly compared with another engine because of those factors. The emissions levels from the HCCI engine in this study are compared with the SI mode at the same operating condition. Figure 7.13 shows the emissions levels of unburned HC, NO_x , CO_2 and CO for the HCCI engine over a range of intake air temperatures and will be discussed in the next sub-sections.

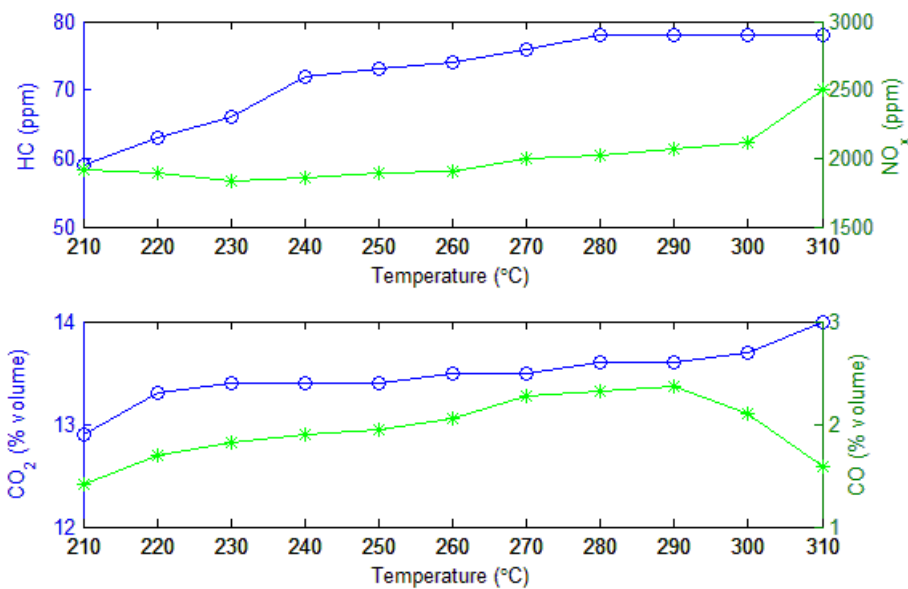


Figure 7.13 Emissions levels of HC and NO_x (above) and CO_2 and CO (below) for HCCI engines for a range of intake air temperatures.

7.4.5.1 NO_x

The NO_x formation is explained by several formation mechanisms: the Zeldovich mechanism, the Fenimore mechanism, the fuel-bound NO_x mechanism, the NO_2 mechanism and the N_2O mechanism. The Zeldovich mechanism, also known as the thermal NO_x mechanism, explains that the NO_x is not formed from the fuel because there is no nitrogen component in the fuel. NO_x is formed in a high temperature

reaction, where the nitrogen in the air dissociates into nitrogen radicals to form NO when it reacts with oxygen. Some NO is converted back to NO₂ when further reactions occur in the chamber. The thermal NO_x is not significant when the combustion temperature is below 1800 K (Kuo 2005).

Under the Fenimore mechanism, also known as the prompt NO_x mechanism, the NO_x is promptly formed in laminar premixed flames long before the NO_x is formed by the thermal mechanism. The Fenimore mechanism explains the additional NO_x produced over the Zeldovich mechanism in the hydrocarbon flames. Prompt NO_x is important for hydrocarbon fuels in fuel-rich conditions, where NO_x is formed by rapid reactions of hydrocarbon radicals (CH, CH₂, C₂, C₂H and C) with molecular nitrogen. Miller and Bowman (Miller & Bowman 1989) reported that NO_x formed by the thermal mechanism is the dominant source of NO_x only in the equivalence ratio range of $\phi = 0.8 - 1.0$. For $\phi < 0.8$, the temperature is sufficiently low and NO_x was formed by the Fenimore mechanism.

The fuel-bound NO_x mechanism is used for coal and coal-derived fuels, where nitrogen exists as chemically bound nitrogen. The NO_x formation is dependent on the local combustion temperature, stoichiometric conditions and the level of the nitrogen compounds in the fuel-air mixture. The NO₂ mechanism, on the other hand, is based on the chemical kinetic calculations near the flame zone, where NO₂ is formed due to the reaction between NO and HO₂. The NO₂ then reacts with H and O radicals to form NO_x. The N₂O mechanism is also based on the chemical kinetic calculations, where the N₂O is formed due to the reactions of various nitrogen radicals with NO. The N₂O will finally react with oxygen radicals to form NO_x. In short, NO_x formation is still under investigation and one cannot claim that all mechanisms have been found (Kuo 2005).

Generally, most of the NO_x formation is determined by the peak temperature during combustion, where the peak temperature is dependent on other parameters as well such as equivalence ratio, fuel composition and the initial temperature of the fuel-air mixture (Kuo 2005). Kim and Lee (2006) reported that a higher inlet temperature causes high NO_x emissions, especially when the mixture is not lean. Note that the same applies to Figure 7.13 (top), where the NO_x in the HCCI engine is higher when the

intake air temperature increases, where the engine was operated at about stoichiometric conditions. This result shows that the NO_x pattern formed in this study is in agreement with Kim and Lee (2006). The NO_x produced in the HCCI engine shows that the NO_x formation is sensitive to the intake air temperature.

However, the NO_x produced by the HCCI engine in this study is higher than that produced by the SI engine, as shown in Figure 7.14 for both SI_1 and SI_2. The NO_x level increased substantially at the onset of knock. Knock easily occurs in HCCI engines, especially when the engine operates in a near stoichiometric condition. This is consistent with Li *et al.* (2007), where they found that the NO_x level was increased when knock occurred. They also reported that the NO_x level can be reduced by reducing the knock intensity. This can be achieved by operating the engine on a leaner mixture. In this study, the mixture condition for the HCCI engine was set to be the same as for the SI engine for a direct comparison.

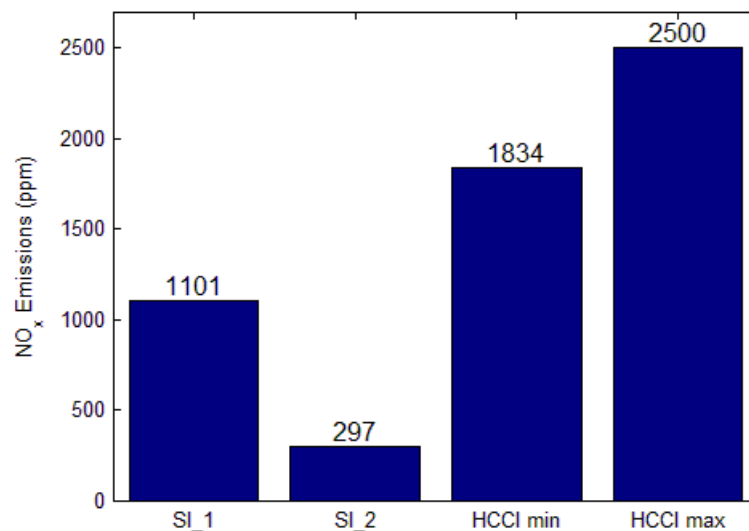


Figure 7.14 NO_x comparison between SI and HCCI modes, where HCCI mode has a minimum and maximum range for different intake air temperatures.

7.4.5.2 Unburned HC

Unburned HC is the consequence of the incomplete combustion of the hydrocarbon fuel and measures the combustion inefficiency. The level of unburned HC is generally specified in total hydrocarbon concentration, which is expressed in parts per million carbon atoms (Heywood 1988). The source of unburned HC is reported from the crevice region, the cylinder wall with a thin layer of oil left when the piston moves down and any combustion wall which has a cold area (Heywood 1988; Komninou 2009a). In Figure 7.13 (top), the unburned HC for HCCI engines increases when the intake air temperature increases, which relates to the CO emissions explained in the next sub-section.

When comparing the unburned HC between SI and HCCI engines, the result in Figure 7.15 shows that the SI_2 has the lowest unburned HC and SI_1 is the highest, with the HCCI engine in the middle. In the literature, the unburned HC in HCCI engines is reported to be higher than the SI engines (Kong & Reitz 2003; Kong *et al.* 2003; Nathan, Mallikarjuna & Ramesh 2010; Yap *et al.* 2006). This is due to the low temperature combustion in the engine which causes low combustion efficiency (Erlandsson, Johansson & Silversand 2000; Li *et al.* 2007). In this study, however, the unburned HC in the HCCI engine is lower than in the SI engine at full load and only slightly higher than in the SI engine at the same engine power. This is possibly due to knocking occurring in the HCCI engine because, when knocking occurred, the combustion temperature was high (Kim & Lee 2006; White, Steeper & Lutz 2006). Therefore, unlike in low temperature combustion, high temperature combustion causes any unburned HC to be burnt and thus reduces the unburned HC emissions levels.

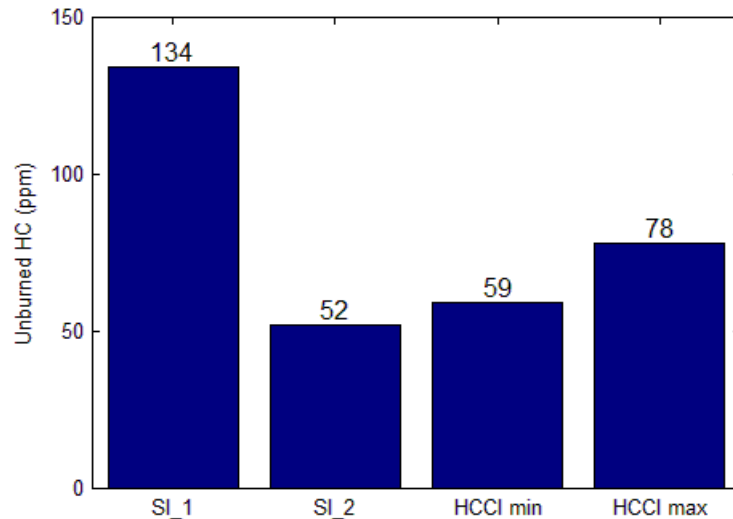


Figure 7.15 Unburned HC comparison between SI and HCCI modes, where HCCI mode has a minimum and maximum range for different intake air temperatures.

7.4.5.3 CO and CO₂

The amount of CO₂ and CO presented in Figure 7.13 (bottom) is dependent on the combustion efficiency, where the combustion efficiency can be defined as the ratio of CO₂ to the total of fuel carbon present in the exhaust including CO, CO₂ and UHC (Li *et al.* 2007). CO emissions are controlled primarily by the fuel-air equivalence ratio (Heywood 1988; Stone 1999). The principal reaction mechanism of CO formation is $RH \rightarrow R \rightarrow RO_2 \rightarrow RCHO \rightarrow RCO \rightarrow CO$, where R is the hydrocarbon radical. The CO₂ is then produced by the reaction of CO with OH radicals, which also forms hydrogen radicals. The conversion of CO to CO₂ occurs when the concentration of OH radicals increases during combustion (Kuo 2005). Thus, if the combustion is efficient, enough OH radicals will be formed to produce CO₂. If the combustion is inefficient, the CO₂ will be less with more CO left after the combustion.

From Figure 7.13, it can be seen that the amount of CO is increased when the amount of unburned HC increases, before it is decreased again when the unburned HC is about constant. This is consistent with Li *et al.* (2007) running an HCCI engine with *n*-heptane at low load condition, where the increase in CO and unburned HC is due to the termination reaction of CO to CO₂. Hence, when unburned HC is about constant, the amount of CO is decreasing and CO is converted to CO₂ resulting in a fast increase in the amount of CO₂, as shown in Figure 7.13.

When comparing the result of CO₂ and CO between HCCI and SI engines, as shown in Figure 7.16, the HCCI engine produces slightly lower CO₂ and higher CO compared to SI₂. The result of higher CO for the HCCI engine is consistent with the literature, where HCCI engines have the disadvantage of producing more CO (Kong & Reitz 2003; Nathan, Mallikarjuna & Ramesh 2010). This indicates that the combustion efficiency in the HCCI engine is low by having less CO₂ converted from CO (Li *et al.* 2007). The combustion efficiency can be represented by the composition of the combustion products, where more unburned HC and CO indicates combustion inefficiency (Heywood 1988).

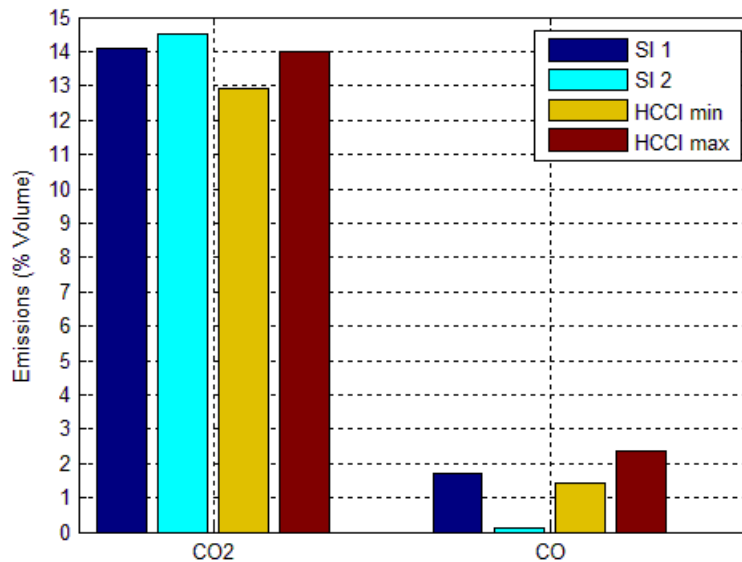


Figure 7.16 CO₂ and CO comparison between SI and HCCI modes, where HCCI mode has a minimum and maximum range for different intake air temperatures

7.5 Conclusion

This chapter has discussed the performance of the HCCI engine and compared it side-by-side with the SI engine. Even though the HCCI engine experienced some knocking issues, a direct comparison with the SI engine is necessary to evaluate the combustion performance before performing any tuning. For full load comparison, the HCCI engine returns a 22.6% lower FC but the engine power is reduced by 27.3%. In turn, the HCCI engine has a slightly lower BSFC than the SI engine, by 4.3%. When comparing the SI and HCCI engines at the same engine power, the SI engine has the advantage over the HCCI engine. This is consistent with the literature, where the HCCI engine has the limitation of operating in a low load condition.

As for the emissions levels, the HCCI engine in this study recorded a high level of NO_x due to a knocking issue when operating the engine in near stoichiometric condition. Unburned HC is lower than in the SI engine at full load condition and slightly higher than in the SI engine at the same engine power. The same applies for CO emissions levels, where the HCCI engine returns higher CO than the SI engine at the same engine power. This is also consistent with the literature where the HCCI engine has the disadvantage of producing more unburned HC and CO than the SI engine.

The HCCI engine can be used in a real world situation, whether in a hybrid engine (two or more power sources) or cruising mode. Both modes aim to reduce the FC of the engine. In cruising mode (low load condition), the engine can be switched to HCCI mode, then operating in SI mode when acceleration is needed. However, the HCCI engine needs more tuning before implementing it in a real world situation. The engine efficiency and emissions levels can be improved further by utilising different control parameters such as compression ratio, leaner mixture, exhaust gas recirculation, etc. Therefore, the HCCI engine could be a viable option in the near future.

Chapter 7

Chapter 8

CMC IN A ZERO-DIMENSIONAL SINGLE-ZONE MODEL OF A GASOLINE HCCI ENGINE

8.1 Introduction

In Chapter 5, the CMC and zero-dimensional models were validated against the experimental data from others, where both diesel and gasoline fuels were used. This chapter will discuss the performance of both models against the experimental setup in this study. The next section will validate the models' performance against the experimental gasoline fuelled HCCI engine. Section 8.3 discusses the CMC model characteristics followed by the parametric study in Section 8.4. The chapter ends with the conclusion in Section 8.5.

8.2 Comparison with Experiment

8.2.1 Boundary and Initial Conditions

The boundary conditions for air in mixture fraction space were set to 79% N₂ and 21% O₂ by mole at $\eta = 0$ and no N₂ and O₂ when $\eta = 1$. For the fuel, the mass fraction of the surrogate components at $\eta = 1$ were set to 0.22 for *n*-heptane, 0.54 for *iso*-octane and 0.24 for toluene, which represents the components of a commercial gasoline fuel (Lee, Kim & Min 2011; Lee & Min 2009). All of the fuel components were set to 0 when $\eta = 0$. Then, all the species mass fractions between $\eta = 0$ and $\eta = 1$ were initialised as a frozen mixture, as shown in Figure 8.1.

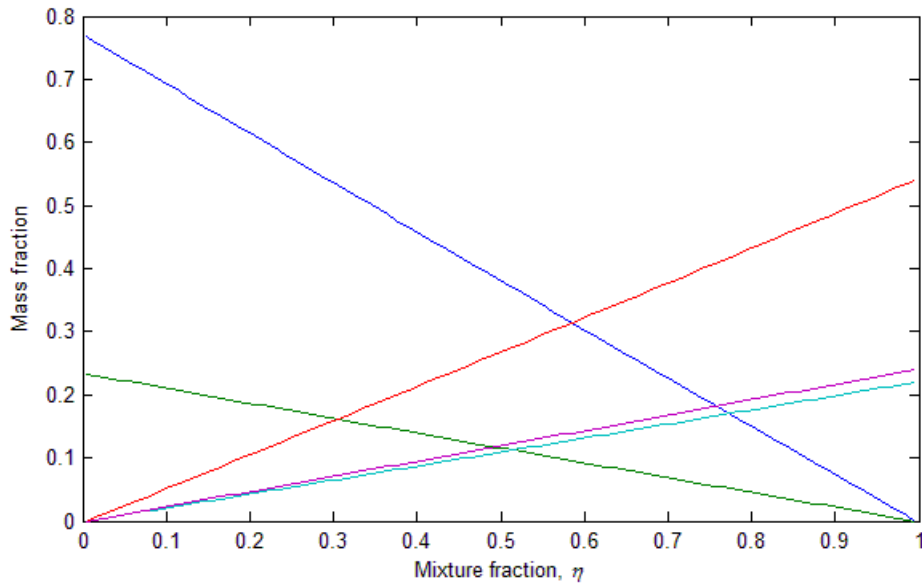


Figure 8.1 Initial condition of the air-fuel mixture in the intake manifold.

The details of the engine is given in Table 6.1. The wall temperature for this HCCI engine was set to 353K for the small single-cylinder gasoline fuelled HCCI engine, which is consistent with Barroso, Escher and Boulouchos (2005) and Su *et al.* (2007). The exhaust temperature of the engine was set to 700K, as recorded by the thermocouple reading during the experiment and the intake pressure was 90.3kPa, as given by the pressure sensor. At the beginning of the simulation, which is before the IVO, the mixture in the chamber was assumed to be only air and the fuel-air mixture was added according to the pre-set AFR value after the IVO.

8.2.2 Validation

The details of the engine used in the experiment are shown in Table 6.1, where the fuel (gasoline) was port injected. The chemical kinetics mechanism used to model the gasoline fuel was discussed in Section 5.1.2, where the surrogate fuel model is a blend between *n*-heptane, *iso*-octane and toluene. Figure 8.2 shows the validation result between CMC and zero-dimensional models against the experiment in this study at the intake temperature of 250°C. The result shows that both the CMC and zero-dimensional models are in good agreement with the experiment. The in-cylinder peak pressure for the models is almost identical for this case, where both models show

slightly lower peak pressure compared to the experiment. The ignition point for both models occurred at the same location and both of them are slightly advanced compared to the experiment. Note that the intake temperature for the zero-dimensional model was set 15°C higher than the actual to account for the mixing effects. This is consistent with Bunting *et al.* (2008) and Guo *et al.* (2010), where the intake temperature for the zero-dimensional model was set 10 - 30°C higher than the actual.

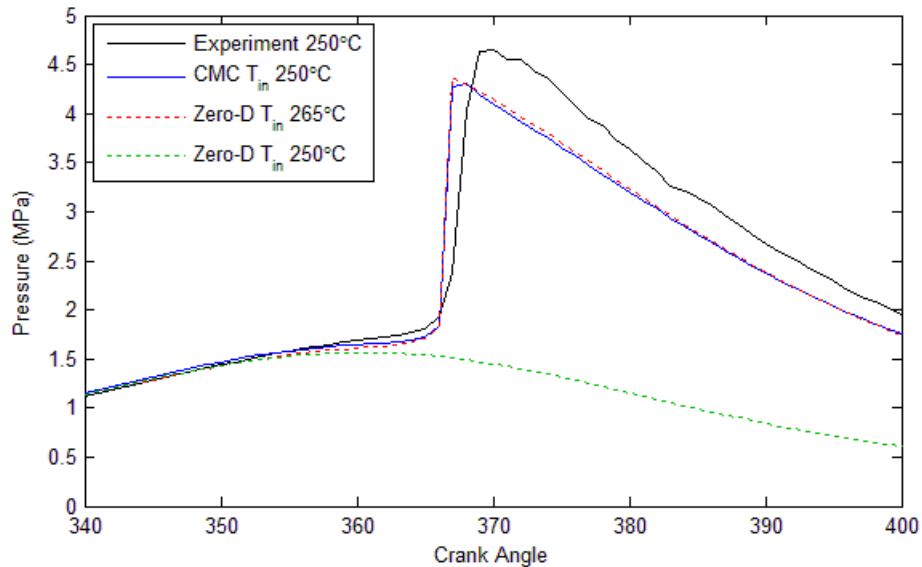


Figure 8.2 In-cylinder pressure comparison between CMC and zero-dimensional models. $T_{in} = 250^{\circ}\text{C}$, $CR=9$, $AFR=16$, $N=1500\text{rpm}$.

When the intake temperature for the zero-dimensional model was set to be the same as the actual, the model produced no combustion activity, as shown in Figure 8.2. This shows that the CMC model yields better results compared to the zero-dimensional alone without any increase in the intake temperature. The result is similar to the other two engine configurations discussed in Chapter 5, where the CMC model can use the actual intake temperature while the zero-dimensional model cannot. Thus, the CMC model is suitable to be used for further analysis, including in understanding the chemical reactions in an HCCI engine.

8.3 CMC Characteristics

8.3.1 Independence Test: Constant C_D

The value of constant C_D in equation (3.47) was also tested in this engine configuration because it is case-specific. Figure 8.3 shows the in-cylinder pressure comparison between the experiment and the CMC model with varying C_D . The result shows that smaller C_D causes slightly retarded combustion with $C_D = 1.0$ retarding the combustion the most. It shows that a smaller C_D value causes slow mixing and this is consistent with Kim (2004), where a higher C_D value is required for fast mixing near the nozzle area. When $C_D = 1.0$, the chemistry reactions become unstable, as shown in Figure 8.4, where a significant amount of O_2 is suddenly created again after the combustion. When $C_D = 1.5$ the amount of O_2 increases before the simulation is finished but only at a slow rate.

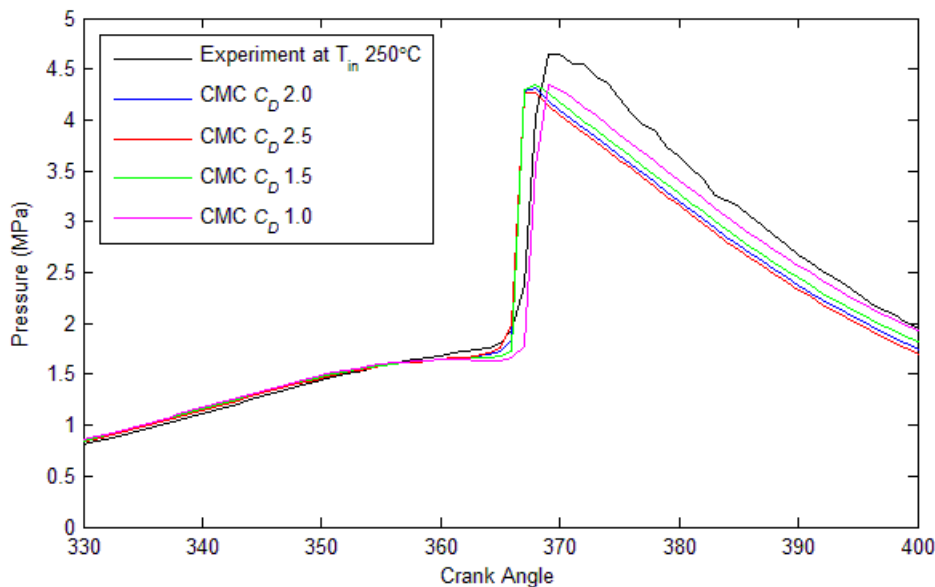


Figure 8.3 In-cylinder pressure comparison between experiment and CMC model with varying C_D . $T_{in} = 250^\circ\text{C}$, $CR = 9$, $AFR = 16$, $N = 1500\text{rpm}$.

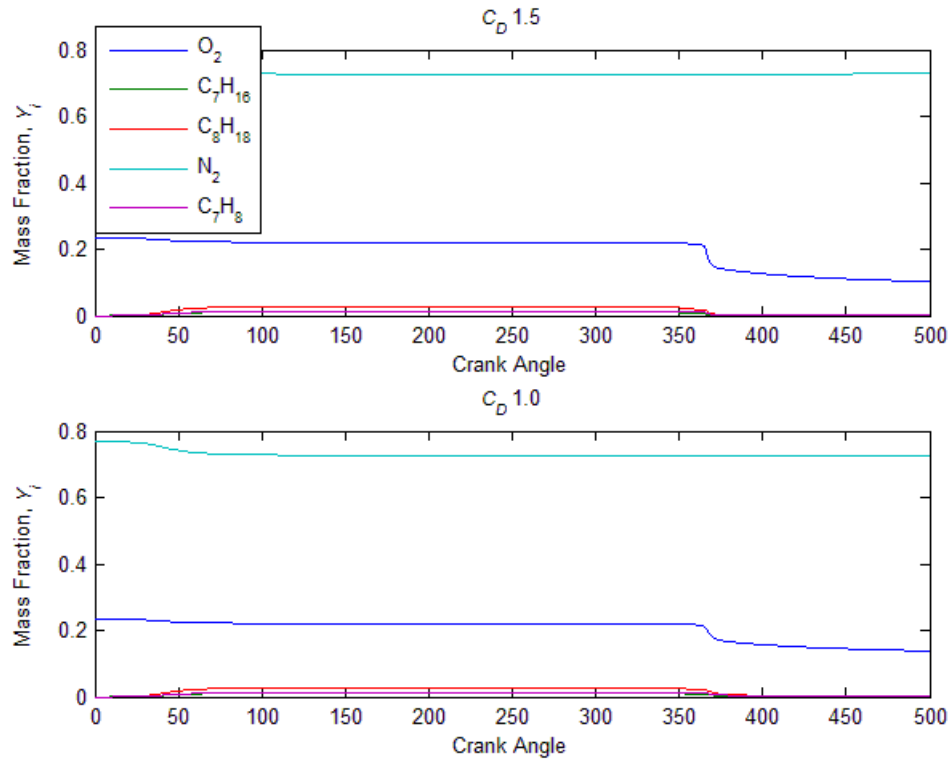


Figure 8.4 Oxidisers (O_2 and N_2) and fuels (C_7H_{16} , C_8H_{18} and C_7H_8) behaviour for the entire simulation for $C_D = 1.5$ and $C_D = 1.0$. $T_{in} = 250^\circ C$, $CR = 9$, $AFR = 16$, $N = 1500 \text{ rpm}$.

Figure 8.5 shows that when $C_D = 2.0$ and $C_D = 2.5$, the combustion behaviour is consistent for all species throughout the simulation. The in-cylinder pressure comparison in Figure 8.3 shows the peak pressure when $C_D = 2.0$ is slightly higher than $C_D = 2.5$, approaching the experimental in-cylinder peak pressure. The effects of C_D on the scalar dissipation rate and variance are shown in Figure 8.6. Kim (2004) reported that increasing the C_D value results in a lower scalar dissipation rate. The result is consistent with Figure 8.6(A), where as the C_D value increases, the scalar dissipation rate is reduced during the combustion (piston near TDC). This is due to the variance diminishing faster with the increasing C_D , as shown in Figure 8.6(B). The turbulent quantities (k and ε) for all C_D values in Figure 8.7 are very similar for the entire simulation and are not significantly affected. A small change in the turbulent quantities for different C_D values is due to a difference in mean density because C_D only directly affects the scalar transport equation. For higher C_D values, the turbulent kinetic energy and dissipation rate during combustion is slightly lower, as shown in Figure 8.7(B) and Figure 8.7(D). High C_D values are required for fast mixing at the

Chapter 8

nozzle area (Kim 2004) and, for the engine model, the flow of the air-fuel mixture is high during the IVO. Thus the C_D value should be high enough during the intake stroke without causing too much retarded combustion. Therefore, $C_D = 2.0$ was used for the rest of the study in this engine configuration, where it gives a good agreement between the model and experiment in terms of in-cylinder pressure trace.

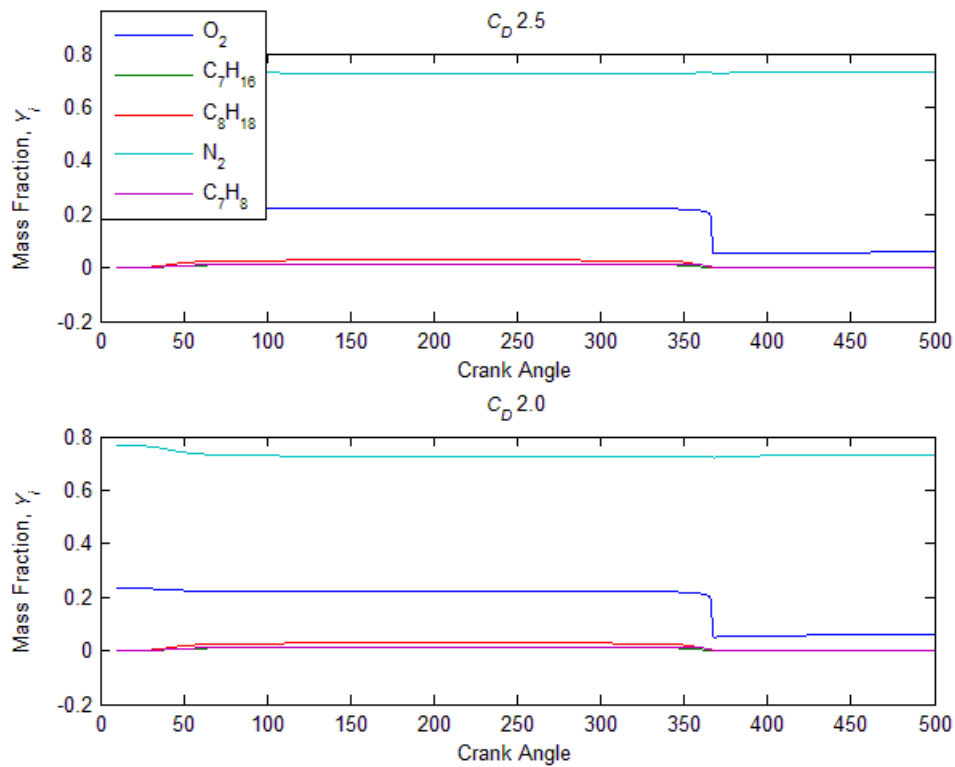


Figure 8.5 Oxidisers (O_2 and N_2) and fuels (C_7H_{16} , C_8H_{18} and C_7H_8) behaviour for the entire simulation for $C_D = 2.5$ and $C_D = 2.0$. $T_{in} = 250^\circ C$, $CR = 9$, $AFR = 16$, $N = 1500$ rpm.

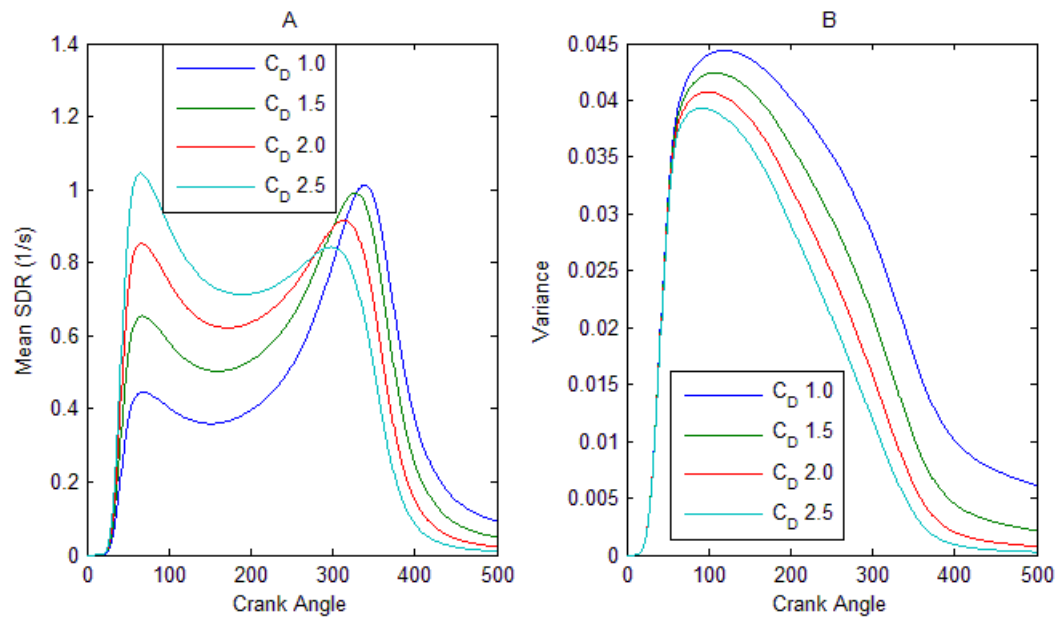


Figure 8.6 The effect of different C_D values on mean scalar dissipation rate (A) and variance (B) for the entire simulation.

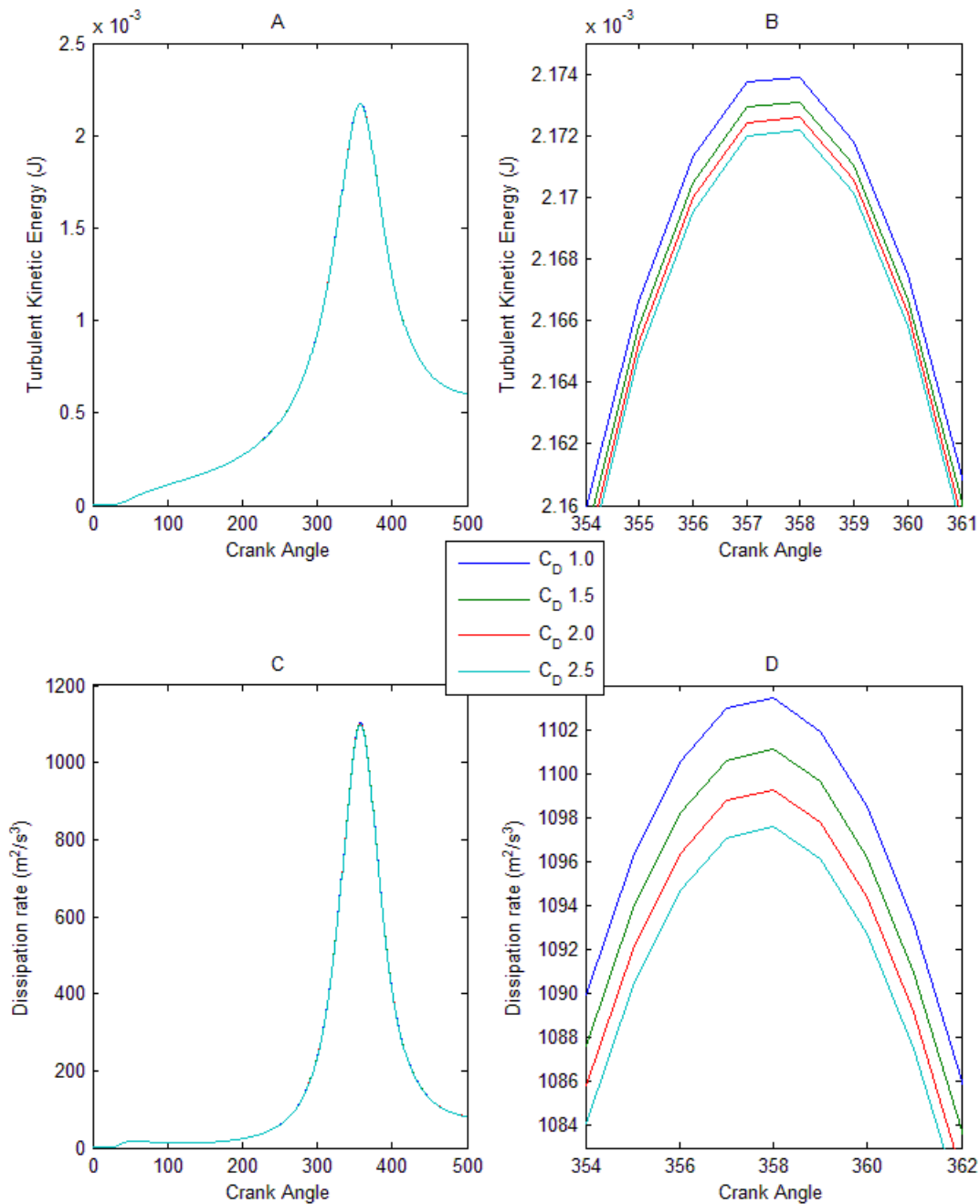


Figure 8.7 Turbulent quantities (k and ε) behaviour when C_D varies. Images B and D are enlarged at the peak of images A and C.

8.3.2 Independence Test: Number of Bins of the CMC Model

The number of bins is also tested for this engine configuration. For the n -heptane case, a higher number of bins causes a big difference in in-cylinder peak pressure. The same occurred for the gasoline test using others' experimental data in Chapter 5. This is due to the big variation between the stoichiometric mixture fraction, Z_{stoic} , and the mean

mixture fraction, Z_{mean} . In the experiment of this study, the AFR was kept close to the stoichiometric condition for a direct comparison between SI and HCCI engines, which is $AFR = 16$. This translates to $Z_{mean} = 0.0588$, where the stoichiometric mixture for gasoline fuel is $Z_{stoic} = 0.0637$. Thus, the high number of bins has not affected the in-cylinder peak pressure by much, as shown in Figure 8.8 and Figure 8.9, where there is a marginal increase in peak pressure when the number of bins is only slightly greater than 100. Therefore, the number of bins used in this engine configuration is 100, which gives faster computation time with very small effect in in-cylinder peak pressure.

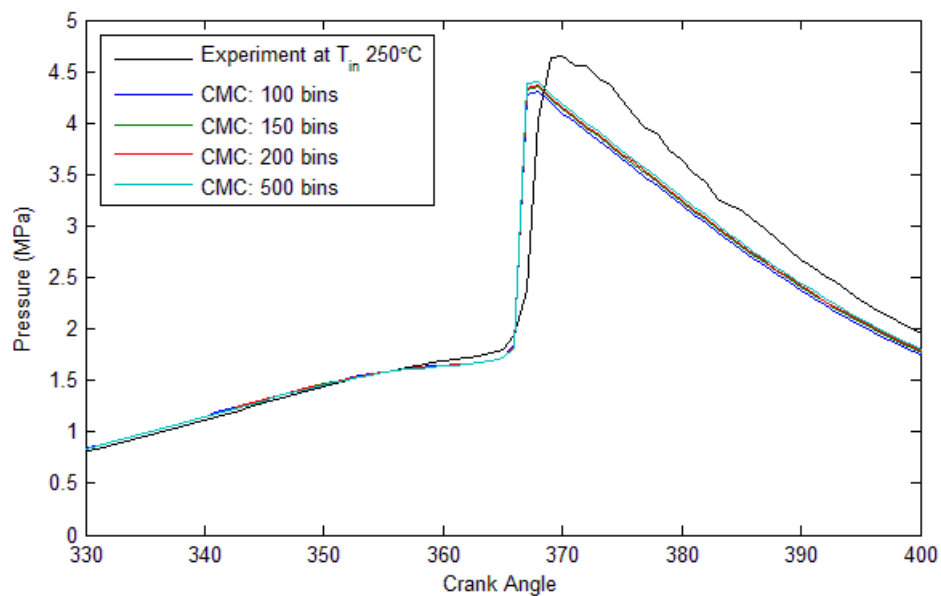


Figure 8.8 In-cylinder pressure comparison between experiment and CMC model with varying number of bins. $T_{in} = 250^{\circ}\text{C}$, $CR = 9$, $AFR = 16$, $N = 1500\text{rpm}$.

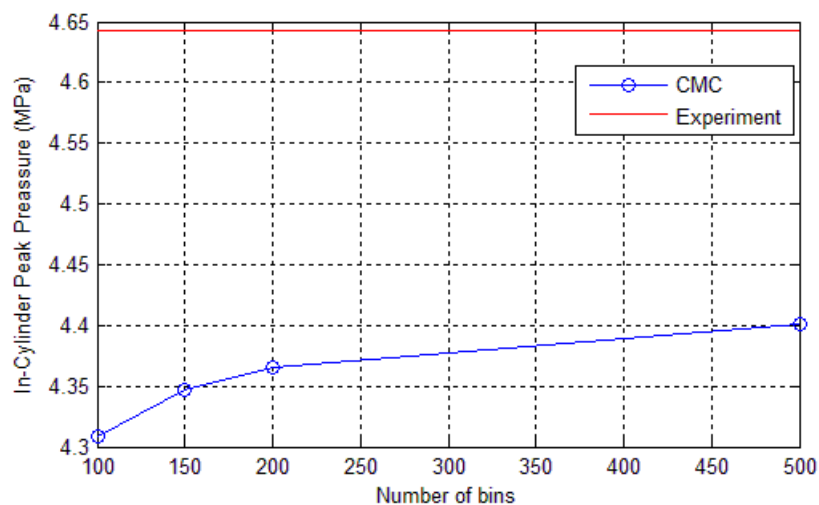


Figure 8.9 In-cylinder peak pressure comparison for different number of bins of the CMC model.

8.3.3 Conditional Mass Fractions

The combustion of gasoline fuel has a single-stage ignition (Kim, Kim & Lee 2004), and this behaviour can be observed in Figure 8.10, where the OH mass fraction shows a single peak compared to *n*-heptane's case with two peaks. The gasoline combustion with single-stage ignition is also observed with a gasoline fuelled HCCI engine in Chapter 5. As discussed before, where ignition is triggered by H₂O₂ decomposition, the same occurs for this engine configuration. The OH mass fraction increases rapidly once the decomposition process of H₂O₂ is nearly finished. The fuel components (C₇H₁₆, C₈H₁₈ and C₇H₈) were slowly consumed and their amounts reached zero once the in-cylinder temperature reached the peak. The species H and HO₂ are consumed at a high temperature, as discussed in Section 5.7.2, and this behaviour is also observed in Figure 8.10. The amount of CO peaks at approximately maximum in-cylinder temperature and CO₂ increases rapidly during the combustion. The oxidation of CO to CO₂ (Figure 8.10D) continues by the decreasing amount of CO matching the corresponding steady increase in CO₂ to complete the combustion.

Figure 8.11 and Figure 8.12 show the conditional mass fraction of the species during the combustion process. The result of O₂ consumption shows that the combustion was started near the mean mixture fraction before further advancing to the stoichiometric mixture fraction and propagating towards the rich region. The same occurs for the fuel components, where the combustion begins at a lean region and moves towards rich compositions as chemical equilibrium is approached. The OH and CO₂ mass fractions reached the peak at the stoichiometric mixture fraction, which is consistent with the CMC model in a multi-dimensional simulation (Bolla *et al.* 2013). The production of species H₂O₂, OH, CO and CO₂ is also observed to start at the lean side and propagate to reach a peak at the stoichiometric condition. Roomina and Bilger (2001) reported that the OH production was over-predicted compared to the experiment because of the limitation in using a first order closure for the chemical source terms. This could also be due to the limitation of using the zero-dimensional model where most of the fluctuations are neglected. The results were expected to improve when the model was run on the multi-dimensional simulation. However, the combustion characteristics in the HCCI engine can be understood using the zero-dimensional model while using modest computational resources and time. Also, the result shown here indicates that

the CMC with zero-dimensional model can be used for future investigation for different fuels, thereby requiring less time to complete without sacrificing much accuracy.

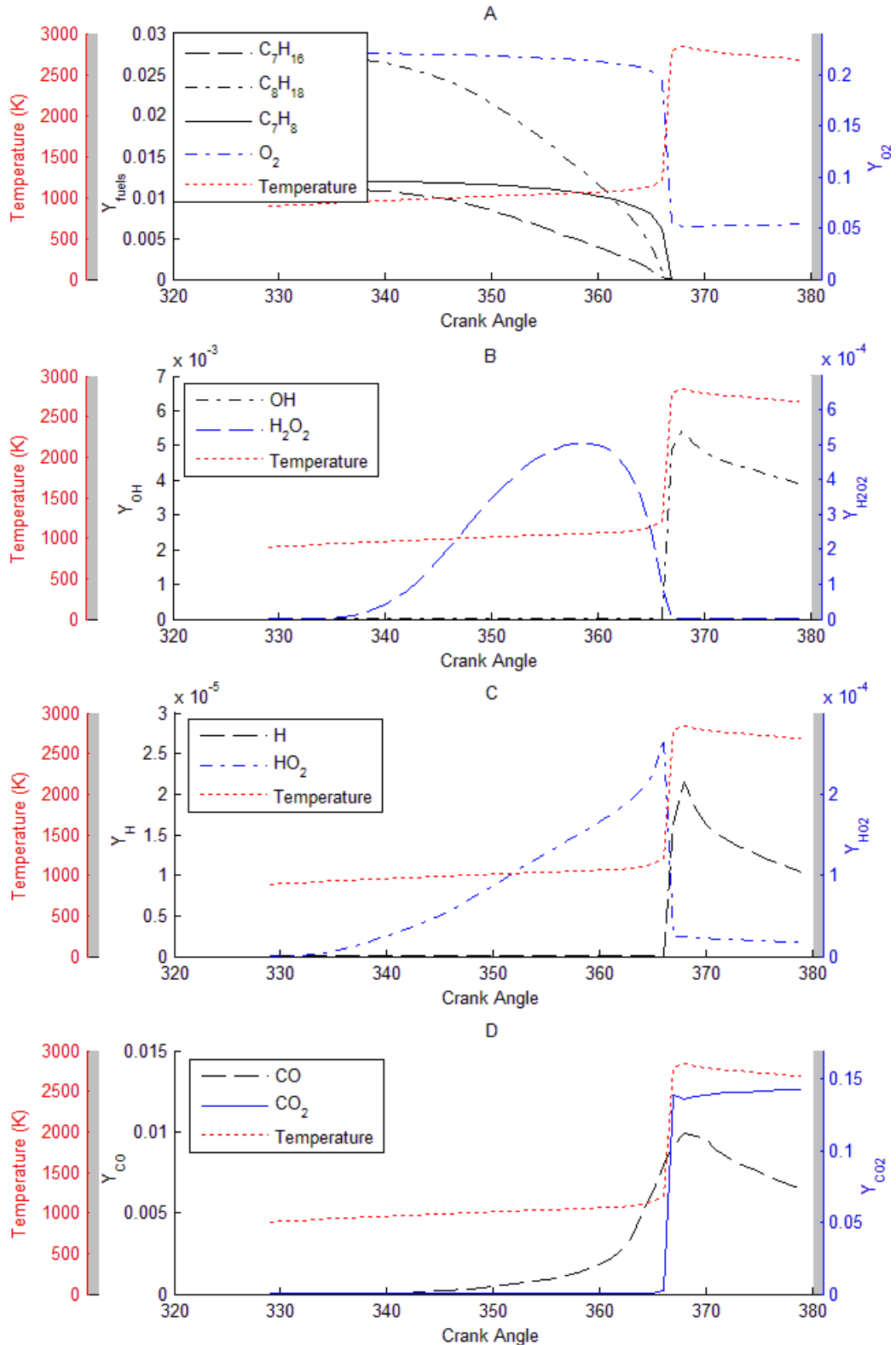


Figure 8.10 Mean mass fractions behaviour during combustion event compared with in-cylinder temperature trace for Honda engine, A: C_7H_{16} , C_8H_{18} , C_7H_8 and O_2 , B: OH and H_2O_2 , C: H and HO_2 , D: CO and CO_2 .

Chapter 8

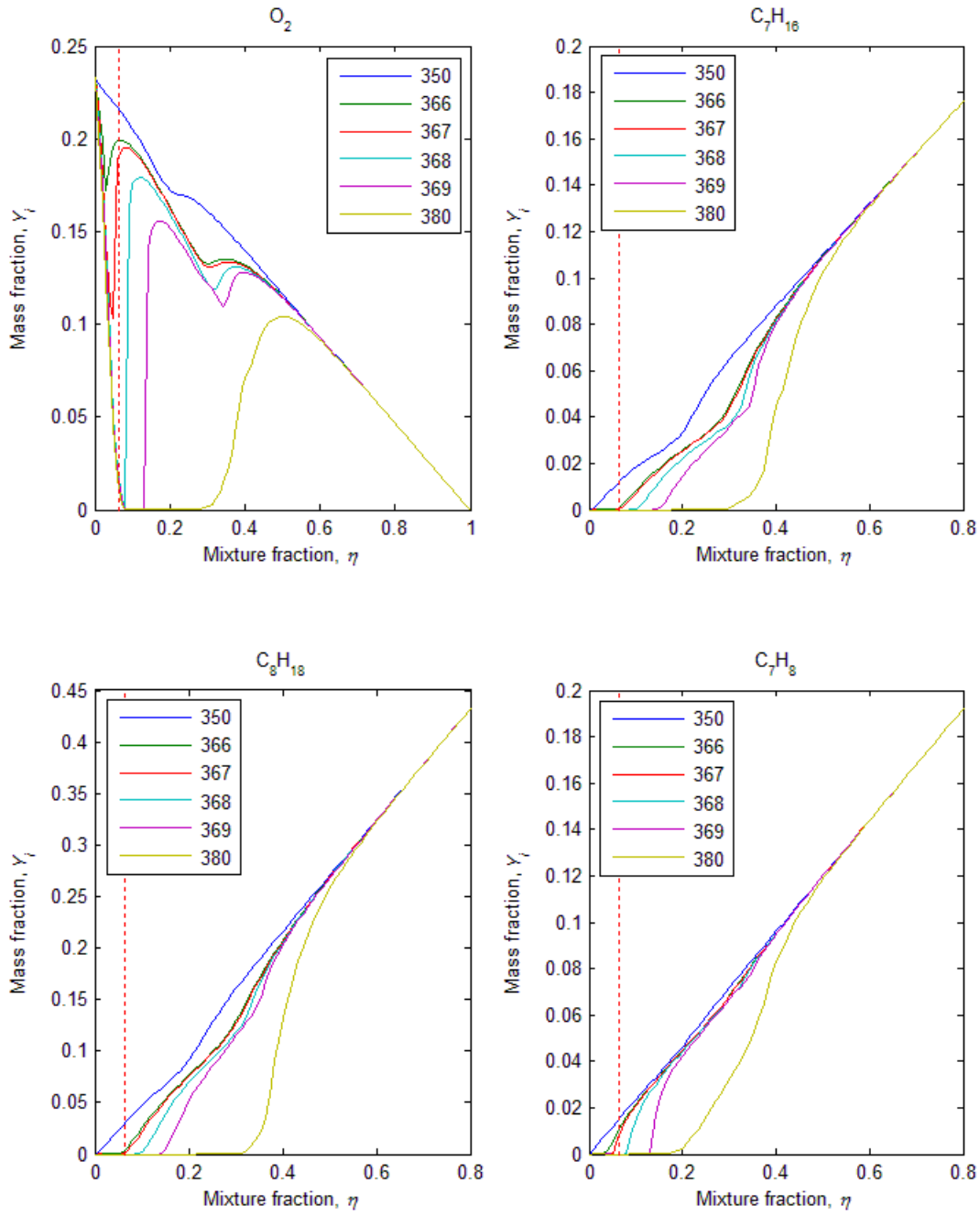


Figure 8.11 Conditional mass fraction comparison for different CA location during combustion for species O_2 , C_7H_{16} , C_8H_{18} and C_7H_8 . The dotted red line shows the location of the stoichiometric mixture fraction.

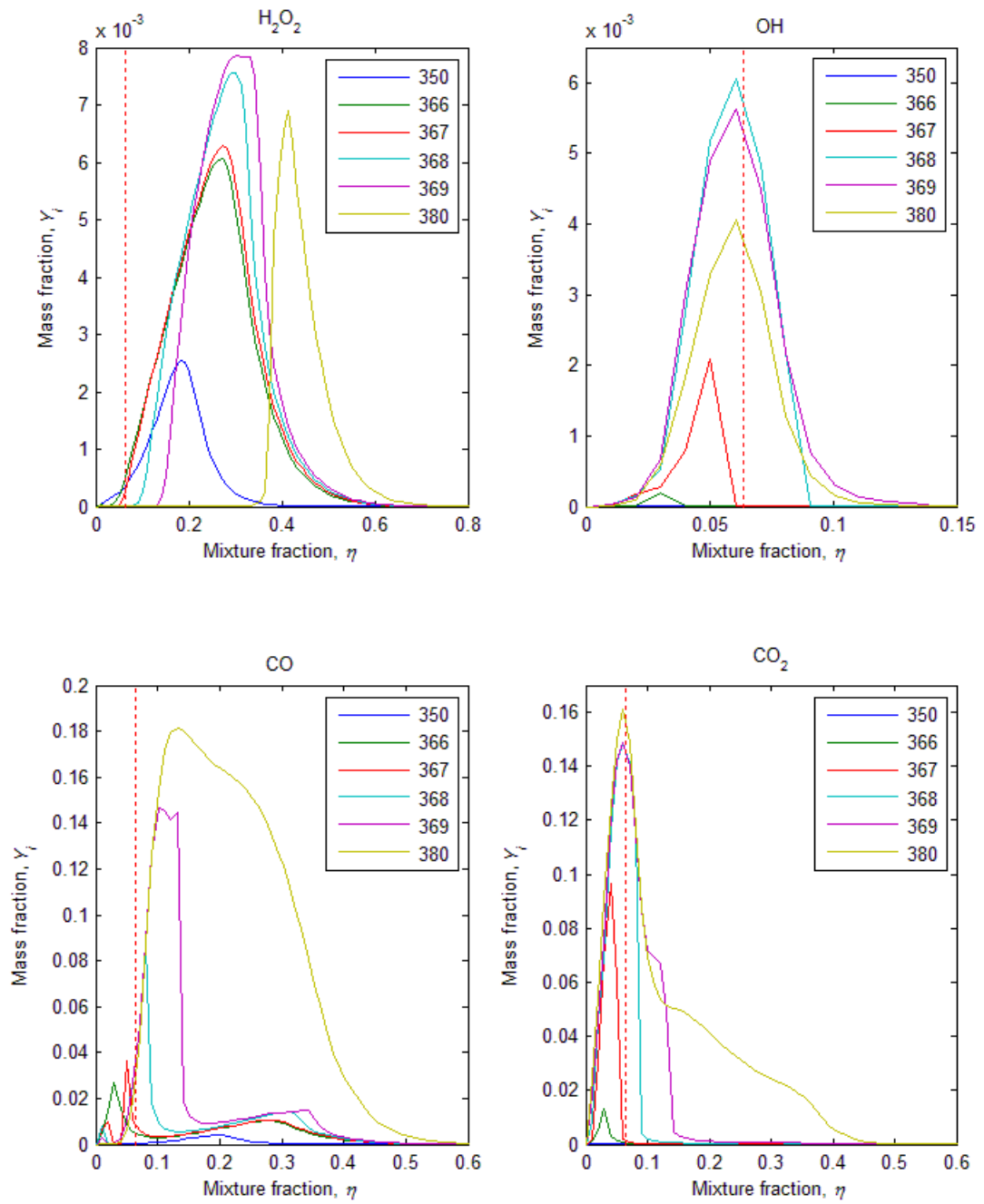


Figure 8.12 Conditional mass fraction comparison for different CA location during combustion for species H_2O_2 , OH , CO and CO_2 . The dotted red line shows the location of the stoichiometric mixture fraction.

8.3.4 Conditional Temperature

The conditional temperature profile for this engine configuration is shown in Figure 8.13, where the profile was observed from an early stage of the combustion at approximately 350°CA until 30°CA ATDC. The result shows that the conditional temperature peaks at $Z = 0.07$, where the stoichiometric mixture fraction is $Z_{stoic} = 0.0637$. The small variation between the peak location and Z_{stoic} is due to the smaller number of bins used in this study. A higher number of bins could resolve more combustion chemistry details with more computational resources and time. The difference in in-cylinder peak pressure for more than 100 bins is not significant, as shown in Figure 8.8, thus a small variation between Z_{stoic} and the in-cylinder peak pressure location is acceptable.

The auto-ignition for this case occurred for lean conditions and diffused towards the rich side when the combustion completed. Unlike the ignition for the *n*-heptane case, the ignition started on the fuel rich side of the stoichiometric boundary and diffused to the lean side to peak at the stoichiometric mixture fraction, which is consistent with Bolla *et al.* (2013). Both gasoline fuelled HCCI engine configurations show the same ignition behaviour with single stage-ignition as reported by Kim, Kim and Lee (2004). Thus, the CMC with zero-dimensional model with the gasoline fuelled HCCI engine configuration can be used to predict the combustion behaviour for different operating conditions, which will be discussed in the next section.

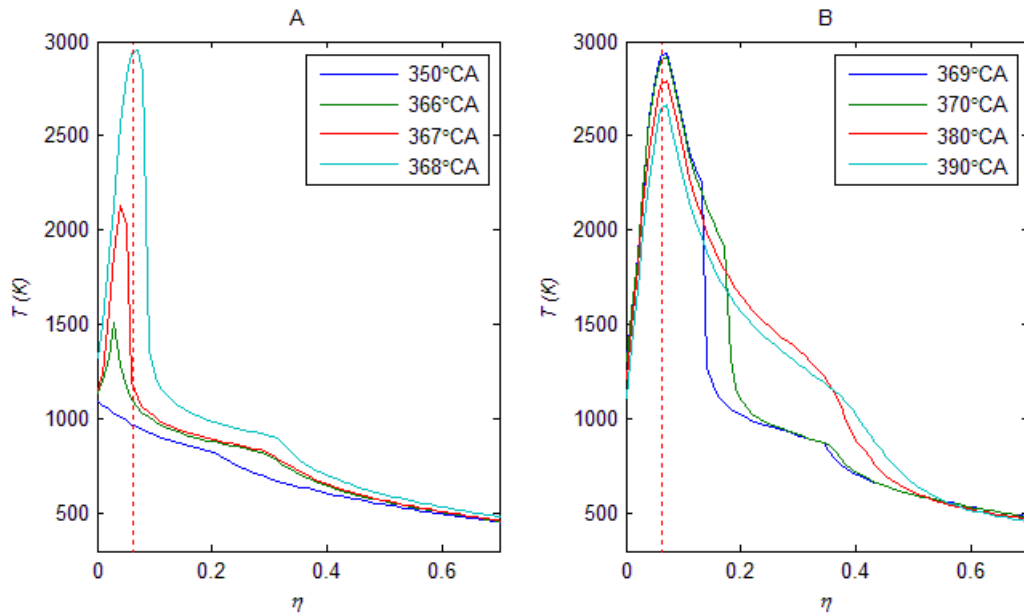


Figure 8.13 Conditional temperature profile during combustion with varying CA. The dotted red line shows the location of the stoichiometric mixture fraction.

8.4 Parametric Study

8.4.1 Intake Temperature

Heating the intake air is one of the useful methods to control the ignition timing of an HCCI engine (Antunes, Mikalsen & Roskilly 2008; Morsy 2007). The HCCI engine used in the experimental work of this study used intake air heating to achieve HCCI mode. Due to the small CR of the engine, the intake air has to be heated to at least 210°C; otherwise the engine cannot run in HCCI mode. A high intake air temperature for a small HCCI engine with low CR is also reported by Charalambides (2006).

Figure 8.14 shows the comparison between the CMC and zero-dimensional models with the experiment for different intake air temperatures. Three different intake temperatures from the experiment were selected: 250°C, 260°C and 270°C. Even though the intake air temperature in the experiment was run from 210°C up to 310°C, the selected readings showed less knocking behaviour compared to the rest. This is because the gasoline fuelled HCCI engine in this study was run at a near stoichiometric condition so that a direct comparison can be made between SI and HCCI engines, as

discussed in Chapter 7. Thus, those intake air temperature ranges were used for the rest of the study.

The result in Figure 8.14 shows that both the CMC and zero-dimensional models are in good agreement with the experiment for different intake air temperatures. Both models show slightly advanced combustion with lower in-cylinder peak pressure compared to the experiment. However, the zero-dimensional model shows further advancement of the ignition compared to the CMC model when the intake air temperature is higher than 250°C. When the in-cylinder peak pressure between the CMC and zero-dimensional models is compared, as shown in Figure 8.15, the in-cylinder peak pressure for the CMC model is slightly lower than for the zero-dimensional model. The peak pressure of those models is close when the intake air temperature is 270°C. Note that the intake air temperature for the zero-dimensional model was set 15°C higher than the actual, while the CMC model uses the actual temperature. The results show that the CMC model performs better than the zero-dimensional model. This is due to the zero-dimensional model's assumption that the combustion chamber is fully homogeneous, while the CMC model takes into consideration the effects of turbulence on the molecular mixing. Practically, the mixture is not perfectly homogenous, nor are the in-cylinder temperature and pressure. By using the CMC model, the variation of fuel in the mixture and turbulent effects were taken into consideration. These two parameters were not considered in the zero-dimensional model. Therefore, the results show that turbulence has a direct effect on the HCCI combustion that could change the temperature distribution across the chamber, where a small temperature difference affects the combustion behaviour, which is also reported in the literature (Cabra *et al.* 2002; Kong 2007)

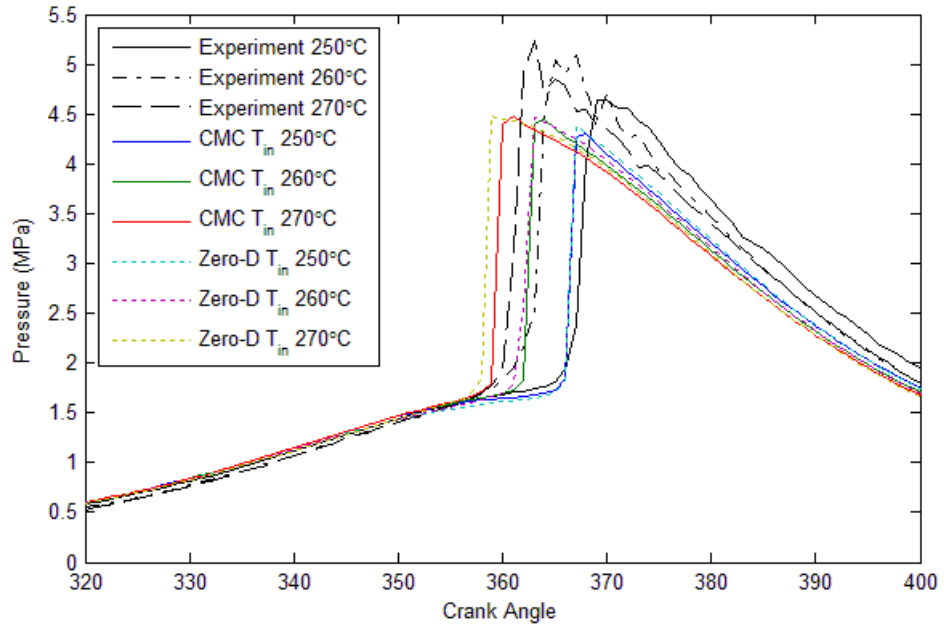


Figure 8.14 Comparison between CMC and zero-dimensional models against experiment with varying intake air temperature. CR= 9, AFR=16, N=1500rpm.

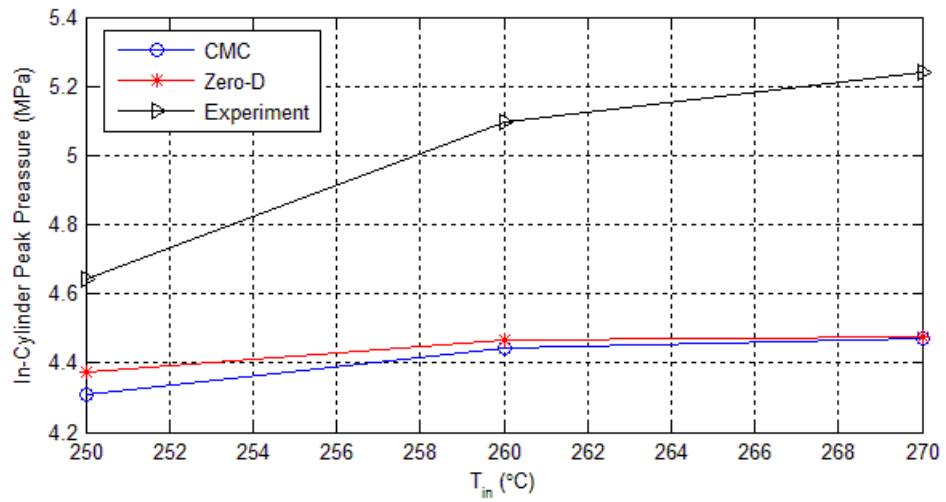


Figure 8.15 Comparison of in-cylinder peak pressure between CMC and zero-dimensional models against experiment. CR= 9, AFR=16, N=1500rpm.

8.4.2 Compression Ratio (CR)

An HCCI engine operating with a high CR has the advantage of a CI engine's efficiency with low emissions levels (Christensen & Johansson 1998; Epping *et al.* 2002). The gasoline fuelled HCCI engine in this study has a low CR and thus the engine efficiency is not as high as in those with a high CR. If the engine has a high CR, the intake air temperature can be lowered to control the combustion. Figure 8.16 shows the effects of a high CR on the in-cylinder peak pressure and ignition point. The zero-dimensional model has an advanced ignition point compared to the CMC model, where the behaviour becomes more significant when the intake air temperature is set to 270°C. The zero-dimensional model only has a similar ignition point to the CMC model at the lowest CR and intake air temperature, which are 9 and 250°C respectively. Then, the zero-dimensional model tends to advance the ignition by more once the CR and intake air temperature are increased. As discussed in the previous section, the intake air temperature for the zero-dimensional model was set 15°C higher than the actual and this shows that the CMC model (using the actual intake air temperature) predicts the combustion better than the zero-dimensional model.

The difference in in-cylinder peak pressure, Figure 8.17(A), and the ignition location, Figure 8.17(B), is determined for varying CR and intake air temperature using the CMC model with the same AFR as the experiment in this study. The results show that the in-cylinder peak pressure increases with the increasing CR. High in-cylinder pressure is useful to obtain high engine BMEP so that the engine can be operated in a high load condition (Tsolakis & Megaritis 2005; Tsolakis, Megaritis & Yap 2008). To obtain high BMEP, the CR of the engine has to be increased. However, the ignition point is advanced significantly when high CR is employed (CR=13), where the ignition occurs long before TDC, which can create knocking. The ignition point is advanced further if the intake air temperature increases. This shows that the ignition point can be controlled using different CR and intake air temperature. If a high CR engine is to be used, a much lower intake air temperature than 250°C is necessary to achieve good combustion characteristics, where the ignition occurs at about TDC. Thus, the HCCI engine can achieve high engine efficiency if a high CR is employed, provided that the ignition point is controlled well.

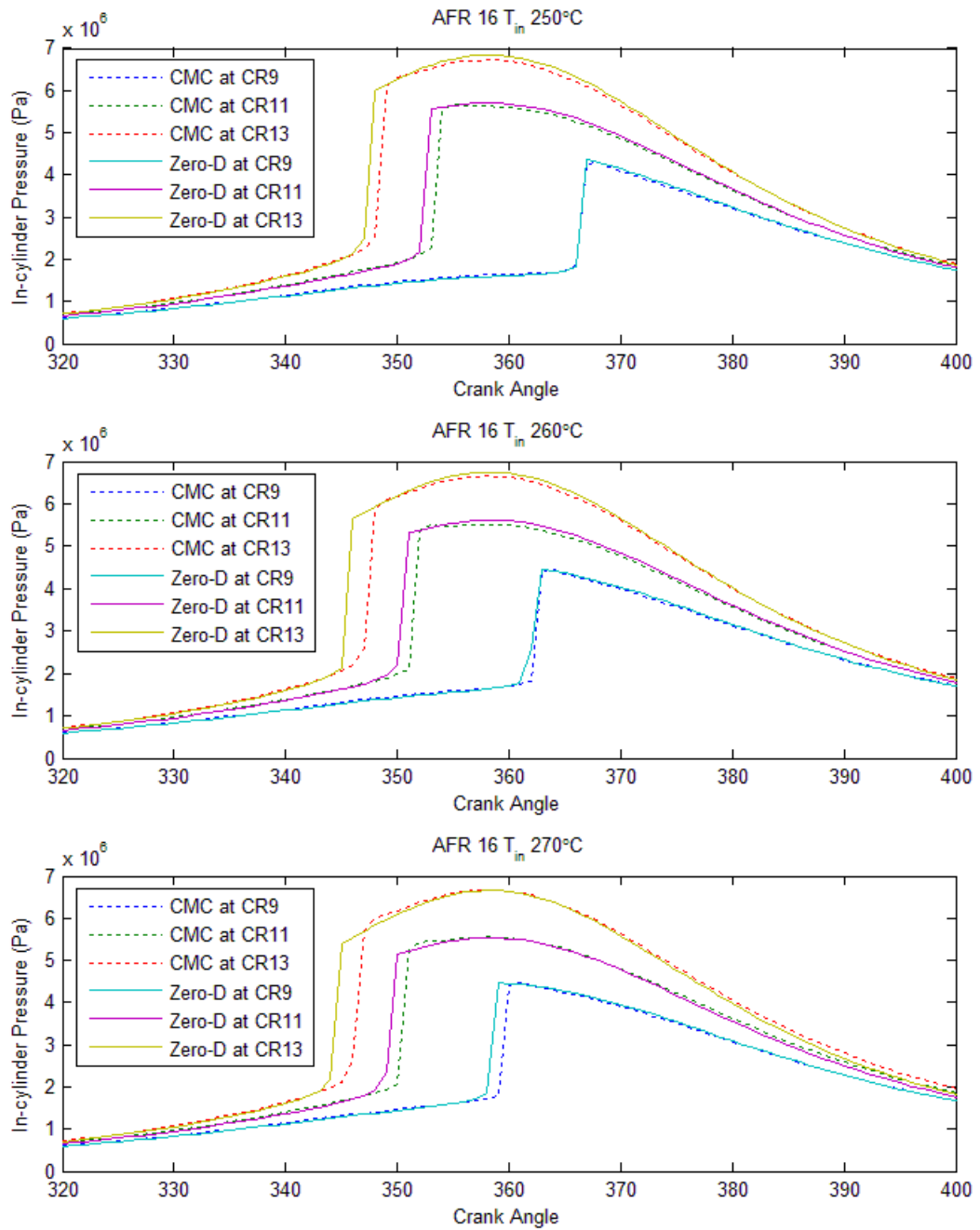


Figure 8.16 In-cylinder pressure comparison between CMC and zero-dimensional models with varying CR and intake air temperature.

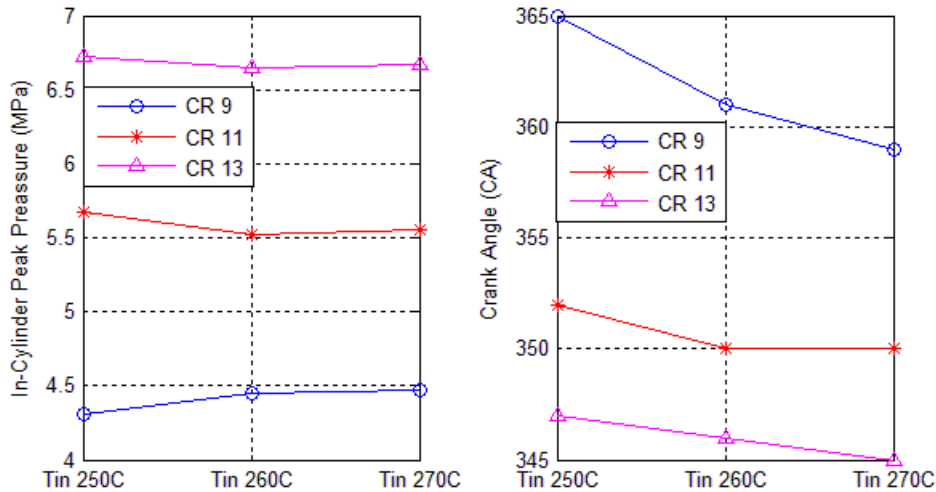


Figure 8.17 A comparison for in-cylinder peak pressure (A) and ignition location (B) with varying CR and intake temperature.

8.5 Conclusion

This chapter has discussed the validation of the CMC and zero-dimensional models against a gasoline fuelled HCCI engine in the experimental work of this study. Also discussed in this chapter is the performance of these models for different engine operating conditions. The CMC model shows a good agreement with the experiment, where the model can use the actual intake air temperature. The zero-dimensional model, on the other hand, is required to increase the intake air temperature, where for this case it was increased 15°C higher than the actual.

When a high intake air temperature is used, the ignition is slightly advanced, but the peak pressure has not been affected much. For varying CR, the ignition point is advanced before TDC when the CR of the engine is increased. The ignition point was further advanced when a high intake air temperature was also used. Thus, to control the combustion for a gasoline fuelled HCCI engine, the intake air temperature can be reduced further if a high CR engine is to be used. Other means of ignition control can also be used for HCCI combustion, such as EGR and valve timing, and the study of these controls is recommended for future work.

Chapter 9

CONCLUSION

9.1 Summary and Future Work

The purpose of this thesis was to implement the CMC model in a zero-dimensional simulation. Most CMC studies utilise a multi-dimensional simulation (Bolla *et al.* 2013; De Paola *et al.* 2008; Seo *et al.* 2010; Wright *et al.* 2005), where the model produces good agreement with the experiment but requires high computational resources. A zero-dimensional single-zone model has the advantage of faster computing time. However, it has the limitation of short burn duration which causes higher in-cylinder peak pressure (Morsy 2007).

There is also an argument in the literature that the turbulent mixing only has a minor direct effect on HCCI combustion (Aceves *et al.* 2000; Aceves *et al.* 2002). Kong and Reitz (2002) suggested that the turbulent mixing effect on HCCI combustion requires further investigation. The use of a zero-dimensional single-zone model assumes that the combustion chamber is fully homogeneous without any turbulence effect. Implementing a CMC model into a zero-dimensional single-zone model will take into consideration the turbulence-chemistry interactions at the molecular level. The use of this combined model (CMC and zero-dimensional single-zone models) in the HCCI combustion area is new in the literature. There is a study by Kwon *et al.* (2011) using CMC in a zero-dimensional model. However, they used a CI engine configuration with a direct-injection spray penetration model. The method in this thesis uses an HCCI engine configuration, where the fuel was port-injected in the intake manifold.

The results in Chapter 5 and Chapter 8 show that the combined model has improved the limitation of the zero-dimensional single-zone model. The combined model has the ability to use the actual intake air temperature directly, while the zero-dimensional model requires the intake temperature to be set 15-30°C higher than the actual

(Bunting *et al.* 2008; Guo *et al.* 2010). The results in Chapter 5 show that the combined model slightly under-predicts the peak pressure with smooth variations throughout the in-cylinder pressure profile. The same behaviour is also observed in Chapter 8 with small differences between the CMC and zero-dimensional models. The combined model, however, has a limitation of inaccurately predicting the ignition point when the AFR varies. This is due to the nature of the homogeneous CMC model where most of the fluctuating quantities are ignored, especially the physical space dependence (Wright 2005), and there may be significant conditional fluctuations which require higher-order modelling than the first-order CMC (Behzadi *et al.* 2013). The rest of the parametric investigations show that the combined model is in good agreement with the experiment. The investigation of the limitation of the combined model is recommended for future work.

Experimental work was also performed in this thesis and used as a third validation tool in Chapter 8. The performance of a gasoline fuelled HCCI engine developed in the experimental test rig was directly compared with the SI engine configuration using the same operating conditions. The results in Chapter 7 are consistent with the literature, where the HCCI engine has the limitation of operating in a low load condition. The emissions levels also show that the HCCI engine returns higher unburned HC and CO compared to the SI engine, which again is consistent with the literature. The HCCI engine, however, produces a high level of knock because the AFR was kept at a near stoichiometric mixture for a direct comparison with the SI engine. Future work is recommended for this engine to gain more control of the combustion timing so that the engine operates without knocking. Direct comparison with the SI engine will no longer be valid, but the aims overall are to obtain better HCCI engine combustion, which can also improve the emissions levels. There are a few ways to control the ignition of the HCCI combustion, e.g. implementing EGR (Ganesh & Nagarajan 2010; Saravanan & Nagarajan 2010), pressurising intake air (Agarwal & Assanis 1998; Liu *et al.* 2009) or hydrogen addition (Saravanan, Nagarajan & Narayanasamy 2008; Tsolakis & Megaritis 2005; Tsolakis, Megaritis & Yap 2008). These ignition control methods for HCCI combustion can be used in future work to improve the operation of the HCCI engine.

REFERENCES

Aceves, S & Flowers, D 2004, *Engine shows diesel efficiency without the emissions*, Lawrence Livermore National Laboratory.

Aceves, SM, Smith, JR, Westbrook, CK & Pitz, JW 1998, 'Compression ratio effect on methane hcci combustion', in proceedings of the *ASME Combustion Engine*, Clymer, New York.

Aceves, SM, Flowers, DL, Martinez-Frias, J, Smith, JR, Dibble, R, Au, M & Girard, J 2001, 'Hcci combustion: Analysis and experiments', *SAE Paper 2001-01-2077*.

Aceves, SM, Flowers, DL, Martinez-Frias, D, Espinosa-Loza, F, Christensen, M, Johansson, B & Hessel, RP 2004, 'Analysis of the effect of geometry generated turbulence on hcci combustion by multi-zone modeling', *SAE Paper 2006-01-0814*.

Aceves, SM, Flowers, DL, Westbrook, CK, Smith, JR, Pitz, W, Dibble, R, Christensen, M & Johansson, B 2000, 'A multi-zone model for prediction of hcci combustion and emissions', *SAE Paper 010327*.

Aceves, SM, Martinez-Frias, D, Flowers, D, Espinosa-Loza, F, Dibble, R, Christensen, M, Johansson, B & Hessel, R 2002, 'Piston-liner crevice geometry effect on hcci combustion by multi-zone analysis', *SAE Paper 2002-01-2869*.

Agarwal, A & Assanis, DN 1998, 'Multi-dimensional modeling of natural gas ignition under compression ignition conditions using detailed chemistry', *SAE Paper 980136*.

Agarwal, A & Assanis, DN 2000, 'Multi-dimensional modeling of ignition, combustion and nitric oxide formation in direct injection natural gas engines', *SAE Paper 011839*.

Agarwal, A, Filipi, ZS, Assanis, DN & Baker, DM 1998, 'Assessment of single- and two-zone turbulence formulations for quasi-dimensional modeling of spark-ignition engine combustion', *Combustion Science and Technology*, vol. 136, no. 1-6, pp. 13-39.

Ahn, K, Rakha, H, Trani, A & Van Aerde, M 2002, 'Estimating vehicle fuel consumption and emissions based on instantaneous speed and acceleration levels', *Journal of Transportation Engineering*, vol. 128, no. 2.

References

Akansu, SO, Dulger, Z, Kahraman, N & Veziroglu, TN 2004, 'Internal combustion engines fueled by natural gas - hydrogen mixtures', *International Journal of Hydrogen Energy*, vol. 29, no. 14, pp. 1527-39.

Alfonsi, G 2009, 'Reynolds-averaged navier-stokes equations for turbulence modeling', *Applied Mechanics Reviews*, vol. 62, no. 4, pp. 040802.

Alkidas, AC 2007, 'Combustion advancements in gasoline engines', *Energy Conversion and Management*, vol. 48, no. 11, pp. 2751-61.

Amin, S 2009, 'Review on biofuel oil and gas production processes from microalgae', *Energy Conversion and Management*, vol. 50, no. 7, pp. 1834-40.

Amneus, P, Nilsson, D, Mauss, F, Christensen, M & Johansson, B 1998, 'Homogeneous charge compression ignition engine: Experiments and detailed kinetic calculations', in proceedings of the *The Fourth International Symposium COMODIA 98*, pp. 567-72.

An, HJ, Wilhelm, WE & Searcy, SW 2011, 'Biofuel and petroleum-based fuel supply chain research: A literature review', *Biomass & Bioenergy*, vol. 35, no. 9, pp. 3763-74.

Andrae, JCG 2011, 'A kinetic modeling study of self-ignition of low alkylbenzenes at engine-relevant conditions', *Fuel Processing Technology*, vol. 92, no. 10, pp. 2030-40.

Andreae, MM, Cheng, WK, Kenney, T & Yang, J 2007, 'On hcci engine knock', *SAE paper 2007-01-1858*.

Antunes, JMG, Mikalsen, R & Roskilly, AP 2008, 'An investigation of hydrogen-fuelled hcci engine performance and operation', *International Journal of Hydrogen Energy*, vol. 33, no. 20, pp. 5823-8.

Antunes, JMG, Mikalsen, R & Roskilly, AP 2009, 'An experimental study of a direct injection compression ignition hydrogen engine', *International Journal of Hydrogen Energy*, vol. 34, no. 15, pp. 6516-22.

Assanis, DN & Heywood, JB 1986, 'Development and use of a computer simulation of the turbocompounded diesel system for engine performance and component heat transfer studies', *SAE Paper 860329*.

References

Assanis, DN & Polishak, M 1990, 'Valve event optimization in a spark-ignition engine', *Journal of Engineering for Gas Turbines and Power-Transactions of the Asme*, vol. 112, no. 3, pp. 341-7.

Audi 2012, Audi glossary: FSI, viewed 19 April 2012, <<http://www.audi.com.au/au/brand/en/tools/advice/glossary/fsi.browser.html>>.

Babajimopoulos, A, Assanis, DN & Fiveland, SB 2002, 'An approach for modeling the effects of gas exchange processes on hcci combustion and its application in evaluating variable valve timing control strategies', *SAE Paper 2002-01-2829*.

Babajimopoulos, A, Lavoie, GA & Assanis, DN 2003, 'Modeling hcci combustion with high levels of residual gas fraction - a comparison of two vva strategies', *SAE Paper 2003-01-3220*.

Barber, EM, Reynolds, B & Tierney, WT 1955, 'Elimination of combustion knock-texaco combustion process', *SAE Paper 510173*.

Bari, S & Esmail, MM 2010, 'Effect of h-2/o-2 addition in increasing the thermal efficiency of a diesel engine', *Fuel*, vol. 89, no. 2, pp. 378-83.

Bari, S, Lim, TH & Yu, CW 2002, 'Effects of preheating of crude palm oil (cpo) on injection system, performance and emission of a diesel engine', *Renewable Energy*, vol. 27, no. 3, pp. 339-51.

Barroso, G, Escher, K & Boulouchos, K 2005, 'Experimental and numerical investigations on hcci-combustion', *SAE Paper 2005-24-038*.

Barths, H, Hasse, C, Bikas, G & Peters, N 2000, 'Simulation of combustion in direct injection diesel engines using a eulerian particle flamelet model', *Proceedings of the Combustion Institute*, vol. 28, pp. 1161-8.

Bates, B, Kundzewicz, ZW, Wu, S & Palutikof, J 2008, *Climate change and water. Technical paper of the intergovernmental panel on climate change*, Geneva.

Behzadi, J, Talei, M, HawkeS, ER, Lucchini, T & D'Errico, G 2013, 'Simulations of auto-ignition in compositionally stratified n-heptane/air mixtures with conditional moment closure', in proceedings of the *Australian Combustion Symposium*, The University of Western Australia.

References

- Benarafa, Y, Cioni, O, Ducros, F & Sagaut, P 2006, 'Rans/les coupling for unsteady turbulent flow simulation at high reynolds number on coarse meshes', *Computer Methods in Applied Mechanics and Engineering*, vol. 195, no. 23-24, pp. 2939-60.
- Bengtsson, J, Gafvert, M & Strandh, P 2004, 'Modeling of hcci engine combustion for control analysis', *2004 43rd Ieee Conference on Decision and Control (Cdc), Vols 1-5*, pp. 1682-7.
- Bhave, A, Kraft, M, Montorsi, L & Mauss, F 2006, 'Sources of co emissions in an hcci engine: A numerical analysis', *Combustion and Flame*, vol. 144, no. 3, pp. 634-7.
- Bilger, RW 1976, 'The structure of diffusion flames', *Combustion Science and Technology*, vol. 13, no. 1-6, pp. 155-70.
- Bilger, RW 1993, 'Conditional moment closure for turbulent reacting flow', *Physics of Fluids a-Fluid Dynamics*, vol. 5, no. 2, pp. 436-44.
- Bisetti, F & Chen, JY 2005, *Les of sandia flame d with eulerian pdf and finite-rate chemistry*, University of California, Berkeley.
- Bisetti, F, Chen, JY, Hawkes, ER & Chen, JH 2008, 'Probability density function treatment of turbulence/chemistry interactions during the ignition of a temperature-stratified mixture for application to hcci engine modeling', *Combustion and Flame*, vol. 155, no. 4, pp. 571-84.
- Bodansky, D 2010, 'The copenhagen climate change conference: A postmortem', *American Journal of International Law*, vol. 104, no. 2, pp. 230-40.
- Böhme, J, Jung, M, Fröhlich, G, Pfannerer, D, Märkle, T & Felsmann, C 2006, 'The new 1.8l four cylinder t-fsi engine by audi', *MTZ worldwide*, vol. 67, no. 10, pp. 2-5.
- Bolla, M, Gudmundsson, T, Wright, YM & Boulouchos, K 2013, 'Simulation of diesel sprays using the conditional moment closure model', *SAE Paper 2013-01-1618*.
- Borgnakke, C, Arpaci, VS & Tabaczynski, RJ 1980, 'A model for the instantaneous heat transfer and turbulence in a spark ignition engine', *SAE Paper 800287*.
- Brakora, JL 2012, 'A comprehensive combustion model for biodiesel-fueled engine simulations', University of Wisconsin.

References

- Brakora, JL, Ra, Y, Reitz, RD, McFarlane, J & Daw, SC 2008, 'Development and validation of a reduced reaction mechanism for biodiesel-fueled engine simulations', *SAE Paper 2008-01-1378*.
- Bression, G, Soleri, D, Savy, S, Dehoux, S, Azoulay, D, Hamouda, HB, Doradoux, L, Guerrassi, N & Lawrence, N 2008, 'A study of methods to lower hc and co emissions in diesel hcci', *SAE Paper 2008-01-0034*.
- Bromberg, L, Cohn, DR, Rabinovich, A & Heywood, J 2001, 'Emissions reductions using hydrogen from plasmatron fuel converters', *International Journal of Hydrogen Energy*, vol. 26, no. 10, pp. 1115-21.
- Bunting, BG, Eaton, S, Naik, CV, Puduppakkam, KV, Chou, CP & Meeks, E 2008, 'A comparison of hcci ignition characteristics of gasoline fuels using a single-zone kinetic model with a five component surrogate fuel', *SAE Paper 2008-01-2399*.
- Burke, MP, Chaos, M, Ju, YG, Dryer, FL & Klippenstein, SJ 2012, 'Comprehensive h₂/o₂ kinetic model for high-pressure combustion', *International Journal of Chemical Kinetics*, vol. 44, no. 7, pp. 444-74.
- Bushe, WK & Steiner, H 1999, 'Conditional moment closure for large eddy simulation of nonpremixed turbulent reacting flows', *Physics of Fluids*, vol. 11, no. 7, pp. 1896-906.
- Cabra, R, Myhrvold, T, Chen, JY, Dibble, RW, Karpetis, AN & Barlow, RS 2002, 'Simultaneous laser raman-rayleigh-lif measurements and numerical modeling results of a lifted turbulent h₂/n₂ jet flame in a vitiated coflow', *Proceedings of the Combustion Institute*, vol. 29, pp. 1881-8.
- Canova, M, Garcin, R, Midlam-Mohler, S, Guezennec, Y & Rizzoni, G 2005, 'A control-oriented model of combustion process in a hcci diesel engine', *ACC: Proceedings of the 2005 American Control Conference, Vols 1-7*, pp. 4446-51.
- Cant, RS & Mastorakos, E 2008, *An introduction to turbulent reacting flows*, Imperial College Press, London.
- Carnahan, B, Luther, HA & Wilkes, JO 1969, *Applied numerical methods*, Wiley, New York.
- Celik, I, Yavuz, I & Smirnov, A 2001, 'Large eddy simulations of in-cylinder turbulence for internal combustion engines: A review', *International Journal of Engine Research*, vol. 2, no. 2, pp. 119-48.

References

Chan, CC 2002, 'The state of the art of electric and hybrid vehicles', in, Institute of Electrical and Electronics Engineers, pp. 247-75.

Chang, J, Guralp, O, Filipi, Z, Assanis, D, Kuo, TW, Najt, P & Rask, R 2004, 'New heat transfer correlation for an hcci engine derived from measurements of instantaneous surface heat flux', in proceedings of the *SAE Paper 2004-01-2996*.

Chapra, SC & Canale, RP 2006, *Numerical methods for engineers*, Fifth Edition edn, McGraw-Hill, New York.

Charalambides, AG 2006, 'Charge stratified hcci engine', Ph.D thesis, University of London, London.

Chemical safety data sheet, 2011, Gas Malaysia, Malaysia.

Chen, Z, Konno, M & Goto, S 2001, 'Study on homogeneous premixed charge ci engine fueled with lpg', *JSAE Paper 200114339*, vol. 22, pp. 265-70.

Chevron 1996, 'Motor gasolines technical review (fr-1)', *Chevron Products Company*.

Cho, HM & He, BQ 2007, 'Spark ignition natural gas engines - a review', *Energy Conversion and Management*, vol. 48, no. 2, pp. 608-18.

Christensen, M & Johansson, B 1998, 'Influence of mixture quality on homogeneous charge compression ignition', *SAE Paper 982454*.

Christensen, M, Johansson, B & Einewall, P 1997, 'Homogeneous charge compression ignition (hcci) using iso-octane, ethanol and natural gas - a comparison with spark ignition operation', *SAE Paper 971676*.

Christodoulou, F & Megaritis, A 2013, 'Experimental investigation of the effects of separate hydrogen and nitrogen addition on the emissions and combustion of a diesel engine', *International Journal of Hydrogen Energy*, vol. 38, no. 24, pp. 10126-40.

Cleary, M & Kronenburg, A 2007, 'Hybrid' multiple mapping conditioning on passive and reactive scalars', *Combustion and Flame*, vol. 151, no. 4, pp. 623-38.

Cleary, M & Klimenko, AY 2011, 'Multiple mapping conditioning: A new modelling framework for turbulent combustion', in T Echehki & E Mastorakos (eds), *Turbulent combustion modeling*, Springer, pp. 143-73.

References

Cleary, MJ & Kronenburg, A 2007, 'Multiple mapping conditioning for extinction and reignition in turbulent diffusion flames', *Proceedings of the Combustion Institute*, vol. 31, pp. 1497-505.

Cleary, MJ & Klimenko, AY 2009, 'A generalised multiple mapping conditioning approach for turbulent combustion', *Flow Turbulence and Combustion*, vol. 82, no. 4, pp. 477-91.

Cleary, MJ, Klimenko, AY, Janicka, J & Pfitzner, M 2009, 'A sparse-lagrangian multiple mapping conditioning model for turbulent diffusion flames', *Proceedings of the Combustion Institute*, vol. 32, pp. 1499-507.

Combustion, 2009, viewed 06/05/2011, <<http://www.cfd-online.com/Wiki/Combustion>>.

Curran, HJ, Gaffuri, P, Pitz, WJ & Westbrook, CK 1998, 'A comprehensive modeling study of n-heptane oxidation', *Combustion and Flame*, vol. 114, no. 1-2, pp. 149-77.

Curran, HJ, Gaffuri, P, Pitz, WJ & Westbrook, CK 2002, 'A comprehensive modeling study of iso-octane oxidation', *Combustion and Flame*, vol. 129, no. 3, pp. 253-80.

de Morais, AM, Mendes Justino, MA, Valente, OS, Hanriot, SdM & Sodr , JR 2013, 'Hydrogen impacts on performance and co2 emissions from a diesel power generator', *International Journal of Hydrogen Energy*, vol. 38, no. 16, pp. 6857-64.

De Paola, G, Mastorakos, E, Wright, YM & Boulouchos, K 2008, 'Diesel engine simulations with multi-dimensional conditional moment closure', *Combustion Science and Technology*, vol. 180, no. 5, pp. 883-99.

de Risi, A, Carlucci, AP, Laforgia, D & Naccarato, F 2008, 'Experimental investigation and combustion analysis of a direct injection dual-fuel diesel-natural gas engine', *Energy*, vol. 33, no. 2, pp. 256-63.

Dec, JE 2009, 'Advanced compression-ignition engines-understanding the in-cylinder processes', *Proceedings of the Combustion Institute*, vol. 32, pp. 2727-42.

Dec, JE & Sjoberg, M 2004, 'Isolating the effects of fuel chemistry on combustion phasing in an hcci engine and the potential of fuel stratification for ignition control', *SAE Paper 2004-01-0557*.

References

Dec, JE & Yang, Y 2010, 'Boosted hcci for high power without engine knock and with ultra-low nox emissions - using conventional gasoline', *SAE Paper 2010-01-1086*.

Duc, PM & Wattanavichien, K 2007, 'Study on biogas premixed charge diesel dual fuelled engine', *Energy Conversion and Management*, vol. 48, no. 8, pp. 2286-308.

Duffy, K, Kieser, A, Liechty, M, Rodman, T, Hardy, B & Hergart, C 2005, 'Heavy duty hcci development activities', in proceedings of the *DOE DEER Conference*, Chicago.

Duret, P 2002, 'A new generation of engine combustion processes for the future?', in proceedings of the *IFP International Congress*, Paris.

Ecotrons 2013, *Small engine fuel injection kit - 35cc to 300cc*, <http://www.ecotrons.com/Small_Engine_EFI_PNP_kit.html>.

EPA 2000, Control of air pollution from new motor vehicles: Tier 2 motor vehicle emissions standards and gasoline sulfur control requirements, U.S. Environmental Protection Agency, United States.

Epping, K, Aceves, S, Bechtold, R & Dec, J 2002, 'The potential of hcci combustion for high efficiency and low emissions', *SAE Paper 2002-01-1923*.

Erlandsson, O, Johansson, B & Silversand, FA 2000, 'Hydrocarbon (hc) reduction of exhaust gases from a homogeneous charge compression ignition (hcci) engine using different catalytic mesh-coatings', *SAE Paper 2000-01-1847*.

Farrell, JT, Cernansky, NP, Dryer, FL, Friend, DG, Hergart, CA, Law, CK, McDavid, RM, Mueller, CJ, Patel, AK & Pitsch, H 2007, 'Development of an experimental database and kinetic models for surrogate diesel fuels', *SAE Paper 2007-01-0201*.

Favre, A 1969, 'Statistical equations of turbulent cases', in proceedings of the *Problems of hydrodynamics and continuum mechanics*, SIAM, Philadelphia, PA, USA, pp. 231-66.

Fayaz, H, Saidur, R, Razali, N, Anuar, FS, Saleman, AR & Islam, MR 2012, 'An overview of hydrogen as a vehicle fuel', *Renewable & Sustainable Energy Reviews*, vol. 16, no. 8, pp. 5511-28.

Fazal, MA, Haseeb, ASMA & Masjuki, HH 2011, 'Biodiesel feasibility study: An evaluation of material compatibility; performance; emission and engine durability', *Renewable & Sustainable Energy Reviews*, vol. 15, no. 2, pp. 1314-24.

References

Fiveland, SB & Assanis, DN 2000, 'A four-stroke homogeneous charge compression ignition engine for combustion and performance studies', *SAE Paper 2000-01-0332*.

Fiveland, SB & Assanis, DN 2001, 'Development of a two-zone hcci combustion model accounting for boundary layer effects', *SAE Paper 2001-01-1028*.

Fiveland, SB & Assanis, DN 2002, 'Development and validation of a quasi-dimensional model for hcci engine performance and emissions studies under turbocharged conditions', *SAE Paper 2002-01-1757*.

Flowers, D, Aceves, S, Westbrook, CK, Smith, JR & Dibble, R 2001, 'Detailed chemical kinetic simulation of natural gas hcci combustion: Gas composition effects and investigation of control strategies', *Journal of Engineering for Gas Turbines and Power-Transactions of the Asme*, vol. 123, no. 2, pp. 433-9.

Frolov, SM, Medvedev, SN, Basevich, VY & Frolov, FS 2013, 'Self-ignition of hydrocarbon-hydrogen-air mixtures', *International Journal of Hydrogen Energy*, vol. 38, no. 10, pp. 4177-84.

Fuerhapter, A, Unger, E & Piock, WF 2004, 'The new avl csi engine: Hcci operation on a multicylinder gasoline engine', *SAE Paper 2004-01-0551*.

Gail, S, Thomson, MJ, Sarathy, SM, Syed, SA, Dagaut, P, Dievart, P, Marchese, AJ & Dryer, FL 2007, 'A wide-ranging kinetic modeling study of methyl butanoate combustion', *Proceedings of the Combustion Institute*, vol. 31, pp. 305-11.

Ganesh, D & Nagarajan, G 2010, 'Homogeneous charge compression ignition (hcci) combustion of diesel fuel with external mixture formation', *Energy*, vol. 35, no. 1, pp. 148-57.

Ganesh, D, Nagarajan, G & Ibrahim, MM 2008, 'Study of performance, combustion and emission characteristics of diesel homogeneous charge compression ignition (hcci) combustion with external mixture formation', *Fuel*, vol. 87, no. 17-18, pp. 3497-503.

Garcia, MT, Aguilar, FJJE & Lencero, TS 2009, 'Experimental study of the performances of a modified diesel engine operating in homogeneous charge compression ignition (hcci) combustion mode versus the original diesel combustion mode', *Energy*, vol. 34, no. 2, pp. 159-71.

Gerty, MD & Heywood, JB 2006, 'An investigation of gasoline engine knock limited performance and the effects of hydrogen enhancement', *SAE Paper 2006-01-0228*.

References

Girimaji, SS 2006, 'Partially-averaged navier-stokes model for turbulence: A reynolds-averaged navier-stokes to direct numerical simulation bridging method', *Journal of Applied Mechanics-Transactions of the Asme*, vol. 73, no. 3, pp. 413-21.

Golovitchev, V 2003, *Mechanisms (combustion chemistry)*, <<http://www.tfd.chalmers.se/~valeri/MECH.html>>.

Goodwin, DG 2003, 'An open-source, extensible software suite for cvd process simulation', in proceedings of the *CVD XVI and EuroCVD Fourteen*, M Allendorf, F Maury, and F Teyssandier (Eds.), Electrochemical Society, pp. 155-62.

Graham, RL, Turner, MG & Dale, VH 1990, 'How increasing co2 and climate change affect forests - at many spatial and temporal scales, there will be forest responses that will be affected by human activities', *Bioscience*, vol. 40, no. 8, pp. 575-87.

Guo, HS, Neill, WS, Chippior, W, Li, HL & Taylor, JD 2010, 'An experimental and modeling study of hcci combustion using n-heptane', *Journal of Engineering for Gas Turbines and Power-Transactions of the Asme*, vol. 132, no. 2, pp. 1-10.

Guo, HS, Hosseini, V, Neill, WS, Chippior, WL & Dumitrescu, CE 2011, 'An experimental study on the effect of hydrogen enrichment on diesel fueled hcci combustion', *International Journal of Hydrogen Energy*, vol. 36, no. 21, pp. 13820-30.

Haraldsson, G, Tunestal, P, Johansson, B & Hyvonen, J 2004, 'Hcci closed-loop combustion control using fast thermal management', *SAE Paper 2004-01-0943*.

Haworth, DC 1999, 'Large-eddy simulation of in-cylinder flows', *Oil & Gas Science and Technology-Revue De L Institut Francais Du Petrole*, vol. 54, no. 2, pp. 175-85.

Haworth, DC 2010, 'Progress in probability density function methods for turbulent reacting flows', *Progress in Energy and Combustion Science*, vol. 36, no. 2, pp. 168-259.

He, BQ & Cho, HM 2007, 'Spark ignition natural gas engines - a review', *Energy Conversion and Management*, vol. 48, no. 2, pp. 608-18.

Herbinet, O, Pitz, WJ & Westbrook, CK 2010, 'Detailed chemical kinetic mechanism for the oxidation of biodiesel fuels blend surrogate', *Combustion and Flame*, vol. 157, no. 5, pp. 893-908.

References

- Hernandez, JJ, Sanz-Argent, J, Benajes, J & Molina, S 2008, 'Selection of a diesel fuel surrogate for the prediction of auto-ignition under hcci engine conditions', *Fuel*, vol. 87, no. 6, pp. 655-65.
- Heywood, JB 1988, *Internal combustion engine fundamentals*, McGraw-Hill, United States of America.
- Heywood, JB 2005, 'Improving the spark-ignition engine', in proceedings of the *ERC Symposium*.
- Hohenberg, GF 1979, 'Advanced approaches for heat transfer calculations', *SAE Paper 790825*.
- Honda, A 2012, *Honda gx160 cross-sectional view*, viewed 5 May, <<http://engines.honda.com/models/model-detail/gx160>>.
- Hosseini, V & Checkel, MD 2009, 'Reformer gas application in combustion onset control of hcci engine', *The Journal of Engine Research*, vol. 14.
- Hou, JX, Qiao, XQ, Wang, Z, Liu, W & Huang, Z 2010, 'Characterization of knocking combustion in hcci dme engine using wavelet packet transform', *Applied Energy*, vol. 87, no. 4, pp. 1239-46.
- Houghton, JT, Ding, Y, Griggs, DJ, Noguera, M, van der Linden, PJ, Dai, X, Maskell, K & Johnson, CA 2001, *Climate change 2001: The scientific basis*, The Press Syndicate of The University of Cambridge, Cambridge.
- Huang, J & Bushe, WK 2006, 'Experimental and kinetic study of autoignition in methane/ethane/air and methane/propane/air mixtures under engine-relevant conditions', *Combustion and Flame*, vol. 144, no. 1-2, pp. 74-88.
- Hughes, KJ, Turanyi, T, Clague, AR & Pilling, MJ 2001, 'Development and testing of a comprehensive chemical mechanism for the oxidation of methane', *International Journal of Chemical Kinetics*, vol. 33, no. 9, pp. 513-38.
- Hyvonen, J, Haraldsson, G & Johansson, B 2003, 'Operating range in a multi cylinder hcci engine using variable compression ratio', *SAE Paper 2003-01-1829*.
- Jahirul, MI, Masjuki, HH, Saidur, R, Kalam, MA, Jayed, MH & Wazed, MA 2010, 'Comparative engine performance and emission analysis of cng and gasoline in a retrofitted car engine', *Applied Thermal Engineering*, vol. 30, no. 14-15, pp. 2219-26.

References

- Janicka, J & Sadiki, A 2005, 'Large eddy simulation of turbulent combustion systems', *Proceedings of the Combustion Institute*, vol. 30, pp. 537-47.
- Janicka, J, Kolbe, W & Kollmann, W 1979, 'Closure of the transport equation for the probability density function of turbulent scalar fields', *Journal of Non-Equilibrium Thermodynamics*, vol. 4, no. 1, pp. 47-66.
- Jayed, MH, Masjuki, HH, Kalam, MA, Mahlia, TMI, Husnawan, M & Liaquat, AM 2011, 'Prospects of dedicated biodiesel engine vehicles in malaysia and indonesia', *Renewable & Sustainable Energy Reviews*, vol. 15, no. 1, pp. 220-35.
- Jia, M, Xie, M & Peng, Z 2008, 'A comparative study of multi-zone combustion models for hcci engines', *SAE Paper 2008-01-0064*.
- Johannes, VE, Tom, P, Nicholas, H, Giorgio, S & Giancarlo, T June 2009, 'Liquid petroleum gas and natural gas combustion engines', in proceedings of the *Technology Brief T03*, I OECD (ed.), Energy Technology System Analysis Program.
- John, ED & Magnus, S 2002, 'Hcci combustion: The sources of emissions at low loads and the effects of gdi fuel injection ', in proceedings of the *8th diesel engine emissions reduction (DEER) conference*, San Diego.
- John, ED & Yang, Y 2010, 'Boosted hcci for high power without engine knock and with ultra-low nox emissions - using conventional gasoline', *SAE Paper 2010-01-1086*.
- Jonathan, P 2006, *Responses to questions on the design elements of a mandatory market-based greenhouse gas regulatory system*, World Resources Institute.
- Jun, D, Ishii, K & Iida, N 2003, 'Autoignition and combustion of natural gas in a 4 stroke hcci engine', *Jsmc International Journal Series B-Fluids and Thermal Engineering*, vol. 46, no. 1, pp. 60-7.
- Kaneko, M, Morikawa, K, Itoh, J & Saishu, Y 2003, 'A study on homogeneous charge compression ignition gasoline engines', *JSME International Journal Series B: Fluids and Thermal Engineering*, vol. 46, no. 1.
- Kawano, D, Suzuki, H, Ishii, H, Goto, Y, Odaka, M, Murata, Y, Kusaka, J & Daisho, Y 2005, 'Ignition and combustion control of diesel hcci', in proceedings of the *SAE Paper 2005-01-2132*.

References

Keum, S, Im, HG & Assanis, DN 2012, 'A spray-interactive flamelet model for direct injection engine combustion', *Combustion Science and Technology*, vol. 184, no. 4, pp. 469-88.

Killingsworth, NJ, Aceves, SM, Flowers, DL & Krstic, M 2006, 'A simple hcci engine model for control', *Proceedings of the 2006 IEEE International Conference on Control Applications, Vols 1-4*, pp. 1479-84.

Kim, DS & Lee, CS 2006, 'Improved emission characteristics of hcci engine by various premixed fuels and cooled egr', *Fuel*, vol. 85, no. 5-6, pp. 695-704.

Kim, DS, Kim, MY & Lee, CS 2004, 'Effect of premixed gasoline fuel on the combustion characteristics of compression ignition engine', *Energy & Fuels*, vol. 18, no. 4, pp. 1213-9.

Kim, IKS 2004, 'Conditional moment closure for non-premixed turbulent combustion', Ph.D thesis, University of Cambridge, Cambridge.

Kim, MY & Lee, CS 2007, 'Effect of a narrow fuel spray angle and a dual injection configuration on the improvement of exhaust emissions in a hcci diesel engine', *Fuel*, vol. 86, no. 17-18, pp. 2871-80.

Kim, MY, Kim, JW, Lee, CS & Lee, JH 2006, 'Effect of compression ratio and spray injection angle on hcci combustion in a small di diesel engine', *Energy & Fuels*, vol. 20, no. 1, pp. 69-76.

Kim, SH & Huh, KY 2004, 'Second-order conditional moment closure modeling, of turbulent piloted jet diffusion flames', *Combustion and Flame*, vol. 138, no. 4, pp. 336-52.

Kim, WT & Huh, KY 2002, 'Numerical simulation of spray autoignition by the first-order conditional moment closure model', *Proceedings of the Combustion Institute*, vol. 29, pp. 569-76.

Klimenko, AY & Bilger, RW 1999, 'Conditional moment closure for turbulent combustion', *Progress in Energy and Combustion Science*, vol. 25, no. 6, pp. 595-687.

Klimenko, AY & Pope, SB 2003, 'The modeling of turbulent reactive flows based on multiple mapping conditioning', *Physics of Fluids*, vol. 15, no. 7, pp. 1907-25.

References

Komninos, NP 2009a, 'Investigating the importance of mass transfer on the formation of hcci engine emissions using a multi-zone model', *Applied Energy*, vol. 86, no. 7-8, pp. 1335-43.

Komninos, NP 2009b, 'Modeling hcci combustion: Modification of a multi-zone model and comparison to experimental results at varying boost pressure', *Applied Energy*, vol. 86, no. 10, pp. 2141-51.

Komninos, NP & Kosmadakis, GM 2011, 'Heat transfer in hcci multi-zone modeling: Validation of a new wall heat flux correlation under motoring conditions', *Applied Energy*, vol. 88, no. 5, pp. 1635-48.

Komninos, NP & Rakopoulos, CD 2012, 'Modeling hcci combustion of biofuels: A review', *Renewable & Sustainable Energy Reviews*, vol. 16, no. 3, pp. 1588-610.

Komninos, NP, Hountalas, DT & Kouremenos, DA 2004, 'Development of a new multi-zone model for the description of physical processes in hcci engines', *SAE Paper 2004-01-0562*.

Komninos, NP, Hountalas, DT & Kouremenos, DA 2005, 'Description of in-cylinder combustion processes in hcci engines using a multi-zone model', *SAE Paper 2005-01-0171*.

Kong, SC 2007, 'A study of natural gas/dme combustion in hcci engines using cfd with detailed chemical kinetics', *Fuel*, vol. 86, no. 10-11, pp. 1483-9.

Kong, SC & Reitz, RD 2002, 'Use of detailed chemical kinetics to study hcci engine combustion with consideration of turbulent mixing effects', *Journal of Engineering for Gas Turbines and Power-Transactions of the Asme*, vol. 124, no. 3, pp. 702-7.

Kong, SC & Reitz, RD 2003, 'Numerical study of premixed hcci engine combustion and its sensitivity to computational mesh and model uncertainties', *Combustion Theory and Modelling*, vol. 7, no. 2, pp. 417-33.

Kong, SC, Reitz, RD, Christensen, M & Johansson, B 2003, 'Modeling the effects of geometry generated turbulence on hcci engine combustion', *SAE Paper 2003-01-1088*.

Koopmans, L & Denbratt, I 2001, 'A four stroke camless engine, operated in homogeneous charge compression ignition mode with commercial gasoline', *SAE Paper 2001-01-3610*.

References

Kronenburg, A & Cleary, MJ 2008, 'Multiple mapping conditioning for flames with partial premixing', *Combustion and Flame*, vol. 155, no. 1-2, pp. 215-31.

Kuo, KK 2005, *Principles of combustion*, John Wiley and Sons, New Jersey.

Kwon, J, Seo, J, Lee, D & Huh, KY 2011, 'Zero-dimensional simulation of diesel engine combustion and emissions based on cmc model and skeletal reaction mechanism', *SAE Paper 010845*.

Lee, BJ & Jeung, IS 2009, 'Numerical study of spontaneous ignition of pressurized hydrogen released by the failure of a rupture disk into a tube', *International Journal of Hydrogen Energy*, vol. 34, no. 20, pp. 8763-9.

Lee, K & Min, K 2009, 'Study of a stratification effect on engine performance in gasoline hcci combustion by using the multi-zone method and reduced kinetic mechanism', *SAE Paper 2009-01-1784*.

Lee, K, Kim, Y & Min, K 2011, 'Development of a reduced chemical kinetic mechanism for a gasoline surrogate for gasoline hcci combustion', *Combustion Theory and Modelling*, vol. 15, no. 1, pp. 107-24.

Li, H, Neill, WS, Chippior, W, Graham, L, Connolly, T & Taylor, JD 2007, 'An experimental investigation on the emission characteristics of hcci engine operation using n-heptane', *SAE Paper 2007-01-1854*.

Lindstedt, RP & Meyer, MP 2002, 'A dimensionally reduced reaction mechanism for methanol oxidation', *Proceedings of the Combustion Institute*, vol. 29, pp. 1395-402.

Liu, C & Karim, GA 2008, 'A simulation of the combustion of hydrogen in hcci engines using a 3d model with detailed chemical kinetics', *International Journal of Hydrogen Energy*, vol. 33, no. 14, pp. 3863-75.

Liu, HG, Yao, MF, Zhang, B & Zheng, ZQ 2009, 'Influence of fuel and operating conditions on combustion characteristics of a homogeneous charge compression ignition engine', *Energy & Fuels*, vol. 23, pp. 1422-30.

Liu, Z 2006, *Diesel combustion chamber*, US6997158B1, United States Patent.

Liu, Z & Chen, R 2009, 'A zero-dimensional combustion model with reduced kinetics for si engine knock simulation', *Combustion Science and Technology*, vol. 181, no. 6, pp. 828-52.

References

Lu, T & Law, CK 2007, 'An efficient reduced mechanism for methane oxidation with no chemistry', in proceedings of the *5th US Combustion Meeting*, San Diego.

Lu, XC, Chen, W & Huang, Z 2005, 'A fundamental study on the control of the hcci combustion and emissions by fuel design concept combined with controllable egr. Part 2. Effect of operating conditions and egr on hcci combustion', *Fuel*, vol. 84, no. 9, pp. 1084-92.

Luo, ZY, Plomer, M, Lu, TF, Som, S, Longman, DE, Sarathy, SM & Pitz, WJ 2012, 'A reduced mechanism for biodiesel surrogates for compression ignition engine applications', *Fuel*, vol. 99, pp. 143-53.

Lutz, AE 2002, *Multi-zone model for homogeneous ignition*, Sandia National Laboratories.

Machrafi, H & Cavadias, S 2008, 'Three-stage autoignition of gasoline in an hcci engine: An experimental and chemical kinetic modeling investigation', *Combustion and Flame*, vol. 155, no. 4, pp. 557-70.

Mack, JH, Aceves, SM & Dibble, RW 2009, 'Demonstrating direct use of wet ethanol in a homogeneous charge compression ignition (hcci) engine', *Energy*, vol. 34, no. 6, pp. 782-7.

Mansouri, SH, Heywood, JB & Radhakrishnan, K 1982, 'Divided-chamber diesel engines, part i: A cycle-simulation which predicts performance and emissions', *SAE Paper 820273*.

Marinov, NM 1999, 'A detailed chemical kinetic model for high temperature ethanol oxidation', *International Journal of Chemical Kinetics*, vol. 31, no. 3, pp. 183-220.

Marinov, NM, Westbrook, CK & Pitz, WJ 1995, 'Detailed and global chemical kinetics model for hydrogen', in proceedings of the *8th International Symposium on Transport Properties*, San Francisco.

Maroteaux, F & Noel, L 2006, 'Development of a reduced n-heptane oxidation mechanism for hcci combustion modeling', *Combustion and Flame*, vol. 146, no. 1-2, pp. 246-67.

Mastorakos, E 2010, *Conditional moment closure*, University of Cambridge, viewed 05/05/2011.

References

Mastorakos, E & Wright, YM 2003, 'Simulations of turbulent spray auto-ignition with elliptic conditional moment closure', in proceedings of the *European Combustion Meeting*, Orleans, France.

Maurya, RK & Agarwal, AK 2011, 'Experimental study of combustion and emission characteristics of ethanol fuelled port injected homogeneous charge compression ignition (hcci) combustion engine', *Applied Energy*, vol. 88, no. 4, pp. 1169-80.

McTaggart-Cowan, GP, Wu, N, Jin, B, Rogak, SN, Davy, MH & Bushe, WK 2009, 'Effects of fuel composition on high-pressure non-premixed natural gas combustion', *Combustion Science and Technology*, vol. 181, no. 3, pp. 397-416.

Meca 1997, *Emission control technology for stationary internal combustion engines*, Manufacturers of Emissions Controls Association (MECA), Washington.

Mehl, M, Curran, HJ, Pitz, WJ & Westbrook, CK 2009, 'Chemical kinetic modeling of component mixtures relevant to gasoline', in proceedings of the *4th European Combustion Meeting*, Vienna.

Mehl, M, Pitz, WJ, Westbrook, CK & Curran, HJ 2011, 'Kinetic modeling of gasoline surrogate components and mixtures under engine conditions', *Proceedings of the Combustion Institute*, vol. 33, pp. 193-200.

Mehl, M, Faravelli, T, Ranzi, E, Miller, D & Cernansky, N 2009, 'Experimental and kinetic modeling study of the effect of fuel composition in hcci engines', *Proceedings of the Combustion Institute*, vol. 32, pp. 2843-50.

Mehl, M, Chen, JY, Pitz, JW, Sarathy, SM & Westbrook, CK 2011, 'An approach for formulating surrogates for gasoline with application toward a reduced surrogate mechanism for cfd engine modeling', *Energy & Fuels*, no. 25, pp. 5215-23.

Mercuri, R, Bauen, A & Hart, D 2002, 'Options for refuelling hydrogen fuel cell vehicles in italy', *Journal of Power Sources*, vol. 106, no. 1-2, pp. 353-63.

Meyer, J 2007, 'Engine modeling of an internal combustion engine with twin independent cam phasing', Bachelor degree thesis, The Ohio State University.

Miller, JA & Bowman, CT 1989, 'Mechanism and modeling of nitrogen chemistry in combustion', *Progress in Energy and Combustion Science*, vol. 15, no. 4, pp. 287-338.

Mitarai, S, Riley, JJ & Kosaly, G 2005, 'Testing of mixing models for monte carlo probability density function simulations', *Physics of Fluids*, vol. 17, no. 4, pp. 047101.

References

Mittal, V, Cook, DJ & Pitsch, H 2012, 'An extended multi-regime flamelet model for ic engines', *Combustion and Flame*, vol. 159, no. 8, pp. 2767-76.

Miyamoto, T, Hasegawa, H, Mikami, M, Kojima, N, Kabashima, H & Urata, Y 2011, 'Effect of hydrogen addition to intake gas on combustion and exhaust emission characteristics of a diesel engine', *International Journal of Hydrogen Energy*, vol. 36, no. 20, pp. 13138-49.

Morsy, MH 2007, 'Ignition control of methane fueled homogeneous charge compression ignition engines using additives', *Fuel*, vol. 86, no. 4, pp. 533-40.

Mosbach, S, Kraft, M, Bhawe, A, Mauss, F, Mack, JH & Dibble, R 2006, 'Simulating a homogeneous charge compression ignition engine fuelled with a dee/etoh blend', *SAE Paper 2006-01-1362*.

Msaad, AA, Belcadi, A, Mahdaoui, M, Aaffad, E & Mouqallid, M 2012, 'Reduced detailed mechanism for methane combustion', *Energy and Power Engineering*, vol. 4, no. 1, pp. 28-33.

Muller, GH & Mich, AA 1983, *Tuned engine intake manifold*, Ford Motor Company, 4501235, United State Patent.

Naik, CV, Pitz, WJ, Sjoberg, M, Dec, JE, Orme, J, Curran, HJ, Simmie, JM & Westbrook, CK 2005, 'Detailed chemical kinetic modeling of surrogate fuels for gasoline and application to an hcci engine', in proceedings of the *2005 Joint Meeting of the U.S. Sections of the Combustion Institute*, Lawrence Livermore National Laboratory, Philadelphia, United States.

Najjar, YSH 2013, 'Hydrogen safety: The road toward green technology', *International Journal of Hydrogen Energy*, vol. 38, no. 25, pp. 10716-28.

Najt, PE & Foster, DE 1983, 'Compression ignited homogeneous charge combustion', *SAE paper 830264*.

Nathan, SS, Mallikarjuna, JM & Ramesh, A 2010, 'An experimental study of the biogas-diesel hcci mode of engine operation', *Energy Conversion and Management*, vol. 51, no. 7, pp. 1347-53.

Navarro-Martinez, S & Kronenburg, A 2009, 'Les-cmc simulations of a lifted methane flame', *Proceedings of the Combustion Institute*, vol. 32, pp. 1509-16.

References

- Navarro-Martinez, S & Rigopoulos, S 2011, 'Large eddy simulation of a turbulent lifted flame using conditional moment closure and rate-controlled constrained equilibrium', *Flow Turbulence and Combustion*, vol. 87, no. 2-3, pp. 407-23.
- Neely, GD, Sasaki, S & Leet, JA 2004, 'Experimental investigation of pcc-di combustion on emission in a light-duty diesel engine', *SAE Paper 2004-01-0121*.
- Nguyen, TA & Mikami, M 2013, 'Effect of hydrogen addition to intake air on combustion noise from a diesel engine', *International Journal of Hydrogen Energy*, vol. 38, no. 10, pp. 4153-62.
- O Conaire, M, Curran, HJ, Simmie, JM, Pitz, WJ & Westbrook, CK 2004, 'A comprehensive modeling study of hydrogen oxidation', *International Journal of Chemical Kinetics*, vol. 36, no. 11, pp. 603-22.
- O'Brien, EE & Jiang, TL 1991, 'The conditional dissipation rate of an initially binary scalar in homogeneous turbulence', *Physics of Fluids a-Fluid Dynamics*, vol. 3, no. 12, pp. 3121-3.
- Ogden, JM, Steinbugler, MM & Kreutz, TG 1999, 'A comparison of hydrogen, methanol and gasoline as fuels for fuel cell vehicles: Implications for vehicle design and infrastructure development', *Journal of Power Sources*, vol. 79, no. 2, pp. 143-68.
- Ogink, R & Golovitchev, V 2001, 'Gasoline hcci modeling: Computer program combining detailed chemistry and gas exchange processes', *SAE Paper 2001-01-3614*.
- Olsson, J-O, Tunesta, P, Johansson, B, Fiveland, SB, Agama, R, Willi, M & Assanis, DN 2002, 'Compression ratio influence on maximum load of a natural gas fueled hcci engine', *SAE Paper 02P-147*.
- Onishi, S, Jo, SH, Shoda, K, Jo, PD & Kato, S 1979, 'Active thermo-atmosphere combustion (atac) - a new combustion process for internal combustion engines', *SAE Paper 790501*.
- Papagiannakis, RG & Hountalas, DT 2004, 'Combustion and exhaust emission characteristics of a dual fuel compression ignition engine operated with pilot diesel fuel and natural gas', *Energy Conversion and Management*, vol. 45, no. 18-19, pp. 2971-87.
- Park, C, Kim, C, Kim, K, Lee, D, Song, Y & Moriyoshi, Y 2010, 'The influence of hydrogen-enriched gas on the performance of lean no(x) trap catalyst for a light-duty diesel engine', *International Journal of Hydrogen Energy*, vol. 35, no. 4, pp. 1789-96.

References

Park, SW & Reitz, RD 2007, 'Numerical study on the low emission window of homogeneous charge compression ignition diesel combustion', *Combustion Science and Technology*, vol. 179, no. 11, pp. 2279-307.

Patel, A, Kong, SC & Reitz, RD 2004, 'Development and validation of a reduced reaction mechanism for hcci engine simulations', *SAE Paper 2004-01-0558*.

Patwardhan, SS, De, S, Lakshmisha, KN & Raghunandan, BN 2009, 'Cmc simulations of lifted turbulent jet flame in a vitiated coflow', *Proceedings of the Combustion Institute*, vol. 32, pp. 1705-12.

Peters, N 2000, *Turbulent combustion*, First edn, Cambridge University Press, Cambridge.

Peucheret, S, Wyszynski, ML, Lehrle, RS, Golunski, S & Xu, H 2005, 'Use of catalytic reforming to aid natural gas hcci combustion in engines: Experimental and modelling results of open-loop fuel reforming', *International Journal of Hydrogen Energy*, vol. 30, no. 15, pp. 1583-94.

Pitsch, H 2006, 'Large-eddy simulation of turbulent combustion', *Annual Review of Fluid Mechanics*, vol. 38, pp. 453-82.

Pitsch, H, Chen, M & Peters, N 1998, 'Unsteady flamelet modeling of turbulent hydrogen-air diffusion flames', in proceedings of the *Twenty-Seventh Symposium (International) on Combustion*, The Combustion Institute, pp. 1057-64.

Pitz, WJ & Mueller, CJ 2011, 'Recent progress in the development of diesel surrogate fuels', *Progress in Energy and Combustion Science*, vol. 37, no. 3, pp. 330-50.

Pitz, WJ, Cernansky, NP, Dryer, FL, Egolfopoulos, FN, Farrell, JT, Friend, DG & Pitsch, H 2007, 'Development of an experimental database and chemical kinetic models for surrogate gasoline fuels', *SAE Paper 2007-01-0175*.

Pope, SB 1985, 'Pdf method for turbulent reactive flows', *Progress in Energy and Combustion Science*, vol. 11, no. 2, pp. 119-92.

Pope, SB 2000, *Turbulent flows*, First Edition edn, Cambridge University Press, Cambridge UK.

Popp, D 2004, 'International innovation and diffusion of air pollution control technologies: The effects of nox and so2 regulation in the u.S., japan, and germany',

References

Premier, AS 2007, 'Hcci could cut fuel consumption by 15%', *Advanced Materials and Processes*, vol. 165, no. 11, pp. 27.

Proton 2013, *Intake air fuel module*, <www.protondarwin.com.au/downloads/IAFM_Info.pdf>.

Puduppakkam, KV, Naik, CV, Wang, C & Meeks, E 2010, 'Validation studies of a detailed kinetics mechanism for diesel and gasoline surrogate fuels', *SAE Paper 2010-01-0545*.

Puduppakkam, KV, Liang, L, Naik, CV, Meeks, E & Bunting, BG 2009, 'Combustion and emissions modeling of a gasoline hcci engine using model fuels', *SAE Paper 2009-01-0669*.

Ra, Y & Reitz, RD 2008, 'A reduced chemical kinetic model for ic engine combustion simulations with primary reference fuels', *Combustion and Flame*, vol. 155, no. 4, pp. 713-38.

Ramli, MZ 2009, 'Adsorption of natural gas and hydrogen on cu₃', Bachelor degree thesis, University Malaysia Pahang, Malaysia.

Rattanapaibule, K & Aung, K 2005, 'Performance predictions of a hydrogen-enhanced natural gas hcci engine', in proceedings of the *International Mechanical Engineering Congress and Exposition (IMECE2005)*, Energy Conversion and Resources, Florida, pp. 289-94.

Reitz, RD 2007, *Cfd combustion models for ic engines*, The University of Wisconsin.

Reitz, RD & Han, Z 1997, 'A temperature wall function formulation for variable-density turbulent flows with application to engine convective heat transfer modeling', *International Journal of Heat and Mass Transfer*, vol. 40, no. 3, pp. 613-25.

Richter, M, Engstrom, J, Franke, A, Alden, M, Hultqvist, A & Johansson, B 2000, 'The influence of charge inhomogeneity on the hcci combustion process', *SAE Paper 2000-01-2868*.

Rizvi, SQA 2009, *A comprehensive review of lubricant chemistry, technology, selection and design*, ASTM International, U.S.A.

References

Rob, G 2005, *Watching earth's climate change in the classroom*, NASA Goddard Space Flight Center, viewed 1 August, <http://www.nasa.gov/vision/earth/everydaylife/climate_class.html>.

Roomina, MR & Bilger, RW 2001, 'Conditional moment closure (cmc) predictions of a turbulent methane-air jet flame', *Combustion and Flame*, vol. 125, no. 3, pp. 1176-95.

Rousseau, S, Lemoult, B & Tazerout, M 1999, 'Combustion characterization of natural gas in a lean burn spark-ignition engine', *Proceedings of the Institution of Mechanical Engineers Part D-Journal of Automobile Engineering*, vol. 213, no. D5, pp. 481-9.

Roy, MM, Tomita, E, Kawahara, N, Harada, Y & Sakane, A 2009, 'Performance and emission comparison of a supercharged dual-fuel engine fueled by producer gases with varying hydrogen content', *International Journal of Hydrogen Energy*, vol. 34, no. 18, pp. 7811-22.

Roy, MM, Tomita, E, Kawahara, N, Harada, Y & Sakane, A 2010, 'An experimental investigation on engine performance and emissions of a supercharged h-2-diesel dual-fuel engine', *International Journal of Hydrogen Energy*, vol. 35, no. 2, pp. 844-53.

Ryu, J, Kim, H & Lee, K 2005, 'A study on the spray structure and evaporation characteristic of common rail type high pressure injector in homogeneous charge compression ignition engine', *Fuel*, vol. 84, no. 18, pp. 2341-50.

Sanli, A, Ozsezen, AN, Kilicaslan, I & Canakci, M 2008, 'The influence of engine speed and load on the heat transfer between gases and in-cylinder walls at fired and motored conditions of an idi diesel engine', *Applied Thermal Engineering*, vol. 28, no. 11-12, pp. 1395-404.

Sarathy, SM, Vranckx, S, Yasunaga, K, Mehl, M, Osswald, P, Metcalfe, WK, Westbrook, CK, Pitz, WJ, Kohse-Hoinghaus, K, Fernandes, RX & Curran, HJ 2012, 'A comprehensive chemical kinetic combustion model for the four butanol isomers', *Combustion and Flame*, vol. 159, no. 6, pp. 2028-55.

Saravanan, N & Nagarajan, G 2008, 'An experimental investigation of hydrogen-enriched air induction in a diesel engine system', *International Journal of Hydrogen Energy*, vol. 33, no. 6, pp. 1769-75.

Saravanan, N & Nagarajan, G 2010, 'An experimental investigation on hydrogen fuel injection in intake port and manifold with different egr rates', *Energy Environ.*, vol. 1, no. 2, pp. 221-48.

References

Saravanan, N, Nagarajan, G & Narayanasamy, S 2008, 'An experimental investigation on di diesel engine with hydrogen fuel', *Renewable Energy*, vol. 33, no. 3, pp. 415-21.

Saravanan, N, Nagarajan, G, Sanjay, G, Dhanasekaran, C & Kalaiselvan, KM 2008, 'Combustion analysis on a di diesel engine with hydrogen in dual fuel mode', *Fuel*, vol. 87, no. 17-18, pp. 3591-9.

Sato, S, Yamasaki, Y, Kawamura, H & Iida, N 2005, 'Research on the influence of hydrogen and carbon monoxide on methane hcci combustion', *Jsmc International Journal Series B-Fluids and Thermal Engineering*, vol. 48, no. 4, pp. 725-34.

Schroll, P 2009, 'Conditional moment closure for spray combustion and ignition', Ph.D thesis, University of Cambridge, Cambridge.

Seiser, R, Pitsch, H, Seshadri, K, Pitz, WJ & Curran, HJ 2000, 'Extinction and autoignition of n-heptane in counterflow configuration', *Proceedings of the Combustion Institute*, vol. 28, pp. 2029-37.

Sengupta, K & Mashayek, F 2008, 'Direct numerical simulation of turbulent flows using spectral methods', in proceedings of the *AIAA Aerospace Sciences Meeting and Exhibit*, American Institute of Aeronautics and Astronautics, Nevada.

Seo, J, Lee, D, Huh, KY & Chung, J 2010, 'Combustion simulation of a diesel engine in the phcci mode with split injections by the spatially integrated cmc model', *Combustion Science and Technology*, vol. 182, no. 9, pp. 1241-60.

Shahbakhti, M & Koch, CR 2008, 'Characterizing the cyclic variability of ignition timing in a homogeneous charge compression ignition engine fuelled with n-heptane/iso-octane blend fuels', *International Journal of Engine Research*, vol. 9, no. 5, pp. 361-97.

Shaver, GM, Gerdes, JC, Jain, P, Caton, PA & Edwards, CF 2003, 'Modeling for control of hcci engines', *Proceedings of the 2003 American Control Conference, Vols 1-6*, pp. 749-54.

Shaver, GM, Gerdes, JC, Roelle, MJ, Caton, PA & Edwards, CF 2005, 'Dynamic modeling of residual-affected homogeneous charge compression ignition engines with variable valve actuation', *Journal of Dynamic Systems Measurement and Control-Transactions of the Asme*, vol. 127, no. 3, pp. 374-81.

Sheppard, CGW, Tolegano, S & Woolley, R 2002, 'On the nature of autoignition leading to knock in hcci engines', *SAE Paper 2002-01-2831*.

References

- Shudo, T & Yamada, H 2007, 'Hydrogen as an ignition-controlling agent for hcci combustion engine by suppressing the low-temperature oxidation', *International Journal of Hydrogen Energy*, vol. 32, no. 14, pp. 3066-72.
- Sjoberg, M & Dec, JE 2006, 'Smoothing hcci heat-release rates using partial fuel stratification with two-stage ignition fuels', *SAE Paper 2006-01-0629*.
- Sjoberg, M & Dec, J 2008, 'Influence of fuel autoignition reactivity on the high-load limits of hcci engines', *SAE Paper 2008-01-0054*.
- Sjoberg, M, Dec, JE & Cernansky, NP 2005, 'Potential of thermal stratification and combustion retard for reducing pressure-rise rates in hcci engines, based on multi-zone modeling and experiments', *SAE Paper 2005-01-0113*.
- Sjoberg, M, Dec, JE, Babajimopoulos, A & Assanis, D 2004, 'Comparing enhanced natural thermal stratification against retarded combustion phasing for smoothing of hcci heat-release rates', *SAE Paper 2004-01-2994*.
- Slavinskaya, NA, Wiegand, M, Starke, JH, Riedel, U, Haidn, OJ & Suslov, D 2013, 'Kinetic mechanism for low-pressure oxygen/methane ignition and combustion', *Progress in Propulsion Physics*, vol. 4, pp. 707-32.
- Smith, GP, Golden, DM, Frenklach, M, Moriarty, NW, Eiteneer, B, Goldenberg, M, Bowman, CT, Hanson, RK, Song, S & Gardiner Jr, WC 1999, *Gri-mech 3.0*, <http://www.me.berkeley.edu/gri_mech>.
- Soberanis, MAE & Fernandez, AM 2010, 'A review on the technical adaptations for internal combustion engines to operate with gas/hydrogen mixtures', *International Journal of Hydrogen Energy*, vol. 35, no. 21, pp. 12134-40.
- Sone, K & Menon, S 2003, 'Effect of subgrid modeling on the in-cylinder unsteady mixing process in a direct injection engine', *Journal of Engineering for Gas Turbines and Power-Transactions of the Asme*, vol. 125, no. 2, pp. 435-43.
- Soyhan, HS, Yasar, H, Walmsley, H, Head, B, Kalghatgi, GT & Sorousbay, C 2009, 'Evaluation of heat transfer correlations for hcci engine modeling', *Applied Thermal Engineering*, vol. 29, no. 2-3, pp. 541-9.
- Soylu, S 2005, 'Examination of combustion characteristics and phasing strategies of a natural gas hcci engine', *Energy Conversion and Management*, vol. 46, no. 1, pp. 101-19.

References

Spalding, DB 1971, 'Mixing and chemical reaction in steady confined turbulent flames', in proceedings of the *Thirteen Symposium (International) on Combustion*, The Combustion Institute, pp. 649-57.

Stiesch, G 2003, *Modeling engine spray and combustion processes*, Springer, Berlin.

Stone, R 1999, *Introduction to internal combustion engines*, 3rd edn, Society of Automotive Engineers Inc, Warrendale.

Su, H, Mosbach, S, Kraft, M, Bhave, A, Kook, S & Bae, C 2007, 'Two-stage fuel direct injection in a diesel fuelled hcci engine', *SAE Paper 2007-01-1880*.

Subramaniam, S & Pope, SB 1998, 'A mixing model for turbulent reactive flows based on euclidean minimum spanning trees', *Combustion and Flame*, vol. 115, no. 4, pp. 487-514.

Sun, ZY, Liu, FS, Liu, XH, Sun, BG & Sun, DW 2012, 'Research and development of hydrogen fuelled engines in china', *International Journal of Hydrogen Energy*, vol. 37, no. 1, pp. 664-81.

Szwaja, S & Grab-Rogalinski, K 2009, 'Hydrogen combustion in a compression ignition diesel engine', *International Journal of Hydrogen Energy*, vol. 34, no. 10, pp. 4413-21.

Takagi, Y 1998, 'A new era in spark-ignition engines featuring high-pressure direct injection', in proceedings of the *Twenty-Seventh Symposium (International) on Combustion*, The Combustion Institute, pp. 2055-68.

Tanaka, S, Ayala, F & Keck, JC 2003, 'A reduced chemical kinetic model for hcci combustion of primary reference fuels in a rapid compression machine', *Combustion and Flame*, vol. 133, no. 4, pp. 467-81.

Tanaka, S, Ayala, F, Keck, JC & Heywood, JB 2003, 'Two-stage ignition in hcci combustion and hcci control by fuels and additives', *Combustion and Flame*, vol. 132, no. 1-2, pp. 219-39.

Taylor, AMKP 2008, 'Science review of internal combustion engines', *Energy Policy*, vol. 36, no. 12, pp. 4657-67.

Taylor, JD 2006, *Fuel performance technologies: Milestone fy06 9.1*, National Renewable Energy Laboratory.

References

- Tennekes, H & Lumley, JL 1972, *A first course in turbulence*, The MIT Press, United States of America.
- Tobin, J, Carlson, ME, Elias, MJ, Keene, WR, O'Sullivan, JP, Tita, MJ, Thompson, J, Todaro, J & Young, L 1999, *Natural gas 1998*, Energy Information Administration (EIA), Washington.
- Tomita, E 2004, 'Dual fuel hcci combustion - high octane and high cetane number fuels', in proceedings of the *HCCI Symposium*, Okayama University, Berkeley.
- Tomita, E, Kawahara, N, Piao, Z & Yamaguchi, R 2002, 'Effects of egr and early injection of diesel fuel on combustion characteristics and exhaust emissions in a methane dual fuel engine', *SAE Paper 2002-01-2723*.
- Tomita, E, Kawahara, N, Piao, Z, Fujita, S & Hamamoto, Y 2001, 'Hydrogen combustion and exhaust emissions ignited with diesel oil in a dual fuel engine', *SAE Paper 2001-01-3503*.
- Totton, TS, Shirley, R & Kraft, M 2011, 'First-principles thermochemistry for the combustion of ticl₄ in a methane flame', *Proceedings of the Combustion Institute*, vol. 33, pp. 493-500.
- Trimm, DL & Onsan, ZI 2001, 'Onboard fuel conversion for hydrogen-fuel-cell-driven vehicles', *Catalysis Reviews-Science and Engineering*, vol. 43, no. 1-2, pp. 31-84.
- Tsolakis, A & Megaritis, A 2005, 'Partially premixed charge compression ignition engine with on-board h₂ production by exhaust gas fuel reforming of diesel and biodiesel', *International Journal of Hydrogen Energy*, vol. 30, no. 7, pp. 731-45.
- Tsolakis, A, Megaritis, A & Yap, D 2008, 'Application of exhaust gas fuel reforming in diesel and homogeneous charge compression ignition (hcci) engines fuelled with biofuels', *Energy*, vol. 33, no. 3, pp. 462-70.
- Vaishnavi, P & Kronenburg, A 2010, 'Multiple mapping conditioning of velocity in turbulent jet flames', *Combustion and Flame*, vol. 157, no. 10, pp. 1863-5.
- Van Blarigan, P 2002, 'Advanced internal combustion electrical generator', in proceedings of the *DOE Hydrogen Program Review*, United States, pp. NREL/CP-610-32405.

References

Verhelst, S & Wallner, T 2009, 'Hydrogen-fueled internal combustion engines', *Progress in Energy and Combustion Science*, vol. 35, no. 6, pp. 490-527.

Veynante, D & Vervisch, L 2002, 'Turbulent combustion modeling', *Progress in Energy and Combustion Science*, vol. 28, no. 3, pp. 193-266.

Villiermaux, J & Devillon, JC 1972, 'Représentation de la coalescence et de la redispersion des domaines de ségrégation dans un fluide per modèle d'interaction phénoménologique', in proceedings of the *Proceedings of the Second International Symposia on Chemical Reaction Engineering (ISCRE)*, Netherlands, p. B1.

Vogiatzaki, K, Cleary, MJ, Kronenburg, A & Kent, JH 2009, 'Modeling of scalar mixing in turbulent jet flames by multiple mapping conditioning', *Physics of Fluids*, vol. 21, no. 2, pp. 025105.

Vogiatzaki, K, Kronenburg, A, Cleary, MJ & Kent, JH 2009, 'Multiple mapping conditioning of turbulent jet diffusion flames', *Proceedings of the Combustion Institute*, vol. 32, pp. 1679-85.

Volkswagen 2009, *Volkswagen aktiengesellschaft - 2009 annual report*, Wolfsburg.

Votsmeier, M 2009, 'Efficient implementation of detailed surface chemistry into reactor models using mapped rate data', *Chemical Engineering Science*, vol. 64, no. 7, pp. 1384-9.

Wandel, AP & Klimenko, AY 2005, 'Testing multiple mapping conditioning mixing for monte carlo probability density function simulations', *Physics of Fluids*, vol. 17, no. 12, pp. 128105.

Wandel, AP & Lindstedt, RP 2009, 'Hybrid binomial langevin-multiple mapping conditioning modeling of a reacting mixing layer', *Physics of Fluids*, vol. 21, no. 1, pp. -.

Wang, G, Shuai, SJ, Wang, JX, Tian, GH & An, XL 2006, 'Modeling of hcci combustion: From 0d to 3d', *SAE Paper 2006-01-1364*.

Wang, H, Jiao, Q, Yao, M, Yang, B, Qiu, L & Reitz, RD 2013, 'Development of an n-heptane/toluene/pah mechanism and its application for combustion and soot prediction', *International Journal of Engine Research*, pp. 1468087412471056.

References

Wang, Z, Shuai, SJ, Wang, JX & Tian, GH 2006, 'A computational study of direct injection gasoline hcci engine with secondary injection', *Fuel*, vol. 85, no. 12-13, pp. 1831-41.

Wesselink, LG, Buijsman, E & Annema, JA 2006, *The impact of euro 5: Facts and figures*, The Netherlands.

Westbrook, CK, Pitz, WJ & Curran, HJ 2006, 'Chemical kinetic modeling study of the effects of oxygenated hydrocarbons on soot emissions from diesel engines', *Journal of Physical Chemistry A*, vol. 110, no. 21, pp. 6912-22.

Westbrook, CK, Pitz, WJ, Mehl, M & Curran, HJ 2009, 'Detailed chemical kinetic models for large n-alkanes and iso-alkanes found in conventional and f-t diesel fuels', in proceedings of the *U.S. National Combustion Meeting*, Ann Arbor.

White, CM, Steeper, RR & Lutz, AE 2006, 'The hydrogen-fueled internal combustion engine: A technical review', *International Journal of Hydrogen Energy*, vol. 31, no. 10, pp. 1292-305.

William, JP & Charles, KW 2011, *Combustion chemistry*, Lawrence Livermore National Laboratory, viewed 9 August 2011, <https://www-pls.llnl.gov/?url=science_and_technology-chemistry-combustion>.

Williams, FA 1985, *Combustion theory*, 2nd edition edn, Benjamin/Cummings.

Woschni, G 1967, 'A universally applicable equation for instantaneous heat transfer coefficient in the internal combustion engine', *SAE Paper 670931*.

Wright, YM 2005, 'Numerical investigation of turbulent spray combustion with conditional moment closure', Swiss Federal Institute of Technology Zurich, Switzerland.

Wright, YM, De Paola, G, Boulouchos, K & Mastorakos, E 2005, 'Simulations of spray autoignition and flame establishment with two-dimensional cmc', *Combustion and Flame*, vol. 143, no. 4, pp. 402-19.

Wright, YM, Boulouchos, K, de Paola, G & Mastorakos, E 2009, 'Multi-dimensional conditional moment closure modelling applied to a heavy-duty common-rail diesel engine', *SAE Paper 2009-01-0717*.

Wurms, R, Grigo, M & Hatz, W 2003, 'Audi fsi technology improved performance and reduced fuel consumption', *ATA-TORINO-*, vol. 56, no. 3/4, pp. 118-25.

References

- Yao, MF, Zheng, ZL & Liu, HF 2009, 'Progress and recent trends in homogeneous charge compression ignition (hcci) engines', *Progress in Energy and Combustion Science*, vol. 35, no. 5, pp. 398-437.
- Yap, D, Peucheret, SM, Megaritis, A, Wyszynski, ML & Xu, H 2006, 'Natural gas hcci engine operation with exhaust gas fuel reforming', *International Journal of Hydrogen Energy*, vol. 31, no. 5, pp. 587-95.
- Yelvington, PE & Green, WH 2003, 'Prediction of the knock limit and viable operating range for a homogeneous-charge-compression-ignition (hcci) engine', *SAE Paper 2003-01-1092*.
- Yingnan, G, Fengjun, G, Fafa, L, Hua, L, Honggang, J & Manzhi, T 2010, 'Control of hcci engine fueled with gasoline with electro-hydraulic variable valve system', in proceedings of the *2nd International Asia Conference on Informatics in Control, Automation and Robotics*, Institute of Electrical and Electronics Engineer (IEEE).
- Yusaf, TF, Buttsworth, DR, Saleh, KH & Yousif, BF 2010, 'Cng-diesel engine performance and exhaust emission analysis with the aid of artificial neural network', *Applied Energy*, vol. 87, no. 5, pp. 1661-9.
- Zeng, K, Huang, ZH, Liu, B, Liu, LX, Jiang, DM, Ren, Y & Wang, JH 2006, 'Combustion characteristics of a direct-injection natural gas engine under various fuel injection timings', *Applied Thermal Engineering*, vol. 26, no. 8-9, pp. 806-13.
- Zeng, P & Assanis, DN 1989, 'Evaluation of alternative thermocouple designs for transient heat transfer measurements in metal and ceramic engine', *SAE Paper 890571*.
- Zheng, J, Yang, W, Miller, DL & Cernansky, NP 2001, 'Prediction of pre-ignition reactivity and ignition delay for hcci using a reduced chemical kinetic model', *SAE Paper 2001-01-1025*.
- Zheng, J, Yang, W, Miller, DL & Cernansky, NP 2002, 'A skeletal chemical kinetic model for the hcci combustion process ', *SAE Paper 2002-01-0423*.
- Zheng, QP, Zhang, HM & Zhang, DF 2005, 'A computational study of combustion in compression ignition natural gas engine with separated chamber', *Fuel*, vol. 84, no. 12-13, pp. 1515-23.
- Zheng, Z & Yao, M 2007, 'Numerical simulation of the effects of charge stratification on combustion and emissions', *Energy & Fuels*, vol. 21, no. 4, pp. 2018-26.

References

Zheng, ZL & Yao, MF 2006, 'Numerical study on the chemical reaction kinetics of n-heptane for hcci combustion process', *Fuel*, vol. 85, no. 17-18, pp. 2605-15.

Zhong, S, Wyszynski, ML, Megaritis, A, Yap, D & Xu, H 2005, 'Experimental investigation into hcci combustion using gasoline and diesel blended fuels', *SAE Paper 2005-01-3733*.

Zhou, P, Zhou, S & Clelland, D 2006, 'A modified quasi-dimensional multi-zone combustion model for direct injection diesels', *International Journal of Engine Research*, vol. 7, no. 4, pp. 335.

Zhukov, VP 2012, 'Verification, validation, and testing of kinetic mechanisms of hydrogen combustion in fluid-dynamic computations', *ISRN Mechanical Engineering*, vol. 2012, pp. 11.

References

APPENDIX A

DERIVATION OF TEMPERATURE EQUATION

This appendix contains the derivation of temperature changes in a zero-dimensional single-zone model from the first law of thermodynamics equation. The first law of thermodynamics equation is

$$U = -W + Q_h + \sum_j m_j h_j \quad (\text{A.1})$$

where j represents each flow entering or leaving the system. For a quasi-static process, where work can be expressed as $W = p d\mathcal{V}$, the first law equation in its differential form is given by

$$\frac{d(mu)}{dt} = -p \frac{d\mathcal{V}}{dt} + \frac{dQ_h}{dt} + \sum_j \dot{m}_j h_j \quad (\text{A.2})$$

The enthalpy for a homogeneous system is defined as

$$h = u + pv \quad (\text{A.3})$$

and can be substituted into equation (A.2) to yield

$$\frac{d(mh)}{dt} - \frac{d(p\mathcal{V})}{dt} = \frac{dQ_h}{dt} - p \frac{d\mathcal{V}}{dt} + \sum_j h_j \dot{m}_j \quad (\text{A.4})$$

Equation (A.4) is manipulated and becomes

Appendix A

$$m \frac{dh}{dt} + h \frac{dm}{dt} - p \frac{d\mathcal{V}}{dt} - \mathcal{V} \frac{dp}{dt} = \frac{dQ_h}{dt} - p \frac{d\mathcal{V}}{dt} + \sum_j h_j \dot{m}_j \quad (\text{A.5})$$

$$m \frac{dh}{dt} = \frac{dQ_h}{dt} + \mathcal{V} \frac{dp}{dt} - h \frac{dm}{dt} + \sum_j h_j \dot{m}_j \quad (\text{A.6})$$

In equation (A.6), dh/dt needs to be expressed in terms of change in temperature. For a multi-component mixture of ideal gasses in a single phase,

$$h = \sum_i Y_i h_i \quad \text{and} \quad h = h(T, p, Y_i) \quad (\text{A.7})$$

where i is the component species in the mixture. Applying the chain rule to the derivative of enthalpy produces

$$\frac{dh}{dt} = \left. \frac{\partial h}{\partial T} \right|_{p, Y_i} \frac{dT}{dt} + \left. \frac{\partial h}{\partial p} \right|_{T, Y_i} \frac{dp}{dt} + \sum_i \left. \frac{\partial h}{\partial Y_i} \right|_{p, T, Y_{i \neq j}} \frac{dY_i}{dt} \quad (\text{A.8})$$

The change of enthalpy with respect to pressure at constant temperature and composition is zero, hence equation (A.8) becomes

$$\frac{dh}{dt} = \bar{c}_p \frac{dT}{dt} + \sum_i h_i \frac{dY_i}{dt} \quad (\text{A.9})$$

The pressure change in equation (A.6) can be obtained by manipulating the equation of state for an ideal gas

$$\begin{aligned} p\mathcal{V} &= mRT \\ p \frac{d\mathcal{V}}{dt} + \mathcal{V} \frac{dp}{dt} &= mR \frac{dT}{dt} + T \frac{d(mR)}{dt} \\ p \frac{d\mathcal{V}}{dt} + \mathcal{V} \frac{dp}{dt} &= mR \frac{dT}{dt} + mT \frac{dR}{dt} + RT \frac{dm}{dt} \\ mT \frac{dR}{dt} &= p \frac{d\mathcal{V}}{dt} + \mathcal{V} \frac{dp}{dt} - mR \frac{dT}{dt} - RT \frac{dm}{dt} \end{aligned} \quad (\text{A.10})$$

The ideal gas law is used to substitute for the coefficients of each derivative so that the quantity being differentiated appears in the coefficient

Appendix A

$$\frac{p\mathcal{V}}{R} \frac{dR}{dt} = \frac{mRT}{\mathcal{V}} \frac{d\mathcal{V}}{dt} + \frac{mRT}{p} \frac{dp}{dt} - \frac{p\mathcal{V}}{T} \frac{dT}{dt} - \frac{p\mathcal{V}}{m} \frac{dm}{dt} \quad (\text{A.11})$$

Dividing both sides of equation (A.11) with $p\mathcal{V}$ gives

$$\begin{aligned} \frac{1}{R} \frac{dR}{dt} &= \frac{mRT}{p\mathcal{V}^2} \frac{d\mathcal{V}}{dt} + \frac{mRT}{p^2\mathcal{V}} \frac{dp}{dt} - \frac{1}{T} \frac{dT}{dt} - \frac{1}{m} \frac{dm}{dt} \\ \frac{1}{R} \frac{dR}{dt} &= \frac{mRT}{mRT\mathcal{V}} \frac{d\mathcal{V}}{dt} + \frac{mRT}{mRTp} \frac{dp}{dt} - \frac{1}{T} \frac{dT}{dt} - \frac{1}{m} \frac{dm}{dt} \\ \frac{1}{R} \frac{dR}{dt} &= \frac{1}{\mathcal{V}} \frac{d\mathcal{V}}{dt} + \frac{1}{p} \frac{dp}{dt} - \frac{1}{T} \frac{dT}{dt} - \frac{1}{m} \frac{dm}{dt} \end{aligned} \quad (\text{A.12})$$

The relationship

$$\frac{dR}{dt} = \sum_i R_i \frac{dY_i}{dt} \quad (\text{A.13})$$

can be substituted into equation (A.12), and rearranging gives

$$\frac{dp}{dt} = p \left[\frac{1}{R} \sum_i R_i \frac{dY_i}{dt} + \frac{1}{m} \frac{dm}{dt} + \frac{1}{T} \frac{dT}{dt} - \frac{1}{\mathcal{V}} \frac{d\mathcal{V}}{dt} \right] \quad (\text{A.14})$$

Hence, substituting equation (A.14) to (A.6)

$$m \frac{dh}{dt} = \sum_j \dot{m}_j h_j + \frac{dQ_h}{dt} + p\mathcal{V} \left[\frac{1}{R} \sum_i R_i \frac{dY_i}{dt} + \frac{1}{m} \frac{dm}{dt} + \frac{1}{T} \frac{dT}{dt} - \frac{1}{\mathcal{V}} \frac{d\mathcal{V}}{dt} \right] - \frac{dm}{dt} h$$

and now substituting equation (A.9) and rearranging yields

Appendix A

$$m \left(C_p \frac{dT}{dt} + \sum_i h_i \frac{dY_i}{dt} \right) = \sum_j \dot{m}_j h_j + \frac{dQ_h}{dt} + p\mathcal{V} \left[\frac{1}{R} \sum_i R_i \frac{dY_i}{dt} + \frac{1}{m} \frac{dm}{dt} + \frac{1}{T} \frac{dT}{dt} - \frac{1}{\mathcal{V}} \frac{d\mathcal{V}}{dt} \right] - h \frac{dm}{dt}$$

$$m C_p \frac{dT}{dt} - p\mathcal{V} \frac{1}{T} \frac{dT}{dt} = \sum_j \dot{m}_j h_j + \frac{dQ_h}{dt} + \frac{p\mathcal{V}}{R} \sum_i R_i \frac{dY_i}{dt} + \frac{p\mathcal{V}}{m} \frac{dm}{dt} - p \frac{d\mathcal{V}}{dt} - h \frac{dm}{dt} - m \sum_i h_i \frac{dY_i}{dt}$$

$$\frac{dT}{dt} \left(m C_p - \frac{p\mathcal{V}}{T} \right) = \sum_j \dot{m}_j h_j + \frac{dQ_h}{dt} + \frac{p\mathcal{V}}{R} \sum_i R_i \frac{dY_i}{dt} + \frac{p\mathcal{V}}{m} \frac{dm}{dt} - p \frac{d\mathcal{V}}{dt} - h \frac{dm}{dt} - m \sum_i h_i \frac{dY_i}{dt}$$

$$\frac{dT}{dt} \left(\bar{C}_p - \frac{p\mathcal{V}}{mT} \right) = \sum_i \left[\left(\frac{p\mathcal{V}}{R} R_i - h_i \right) \frac{dY_i}{dt} \right] + \sum_j \frac{\dot{m}_j h_j}{m} + \frac{1}{m} \frac{dQ_h}{dt} + p\mathcal{V} \frac{1}{m} \frac{dm}{dt} - h \frac{1}{m} \frac{dm}{dt} - \frac{p}{m} \frac{d\mathcal{V}}{dt}$$

The final equation is

$$\frac{dT}{dt} = \frac{1}{C_A} \left[\sum_i \left[\left(\frac{p\mathcal{V}}{R} R_i - h_i \right) \frac{dY_i}{dt} \right] - \frac{C_B}{m} \frac{dm}{dt} + \frac{1}{m} \left(\frac{dQ_h}{dt} - p \frac{d\mathcal{V}}{dt} + \sum_j \dot{m}_j h_j \right) \right] \quad (\text{A.15})$$

where

$$C_A = \bar{C}_p - \frac{p\mathcal{V}}{T} \quad (\text{A.16})$$

$$C_B = h - p\mathcal{V} \quad (\text{A.17})$$

APPENDIX B

EXPERIMENTAL SETUP DETAILS

B.1 In-Cylinder Pressure Calibration

The calibration involves the entire pressure transducer system, which includes the amplifier. A dead weight tester from DH Budenberg was used in the calibration. It uses hydraulic oil as a medium to transfer pressure between the static load and the pressure transducer. A load was placed on top of the piston, as shown in Figure B.1, and the wheel was turned clockwise to transmit the hydraulic oil to the piston. The pressure was read using the data logger. Then, the load was changed with a different weight and the process repeated for all loads. Each load has different a weight with an equivalent static pressure stated on it and, therefore, the pressure transducer must be able to produce the same pressure reading as the load.

Different types of loads were used for calibration, and the linear relationship was obtained between the static pressure from the load and the voltage from the pressure transducer, as shown in Figure B.2. The calibration factor for the pressure transducer was 10 bar/V. Multiplication of the calibration factor with voltage shows that the pressure reading from the pressure transducer is identical to the load's static pressure. Therefore, the reading from the pressure transducer is correct.

Appendix B

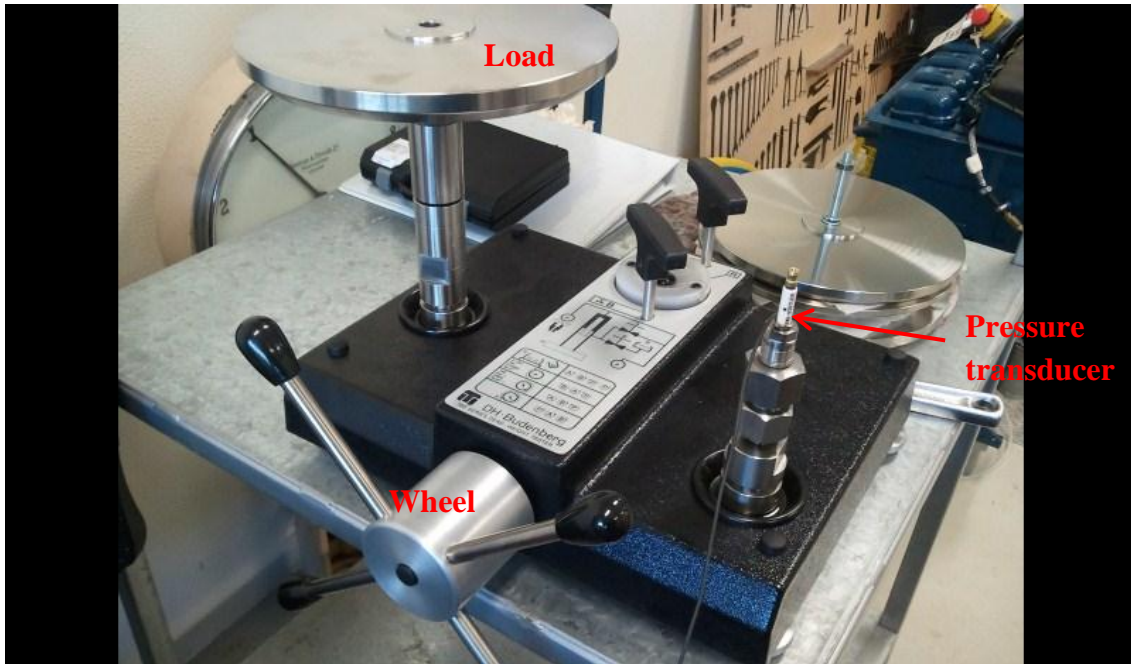


Figure B.1 A dead weight tester was used for calibrating the pressure transducer, where the load was placed on top of the piston to measure the equivalent static pressure.

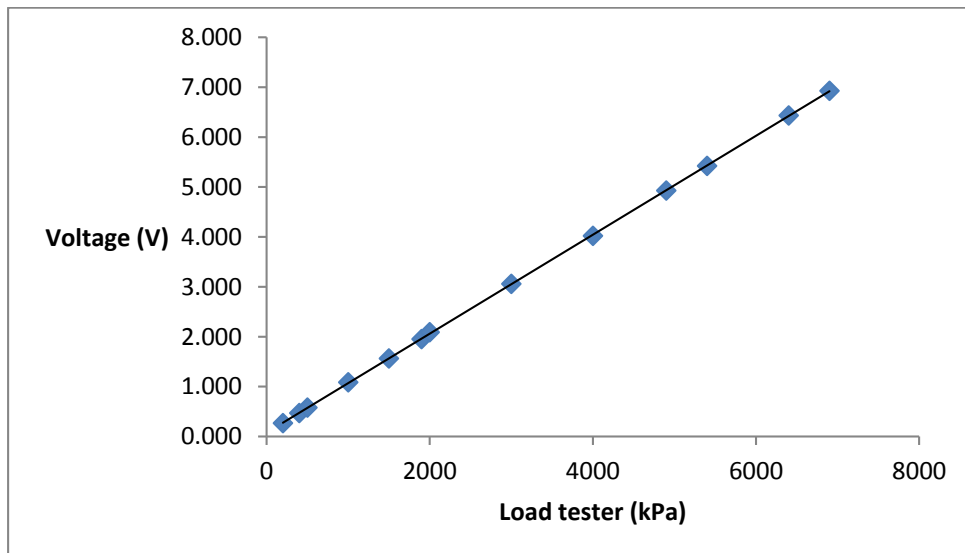


Figure B.2 Linear relationships obtained between voltage reading from the pressure transducer and load tester.

B.2 Electronic Control Unit (ECU)

The ECU is an electronic control unit that is used to optimise the engine running conditions by controlling various parameters. The ECU reads the data from different sensors such as hall effect, throttle position, intake manifold pressure, intake temperature and engine temperature and then compares the reading with a pre-determined table programmed in the ECU. Then the ECU controls the Capacitive Discharge Ignition (CDI) and the EFI as well as the engine's idling operation to give an optimised spark timing and fuel-air mixture. This is illustrated in Figure B.3, where it shows the communication between the ECU and different sensors. The program in the ECU can be changed and gives full control over the engine parameters to achieve different engine performance. The ECU was operated using a 12V DC power supply and software called ProCAL was used to modify the program as well as to read/record the sensors' data.

The fuel-air mixture is optimised by controlling the fuel injection rate to the air stream in the intake manifold. The fuel is controlled by adjusting the pulse-width of the fuel injector: a higher pulse-width means a longer injection time and results in more fuel being injected. The fuel injection rate is controlled based on a number of parameters, which are intake temperature and pressure, throttle position, engine load, engine temperature and engine speed. When the engine is cold, more fuel is required to start the engine and the engine will run rich during the warming-up process. Once the engine has been warmed up and is running at an idle speed, the engine will operate with a near stoichiometric mixture. The engine will run rich again if more loads are required. Typically, a port fuel injection system employs an injection pressure between 3 and 4 bar. The high injection pressure is achieved by using a fuel pump installed in the fuel line.

Appendix B

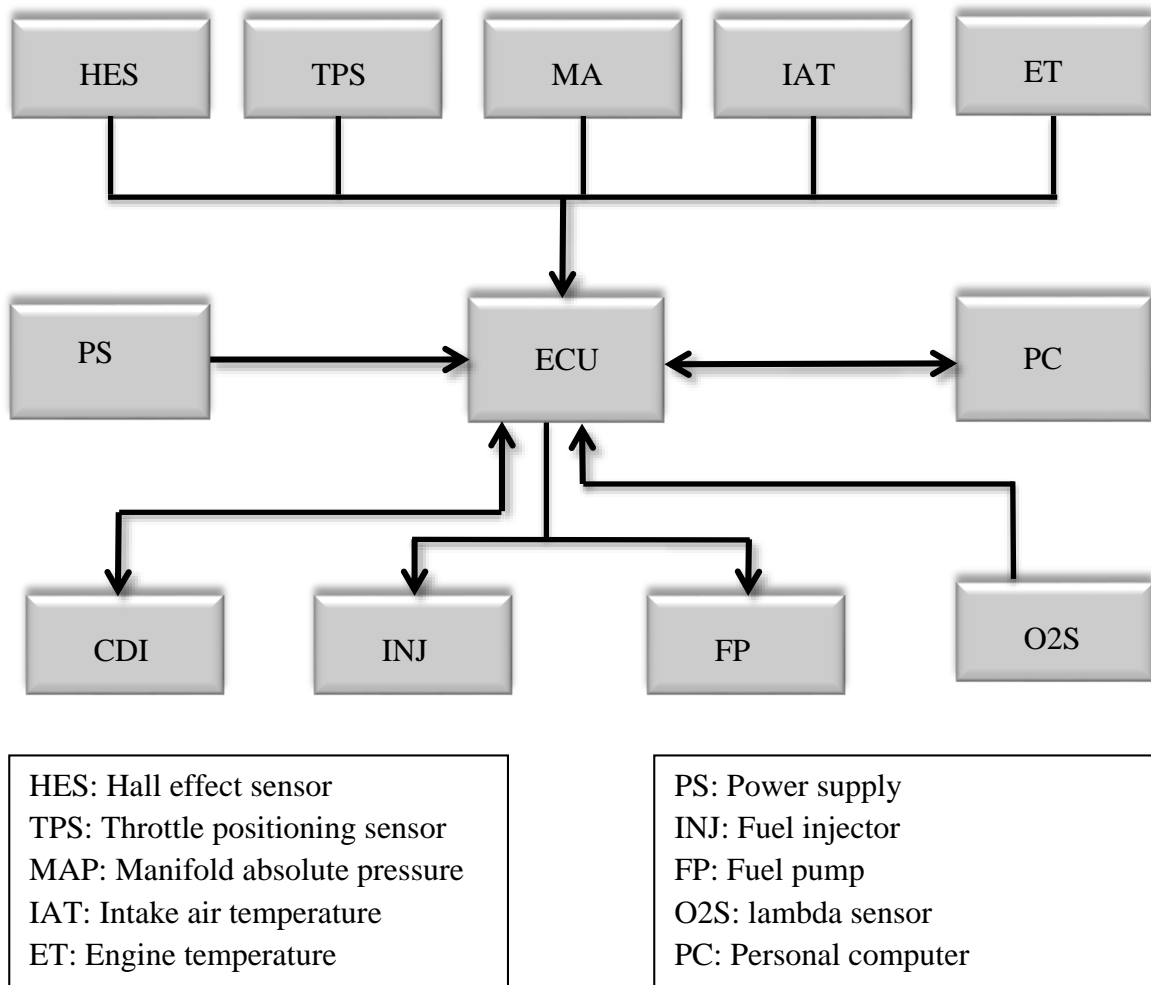


Figure B.3 ECU configurations with different sensors.

A lambda sensor is necessary to give a closed loop control between the lambda and the fuel injection rate. When a lambda sensor is installed, the ECU compares the reading from this sensor to the desired lambda table programmed in the ECU, and the ECU then controls the fuel injection rate accordingly. There are two types of lambda sensor that can be used: narrowband or wideband sensor. A narrowband sensor only gives a reading indicating either a rich or lean mixture, based on the output voltages. In this case, the narrowband sensor showed a rich mixture when the voltage was more than 450 mV and a lean mixture if it was less. A wideband lambda sensor, on the other hand, will show how rich or lean the mixture is. Real-time lambda will be recorded and the ECU will know the exact lambda reading. This will give more control for tuning the engine. In this study, a wideband lambda sensor (Bosch LSU 4.2) was used together with the Accurate Lambda Meter (ALM) from Ecotrons. The ALM was connected to the ECU to record the lambda reading.

Appendix B

A CDI is an important addition to the ECU because it is used to control the ignition timing. Ignition timing is defined as the point at which the spark plug starts to fire the cylinder. Therefore, the combustion in an SI engine occurs at the ignition point or slightly retarded based on the ignition delay of the fuel. A hall effect sensor was used to monitor the engine speed and the crank angle position. Once the ECU knows the piston is at a pre-set location based on the crank angle position, the ECU starts firing the spark plug. If the spark timing is too early (advanced), the combustion occurs while the piston is moving towards the TDC. This will push the piston down while in the compression process, hence compression work (negative work) increases and the same for peak in-cylinder pressure. This leads to reduced power, high combustion temperatures, backfires and knocking if it is over-advanced. If the spark timing is retarded, the combustion occurs while the piston is moving down to the bottom dead centre (BDC). This will reduce the expansion work (positive work), as does the peak in-cylinder pressure. In this case, the energy is wasted leading to loss of power and incomplete combustion.

To achieve optimised combustion, the ignition timing must occur at Maximum Brake Torque (MBT). MBT is a point where optimal combustion occurs, which gives maximum power and efficiency. Engine torque is reduced if the ignition timing is advanced or retarded from MBT. This is explained in Figure B.4 where MBT is at 30° before TDC (BTDC). In Figure B.4 (a), the in-cylinder peak pressure is higher if the ignition timing is advanced, while it is lower with retarded ignition timing. The relative torque, on the other hand, is at its maximum at MBT, as shown in Figure B.4 (b). In this study, the MBT for the engine was kept at 26° BTDC when the engine operated in SI mode, to comply with the manufacturer's specification.

Appendix B

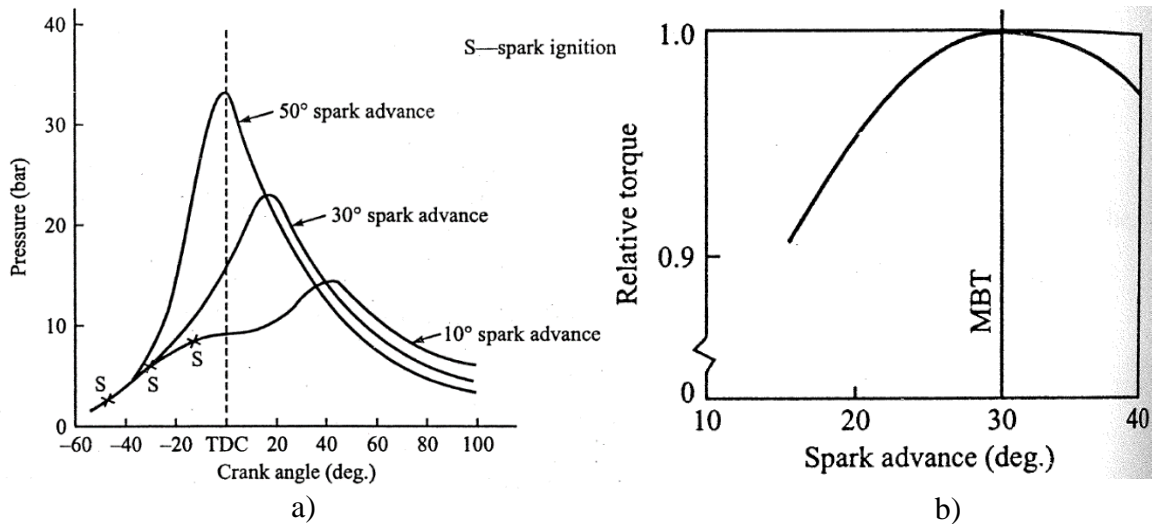


Figure B.4 a) In-cylinder peak pressure difference with advanced and retarded ignition timing. b) Relative torque decreases when the ignition timing is not at MBT (Gupta, 2006).

B.3 Fuel Delivery System

In an old engine setup, a carburettor was used to mix the air and fuel in the intake manifold. The carburettor uses a pressure difference concept to bring the fuel to the intake manifold. The air flows through a converging-diverging nozzle, called venturi, as shown in Figure B.5 (a) and creates a pressure difference between the throat and float chamber. The float chamber contains a large quantity of fuel located close to the intake manifold (Figure B.5a). The fuel is discharged to the air stream through the fuel port and atomization occurs inside the intake manifold.

An EFI system, on the other hand, uses port fuel injection to inject the fuel into the air stream, where the fuel is injected straightaway from the fuel line (Figure B.5b). The EFI is electronically controlled by the ECU. In the current engine setup, the EFI was used to replace the carburettor due to safety reasons.

The boiling point of the fuel is between 303K and 478K and the auto-ignition temperature is 643K. Due to the low boiling point of the gasoline, the carburettor is not advisable to use with a heated air stream. The carburettor body is made of aluminium and a high air stream temperature will increase the chances of the fuel in the float chamber being heated as well. This may cause a fire if not well controlled.

Appendix B

Because of this safety reason, an EFI system was chosen to replace the carburettor. The EFI has no fuel in a large quantity close to the heated body and the injector will be easily cooled down using the water jacket. One of the advantages of using an EFI system is that the likelihood of fire in HCCI mode can be reduced. Other advantages of EFI over carburettor systems are: 1) increased volumetric efficiency because there is no restriction in the mixture flow; 2) good engine response with varying throttle opening; 3) consistent fuel delivery in each cycle; and 4) lower fuel consumption leads to more efficient combustion by optimising the fuel-air mixture.

In this study, the fuel injection pressure of the EFI was kept constant at 3 bar supplied by the fuel pump. A pressure regulator was used in the fuel line to ensure the fuel pressure is constant, as shown in Figure B.6 (top). The EFI, as shown in Figure B.6 (bottom), has a characteristic flow rate of 80 g/min. The fuel temperature was kept constant at room temperature, about 300 K.

Appendix B

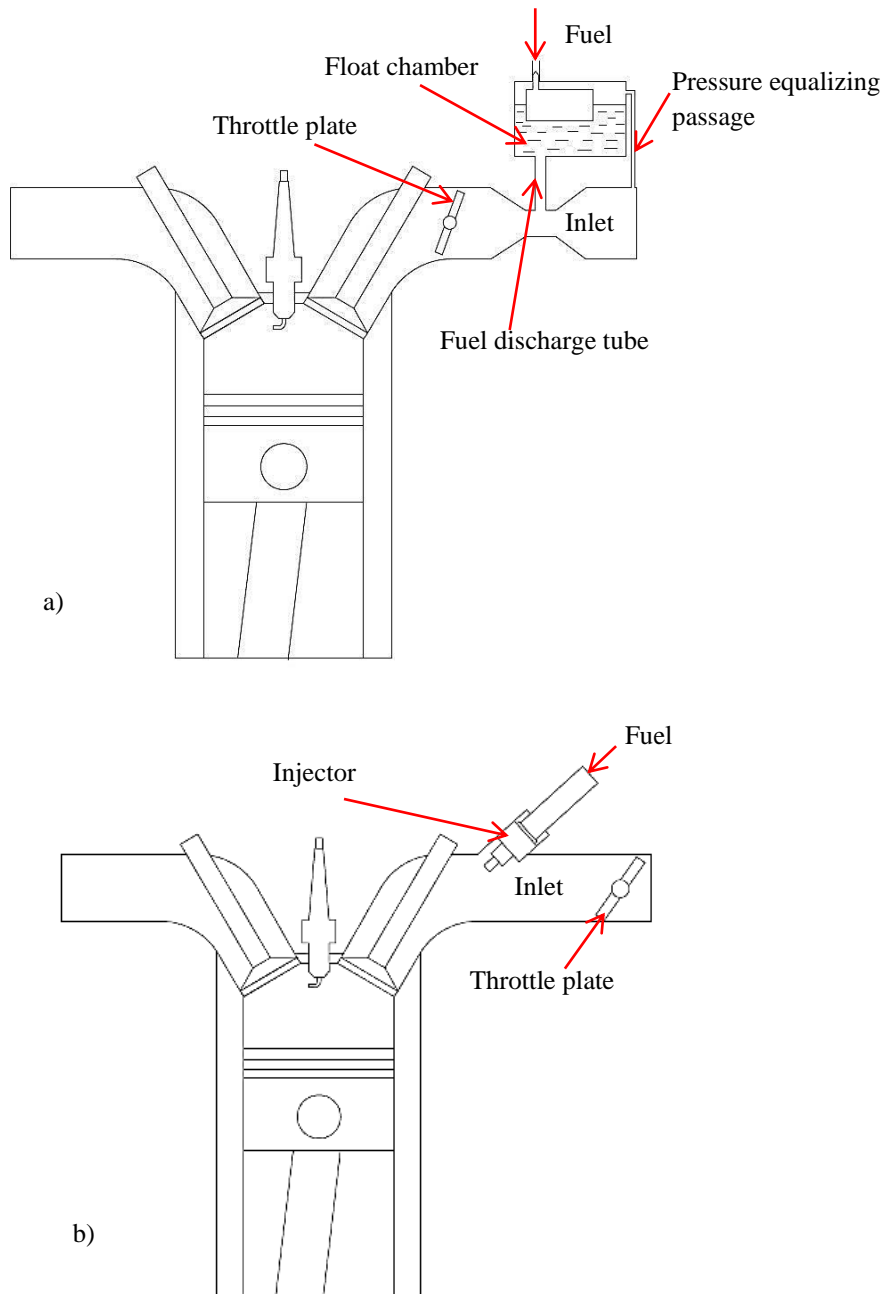


Figure B.5 The difference between the carburettor and the EFI system is in the fuel delivery system a) The carburettor system uses pressure difference to suck the fuel from the float chamber b) In the EFI system, the fuel is injected straightaway from the fuel line at a pressure of about 3 bar.

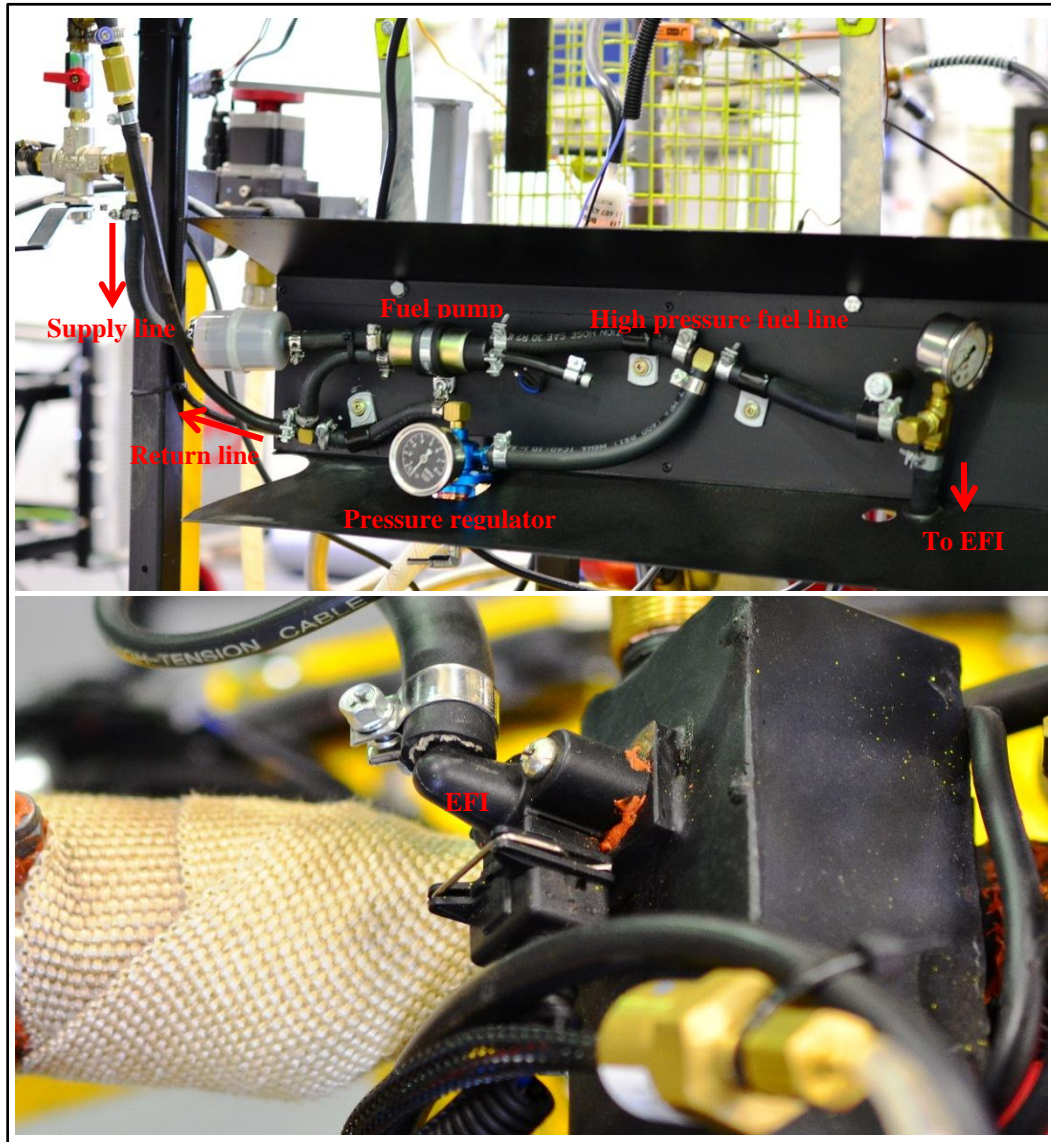


Figure B.6 Fuel delivery to EFI.

B.4 Ignition System: TCI vs. CDI

The ignition system of the old engine setup used a Transistorized Charging Ignition (TCI) before being replaced with a CDI for using the ECU. For small engines, usually the ignition module is installed next to the flywheel. Most small engines with carburettor systems use TCI for the ignition and many of them do not have CDI. TCI is an induction ignition system, where it has the ignition module installed next to the flywheel. The coil inside the ignition module is always charged and uses a transistor switch to disconnect the coil. When the magnet (in-built onto the flywheel) passes by the ignition module, the charge in the coil collapses and fires the spark plug via a high

Appendix B

voltage cable. The voltage stored in the coil is approximately 20,000 V. In the TCI system, there is no standalone pickup sensor, no throttle position sensor and no ambient air sensor. The only variable reported by the pickup coil is the engine speed. The pickup coil will then determine the spark timing based on the engine speed.

A CDI, on the other hand, works in the opposite way. The coil does not store charge. When the pickup sensor triggers the signal, the CDI will amplify the charge to a higher voltage. The mechanism is similar to transformers, and typically the voltage will step up 100:1. The voltage from the CDI is between 250-500 V and thus the output voltage to the spark plug is between 25,000 and 50,000 V. The disadvantage of the CDI is a short high voltage pulse duration compared to TCI. However, it gives a good result at a high engine speed (consistent spark voltages).

The CDI works with the ECU, which has a fully programmable ignition control system. To modify the engine from TCI to CDI, a hall effect sensor was used to replace the old ignition module, as shown in Figure B.7. The hall effect sensor was installed at the same location as the old ignition module, right next to the flywheel, as shown in Figure B.8. When the magnet on the flywheel passes by the sensor, the hall effect sensor acts as a pickup sensor that will trigger a signal to the ECU. Then, the ECU can control the ignition timing accordingly.

Appendix B



Figure B.7 Old ignition module using TCI system.

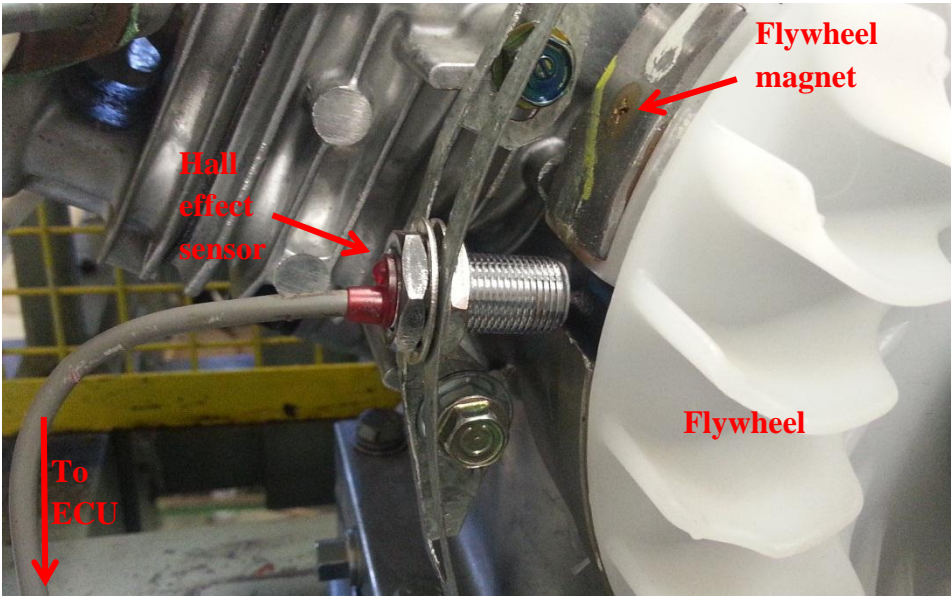


Figure B.8 A hall effect sensor was installed next to the flywheel and connected to the ECU.

Appendix B

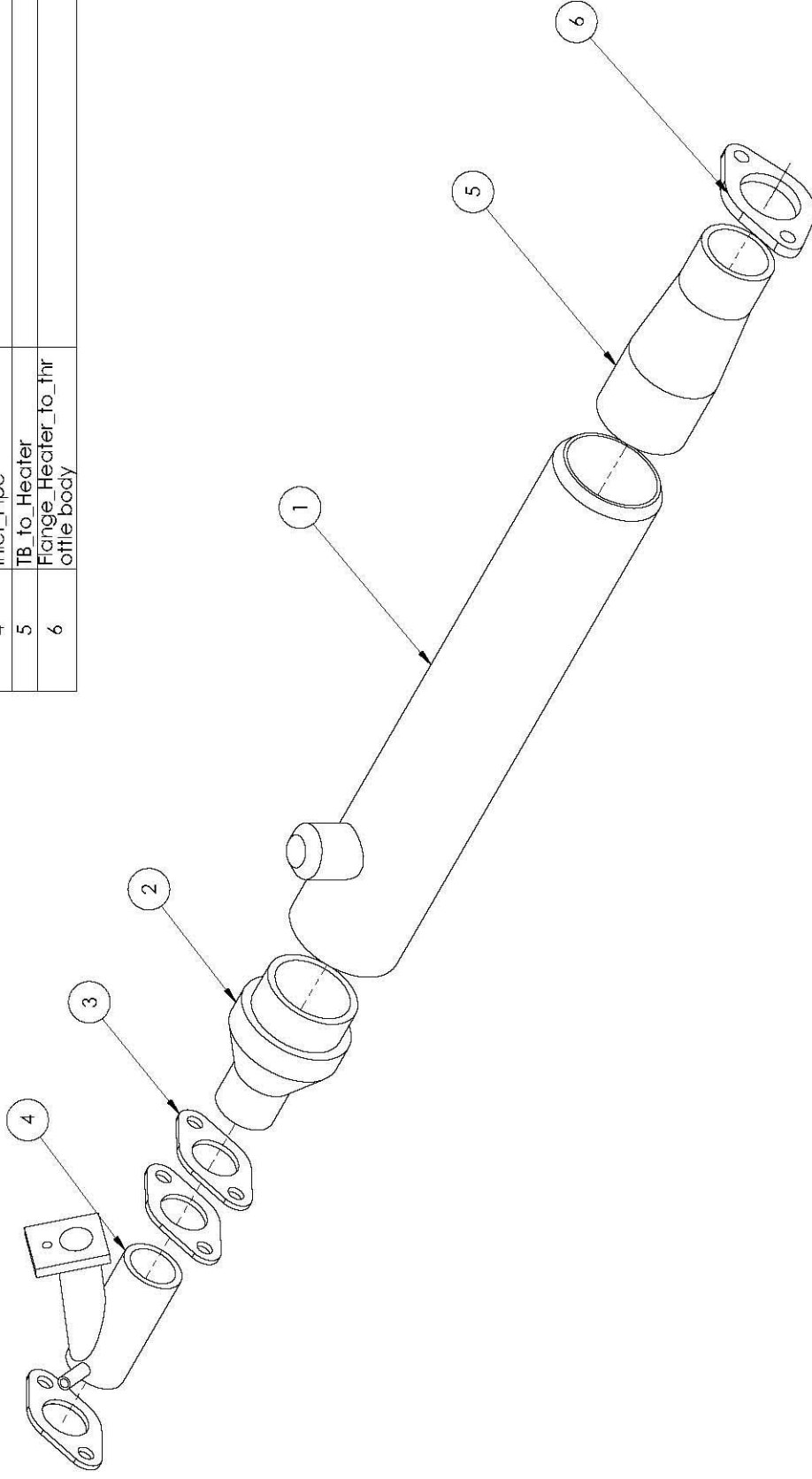
APPENDIX C

ENGINEERING DRAWINGS

Heater Body

This appendix contains the engineering drawings of the complete installation of the heater in the intake manifold. The parts were fabricated in the university's mechanical engineering workshop.

ITEM NO.	PART NUMBER	DESCRIPTION	QTY.
1	TufcoFamam_Heater		1
2	Heater_to_Inlet		1
3	Flange		3
4	Inlet_Pipe		1
5	TB_to_Heater		1
6	Flange_Heater_to_thr ottle_body		1



UNLESS OTHERWISE SPECIFIED:
DIMENSIONS ARE IN MILLIMETERS
SURFACE FINISH:
TOLERANCES:
LINEAR:
ANGULAR:

FINISH:
DEBUR AND
BREAK SHARP
EDGES

DRAWN	NAME	SIGNATURE	DATE
	AEDJLAZE		27/03/2012
CHK'D			
APPY'D			
MFG			
Q.A.			

MATERIAL:
Stainless/Mild Steel

DC/NOT SCALE DRAWING

REVISION: 1

UNIVERSITY OF SOUTHERN QUEENSLAND

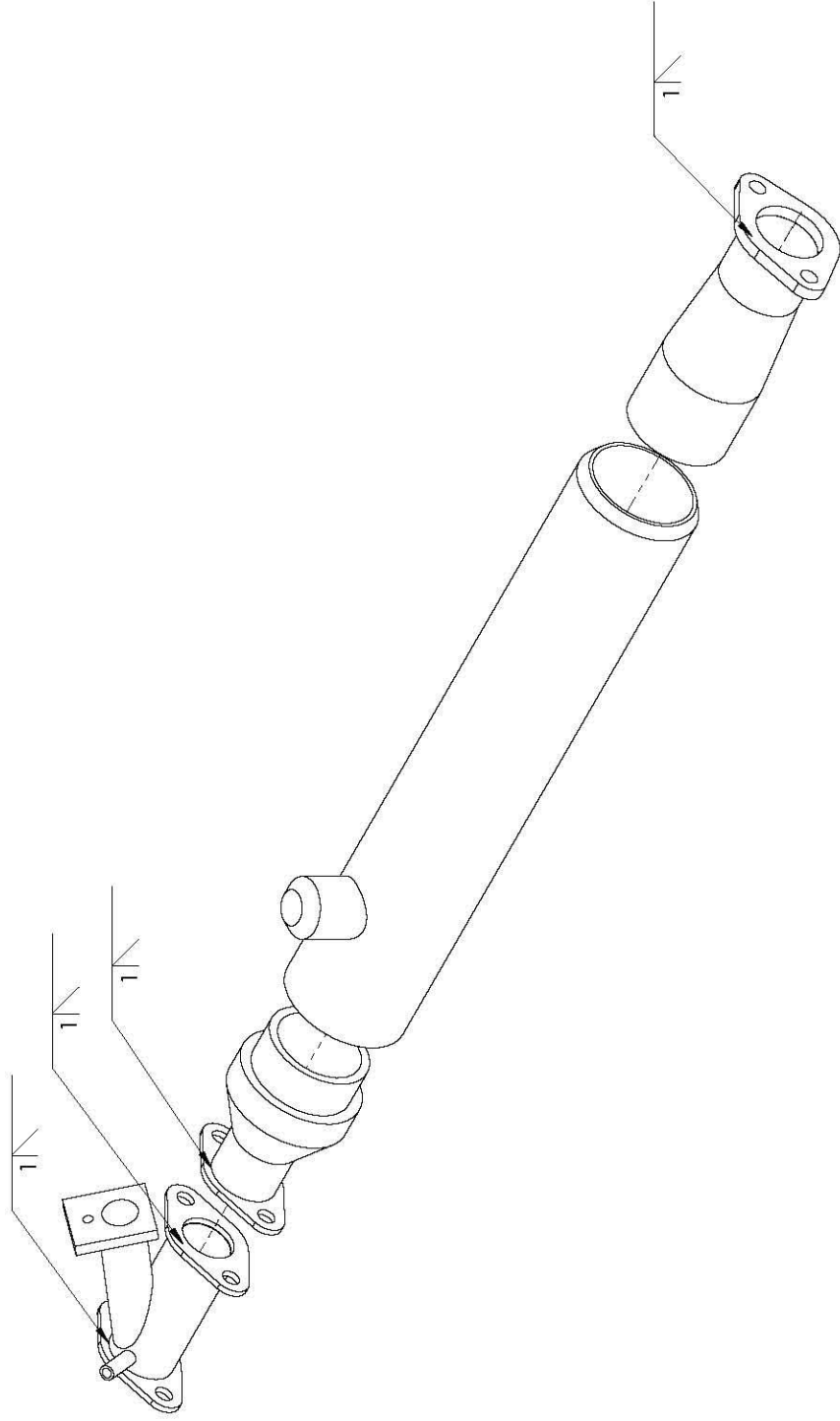
TITLE:

BILL OF MATERIAL: EXPLODED VIEW

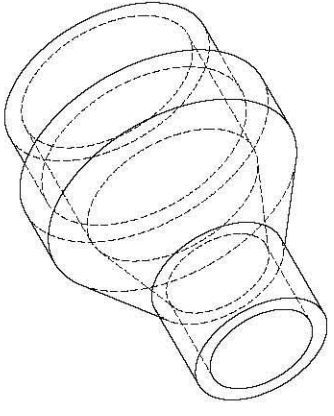
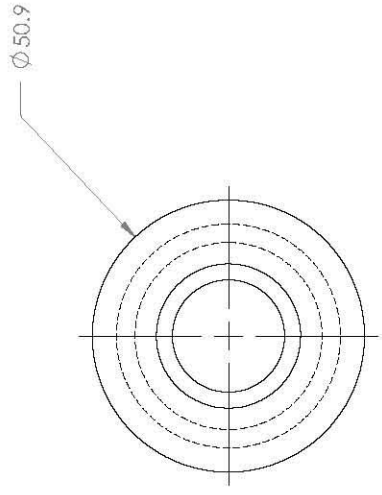
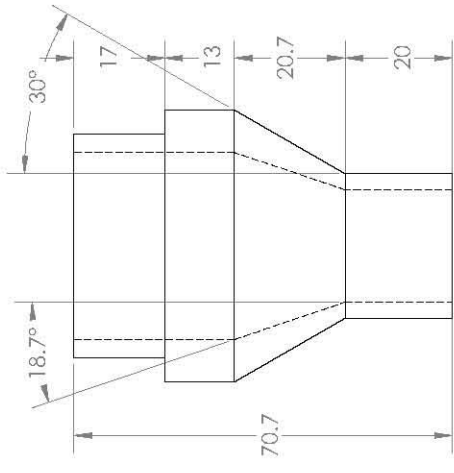
DWG NO. Heater_Exploded A3

SCALE: 1:2

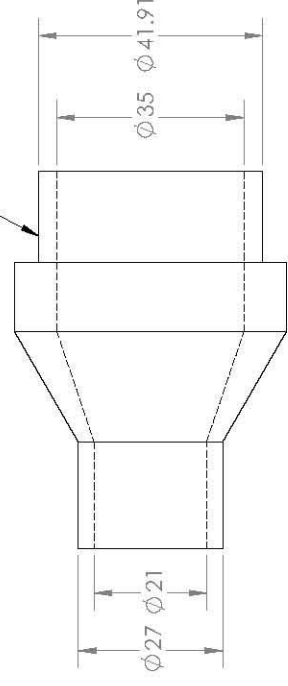
SHEET 2 OF 8



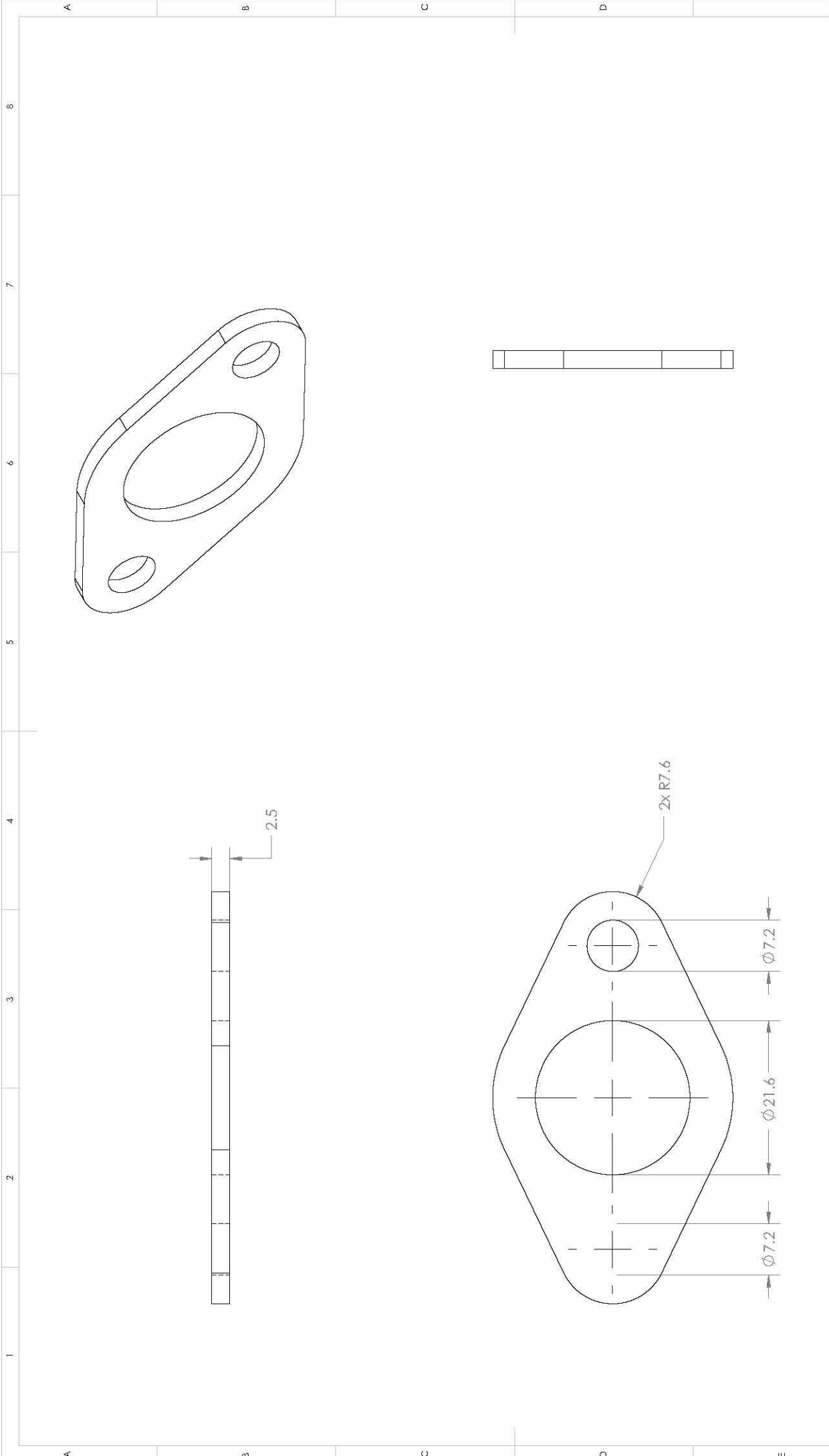
UNLESS OTHERWISE SPECIFIED: DIMENSIONS ARE IN MILLIMETERS SURFACE FINISH: TOLERANCES: LINEAR: ANGULAR:		FINISH: DRAWN: ABDULAZIZ CHK'D: APP'D: MFG: Q.A.		SIGNATURE		DATE 27/8/2012		DEBUR AND REMOVE SHARP EDGES		DO NOT SCALE DRAWING		REVISION: 1	
UNIVERSITY OF SOUTHERN QUEENSLAND										TITLE: WELDED PART OF THE SYSTEM			
STAINLESS/MILD STEEL										DWG NO: Heater_Welded			
MATERIAL										A3			
WEIGHT:										SCALE: 1:2			



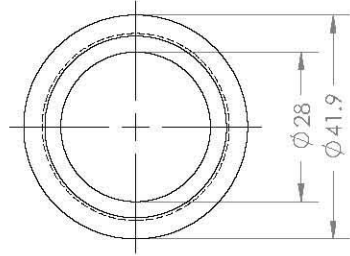
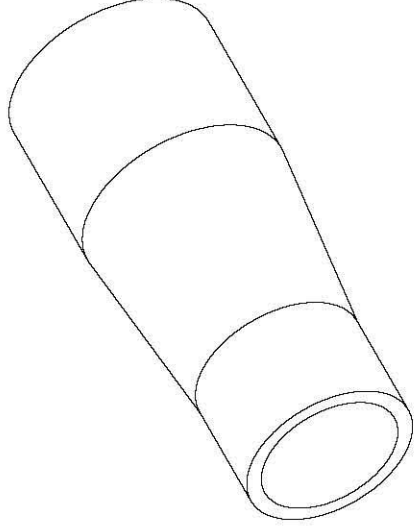
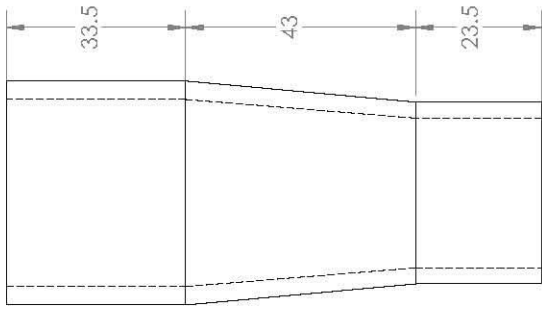
Drill & Tap: 1 1/4" BSPP ~Typical, As Sampled



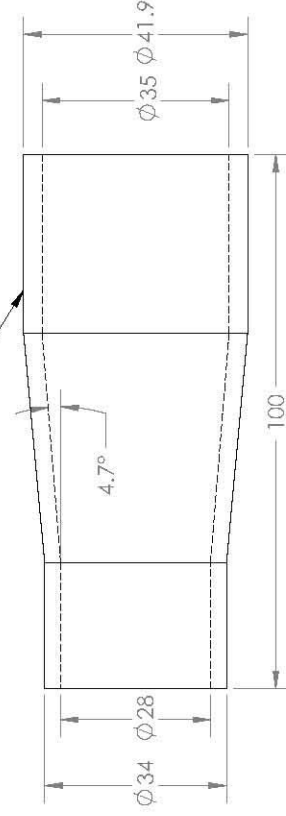
UNLESS OTHERWISE SPECIFIED: DIMENSIONS ARE IN MILLIMETERS		FINISH:		DEBUR AND BREAK SHARP EDGES		DO NOT SCALE DRAWING		REVISION: 1	
TOLERANCES:						UNIVERSITY OF SOUTHERN QUEENSLAND			
FRACTIONS:						TITLE:			
DECIMALS:						HEATER TO MIXING CHAMBER			
LINEAR:						DWG NO:		2. Heater_to_Inlet	
ANGULAR:						MATERIAL:		A3	
DRAWN	NAME	SIGNATURE	DATE						
CHK'D	ABDULAZIZ		27/8/2012						
APPR'D									
MFG									
Q.A.									
				MATERIAL:		MILD STEEL			
				WEIGHT:					



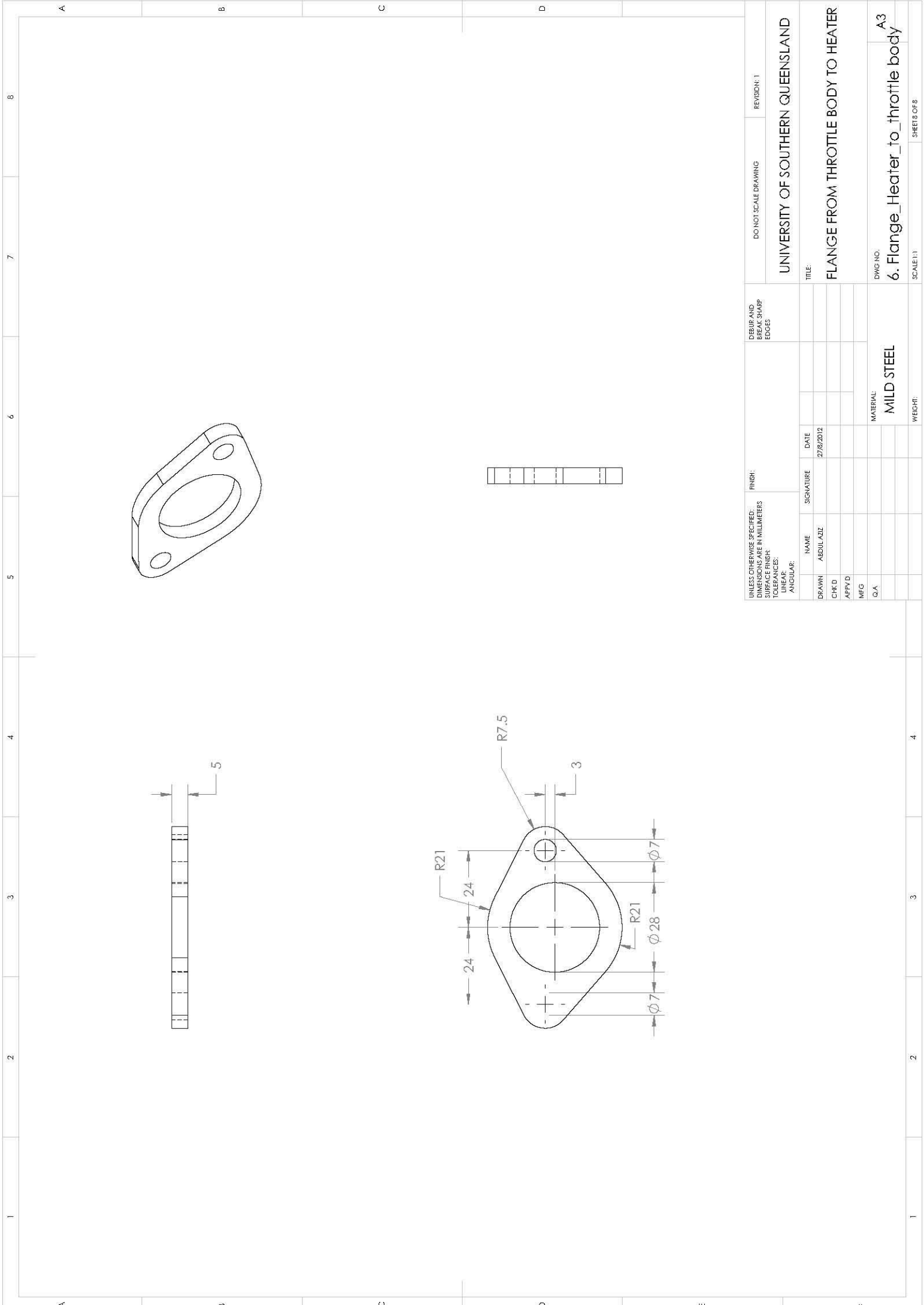
UNLESS OTHERWISE SPECIFIED: DIMENSIONS ARE IN MILLIMETERS SURFACE FINISH: AS SUPPLIED TOLERANCES: LINEAR: ANGULAR:		FINISH:	DIBUF AND MATERIAL: SHARP EDGES		DO NOT SCALE DRAWING	REVISION: 1
DRAWN: AEDULL AZIZ	NAME: AEDULL AZIZ	SIGNATURE:	DATE: 27/8/2012	UNIVERSITY OF SOUTHERN QUEENSLAND		
CHK'D:				TITLE: FLANGE		
APP'VD:				DWG NO: 3. Flange		
MFG:				SCALE: 2:1		
Q.A.:				SHEETS OF 8		
				MATERIAL: MILD STEEL		
				WEIGHT:		



Drill & Tap: 1 1/4" BSPP ~Typical, As Sampled



UNLESS OTHERWISE SPECIFIED: DIMENSIONS ARE IN MILLIMETERS		FINISH:		DEBUR AND BREAK SHARP EDGES		DO NOT SCALE DRAWING		REVISION 1	
TOLERANCES:		NAME		SIGNATURE		DATE		TITLE:	
FRACTIONAL:		DRAWN		ABDULAZIZ		26/8/2012		UNIVERSITY OF SOUTHERN QUEENSLAND	
DECIMAL:		CHK'D						ADAPTER FROM THROTTLE BODY TO HEATER	
LINEAR:		APPY'D						DWG NO: 5. TB_to_Heater	
ANGULAR:		MFG						A3	
		Q.A.						MATERIAL: MILD STEEL	
								SCALE: 1:1	
								SHEET 1 OF 1	



UNLESS OTHERWISE SPECIFIED: DIMENSIONS ARE IN MILLIMETERS		FINISH:		DEBUR AND BREAK SHARP EDGES		DO NOT SCALE DRAWING		REVISION: 1	
TOLERANCES:						UNIVERSITY OF SOUTHERN QUEENSLAND			
HOLE FINISH:						TITLE:			
LINEAR:						FLANGE FROM THROTTLE BODY TO HEATER			
ANGULAR:						DWG NO:		A3	
		DRAWN ABDULAZIZ		SIGNATURE		DATE		6. Flange_Heater_to_throttle body	
		CHK'D				27/8/2012		SCALE: 1:1	
		APPY'D						SHEET 8 OF 8	
		MFG							
		Q.A.							
				MATERIAL:		MILD STEEL			
				WEIGHT:					

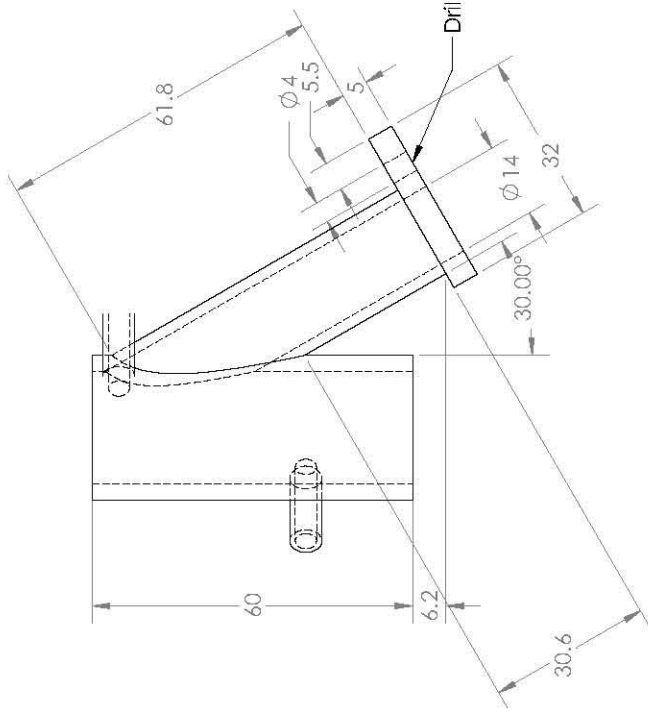
Appendix C

APPENDIX D

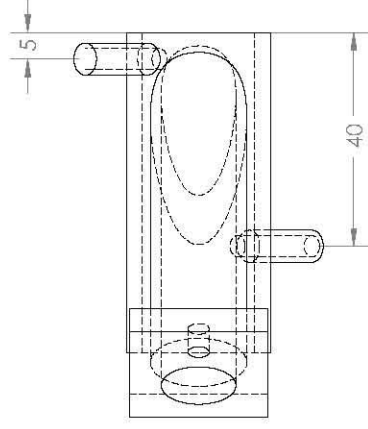
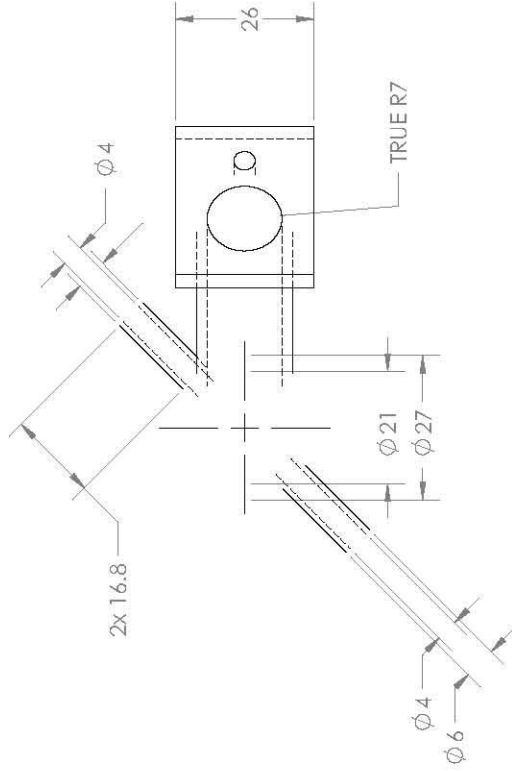
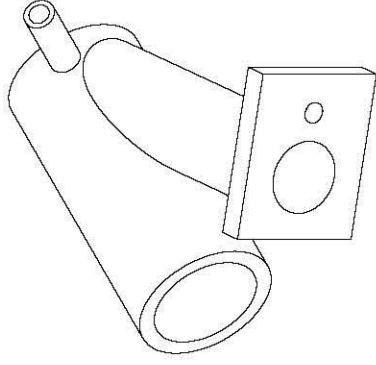
ENGINEERING DRAWINGS

Cooling System

This appendix contains the engineering drawings of the EFI cooling system, where all the parts were also fabricated in the university's mechanical engineering workshop.



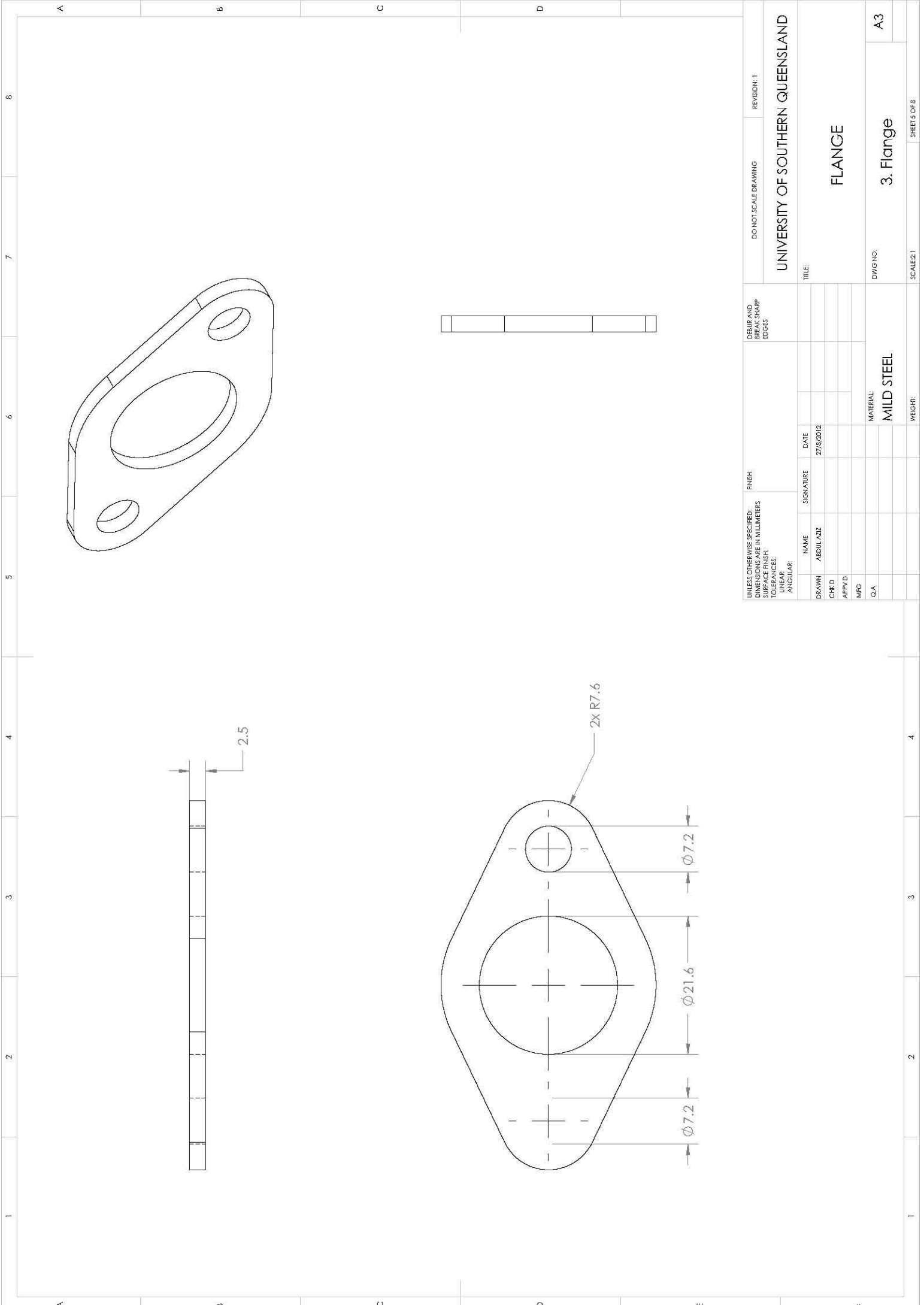
Drill & Tap: M4.5x0.5 ~Typical, As Sampled



UNLESS OTHERWISE SPECIFIED: DIMENSIONS ARE IN MILLIMETERS SURFACE FINISH: TOLERANCES: LINEAR: ANGULAR:		FINISH:	DEBUR AND BREAK SHARP EDGES		DO NOT SCALE DRAWING	REVISION: 1
DRAWN	NAME	SIGNATURE	DATE	TITLE:		
CHK'D	ABDUL AZIZ		27/8/2012	UNIVERSITY OF SOUTHERN QUEENSLAND		
APPY'D				MIXING CHAMBER		
MFG				DWG NO: 4. Inlet_Pipe		
Q.A.				SCALE: 1:1		
				SHEET 6 OF 8		

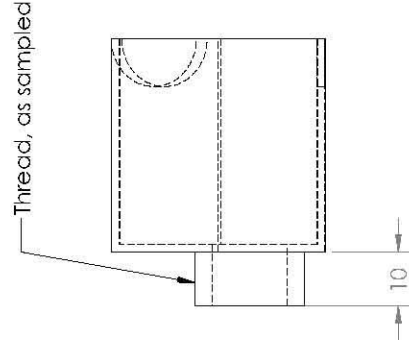
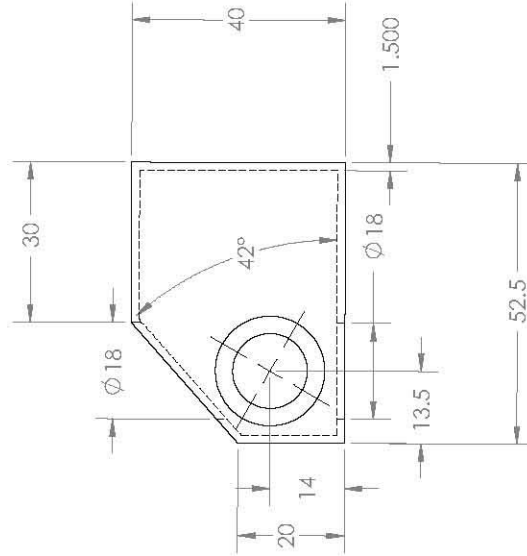
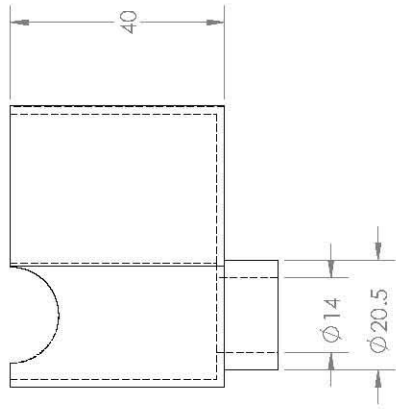
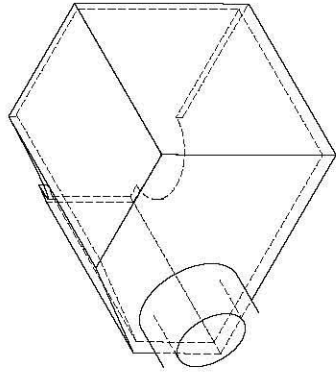
MATERIAL: STAINLESS STEEL

WEIGHT:



1 2 3 4 5 6 7 8

A B C D E F



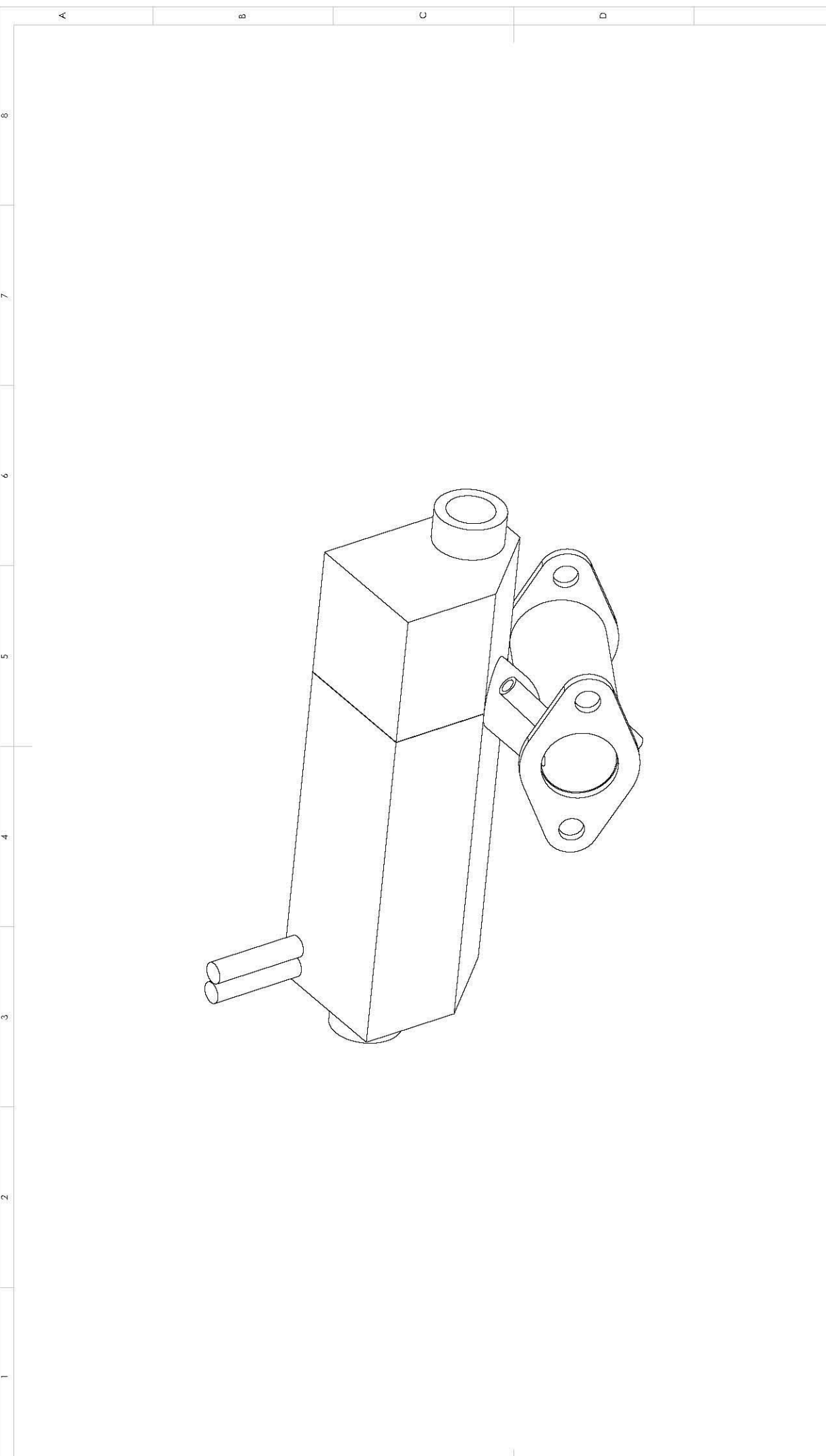
UNLESS OTHERWISE SPECIFIED: DIMENSIONS ARE IN MILLIMETERS SURFACE FINISH: TOLERANCES: LINEAR: ANGULAR:		FINISH:		DEBUR AND BREAK SHARP EDGES		DO NOT SCALE DRAWING		REVISION	
DRAWN	NAME	SIGNATURE	DATE	TITLE:		UNIVERSITY OF SOUTHERN QUEENSLAND			
CHK'D	ABDUL AZIZ								
APPY'D									
MFG									
Q.A.						DWG NO: A3			
						SCALE: 1:1			
						SHEET 1 OF 1			

WATER JACKET: LEFT

A3

SCALE: 1:1

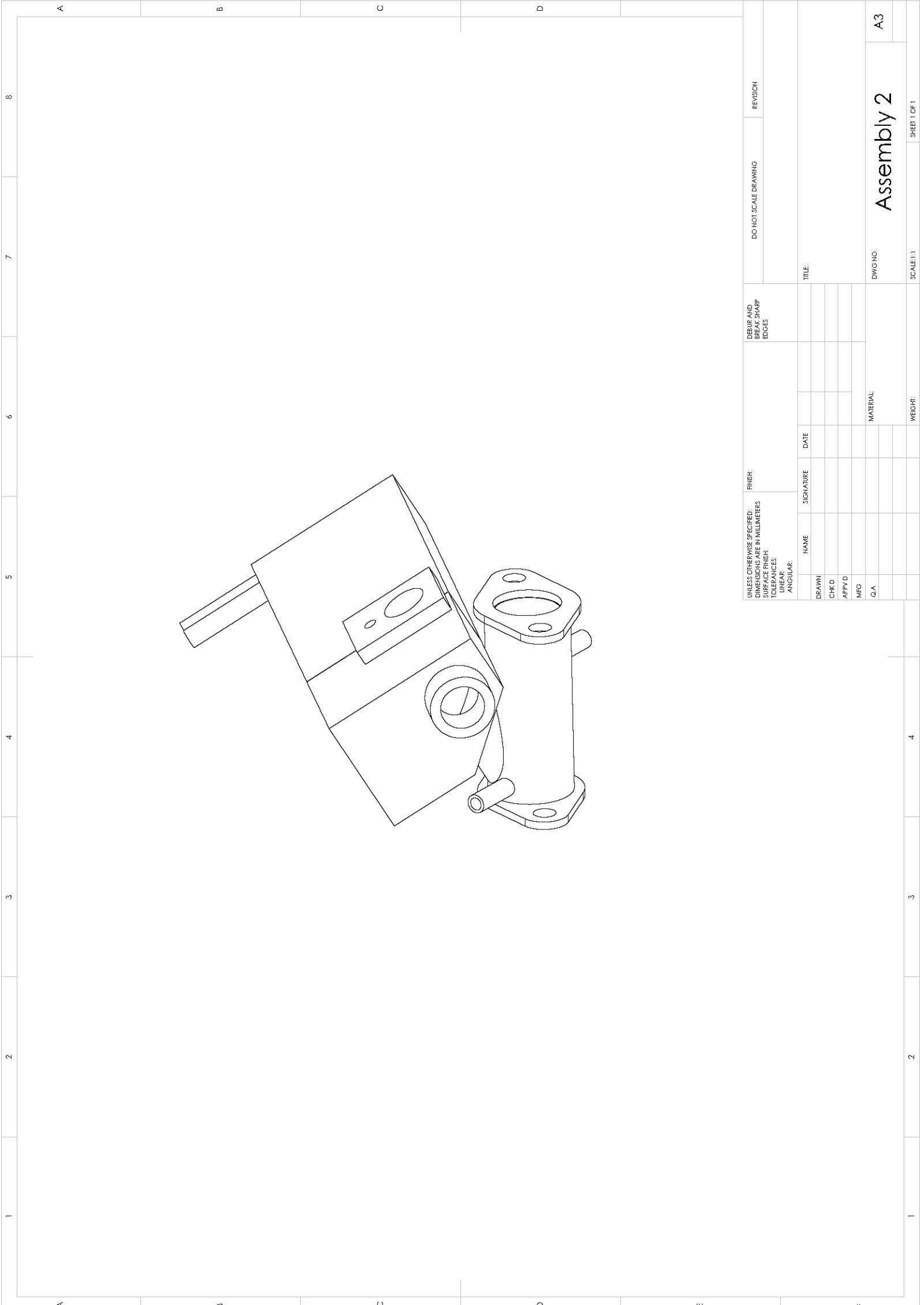
SHEET 1 OF 1



UNLESS OTHERWISE SPECIFIED: DIMENSIONS ARE IN MILLIMETERS SURFACE FINISH: TOLERANCES: LINEAR: ANGULAR:		FINISH:		DEBUR AND REMOVE SHARP EDGES		DO NOT SCALE DRAWING		REVISION	
DRAWN	NAME	SIGNATURE	DATE						
CHK'D	AEDULLAZZ								
APP'VD									
MFG									
Q.A.									
				MATERIAL		TITLE		DWG NO.	
						Assembly 1		A3	
				WEIGHT:		SCALE: 1:1		SHEET 1 OF 1	

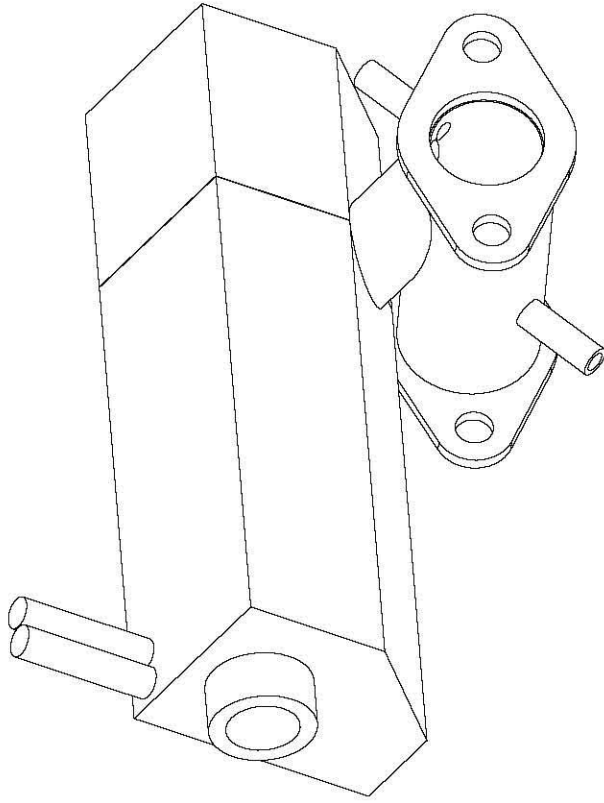
1 2 3 4 5 6 7 8

A B C D E F



UNLESS OTHERWISE SPECIFIED: DIMENSIONS ARE IN MILLIMETERS SURFACE FINISH: TOLERANCES: LINEAR: ANGULAR:		FINISH:		DEBUR AND REMOVE SHARP EDGES		DO NOT SCALE DRAWING		REVISION	
DRAWN	NAME	SIGNATURE	DATE						
CHK'D									
APPY'D									
MFG									
Q.A									
				TITLE:					
				MATERIAL:		DWGNO:		Assembly 2	
				WEIGHT:		SCALE:1:1		SHEET 1 OF 1	

A3



UNLESS OTHERWISE SPECIFIED: DIMENSIONS ARE IN MILLIMETERS		FINISH:		DEBUR AND REMOVE SHARP EDGES		DO NOT SCALE DRAWING		REVISION	
SURFACE FINISH:		TOLERANCES:		NAME		SIGNATURE		DATE	
LINEAR:		ANGULAR:		DRAWN		CHK'D		APPR'D	
				MFG		QA		MATERIAL	
								TITLE:	
								DWG NO. Assembly 3	
								SCALE: 1:1	
								WEIGHT:	
								SHEET 1 OF 1	

Assembly 3

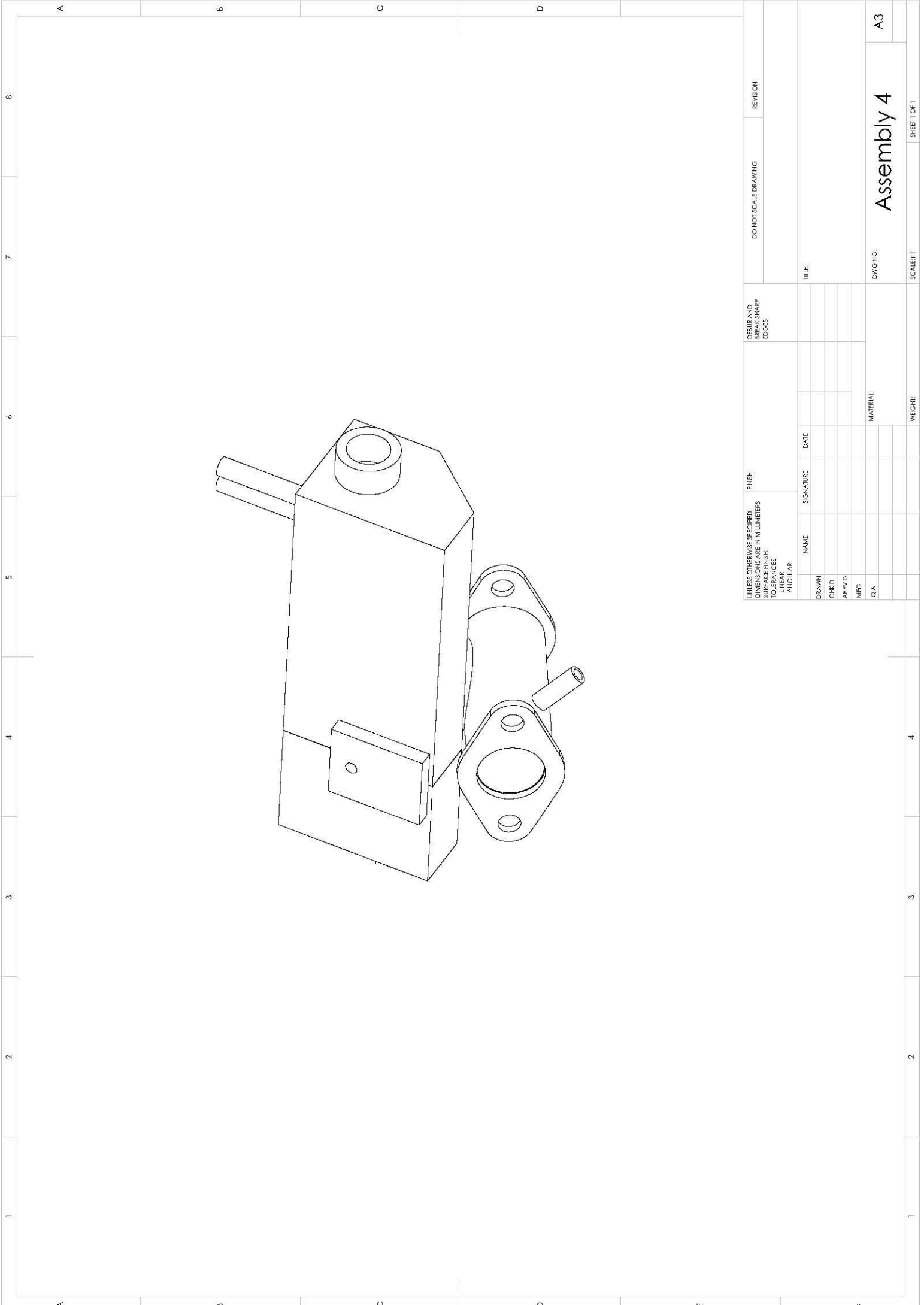
DWG NO.

A3

SCALE: 1:1

WEIGHT:

SHEET 1 OF 1



1 2 3 4 5 6 7 8

UNLESS OTHERWISE SPECIFIED:		FINISH:		DO NOT SCALE DRAWING		REVISION	
DIMENSIONS ARE IN MILLIMETERS		DRAWING AND PART SHARP EDGES					
SURFACE FINISH:							
TOLERANCES:							
LINEAR:							
ANGULAR:							
		NAME	SIGNATURE	DATE	TITLE:		
		DRAWN					
		CHK'D					
		APPY'D					
		MFG					
		Q.A					
		MATERIAL:		DWGNO: Assembly 4			
				A3			
				SCALE: 1:1			
				WEIGHT:			
				SHEET 1 OF 1			

Appendix D

APPENDIX E

EXPERIMENT: SWP

Safe Working Procedures (SWP)

This appendix contains the safe working procedures for operating the engine test bed. All precautionary steps must be adhered to for safety reasons.

SAFE WORKING PROCEDURES
HCCI Engine Operation

DO NOT use the HCCI Engine unless a competent person has instructed you in its safe use and operation and you are authorised to use it.

Procedure for Startup, Operation and Shutdown of HCCI System.

Pre-Startup

1. Notify others (supervisor, lab tech or USQ safe) that you will be running the engine.
2. Do not operate the engine after hours.
3. Check of gas detection alarms
4. Turn ON ventilation system, exhaust gas extraction fan and the cooling water system. The switches are in the Control Room.
5. Put on PPE (boot, eye and ear protection, gloves if dealing with fuel)
6. Perform safety and pre-system checks on engine
 - a. Oil Level correct, and no oil leaks. To top-up or change oil, refer to Honda owner's manual.
 - b. Fuel level in tank OK. If fuel is required, see Fuel Handling SWP.
7. Ensure all the switches are within reach.
8. Confirm all guards are in place.
9. Confirm there are no entanglement risks (sensor cabling is appropriately tied back)
10. Refer to engine owner's manual for operating instructions.
11. Check the heater system located at inlet manifold (the earth cable is connected properly).
12. Check the plastic parts close to the heater, especially the injector. Make sure the parts physically are in good condition (not melted).
13. Turn ON the DAQ system and all the engine switches.

This SOP does not necessarily cover all possible hazards associated with the machine and should be used in conjunction with other references. It is designed to be used as an adjunct to Safety Procedures and to act as a reminder to users prior to machine use.

Date of last review

Signature

Appendix E

14. Turn ON the water supply valves to the dynamometer and the injector cooling system
15. Turn ON the fuel line (ball valve)
16. Make sure the operator is located at the Operator's Console behind the safety screen.

Running the Engine (Normal Operation)

17. Start the engine
18. Check for any oil, fuel or exhaust gas leaks from the engine (no oil or smoke from any part of the engine)
19. If there is a leak, stop the engine and troubleshoot. Read the engine owner's manual.
20. Let the engine running for about 5-10 minutes to warm up to an operating temperature.
21. Turn ON the air heater.
22. Check for evidence of any melting parts.
23. Conduct data collection

Normal Shut-Down Procedure

24. To Shut down the engine:
 - a. Turn OFF engine's main switch
 - b. Turn OFF DAQ system
 - c. Turn OFF the fuel line (ball valve)
 - d. Turn OFF the valves for the water supply to the dyno and injector cooling system
 - e. Turn OFF the cooling water system in the control room
25. Isolate the gas supply (if connected): wait for about 5-10 minutes before turning off the air ventilation and exhaust gas extraction fan.

For non-HCCI mode, skip step 21 & 22.

This SOP does not necessarily cover all possible hazards associated with the machine and should be used in conjunction with other references. It is designed to be used as an adjunct to Safety Procedures and to act as a reminder to users prior to machine use.

Date of last review

Signature

Appendix E

Emergency Shut-Down Procedure

1. Turn OFF the main engine switch, or press emergency button
2. Call security or 2222 if someone has been injured, there is a fire emergency or there is a major escape of flammable gas or liquid posing a risk of explosion.
3. If Evacuation is necessary, sound the emergency alarm/(air horn)
4. Exit the building following the exit sign
5. Follow USQ emergency guidelines

This SOP does not necessarily cover all possible hazards associated with the machine and should be used in conjunction with other references. It is designed to be used as an adjunct to Safety Procedures and to act as a reminder to users prior to machine use.

Date of last review

|

Signature